AD-A218 981

SOIL LIQUEFACTION RESULTING FROM BLAST-INDUCED SPHERICAL STRESS WAVES

Thomas E. Bretz, Jr, Lt Col, USAF

January 1990

Final Report

Approved for public release; distribution unlimited.

DTIC
ELECTE
MAR 07 1990
S B D

Weapons Laboratory
Air Force Systems Command
Kirtland Air Force Base, NM 87117-6008

90 03 06 009

This final report was prepared by the Weapons Laboratory, Kirtland Air Force Base, New Mexico, under Job Order 2302Y202. Lt Col Thomas E. Bretz, Jr (NTES) was the Laboratory Project Officer-in-Charge.
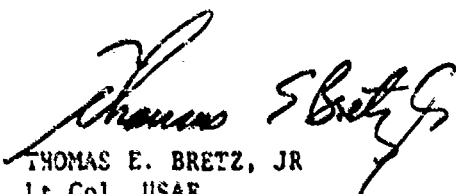
When Government drawings, specifications, or other data are used for any purpose other than in connection with a definitely Government-related procurement, the United States Government incurs no responsibility or any obligation whatsoever. The fact that the Government may have formulated or in any way supplied the said drawings, specifications, or other data, is not to be regarded by implication, or otherwise in any manner construed, as licensing the holder, or any other person or corporation; or as conveying any rights or permission to manufacture, use or sell any patented invention that may in any way be related thereto.

This report has been authored by an employee of the United States Government. Accordingly, the United States Government retains a nonexclusive, royalty-free license to publish or reproduce the material contained herein, or allow others to do so, for the United States Government purposes.
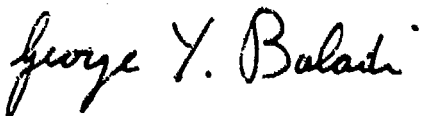
This report has been reviewed by the Public Affairs Office and is releasable to the National Technical Information Service (NTIS). At NTIS, it will be available to the general public, including foreign nations.

If your address has changed, if you wish to be removed from our mailing list, or if your organization no longer employs the addressee, please notify WL/NTES, Kirtland AFB, NM 87117-6008 to help us maintain a current mailing list.

This report has been reviewed and is approved for publication.

THOMAS E. BRETZ, JR
Lt Col, USAF
Project Officer

GEORGE Y. BALADI, GM-15
Technical Advisor
Civil Engineering Research Division

FOR THE COMMANDER

CARL L. DAVIDSON
Colonel, USAF
Chief, Civil Engineering Research Div

REPORT DOCUMENTATION PAGE

1. AGENCY USE ONLY (Leave blank)	2. REPORT DATE 1990 January	3. REPORT TYPE AND DATES COVERED Final Fall 1989	
4. TITLE AND SUBTITLE SOIL LIQUEFACTION RESULTING FROM BLAST-INDUCED SPHERICAL STRESS WAVES			**5. FUNDING NUMBERS** PE # 61102F DGO 626233 PR # 2302 TA # Y2 WU # 02
6. AUTHOR(S) Bretz, Thomas E., Jr, Lt Col, USAF			
7. PERFORMING ORGANIZATION NAME(S) AND ADDRESS(ES) Weapons Laboratory Kirtland AFB, NM 87117-6008			**8. PERFORMING ORGANIZATION REPORT NUMBER** WL-TR-89-100
9. SPONSORING/MONITORING AGENCY NAME(S) AND ADDRESS(ES)			**10. SPONSORING/MONITORING AGENCY REPORT NUMBER**

11. SUPPLEMENTARY NOTES

12a. DISTRIBUTION/AVAILABILITY STATEMENT Approved for public release; distribution unlimited.	**12b. DISTRIBUTION CODE**

13. ABSTRACT (Maximum 200 words)

Soil liquefaction resulting from blast-induced spherical stress waves is evaluated analytically and experimentally. An analytical model developed in this research predicts the dynamic and dissipation stages of porewater pressure in saturated sand subjected to the blast-induced spherical stress waves. Experimental test data are from detonations of explosive masses varying from 0.03 to 7.02 kg in water 1.8 m above a 1.8 m deep by 4.3 m diameter saturated sand sample placed at 84 percent relative density. The sand was saturated to 100 percent and instrumentation included porewater pressure transducers, accelerometers, inductance strain gages, total stress gages, and piezometers. Results of the tests are combined with results from a subsequent series of tests at 50 percent relative density and with charge masses from 0.00044 to 0.0588 kg to form the data base from which the analytical model is substantiated and empirical relations are developed for peak strain, peak porewater pressure, peak particle velocity, and peak residual porewater pressure as functions of scaled distance. Thresholds at which liquefaction is shown to occur are scaled distances <8 m/kg$^{1/3}$, peak radial stresses over 2200 kPa, and peak particle velocities >0.6 m/s. Keywords

14. SUBJECT TERMS Soil liquefaction; blasting; pore water pressure response; blast-induced liquefaction; stress wave; spherical stress wave; saturated sand; saturating sand; explosive testing; blast testing. (KT)			**15. NUMBER OF PAGES** 272
			16. PRICE CODE
17. SECURITY CLASSIFICATION OF REPORT UNCLASSIFIED	**18. SECURITY CLASSIFICATION OF THIS PAGE** UNCLASSIFIED	**19. SECURITY CLASSIFICATION OF ABSTRACT** UNCLASSIFIED	**20. LIMITATION OF ABSTRACT** UL

GENERAL INSTRUCTIONS FOR COMPLETING SF 298

The Report Documentation Page (RDP) is used in announcing and cataloging reports. It is important that this information be consistent with the rest of the report, particularly the cover and title page. Instructions for filling in each block of the form follow. It is important to *stay within the lines* to meet *optical scanning requirements.*

Block 1. Agency Use Only *(Leave blank)*.

Block 2. Report Date. Full publication date including day, month, and year, if available (e.g. 1 Jan 88). Must cite at least the year.

Block 3. Type of Report and Dates Covered. State whether report is interim, final, etc. If applicable, enter inclusive report dates (e.g. 10 Jun 87 - 30 Jun 88).

Block 4. Title and Subtitle. A title is taken from the part of the report that provides the most meaningful and complete information. When a report is prepared in more than one volume, repeat the primary title, add volume number, and include subtitle for the specific volume. On classified documents enter the title classification in parentheses.

Block 5. Funding Numbers. To include contract and grant numbers; may include program element number(s), project number(s), task number(s), and work unit number(s). Use the following labels:

C	- Contract	PR	- Project
G	- Grant	TA	- Task
PE	- Program Element	WU	- Work Unit Accession No.

Block 6. Author(s). Name(s) of person(s) responsible for writing the report, performing the research, or credited with the content of the report. If editor or compiler, this should follow the name(s).

Block 7. Performing Organization Name(s) and Address(es). Self-explanatory.

Block 8. Performing Organization Report Number. Enter the unique alphanumeric report number(s) assigned by the organization performing the report.

Block 9. Sponsoring/Monitoring Agency Name(s) and Address(es). Self-explanatory.

Block 10. Sponsoring/Monitoring Agency Report Number. *(If known)*

Block 11. Supplementary Notes. Enter information not included elsewhere such as: Prepared in cooperation with...; Trans. of...; To be published in.... When a report is revised, include a statement whether the new report supersedes or supplements the older report.

Block 12a. Distribution/Availability Statement. Denotes public availability or limitations. Cite any availability to the public. Enter additional limitations or special markings in all capitals (e.g. NOFORN, REL, ITAR).

DOD - See DoDD 5230.24, "Distribution Statements on Technical Documents."
DOE - See authorities.
NASA - See Handbook NHB 2200.2.
NTIS - Leave blank.

Block 12b. Distribution Code.

DOD - Leave blank.
DOE - Enter DOE distribution categories from the Standard Distribution for Unclassified Scientific and Technical Reports.
NASA - Leave blank.
NTIS - Leave blank.

Block 13. Abstract. Include a brief *(Maximum 200 words)* factual summary of the most significant information contained in the report.

Block 14. Subject Terms. Keywords or phrases identifying major subjects in the report.

Block 15. Number of Pages. Enter the total number of pages.

Block 16. Price Code. Enter appropriate price code *(NTIS only)*.

Blocks 17. - 19. Security Classifications. Self-explanatory. Enter U.S. Security Classification in accordance with U.S. Security Regulations (i.e., UNCLASSIFIED). If form contains classified information, stamp classification on the top and bottom of the page.

Block 20. Limitation of Abstract. This block must be completed to assign a limitation to the abstract. Enter either UL (unlimited) or SAR (same as report). An entry in this block is necessary if the abstract is to be limited. If blank, the abstract is assumed to be unlimited.

PREFACE

This report describes research performed by the author in partial fulfillment of the requirements for the Degree of Doctor of Philosophy at Colorado State University, Fort Collins, Colorado. The research consisted of an analytical and experimental evaluation of soil liquefaction resulting from blast-induced spherical stress waves.

The research was performed under the guidance of Dr Wayne A. Charlie, the author's graduate committee chairman. Dr Charlie and the remaining committee members, Dr Eric Rinehart, Dr Michael Harvey, and Dr Thomas Siller, all provided review, comments, and helpful discussions regarding this dissertation.

CONTENTS

LIST OF TABLES

LIST OF FIGURES

LIST OF SYMBOLS

a	cavity radius (m)
a_{max}	maximum acceleration (g or m/sec^2)
B	material constant
$\bar{B}$	material constant (1/msec)
B_m	bulk modulus of soil-water mixture (kPa)
B_s	bulk modulus of solid particles (kPa)
B_{sk}	bulk modulus of soil skeleton (kPa)
B_{sr}	rebound bulk modulus of soil skeleton (kPa)
B_u	unloading bulk modulus (kPa)
B_w	bulk modulus of water (kPa)
^{o}C	degrees in centigrade
C_c	coefficient of curvature
cm	centimeter
cm/sec	centimeters per second
cm/sec^2	centimeters per second per second
C_R	empirical coefficient
C_t	empirical coefficient
C_u	coefficient of uniformity
C_v	coefficient of consolidation (cm^2/sec)
D	constrained modulus (kPa)
D_B	scaled depth of burial ($m/kg^{1/3}$)
dB	decibel
DC	direct current
D_R	relative density (%)
D_v	detonation velocity (m/sec)
D_{50}	50th percentile diameter (mm)
E	modulus of elasticity (kPa)
e	void ratio
E_{sk}	soil skeleton modulus of elasticity (kPa)
F	depth of burst coupling factor
^{o}F	degrees in Fahrenheit

xi

f	site constant
FS	full scale
FSO	full scale output
G	shear modulus (kPa)
g	acceleration of gravity (9.81 m/sec^2)
gm	gram
G_s	specific gravity
H_c	post consolidation height (cm)
h_1	depth of liquefaction (m)
h_o	optimum depth of burst (m)
Hz	hertz (cycles/sec)
k	permeability (cm/sec)
kg	kilogram
kg/m^3	kilograms per cubic meter
kHz	kilohertz
km	kilometer
kPa	kilopascal
1	liter
ΔL_{pp}	peak-to-peak axial deformation
m	meter
M	inelastic skeleton modulus (kPa)
mA	milliampere
$m/kg^{1/3}$	scaled distance
mm	millimeter
mPa	megapascal
m/sec	meters per second
m/sec^2	meters per second per second
msec	millisecond
mV	millivolt
n	porosity
n_o	initial porosity
p'	material constant
P_D	detonation pressure (kilobars)
PETN	pentaerythritol tetranitrate
PPR	pore pressure ratio
PVC	polyvinyl chloride
R	radius of liquefaction (m)

r	distance from source (m)
r_d	stress reduction factor
rms	root-mean-square
sec	second
S	degee of saturation
s	site constant
t	time (sec)
TDR	transient data recorder
t_L	time of liquefaction (sec)
TNT	trinitrotoluene
u	porewater pressure (kPa)
u^*	radial movement (m)
u_e	excess porewater pressure (kPa)
u_{pk}	peak porewater pressure (kPa)
UPS	uninterruptible power supply
v	volt
VAC	voltage, alternating current
v_c	compression wave velocity (m/sec)
VDC	voltage, direct current
v_p	particle velocity (m/sec or cm/sec)
v_{pk}	peak particle velocity (m/sec or cm/sec)
v_r	radial particle velocity (m/sec or cm/sec)
v_s	shear wave velocity (m/sec)
w	charge mass (kg)
z	depth (m)
α	site constant
α_d	time decay constant (1/msec)
α_o	material and geometry constant (1/sec)
β	material constant
γ_c	cyclic shear strain
γ_v	volumetric shear strain
Δ	change in
ϵ	strain
ϵ^p	inelastic strain increment
ϵ_{pk}	peak strain
ϵ_r	radial strain

ϵ_t	tangential strain
ϵ_v	volumetric strain
ϵ_{vd}	irrecoverable volumetric strain
λ	elastic constant (kPa)
μ	Poisson's ratio
μ_s	soil skeleton Poisson's ratio
ϕ	stress function
ϕ'	effective angle of internal friction (degrees)
ρ	density (kg/m^3)
ρ'	submerged density (kg/m^3)
ρ_d	dry density (kg/m^3)
ρ_m	soil-water mixture density (kg/m^3)
ρ_{max}	maximum dry density (kg/m^3)
ρ_{min}	minimum dry density (kg/m^3)
ρ_w	density of water (kg/m^3)
σ	stress or total stress (kPa)
$\bar{\sigma}$	effective stress (kPa)
$\bar{\sigma}_e$	skeleton stress at elastic limit (kPa)
σ_i	initial total stress (kPa)
$\bar{\sigma}_i$	initial effective stress (kPa)
σ_o	peak stress (kPa)
σ_p	dynamic stress (kPa)
σ_r	radial stress (kPa)
$\bar{\sigma}_r$	radial effective stress (kPa)
σ_t	tangential stress (kPa)
$\bar{\sigma}_t$	tangential effective stress (kPa)
σ_v	vertical total stress (kPa)
τ	time after arrival of stress wave (msec)
τ_d	dynamic shear stress (kPa)
τ_s	shear stress (kPa)
ω	material constant (1/msec)
ω_o	material and geometry constant (1/msec)

CHAPTER 1

INTRODUCTION

1.1   SUMMARY OF RESEARCH

This dissertation documents research to investigate blast-induced soil liquefaction. An analytical model derived to predict the response of saturated sand to blast-induced spherical stress waves is presented. An experimental effort is described in which spherically shaped explosives were detonated in water above fully saturated sand instrumented to obtain porewater pressure, acceleration, total stress, and strain data. Results of the experimental testing are used to validate the analytical model and to establish empirical relationships for predicting blast-induced liquefaction.

The program was performed under a basic research grant from the Air Force Office of Scientific Research. As part of the program, a test site was developed at Colorado State University, Fort Collins, Colorado. The site was suitable for blasting operations, and all explosives were detonated by licensed blasters following strict local and federal controls.

Literature pertaining to blast-induced soil liquefaction is summarized in Chapter 2. Chapter 3 describes development of the analytical model to predict liquefaction induced by spherical stress waves from an explosive detonation. Chapters 4, 5, and 6, respectively, describe the test site; test materials, equipment and explosives; and test procedures. The test results are given in

Chapter 7, and the analysis of the results is presented in Chapter 8. The conclusions developed from the research are presented along with recommendations for additional research in Chapter 9.

1.2 SOIL LIQUEFACTION - BACKGROUND

1.2.1 Definition of Soil Liquefaction

In 1978, the Committee on Soil Dynamics of the Geotechnical Engineering Division, American Society of Civil Engineers, defined liquefaction as

> ...the act or process of transforming any substance into a liquid. In cohesionless soils, the transformation is from a solid state to a liquefied state as a consequence of increased pore pressure and reduced effective stress.

In this definition the key phrase is increased pore pressure. In a cohesionless soil subjected to external forces, the individual grains will shear against one another. If the void space in the soil is saturated with water and if the shear action causes a decrease in the void space, the porewater pressure will increase. When the porewater pressure equals the total stress, the effective stress becomes zero, the shear strength is zero, and the soil has become fully liquefied. The soil will remain in this liquified state until the excess porewater pressure dissipates to a level less than the total stress. As this dissipation occurs, the effective stress and shear strength increase until hydrostatic conditions are achieved and strength is regained.

1.2.2   Effects of Soil Liquefaction

The most catastrophic effect of liquefaction is the flow failure of slopes or earthfilled dams. Flows may be composed of liquefied soil or blocks of intact material riding on a layer of liquefied soil. These flows usually develop in loose, saturated sands or silts with slopes greater than 3 degrees. Other dramatic effects are settlement or tipping of buildings and piers, collapse of retaining walls, lateral spreading of inclined ground, ground surface deformation, and ground settlement with mud volcanoes and flooding of large areas (Committee on Earthquake Engineering, 1985).

An example of the effects of liquefaction is the result of the 1964 Niigata, Japan, earthquake in which the soil liquefied. Many structures settled over a meter; multi-story buildings tilted; underground tanks, manholes and conduits floated upwards; and large areas subsided over a meter (Seed and Idriss, 1967). In low lying areas, sand flows and mud volcanoes ejected water for up to 20 minutes after the earthquake (Gilbert, 1976).

Blasting has, likewise, resulted in dramatic liquefaction failures. The Calaveras earthfilled dam near San Francisco, California, had a slope failure during the later stages of construction. The slope moved approximately 100 meters upstream and dropped 30 meters in elevation. Blasting operations were reported to have occurred at this site (Hazen, 1920). Terzaghi (1956) noted that "spontaneous liquefaction" caused the failure of the SWIR III Dam in Russia in 1935. This liquefaction was due to nearby blasting operations. The effect of liquefaction was that the dam embankment flowed away and was reduced from a 2:1 to a 10:1 slope.

The effects of soil liquefaction are essentially the same regardless of the cause of the liquefaction. Whether an earthquake induces sufficient porewater pressure to liquefy a soil or whether blasting induces the pressure, the result is the same.

1.2.3 Blast-Induced Liquefaction Background

Considerable interest in blast-induced liquefaction occurred during the 1960's and 1970's. Many countries were performing or supporting research during this period, and several still are. The Dutch concern was evidenced by Kok's statement (Kok, 1978) on possible effects from the detonation of a 500,000 kilogram nuclear weapon. He stated that "everything will be liquefied ... all the structures will fall to pieces." Rischbieter (1977) noted that Germany and the Netherlands were interested because their coastal plains lay below sea level, and in Switzerland, the concern was with lake shore deposits consisting of soft, post-glacial alluvium. In Norway, Kummeneje and Eide (1961) conducted field tests which showed that excess porewater pressure and liquefaction could be induced by blasting. The Russians conducted extensive tests to better understand liquefaction and to develop methods to predict whether a soil is liquefaction prone (Lyakhov, 1961; Ivanov, 1967; and Florin and Ivanov, 1961).

The United States Army's concern with blast-induced liquefaction was the effect on explosive craters. Explosives set off in saturated, cohesionless sands can result in large, flat bottomed craters that extend to the depth of the water table. These craters offer a significant barrier to the mobility of tanks and construction equipment. In one case, a bulldozer drove into the bottom of a crater

and sank out of sight due to the presence of liquefied sand (Drake, 1978).

The United States Air Force expressed concern with blast-induced liquefaction. McCracken (1978), in introductory remarks to attendees at the 1978 International Workshop on Blast-Induced Liquefaction, stated that "we within the United States Air Force now believe that blast-induced soil liquefaction could be a far more serious threat to both civilian and military targets than we have given it credit for in the past." Charlie, et al. (1979) noted that there is a need to understand blast-induced liquefaction in order to evaluate military installations and to identify sites of high liquefaction potential.

Since the late 1970's, there appears to have been a decrease in interest with blast-induced liquefaction in some countries. This decrease may stem from the results of a test at the Meppen Proving Grounds, Federal Republic of Germany, in 1978. In this test, a structure was placed in a saturated soil and explosives were detonated nearby in an attempt to liquefy the soil and cause the structure to move. The test, however, resulted in only minor movement of the structure (Shaepermaier, 1978 a,b,c). Possible reasons for this non-dramatic response are that the soil around and beneath the structure may not have been fully saturated, the soil was probably quite dense due to earlier glacial activity, and explosives tests may have further densified the soil. All these factors decrease liquefaction susceptibility. The results of this one tests seem non-conclusive, and, as stated by Schaepermaier (1978b), give only initial information on structure stability with a number of open questions remaining.

1.3   OBJECTIVES

Objectives of this research were to:

-Develop an analytical model that predicts and mathematically describes porewater response to blast-induced spherical stress waves in saturated sand.

-Establish a data base by performing experimental explosives tests to generate spherical stress waves in saturated sand.

-Use the data base to substantiate the analytical model and to develop new and evaluate existing empirical relationships describing blast-induced liquefaction.

1.4   METHODOLOGY

1.4.1   Analytical Model

An analytical model was developed to predict and mathematically describe porewater pressure response to spherical stress waves in saturated sand due to detonation of explosives. The model combines empirical methodology to determine peak radial stress with a theoretical treatment of radial and tangential strains, stresses, and porewater pressure.

The initial calculation in the analytical model is peak radial stress which is performed with empirically derived scaled distance equations (scaled distance is distance from the charge divided by cube root of charge mass which represents explosive energy). The soil-water mixture is assumed to behave elastically during exposure to the stress wave, and radial and tangential strains are determined with dynamic elastic stress-strain equations. It is further assumed that the soil skeleton undergoes the same strains as the elastic soil-water mixture; however, the stress-strain behavior of the skeleton is considered inelastic; i.e., hysteresis occurs. Thus, the inelastic change in radial and tangential effective stresses is determined as a

function of time during passage of the stress wave. These effective stresses are combined with the change in total stresses occurring over time to calculate the dynamic porewater pressure response as a function of time. Once the stress wave has passed, the porewater pressure is at an elevated residual level. One-dimensional consolidation theory is assumed for dissipation of the excess porewater pressure. The rate of dissipation is based on drainage distance, soil permeability and soil compressibility.

The above procedures were incorporated into a BASIC program to run on a personal computer. The program, named POUDRE, permits rapid calculation of the porewater pressure and effective stress response during and after passage of the spherical stress wave. The analytical model provides a mathematical description of the phenomena associated with blast-induced spherical stress wave passage through saturated sand. The results of model calculations indicate that the observed porewater pressure response does, indeed, have a theoretical explanation.

1.4.2 Explosive Testing

Explosive testing to establish a data base and to permit validation of the analytical model described above was performed at a site developed in this research program at the Colorado State University Engineering Research Center where blasting is permitted with up to 7 kilograms of explosives. Controlled soil conditions were achieved by placing 26 cubic meters of sand in a container below the regional groundwater table. Locating the sand below the water table minimizes potential stress wave reflections from the sample's boundaries. The sand was placed at controlled and repeatable relative

densities and was fully saturated with deaired water. Porewater pressure transducers, accelerometers, stress and strain gages, and variable density inclusions were located in the sand at specified locations. A piezometer was used to obtain late time porewater pressure response. Digital transient data recorders recorded the response of the embedded instruments, and video cameras recorded the tests and the piezometer response.

All tests in the program were performed by detonating explosives in water above the saturated sand to minimize noise and debris hazards and to maximize the explosive effects. Testing consisted of single detonations of explosives of different masses. Data were recorded during and immediately after each detonation. The settlement of the sand sample was measured by a scuba diver and checked against measurements recorded by strain gages. After the final test, the locations of the pre-placed, varying density inclusions were recorded.

1.4.3 Empirical Relationships

The explosives tests provided data that were statistically analyzed to develop empirical equations relating peak values of stress, strain, particle velocity, and pore pressure ratio to scaled distance. Equations relating pore pressure ratio to peak strain and peak particle velocity were compared to similar equations reported in the literature. Threshold values for peak strain, peak particle velocity, and scaled distance defining liquefaction limits were determined and are considered accurate estimates of the probability and extent of blast-induced liquefaction.

CHAPTER 2

LITERATURE REVIEW

2.1 BLAST-INDUCED LIQUEFACTION EVENTS

Numerous cases have been reported in which blast-induced liquefaction may have occurred. Table 2.1 is a summary of many of these cases, and a brief description is provided in the following paragraphs.

Table 2.1 Blast-Induced Liquefaction Cases

Calaveras Dam, California	1918
Svir III Dam, Russia	1935
Hague, the Netherlands	World War II
Pacific Attolls	1950's
Snowball Event, Canada	1964
Prairie Flat Event, Canada	1968
Dial Pack Event, Canada	1970
Pre-Dice Throw, New Mexico	1975
Hayman Igloo Test, Utah	1988

The earliest case reported in which blast-induced liquefaction may have occurred was the Calaveras dam in California which failed as it was nearing completion in 1918 (Hazen, 1920). The failure consisted of a 600,000 cubic meter (m) sand flow from the face of the dam after a shock had occurred. The sand moved 90 m and dropped over 30 m in elevation. It was not stated that blasting was the cause of the shock, but blasting activities at the site were mentioned.

Terzaghi (1956) and Gilbert (1976) reported on the 1935 failure of the Svir III Dam in Russia. The dam consisted of a concrete core with sand embankments formed by dumping moist sand on

both the upstream and downstream sides. After the reservoir was filled, blasting operations were performed about 100 m upstream from the dam. Shortly after the blasting, the sand embankment liquefied and flowed away. Terzaghi (1956) stated that "spontaneous" liquefaction caused a slope reduction in the embankment from 2:1 to less than 10:1. A detailed description of this dam is given by Graftio (1936).

Trense, in a discussion of Kok's paper (Kok, 1978), noted that during World War II, a large part of the Hague, the Netherlands, was damaged due to explosive-induced liquefaction. The Hague had been built on sand dunes, and liquefaction was reported to have occurred.

Blouin (1978) discussed possible liquefaction from nuclear tests in the Pacific atolls of Eniwetok and Bikini in the 1950's. Evidence of liquefaction included the shape of the craters, which were unusually broad and shallow, significant settlements, and sand boils. It was estimated that a 15,000 kiloton above ground burst resulted in liquefaction as far as 1300 m from ground zero.

Another cratering study showing liquefaction evidence was the Snowball cratering test in which a 500 ton hemisphere of trinitrotoluene (TNT) was detonated on the ground surface at the Watching Hill Range in Alberta, Canada. The crater's floor was comparatively flat, formed by a "great thickness" of sedimentary infilling. There was an uplift in the center of the crater with extrusion of "fluidized" material forming a single pseudo-volcanic cone on top of the uplift (Jones, 1976). Sand boils existed in and around the crater, and ground subsidence with circumferential surface cracks occurred out to 155 m from ground zero (Gilbert, 1976).

Another crater test was the Prairie Flat event in 1968. In this test, also at the Watching Hill Range, a 500-ton TNT surface charge was again detonated (Melzer, 1978a). The results were geysering, a rise in water table from an initial depth of 7 m, and formation of springs (Langley, et al., 1972 and Charlie, 1978).

The Dial Pack Event was also a 500-ton surface TNT test performed at the Watching Hill Range in 1970. About 20 minutes after detonation of the spherically shaped charge, geysers began occurring in cracks, open boreholes, and a nearby well. The well, which had a pre-test water level at 6.7 m below the ground, had water flowing to the surface for an hour after the blast. A geyser, 82 m from the detonation, flowed for about 10 hours. Springs inside the crater flowed for about 36 hours (Charlie, 1978).

Pre-Dice Throw Events I and II were crater tests performed at the White Sands Missile Range in 1975. In the tests, 100 tons of high explosives were detonated above ground. The local geology consisted of 2 m of dry to moist, silty clay over saturated clays, sands, and silts. The resulting craters were flat, and water springs flowed for several hours (Melzer, 1978a).

The Hayman Igloo test consisted of detonation of 200,000 kilograms (kg) of TNT equivalent high explosives in a weapons storage structure. The test, performed by the United States Air Force at the Utah Test and Training Range near the Great Salt Lake, was an evaluation of the effects of a detonation on surrounding weapons storage structures. The result was a crater about 120 meters in diameter and dish-shaped. A great deal of water was present in the crater following the test. The original water table was at a depth of about 5-6 meters. One of the surrounding structures was "swallowed"

and ended up 0.6 meters below the level of the apparent crater (Gill, 1989).

2.2 LIQUEFACTION PROCESS

2.2.1 General

Blouin and Schinn (1983) discussed the liquefaction process as the collapse of a loose, saturated soil skeleton, resulting in pore volume reduction. The soil behaves like a dense fluid, with no effective stress and no shear strength, and loses its capacity for structural support. Terzaghi (1956) called this process "spontaneous liquefaction."

In any process where porewater pressure generation is important, the basic variable that must be understood and determined is irrecoverable strain of the soil skeleton. This strain could result from either shear or compression waves. The irrecoverable volumetric strains in the soil skeleton are responsible for pore pressure changes. Put basically, particles move and the skeleton changes volume (Marti and Cundall, 1978). If the strains are compressive, the porewater will also be strained compressively; thus, the porewater pressure will increase (Prater, 1977) and will remain at increased levels until drainage occurs, which can be minutes, hours or even days (Charlie, et al., 1985a).

Liquefaction may also occur in areas that were not stressed or did not initially liquefy (Studer and Kok, 1980; Blouin and Schinn, 1983). It may originate at a deep layer within a mass of soil, and due to localized movement of the porewater there can be a loss of strength in adjacent soils (Committee on Earthquake Engineering, 1985). A situation termed hydrodynamic uplift is caused by the excess

water flowing toward the surface (Rischbieter, 1977). This upward flow of water may be the cause of surface features associated with liquefaction, such as sand boils, "quick conditions," or water seepage causing inundation. Lyakhov (1961) noted that the formation of a new soil structure begins in lower regions and expands gradually upward, with an average speed of 0.2 meters per second (m/sec).

2.2.2   Blast-Induced Liquefaction

Detonation of explosives in soil causes a stress wave to propagate radially from the charge. The duration of this high pressure pulse is only milliseconds (Dowding and Hryciw, 1986). During passage of a stress wave, compression occurs, which is a function of the volumetric compressibility of the porewater, the air bubbles, and the solid particles (Ivanov, 1967). In sands that are loose and saturated, the stress wave can cause a residual porewater pressure higher than hydrostatic levels if radial compressive strains and tensile circumferential strains disrupt the grain structure. If the residual porewater pressure reaches the total stress, shearing resistance is lost. Dissipation of the residual porewater pressure can take minutes or days depending on permeability, soil skeleton compressibility, and drainage conditions (Dowding and Hryciw, 1986).

Studer and Kok (1980) identified three categories of porewater pressures associated with a blast-induced stress wave. They are hydrostatic, dynamic and semi-dynamic (residual). Hydrostatic porewater pressure exists before and well after the impulse load on the sand mass. It is essentially constant other than during and following passage of the stress wave. The dynamic porewater pressure is directly related to the amplitude of the stress wave. This

pressure can be strongly irregular and alternating, and it generally occurs within a few milliseconds (msec) for conventional explosives and longer for nuclear explosives. The residual porewater pressure is governed by the soil conditions and intensity of loading. If the soil structure collapses, residual porewater pressure may result and remain above hydrostatic levels for several days. Charlie and Veyera (1985) further categorized the porewater pressure response during blasting. They divided the dynamic pressure into transient response during loading and a short-term residual response immediately after passage of the stress wave.

2.2.3 Earthquake versus Blast-Induced Liquefaction

In earthquakes, loading results from oscillatory shear waves, with the predominate motion being in the horizontal plane. There are usually many cycles with periods of around one second, and the accelerations are less than gravity (g). The loadings from a blast tend to be more complicated. When a charge is detonated in soil, a compression pulse propagates radially outward. Compression waves dominate, but shear waves are also a factor. Dominant frequencies depend on the explosive yield and can range up to 100 Hertz (Hz) or higher. Blast-induced accelerations are orders of magnitude higher than accelerations from earthquakes (Blouin and Schinn, 1983). Charlie, et al. (1981) stated that during blasting, both shear and compressive waves are important, and intense radial and tangential compressive strains result.

Blouin and Schinn (1983) noted that sand boils following the Niigata, Japan, earthquake were very similar to those that developed after a 500 ton surface explosion in Canada as well as a nuclear

explosion in the Pacific. In both cases, these sand boils resulted from liquefied material flowing upward though sediments to the ground surface.

Arya, et al. (1978), in a study of earthquake induced liquefaction potential, attempted to use blasting to simulate earthquake ground motions. It was concluded that a single large acceleration from blasting can produce a rise in porewater pressure that could be produced by several cycles of small acceleration pulses as in earthquakes. The significance is that the end product is the same; i.e., rise of porewater pressure. Melzer (1978a) had the same basic conclusion: the mechanisms creating liquefaction can be very dissimilar, but the end products are the same.

2.3 GROUND SHOCK FROM EXPLOSIONS.

In order to better understand blast-induced liquefaction, it is necessary to consider the effects of blasting in soil. This section provides a summary of the explosive process, stress wave propagation in soil, and the theory of spherical stress waves in elastic media.

2.3.1 Explosive Cavity

During contained explosions in water and water-saturated soil, a high pressure, gaseous cavity forms around the charge. As the cavity enlarges, there is a decrease in the pressure to a value less than static conditions. A reversal in movement results, the cavity becomes smaller, and the pressure again increases. A secondary expansion then occurs, the cavity enlarges, pressure drops, and reversals result. In this way, pulsations occur. The second and

subsequent pulsations are markedly less intense than the initial swell. Immediately after the explosion, the walls of the cavity collapse. It fills with soil, and the gases escape to the surface if the explosion is above a certain depth. For a totally confined detonation, up to 75 percent of the explosive energy can be transferred into the soil (Ivanov, 1967). The Blaster's Handbook (DuPont, 1980) gave an equation for the detonation pressure, P_D, in kilobars, as follows:

$$P_D = 2.5 \, \rho \, D_v^2 \times 10^{-6} \qquad (2.1)$$

where ρ is density (grams per cubic centimeter) and D_v is detonation velocity (m/sec). It was noted that the explosion pressure after adiabatic expansion to the original explosive volume is theoretically about 45 percent of the detonation pressure. Henrych (1979) provided a detailed discussion of the dynamics involved with explosions in soils.

2.3.2 Stress Wave Propagation in Soil

Crawford, et al. (1974) discussed the propagation of stress waves through soil. The distance these waves propagate depends on the type and weight of explosive, depth of burial, and properties of soil. The magnitude of the pressure wave is dependent on the properties of the soil, distance from the charge, coupling of explosives energy into the soil, and explosive type and quantity. Drake and Little (1983) stated that ground shock propagation in earth media is a complex function of dynamic constitutive properties of the soil, the explosive, and the geometry of the situation. The effect of

saturation is significant. As saturation nears 100 percent, increases in peak stresses and accelerations occur, and the compression wave velocity can be over 1,500 m/sec. The importance of saturation is illustrated in Figure 2.1 from Allen, et al. (1980).

2.3.3 Theory of Stress Wave Propagation

The theory of propagating stress waves has been discussed in many text books and research publications. References on this subject include Rinehart (1975), Richart, et al. (1970), Griffiths and King (1965), Miklowitz (1978), and others. This section briefly summarizes some key aspects of stress wave propagation applicable to detonations in soil.

As a stress wave with an instantaneous rise time propagates through an elastic medium, an instantaneous movement of particles will occur. These particles move with velocity, v_p, which is linearly related to an instantaneous stress, σ, at the same point as

$$\sigma = \rho \, v_c \, v_p \qquad (2.2)$$

The product $\rho \, v_c$ is called the acoustic impedance of the medium where ρ is density and v_c is compression wave velocity (Rinehart, 1975).

A second useful relationship is between strain and velocity. A compressive strain, ϵ, will occur due to the passage of a stress wave, and this strain is linearly proportional to the particle velocity (Timoshenko and Goodier, 1970) as

$$\epsilon = v_p \, / \, v_c \qquad (2.3)$$
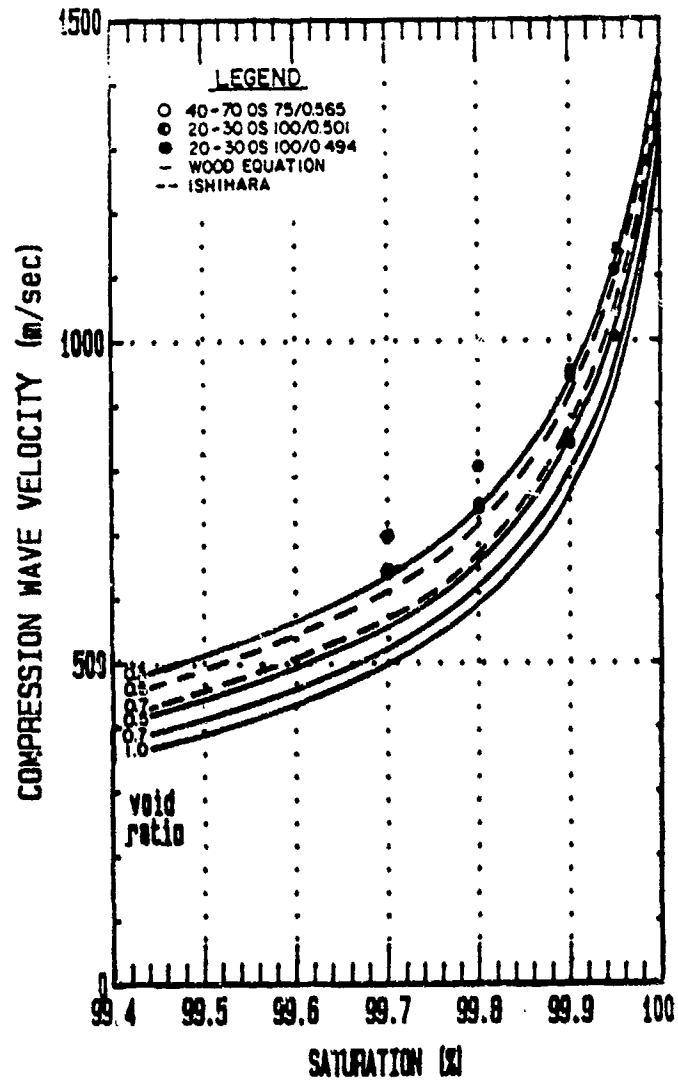
Figure 2.1 Range of compression wave velocities in Ottawa sand as a
function of void ratio and saturation (from Allen, et al., 1980).

By combining the two above equations and the relationship between stress, strain and unconstrained modulus of elasticity, E ($E = \sigma/\epsilon$), the resulting equation is

$$v_c = (E/\rho)^{1/2} \tag{2.4}$$

Timoshenko and Goodier (1970) and Rinehart (1975) described spherical stress waves in an elastic medium. With a spherical stress wave propagating outward from a spherical cavity, the expressions for radial, tangential, and volumetric strains (ϵ_r, ϵ_t, and ϵ_v) are

$$\epsilon_r = \frac{\partial u^*}{\partial r} \tag{2.5a}$$

$$\epsilon_t = \frac{u^*}{r} \tag{2.5b}$$

$$\epsilon_v = \epsilon_r + 2\epsilon_t \tag{2.5c}$$

where u^* is the radial movement and r is the distance from the source. Applying Hooke's laws yields expressions for radial and tangential stresses (σ_r and σ_t):

$$\sigma_r = \frac{E}{(1+\mu)(1-2\mu)} [(1-\mu)\epsilon_r + 2\mu\epsilon_t] \tag{2.6a}$$

$$\sigma_t = \frac{E}{(1+\mu)(1-2\mu)} [\mu\epsilon_r + \epsilon_t] \tag{2.6b}$$

where μ is Poisson's ratio and E is the modulus of elasticity. The expression for u^* is

$$u^* = \frac{\partial \phi}{\partial r} \qquad (2.7)$$

where ϕ is a stress function.

At the wave front, i.e., where the stresses are maximum, Rinehart (1975) gave relations for radial particle velocity, v_r, and stresses, which are

$$v_r = \sigma_o \, a \, / \, \rho \, r \, v_c \qquad (2.8)$$

$$\sigma_r = \sigma_o \, a \, / \, r \qquad (2.9)$$

$$\sigma_t = \lambda \, \sigma_o \, a \, / \, (\lambda + 2G)r \qquad (2.10)$$

$$\sigma_r = \rho \, v_c \, v_r \qquad (2.11)$$

where σ_o is peak stress at the source, a is the radius of the cavity at the source, ρ is density, and λ and G are elastic constants defined as

$$\lambda = \frac{E \, \mu}{(1+\mu)(1-2\mu)} = \frac{2\mu G}{(1-2\mu)} \qquad (2.12)$$

$$G = \frac{E}{2(1+\mu)} \qquad (2.13)$$

These elastic equations may be applicable to spherical explosions in saturated soil, although saturated soil is not a perfectly elastic medium. The theoretical relationships do, however, provide an

approximation and help in the understanding of the blast-induced liquefaction phenomenon.

2.4   THEORETICAL TREATMENTS OF LIQUEFACTION

Blast-induced liquefaction has received a great deal of attention in the past few years, but there is no generally accepted theory to explain the mechanism or to predict its occurrence or effects (Fragaszy, et al., 1983). More specifically, there appears to be no generally agreed upon theory to enable simple and accurate prediction of blast-induced porewater pressures (Studer and Kok, 1980). This section summarizes different theoretical treatments used to describe the liquefaction phenomenon.

2.4.1   Threshold Strain and Threshold Particle Velocity

A theory frequently discussed in earthquake-induced liquefaction is that of a threshold strain level. In this theory, cyclic shear strains must exceed a threshold level before excess porewater pressure is generated (Committee on Earthquake Engineering, 1985). Dobry and Swiger (1979) stated that there is a threshold cyclic strain that determines the stability of sands. When a cyclic strain is less than the threshold strain, there is no densification nor porewater pressure increase. If, however, the cyclic strain is greater than the threshold strain, densification and porewater pressure increases will occur. For a range of stresses from 50 to 200 kilopascals (kPa), the threshold strain should be between $1x10^{-2}$ and $2x10^{-2}$ percent. In 32 case histories of sites that did or did not liquefy during strong earthquakes, and for cyclic strains greater than 10^{-2} percent, liquefaction was reported. The Committee on Earthquake

Engineering (1985) stated that repeated back and forth straining of dry sands showed a threshold strain of approximately 1×10^{-2} percent below which no further densification occurred. Charlie, et al. (1985a) noted that compressive strains of less than 1×10^{-2} percent should be in the elastic range of soil; therefore, residual porewater pressures would not be induced after passage of a stress wave. Since peak particle velocity (v_{pk}) is directly related to peak strain (from Equation 2.3), a soil with a compression wave velocity of 1,500 m/sec (i.e., a saturated soil) has a threshold particle velocity of 0.15 m/sec. Exceeding this threshold could result in liquefaction. This value corresponds to a peak strain of 1×10^{-2} percent.

2.4.2 Critical Acceleration

Maslov (1985) discussed a critical acceleration of a soil mass causing an increase in porewater water pressure. If an induced acceleration is greater than a "critical acceleration," a dynamic porewater pressure increase occur. Acceleration correlates well with earthquake-induced damage potential; however, it does not correlate well with blast induced damage potential.

2.4.3 Elastic-Plastic Behavior

Several researchers stated that the water phase in saturated soil remains elastic during load-unload cycles. For example, Charlie, et al. (1985b) noted that as compression waves act on vibration sensitive, two phase materials like loose saturated sands, there can be elastic strain in the water phase but plastic strain in the sand skeleton. The result of this behavior is an increase in porewater pressure. Rischbieter (1977) and Shaepermeier (1978d) made the same

assumption: stress-strain behavior of the porewater is linearly elastic; however, the grain matrix exhibits non-linear behavior and hysteresis (i.e., loading and unloading follow different paths and permanent strain results). Baladi and Rohani (1979) also presented an elastic-plastic model to simulate stress-strain-pore pressure response of saturated granular materials. This constitutive model contains seven material constants and is capable of reproducing the hysteretic behavior of the material.

2.4.4   B- and C- Porewater Pressure Parameters

Fragaszy and Voss (1986) and Bolton (1989) assumed that the dynamic strain in the skeleton is equal to the overall strain of the total soil-water mixture and that hysteresis occurs in the soil skeleton. Skempton's B parameter is used to predict the increase of porewater pressure for isotropic compression, and Skempton's C parameter is used for confined compression. With B or C less than unity, this pressure increases less than the total stress. Thus, during loading, there is an increase in effective stress. During unloading, the B or C value is assumed to be less than during loading, and the porewater pressure drops more slowly than the total stress. At some point, the porewater pressure may equal the total stress, which is liquefaction. Bishop and Hight (1977) provide an extensive discussion of the derivation of the B parameter. Lambe and Whitman (1969) provide the derivation of the C parameter.

2.4.5   Tensile Strain

The above theories were based on liquefaction or porewater pressure increase due to compressive strain. Melzer (1978) attributed

blast-induced liquefaction to geometric dispersion of explosive waves.
Since large magnitude ground waves diverge in a cylindrical or
spherical mode, late time tensile strains are created perpendicular to
the compression wave direction. As saturated sand particles are
radially displaced and tangentially separated, the soil fabric loses
its strength, and the porewater carries the load.

2.4.6 Water-Grain Coupling

Biot's theory (Biot, 1956) of wave propagation in a fluid
saturated porous medium has been used to explain the influence of
coupling between the soil grain structure and the pore fluid (eg.,
Hardin and Richart, 1963). In this theory, stress-strain
relationships include coupling coefficients and elastic constants. A
major difficulty in applying the theory is determination of the
material parameters (Studer and Kok, 1980).

2.4.7 Porewater Pressure Dissipation

Tanimoto (1967) and True (1969) derived equations relating
porewater pressure dissipation to time based on soil consolidation.
Finn, et al. (1977) and Finn (1978a) derived a model to predict
porewater pressure dissipation during earthquake loading when there is
simultaneous generation and dissipation of pressure due to reversing
shear stresses. In this model, equations are solved simultaneously
and continually updated values of porewater pressure are calculated.
An additional approach by Florin and Ivanov (1961) describing the time
period when liquefaction is occurring is based on seepage and water
equilibrium in elementary boundary layers.

2.5   LABORATORY TESTS

This section is a review of laboratory tests performed to investigate blast-induced liquefaction. Four types of tests are discussed including shock tube tests, impact tests, small scale blast tests, and quasi-static tests. In addition to the following summaries, a comprehensive review of the tests is provided by Charlie, et al. (1988).

2.5.1   Shock Tube Tests

Perry (1972) reported on laboratory tests to determine whether variable density inclusions would sink or rise in wet sand subjected to one-dimensional dynamic shock loading. Cubes of wood, wax, brick, aluminum and steel were placed in sand in a steel container. Saturation was attempted by adding water and applying a vacuum. In thirteen tests, the highest computed saturation was 99.91 percent. The movement of the cubes did not yield conclusive results.

Studer (1978) and Studer and Hunziker (1977) discussed shock tube tests to investigate the behavior of saturated sands exposed to an air-blast wave which induced a direct pressure into the sands. Three uniform grade quartz sands were used, and saturation was 99 to 99.5 percent. The results of 25 tests on 5 specimens showed a residual porewater pressure in the sand and expulsion of water to the surface. The coarser grained sands behaved basically the same as the finer grained material except that porewater pressures dissipated much more quickly. The fine sand took about 9 seconds for dissipation. Also, in successive blast tests, it was noted that the results were very similar; i.e., "if liquefaction occurs once, it does not prevent it occurring a second or more times."

Studer (1978) also reported on tests in a tunnel in which charges were detonated. A test container was placed just outside the tunnel. In all tests, porewater pressures increased and fluctuated from high peak values to negative values (less than static) and then to residual levels for a finite time.

Quaak (1978) discussed shock-tube tests where sand was placed in a tank and saturation was attempted by slowly adding water from the bottom which created a loosely packed sand sample. The sand-filled tank was placed in the shock tube, and a bunker model was put in the sand prior to the shock. A "short while" after the ground shock was applied, the bunker floated up.

Veyera (1985), Hubert (1986), and Bolton (1989) described laboratory experiments in which fine, uniform sands were placed in a shock tube and subjected to one-dimensional, high amplitude, short duration compression loads. Fully saturated sands were tested at varying relative densities in undrained conditions. Liquefaction was generally more difficult to induce as density and effective stress increased. The threshold compressive strain, below which liquefaction did not occur, was less than 0.01 percent and liquefaction was generally observed at strains greater than 0.1 percent (Veyera, 1985). Veyera tested Monterey No. 0/30 sand, Hubert tested Eniwetok coral sand, and Bolton tested Poudre Valley sand.

2.5.2 Impact Tests

Tanimoto (1967) presented results of impact experiments on saturated, fine grained sand which was placed loosely in a container completely submerged in water. An impact was applied with a free falling hammer. After one impact, it was observed that porewater

pressure peaked at 0.36 seconds near the bottom of the sand and gradually decreased to hydrostatic levels at 25 seconds. An approximately linear triangular distribution of settlement versus time occurred until 90 percent consolidation.

Ruygrok and Van der Kogel (1980) discussed tests to simulate wave action in asphalt covered sand-dikes. The concern was that due to the impact of ocean waves on these dikes, the soils could liquefy. A polyurethane "slab" was placed over a sandbed with varying porosity and moisture contents. A falling weight impact load was applied to a circular area on the slab over the sand in a test bin. In three consecutive tests, liquefaction was reported due to porewater pressure increases. The porewater pressure rose, and it remained at the liquefaction level for finite lengths of times (tens of seconds) in the shallower regions of the test bin. At deeper levels, the porewater pressure showed liquefaction for only a few tenths of a second.

2.5.3 Blast Tests

Ivanov (1967) reported on laboratory experiments to investigate compaction of Volga sand with surface, underwater, and buried detonations. The charges consisted of 1.5 gram (gm) explosives. In these tests, charges were either placed on the soil surface, suspended in water above the sand, or buried sufficiently deep enough to prevent crater formation. The experiments were conducted in a concrete container with a sand height of about 1 m. The saturation of the sand was at a level less than 100 percent. The results showed increased porewater pressures for over 200 seconds after some detonations. Ivanov also reported on laboratory

investigations with 1.5 to 4.5 gm charges placed at depths of 30-50 centimeters (cm). Immediately after detonation, gases "gushed" out at the surface, camouflets were formed, and heavy objects sank into the soil. After 10 to 15 explosions, porewater pressure increases practically stopped.

Vesic, et al. (1967) performed small scale cratering experiments by detonating hemispherical explosives charges in wet, dense sand in an aluminum box. The sand was saturated by adding water from the bottom. These tests were performed to match previous studies with dry sand, and significant differences in crater size and shapes were observed. The apparent volumes of the craters were about ten times greater than those observed in the dry sand, and the shapes were flatter and broader. It was concluded that the porewater had a significant effect on the cratering mechanisms.

Dowding and Hryciw (1986) reported on a laboratory investigation in which explosives were detonated in a 102 cm high tank of loose saturated sand. The surface settlements and maximum water rise in piezometer standpipes ranged from 0.8 to 1.7 cm and 152 to 178 cm, respectively.

2.5.4 Quasi-Static Tests

Fragaszy, et al. (1983) reported on a series of high pressure undrained, isotropic compression tests on Eniwetok coral sands, Ottawa sands, and Monterey No. 0 sands. A high pressure triaxial system was used in the tests in which soil samples were saturated and brought to an initial confining and porewater pressure. Typical tests consisted of loading and then unloading to the original value. One cycle of load-unload took 1-2 minutes. All the initial tests on Eniwetok sand

resulted in liquefaction during unloading. The Ottawa sands did not liquefy; however, the residual porewater pressure increased by 50 percent. A sieve analysis showed that significant particle crushing and cracking occurred in the Eniwetok sand. It was concluded that this breakage may have been a significant factor in the development of liquefaction.

Bolton (1989) conducted similar tests on water saturated Monterey No. 0/30 sand in confined loading-unloading. Bolton was able to liquefy the sand.

2.6 FIELD EXPERIENCE

This section is a summary of field experience with blast-induced liquefaction. Field experience is categorized into site investigation efforts and experimental research. In addition to the summaries provided below, a comprehensive review is provided by Charlie, et al. (1988).

2.6.1 Site Investigations

Ivanov (1967) discussed field tests to investigate compressibility of soils with explosives. In one test on the banks of a stream near the Volga River, 5 kg charges detonated at depths less than 9 m resulted in liquefaction. Metallic objects on the surface sank as well as workers in the vicinity who were observed to sink up to their waists in liquefied sand. Water geysered and discharged for 10-20 minutes, and sand boils resulted. The majority of surface settlement occurred within 4-5 minutes. A net of concentric cracks appeared around the charge borehole, and in some shots, nearby sloping soil masses liquefied and moved into low lying regions.

Numerous references discuss the use of explosives to investigate or improve construction sites. Queiroz, et al. (1967) reported on a program to densify a sandy foundation at the Rio Casca III, Brazil, dam site. Maximum settlements of 0.25 m occurred, and there was a significant increase in relative density. Klohn, et al. (1981) reported on successful efforts to densify sand tailings in Canada by blasting. Solymar, et al. (1984) discussed a project to treat a dam site at Jebba, Nigeria. The results were improved relative densities. Prakash and Gupta (1970) reported on a field test program to investigate liquefaction potential at the Tenughat dam site in India. Long, et al. (1981) documented a program to evaluate blast-induced liquefaction potential at a nuclear power plant site in Italy. In all these cases, excess porewater pressure was generated due to blasting, and notable surface settlements resulted.

There have also been cases in which blasting was done underwater to improve or investigate sites. Ivanov (1967) discussed tests at Gorki, Russia, in fine grained sands deposited underwater. The sand had low relative densities (10-20 percent), and a 5 kg charge detonated at a depth of 4.9 m caused geysering and upward flow of water for 10 minutes. The supports of a bridge, 35 m away, sank into the sand. Kummenje and Eide (1961) described blasting by the Norwegian Geotechnical Institute to investigate sea-bottom sands at four sites. Charges varying from 0.07 kg to 2.4 kg were detonated up to 10 m below the sea bed, and porewater pressure response was measured. Large settlements of the sea floor were reported, and it was concluded that blasting may be an economical site improvement technique.

2.6.2   Experimental Blasting for Liquefaction Research

Puchkov (1962) described the effects of seismic ground motions on the liquefaction phenomenon. He presented recordings of seismic oscillations as a result of various sized explosions at an unreported site. Table 2.2 gives peak particle velocities at different distances from charges in water-saturated sands.

Table 2.2   Peak Particle Velocities (from Puchkov, 1962)

Charge (kg)	Depth (m)	Distance (m)	Particle Velocity (cm/sec)	Radius of Liquefaction (m)
5	5	15	6.3	8
25	2.5	12	6.7	14
40	2.6	10	11.4	16
100	10	25	7.2	24
1000	7.5	40	7.0	47

Puchkov concluded that particle velocity is a "necessary, but insufficient criteria of sand liquefaction." The average was 7.7 centimeters per second (cm/sec), and it was assumed that this velocity was the seismic parameter that characterized destruction of the solids and the occurrence of liquefaction in water saturated sand.

Trense (1977) reported on the results of Dutch tests at the Peel area, Holland, in which porewater pressure response to blasting was measured. The water table was at a depth of 1.20 m. The soil was mostly medium sized sand with small clay layers and pieces of shells. Excess porewater pressure was measured at a depth of 11.2 m and a distance of 6.5 m from a 3 kg charge. The peak porewater pressure measured was 9500 kPa.

Rischbieter, et al. (1977) discussed liquefaction tests performed at the Meppen Proving Ground, Holland. During these tests, the ground water table was fairly low; therefore, a pit was dug and

lined with polyethylene sheeting. The pit was filled with fine grained sand and water. Porewater pressure and soil stress gages were placed in the pit, and 1.25 kg charges were placed in boreholes around the pit. After detonation of each charge, the measurements indicated that liquefaction had occurred.

Schaepermeier (1978 a,b,c), and Studer, et al. (1978) reported on tests at the Meppen Proving Ground to assess the stability of a shelter buried in saturated soil. The water table depth was 4 m. The soil's grain size distribution showed mostly uniform, fine sands of glacial origination. The shelter, a 6x4x2.6 m structure, was placed in the soil with the top nearly flush with the ground surface. One test was with 200 kg of TNT detonated at a distance of 30 m and depth of 10 m. A second test was performed with 50 kg of TNT 9 m deep at a 15 m distance. In the 200 kg test, a crater resulted which indicated that only 30 percent of the energy was effective in producing a ground shock. In the vicinity of the shelter, some small sand boils lasting 10-15 minutes were observed. The 50 kg test also caused small, short duration sand boils. Significant movement of the buried structure did not occur in either test.

Yamamura and Koga (1974) performed blast tests to estimate liquefaction potential of sandy soil during earthquakes. The site of these tests was the Agano River in Niigata Prefecture, Japan. Arya, et al. (1978) also used blasting to investigate the liquefaction potential at a site that had previously been analyzed using earthquake liquefaction technology. Blasting with 1 kg of dynamite resulted in excess residual porewater pressure, and it was concluded that the technique was a reasonable method for estimating a site's liquefaction potential.

Carnes (1981) and Drake (1978) reported on a study to determine the influence of shallow water tables on cratering and soil stability. Small explosives tests were conducted at different sites to provide cratering and ground shock data. Drake reported that partially buried charges did not result in liquefied craters which only occurred when the depth of burst was greater than the water table. Also, no liquefied craters were observed for deeply buried bursts. Drake felt that liquefaction occurred at late times and not upon initial shock unloading.

Kok (1977) discussed field tests to investigate liquefaction potential in the Netherlands. Explosives were detonated in loosely deposited sands, and an empirical equation was obtained that related porewater pressure increase to scaled distance from the charge.

Jacobs (1988) reported on a series of field tests at the South Platte River, Colorado. In these tests, explosives were detonated on the river's bank, and piezometers were used to obtain porewater pressure response. Scaled distance was correlated with this response.

2.7   FACTORS AFFECTING LIQUEFACTION

This section discusses the factors that affect liquefaction potential. These factors, which are based on evaluations of historical earthquake and blast liquefaction cases, laboratory tests, and field investigations, are shown in Table 2.3 and each is discussed below.

The degree of saturation of a soil mass has a marked influence on liquefaction potential. In soils that are not fully saturated, capillary tension occurs; thus, an apparent cohesion exists. Ivanov (1967) observed that soil compaction from impact loading is maximum

Table 2.3 Factors Affecting Liquefaction Potential

> Saturation
> Relative Density
> Gradation
> Cohesion
> Particle Characteristics
> Soil Fabric
> Overburden Pressures
> Cementation
> Permeability
> Loading

for dry or fully saturated, non-cohesive soils. At intermediate moisture contents, compaction decreases due to capillary coherence between grains. Dowding and Hryciw (1986), Prugh (1963), and Lyakhov (1961) noted similar trends. A second reason for the importance of saturation is that the bulk modulus for water and air is much less than that of water only. Air inclusions of less than one percent can reduce the modulus by an order of magnitude (Studer and Kok, 1980). Prakash (1981) noted that when the soil-air-water mixture is stressed, the water will not strain as much with air present because it is forced into space occupied by the air. When the load is removed the water will not show a residual pressure since it will occupy previous air space.

Relative density is one of the most important factors affecting liquefaction potential of a soil (Prakash, 1981; Studer and Kok, 1980; and the Committee on Earthquake Engineering, 1985). Gilbert (1976) explained that when a granular material experiences a shear strain, it tends to change in volume. A loose sand will tend to decrease in volume, and a dense sand will tend to increase in volume; therefore, dense cohesionless materials are generally not as

susceptible to liquefaction as loose, cohesionless materials. With loose saturated sands, grains·are forced into void space, and water will compress with a pressure increase. Rischbieter (1977) stated that soils with relative densities less than 35 percent are highly liquefaction susceptible, and soils with relative densities over 85 percent are insensitive. Charlie, et al. (1985a) stated that soils with relative densities less than 65 percent are liquefaction prone.

The gradation of a soil has a significant effect on liquefaction susceptibility of that soil. Studer and Kok (1980) stated that the general range of grain size distribution that, from earthquake studies, appears to be most liquefaction susceptible is uniform, fine sand. Coarser grained cohesionless soils may exhibit substantial porewater pressure increases, but the dissipation is much more rapid than with finer grained soils; thus, liquefaction may not be apparent. Also, coarser grained soils usually possess higher shear strength. Damitio (1978a), Prakash (1981), Charlie, et al. (1985a), Rischbieter (1977), and Gilbert (1976) also stated that uniformly graded sands are more susceptible to liquefaction.

Only soils with very little or no cohesion are prone to liquefaction (Rischbieter, 1977 and Damitio, 1978a). Charlie, et al. (1985a) stated that soils containing over ten percent clay material are generally not prone to liquefaction during earthquakes.

Soil particle characteristics that influence liquefaction susceptibility include crushibility, roughness, and roundness. Fragaszy and Voss (1986) discussed laboratory tests that showed that a highly crushable sand was more liquefaction prone than a less crushable sand. Charlie, et al. (1985a) noted that in one case, a graded, angular sand showed more evidence of liquefaction than a

uniform, rounded sand under shock loadings. In another case, however, angular to subangular sands were more stable than rounded, cohesionless sands. Thus, the evidence does not seem conclusive concerning the effect of particle shape.

Fabric, eg., the orientation of sand grains, contributes to liquefaction susceptibility of soil (Committee on Earthquake Engineering, 1985; Maslov and Ivanov, 1985; Prakash, 1981; and Seed, et al., 1977). Nemat-Nasser and Takahashi (1984), in studying the effects of fabric on liquefaction, noted that a sand's resistance to liquefaction may be increased as a result of earlier liquefaction even though the density may be greater. On the other hand, it was also noted that some sands' resistance to second liquefaction occurrences may be considerably reduced depending on the orientation of sand grains.

As overburden pressures increase, liquefaction susceptibility decreases (Rischbieter, 1977 and Charlie, et al., 1985a). The reason cited was that with increased overburden pressures, the effective stress and soil skeleton stiffness increase, and these effects cause a diminished liquefaction potential.

Sand particle cementation or welding at contact points seems to decrease liquefaction potential (Seed, et al., 1977; Seed, 1979; Committee on Earthquake Engineering, 1985; Youd, 1977; Prakash, 1981; and Mulilis, et al., 1977). This cementation can be a function of age and history of soil deposits.

In high permeability soils, dissipation may be so rapid that liquefaction is not observed (Prater, 1977 and Studer and Kok, 1980). Prakash (1981) noted that drainage factors include not only permeability, but also drainage paths. The shorter the paths, the

quicker the excess porewater pressure decreases; thus, liquefaction duration depends on drainage paths. Jacobs (1988) noted similar behaviour.

Liquefaction can be induced by a variety of loading mechanisms including monotonic stress changes, earthquakes, and blast vibrations (Gilbert, 1976). Studer and Kok (1980) noted that the intensity and nature of the applied stress is important in producing porewater pressure increase.

2.8   PREDICTION MODELS

This section provides a summary of models for predicting peak stress and porewater pressure response to explosives detonated in soil. Methods for predicting dissipation after passage of a stress wave are also discussed.

2.8.1   Empirical Equations for Peak Stress

Several references cite empirical equations for predicting peak stresses caused by confined detonations of explosives in saturated sand or water. All the equations are of the same form for peak stress, σ_0, and are represented as

$$\sigma_0 = f \; (\frac{r}{w^{1/3}})^{-\alpha} \tag{2.14}$$

where f and α are constants depending on site characteristics, and r and v are distance from charge and mass of charge, respectively. Table 2.4 provides values reported for f and α that represent fully

saturated sandy soils (or water in the case of Cole) in which point charges are detonated.

Table 2.4 Constants for Empirical Peak Stress Equations

Reference	f		α
	SI[1]	English[2]	
Lyakhov (1961)	59,000	22,500	1.05
Crawford, et al. (1971)	10,000	22,500	3.00
Drake and Little (1983)	47,000	27,000	1.50
Jacobs (1988)	50,093	65,600	2.38
Cole (1948)	52,000	21,600	1.13

Note: 1 - σ_0 in kPa, r in m, w in kg
       2 - σ_0 in pounds per square inch, r in feet, w in pounds

In Table 2.4, f is presented in both SI and English units for comparison purposes. The explosive type is TNT (except for Lyakhov, where the explosive type was not reported).

2.8.2 Equations for Porewater Pressure Response to Blast Loading

Several references presented equations to predict the change in porewater pressure in saturated sand due to blast loading. The equations from those references are shown in Table 2.5, and each is briefly discussed in the following paragraphs.

Ivanov (1967) presented a derivation of increased porewater pressure-strain relationships for one-dimensional conditions in which a water saturated soil is subjected to a high amplitude load. The volume change of the mass is represented as the sum of the volume changes of the solids, the water, and the air, assuming negligible volume change of the solids compared to that of air and water (and in a saturated soil, there is no air). Therefore, the volume change of the mass equals the volume change of the water.

Table 2.5   Porewater Pressure Equations

Reference	Equation	
Ivanov (1967)	$\Delta u = \epsilon_v B_w / n$	(2.15)
Begeman, et al. (1977)	$\Delta u = \epsilon_v B_w / n + \Delta \dot{\sigma} B_w / (n/B_{sk})$	(2.16)
Finn (1978b)	$u_e = \epsilon_{vd} B_{sr} / (1 + nB_{sr}/B_w) \approx \epsilon_{vd} B_{sr}$	(2.17)
Charlie, et al. (1985a)	$u_{pk} = \epsilon \, \rho_m \, v_c^2$	(2.18
Charlie, et al. (1981)	$\Delta u = \epsilon^P / B_m$	(2.19)
Yamamura and Koga (1974)	$u_{pk} = r_d / (nGB_w)$	(2.20)
Veyera (1985)	$u_e = 16.30 \, \epsilon_{pk}^{(.331)} \dot{\sigma}_i^{(.692)} D_R^{(-.179)}$	(2.21)
Hubert (1986)	$u_e = 5.81 \, \epsilon_{pk}^{(.429)} \dot{\sigma}_i^{(.824)} D_R^{(-0.22)}$	(2.23)
Bolton (1989)	$u_e = 10.59 \, \epsilon_{pk}^{(.429)} \dot{\sigma}_i^{(.829)} D_R^{(-0.181)}$	(2.23)
Studer and Kok (1980)	$u_{pk} = \dot{\sigma}_i \, (1.65 + 0.64 \, \ln \frac{w^{1/3}}{r})$	(2.24)
Jacobs (1988)	$u_e = 4.82 \, \dot{\sigma}_i \, (\frac{r}{w^{1/3}})^{-1.478}$	(2.25b)
Jacobs (1988)	$u_e = 11.2 \, \dot{\sigma}_i \, \epsilon_{pk}^{(0.84)}$	(2.25b)

Key to Symbols

B_m=bulk modulus of mixture (kPa)

B_{sk}=modulus of soil skeleton (kPa)

B_{sr}=rebound modulus of skeleton (kPa)

B_w=bulk modulus of water (kPa)

D_R=relative density (%)

G=modulus of rigidity (kPa)

n=porosity

r=distance (m)

u_e=excess residual porewater pressure (kPa)

u_{pk}=peak change in porewater pressure (kPa)

Δu=porewater pressure change (kPa)

v_c=compression wave velocity (m/sec)

w=charge mass (kg)

ϵ=strain

ϵ_{pk}=peak strain (%)

ϵ_v=volumetric strain

ϵ_{vd}=irrecoverable volumetric strain

ϵ^P=inelastic strain increment

$\dot{\sigma}_i$=initial effective stress (kPa)

$\Delta \dot{\sigma}$=change in effective stress (kPa)

ρ_m=water-soil density (kg/m^3)

r_d=dynamic shear stress (kPa)

Begeman, et al. (1977) presented a model similar to Ivanov's. In this model the skeleton compressibility was also considered. Finn (1978b) obtained a similar expression for porewater pressure change, but the rebound of the soil skeleton after passage of the stress wave was included. During rebound, the effective stress decreases, and there is a volume change in the skeleton dependant upon the rebound modulus of the soil. In order for residual or sustained porewater pressure to occur, there must be irrecoverable deformation (i.e., permanent volume reduction). The relation was developed for earthquake loadings; however, according to Finn, with modifications, it may be applicable to blasting.

Charlie, et al. (1985a) presented equations to calculate the peak porewater pressure based on dynamic loading due to a passing stress wave. The saturated soil mass is considered a mixture of soil and water. A mixture bulk modulus and density is determined by the Wood equation reported in Richart, et al. (1970). The mixture is treated as elastic, and relationships between stress, strain, particle velocity, and compression wave velocity given in Section 2.3.3 are used to determine peak strain. Given this strain, it is assumed that the peak change in porewater pressure equals the peak change in total stress. The change in porewater pressure is, thus, calculated.

In another approach, Charlie, et al. (1981) derived an expression for the porewater pressure increase as a result of a detonation in saturated soil. The soil is considered a porous elastic solid, and a numerical model couples Biot's theory and an empirical relation for compaction during shear strain. Incremental increases in porewater pressure are equated to incremental inelastic strains, which are a function of four soil constants, a fluid variation factor, and

load amplitude. In comparing the model results with the recorded field data, it was observed that the model predicted values less than those recorded. The analytical results did, however, show a similar pattern of behavior. It was concluded that the analytical method, with refinements, would yield a closer correlation.

Yamamura and Koga (1974) presented an approximation for porewater pressure increase in sands immediately after an explosion based on the ratio between the principal stress and the dynamic shear stress. The equations of motion are combined with theoretical expressions for radial and tangential stresses to determine this stress ratio, which is shown to be a function of Poisson's ratio. It is assumed that the porewater pressure increase is equivalent to the mean principal stress, and Poisson's ratio for saturated soil is a function of porosity, shear modulus, and bulk modulus of water. The resulting equation shows that the porewater pressure immediately after an explosion is proportional to the dynamic shear stress.

Veyera (1985), Hubert (1986), and Bolton (1989), described equations developed from laboratory tests discussed in Section 2.5.1. The equations were developed from statistical analyses of test results where strains are calculated values, and initial effective stresses and relative densities are determined from measured values.

Studer and Kok's (1980) equation is based on field tests where porewater pressure response to detonations of different explosive types was correlated to develop the equation shown. Jacob's (1988) equation was from field tests on the South Platte River, Colorado, where varying explosive masses were detonated at depths of 3 to 3.5 m in a poorly graded sand below the water table.

2.8.3 Porewater Pressure Dissipation

Terzaghi (1956) discussed the dissipation of excess porewater pressure as a consolidation problem. The equation for one-dimensional consolidation, which is discussed in most soil mechanics text books such as Lambe and Whitman (1969), is :

$$\frac{\partial u_e}{\partial t} = C_v \frac{\partial^2 u_e}{\partial z^2} \qquad (2.26)$$

where u_e is excess porewater pressure, t is time, C_v is the coefficient of consolidation, and z is depth. Tanimoto (1967), in a liquefaction study, used this equation in a theoretical treatment of porewater pressure dissipation. An initial triangular distribution of excess water pressure versus depth is assumed with surface porewater pressure zero and with an impermeable lower boundary. The partial differential equation is solved for porewater pressure as a function of time and depth. True (1969) used the consolidation equation to predict porewater pressure response to a one-dimensional stress wave. Jacobs (1988) also used the equation to analyze porewater pressure response to point charges detonated in alluvial saturated sands.

Ivanov and Sinitsyn (1977) presented an equation based on two-dimensional consolidation of a two-phase, non-cohesive saturated soil. Vibro-creep parameters of the soil skeleton are combined with excess porewater pressure dissipation to obtain an equation for the case of a loaded layer of a saturated soil located on an impermeable barrier.

Finn, et al. (1977) and Finn (1978a) used a different approach to predict porewater pressure dissipation with porewater pressure

gradients and redistribution. The relationship for the change of porewater pressure with respect to time considers the soil rebound modulus and strain rate, along with permeability and depth. The equation is solved simultaneously with the equations of motion and porewater pressure generation to provide continually updated values of porewater pressure. This model is for earthquake loading, during which there is simultaneous generation and dissipation of porewater pressure due to reversing shear stresses.

2.9   PREDICTIVE TECHNIQUES

The evaluation of liquefaction hazards, according to the Committee on Earthquake Engineering (1985), is an "engineering art requiring judgement and experience in addition to testing and analysis." The primary goal is to identify the conditions for reaching a zero effective stress condition. The determination of liquefaction potential is an integral part of earthquake resistant construction design. Less known, indicated by Studer and Kok (1980), is that "identical effects" can also be triggered by explosions. Charlie, et al. (1985a) stated that field observations and limited empirical relationships are the current basis for evaluating sites for potential blast-induced liquefaction conditions. Peck (1979) provided a note of caution in evaluating liquefaction potential. He stated that "we should certainly not accept the scientific findings of the moment in lieu of judgement..."

There are two basic methods reported in the literature for predicting liquefaction probability at a site. One method involves the use of empirically or theoretically derived equations to calculate threshold values of stress, strain, or particle velocity based on site

conditions. In using these equations, if response predictions to a dynamic event exceed thresholds, liquefaction is highly probable. The other method involves an in-situ evaluation of a site in the form of penetration testing or small scale blast testing. In addition to the methods for predicting liquefaction probability, there are also procedures for predicting the extent (radius, depth, and time) of liquefaction.

2.9.1 Liquefaction Prediction Equations

Threshold techniques and equations for predicting blast-induced liquefaction potential are provided in Table 2.6, and a brief description of each technique is in the following paragraphs.

Volumetric Compressive Strain

Blouin and Schinn (1983) derived a model based on a unit volume of saturated soil undergoing a change in volume due to compressive loading. The volume change results in compression of the soil skeleton and porewater and subsequent increase in porewater pressure. The model treats the peak strain in the solid-water mixture as being equal to the peak strain of the skeleton. The peak dynamic stress can be predicted from explosives yield, soil conditions, etc. Liquefaction is assumed to occur if this value is greater than or equal to the value calculated from Equation 2.27.

Peak Compressive Strain

Charlie, et al. (1985a) presented Equation 2.28 for predicting peak compressive strain following a detonation. The equation is from the elastic relationship that peak strain equals the ratio of peak

Table 2.6 Threshold Equations for Predicting Liquefaction

Volumetric Compressive Strain
$$\sigma_p = (\frac{B_m + B_u}{B_u - M})[\bar{\sigma}_e(1 - \frac{M}{E_{sk}}) + \sigma_i(1 + \frac{M}{B_m})]$$
(2.27)

Peak Compressive Strain
$$\epsilon_{pk} = \frac{f}{v_c}(\frac{r}{w^s})^{-\alpha}$$
(2.28)

Peak Particle Velocity
$$v_{pk} = f(\frac{r}{w^s})^{-\alpha}$$
(2.29)

Key to Symbols

B_m=bulk modulus of soil-water mixture (kPa)

B_u=unloading bulk modulus (kPa)

E_{sk}=elastic skeleton modulus (kPa)
f=site constant

g=gravitational constant (9.8 m/sec^2)

M=inelastic skeleton loading modulus (kPa)

s=site constant
r=distance from detonation (m)
v_c=compression wave velocity (m/sec)

v_{pk}=peak particle velocity (m/sec)

w=charge mass (kg)

ϵ_{pk}=peak strain (%)

α=site constant

$\bar{\sigma}_e$=skeleton stress at elastic limit (kPa)

σ_i=initial total stress (kPa)

$\bar{\sigma}_i$=initial effective stress

σ_p=dynamic stress (kPa)

particle velocity to compression wave velocity, and peak particle velocity can be determined through empirical scaled distance equations. It was concluded that the threshold below which liquefaction was unlikely is about 0.01 percent for undrained, one-dimensional compressive loading.

Peak Particle Velocity

According to Langley, et al. (1972), a major parameter associated with sand liquefaction is peak particle velocity induced by a charge. Several references cite peak particle velocity criteria as a technique to determine blast-induced liquefaction potential. In these techniques, peak particle velocity thresholds are used to predict whether liquefaction will occur. Puchkov (1962) used peak particle velocity as a criterion for liquefaction potential. He stated that an average magnitude of 7.7 cm/sec possibly characterizes the destruction of the soil skeleton in water saturated sand and, therefore, is a sign of potential liquefaction (see Section 2.6.2). A common empirical scaling law that relates scaled distance to peak particle velocity is shown as Equation 2.29. Table 2.7 lists values of f, s, and α found in the literature.

Table 2.7 Coefficients for Peak Particle Velocity

Coefficient			Remarks	Reference
f	s	α		
12	1/3	1.5	point charge	Charlie, et al. (1985a)
0.6	1/2	1.67	small buried charge	Long (1981)
8.7	1/3	2.06	point charge	Jacobs (1988)
5.6F	1/3	1.50	contained point charge	Drake and Little (1983)
7.2	1/3	1.15	row charges	Sanders (1982)

Note: r and w are meters and kilograms, velocity is m/sec, and F is a depth of burst coupling factor (0.14 to 1)

An example of the use of peak particle velocity was given by Sanders (1982) to assess the liquefaction hazard that could result from explosively removing the Bird's Point - New Madrid Fuze plug levee on the Mississippi River below Cairo, Illinois. It was calculated that the threshold peak particle velocity would occur only within a range of 300 m. This distance was less than the distance to the nearest structure which was, thus, considered safe from liquefaction. Drake and Ingram (1981) also discussed the hazards associated with blasting in this area.

2.9.2 Blast Testing for Liquefaction Potential

Kummeneje and Eide (1961) reported on a Norwegian "blasting test" method to determine the susceptibility of sand deposits to flow sliding. In this method, a charge of dynamite (mass between 0.07 and 2.4 kg) is lowered into a bore hole and detonated. Subsequent settlements of the ground surface and pore pressure at different range are recorded. The procedure may be repeated several times at given sites. From the results, the susceptibility to liquefaction and slope sliding is determined.

Florin and Ivanov (1961) discussed standard blasting, a Russian-developed technique to determine liquefaction potential. For this technique, 5 kg of explosives are placed at a confining depth. Within a few seconds after detonation, gas expulsion and surface settlement are followed by "squeezing" of water through the pores. The magnitude of average surface settlement in a 5 m radius and the ratios of settlement resulting from three successive standard blasts are determined. If the average settlement is less than 8-10 cm, liquefaction potential is low. The greater the difference of average

settlements after the three blasts, the looser the sand, and the higher the probability of liquefaction. Also, if the ratio between two successive blasts is over 1:0.6, there is danger of an undesirable spreading of liquefaction. Damitio (1978 a,b) provided additional detail and reported that the degree of liquefaction (pore pressure ratio) does not depend on the mass of the charge. The mass of the charge only changes the volume of liquefied soil.

2.9.3 Extent of Blast-Induced Liquefaction

Several references cited empirical relationships to predict the radius of liquefaction resulting from a buried detonation in saturated sand. These relationships are all of the form

$$R = C_R w^{1/3} \qquad (2.30)$$

where R is the radius of liquefaction in meters, w is charge mass in kg, and C_R is an empirical coefficient. Lyakhov (1961) stated that the maximum radius of liquefaction depended on scaled depth of burial, D_B, where $D_B = z/w^{1/3}$ (z is depth of burial in m, and w is charge mass in kg). Table 2.8 gives Lyakhov's values for C_R at different scaled depths.

Table 2.8 Values of Constants from Lyakhov (1961)

Scaled Depth $(m/kg^{1/3})$	C_R	C_t
5	4	60
2.5	8	40
1.25	5	30
0	2	10

Lyakhov also noted also that deviations in C_R were as much as 30 percent. Puchkov (1962) cited several tests in saturated sands in which liquefaction occurred. The average value of C_R from these tests, in which charge mass varied from 5 to 1,000 kg, was 4.8. Ivanov (1967) reported on the results of many field tests which showed that for optimum depths of burst, C_R varied depending on the relative density (D_R) of the sand. His C_R values are shown in Table 2.9.

Table 2.9 Values of Constant from Ivanov (1967)

Soil	D_R (%)	C_R
fine grained sand	0 - 20	25 - 15
	30 - 40	9 - 8
	> 40	< 7
medium grained sand	30 - 40	8 - 7
	> 40	< 6

Ivanov (1967) also gave empirical relationships for depth of liquefaction, h_1, from a charge buried at optimum depth for confinement, h_o, which is

$$h_o = 0.66 \ h_1 \quad (m) \qquad (2.31)$$

where charge mass is:

$$w = 0.055 \ h_o^3 \quad (kg) \qquad (2.32)$$

Based on these two equations, the depth of liquefaction is

$$h_1 = 3.98 \ w^{1/3} \quad (m) \qquad (2.33)$$

Florin and Ivanov (1961) presented an empirical equation that represents the time, t_L, during which sand remains liquefied. The equation is based on water equilibrium in elementary boundary layers and conditions for seepage of water through a medium. The equation is

$$t_L = \frac{1}{k} \left(\frac{\rho_w}{\rho'}\right) \left(\frac{n_o - n}{1 - n}\right) z \qquad (2.34)$$

where k is a coefficient of seepage, n_o and n are initial and final porosities, respectively, z is depth, ρ_w is the density of water, and ρ' is the density of suspended sand.

Lyakhov (1961) presented another empirical relationship for the duration of liquefaction. His equation was

$$t_L = C_t \, w^{1/3} \text{ (seconds)} \qquad (2.35)$$

where C_t is a coefficient dependent on scaled depth of burial, D_B. Table 2.8 provides values of C_t for different scaled depths. It was noted that deviations in C_t from mean values reached 30 percent.

CHAPTER 3

ANALYTICAL MODEL

3.1 SUMMARY OF MODEL

An analytical model was developed to predict and
mathematically describe porewater pressure response to spherical
stress waves in saturated sand following detonation of an explosive in
water above the sand. The model combines empirical relationships to
determine peak radial stress with theoretical treatments of radial,
tangential, and volumetric strains, stresses, and porewater pressures,
which are determined as functions of time. Dissipation of excess
porewater pressure is considered using consolidation theory. The
calculations in the model are accomplished using a program called
POUDRE written in BASIC for a personal computer.

The peak radial stress in saturated sand caused by detonation
of a charge is determined empirically using scaled distance
relationships. It is assumed that the soil-water mixture behaves
elastically while subjected to the impulsive loading from the
detonation. With this assumption, radial and tangential strains are
determined as a function of time by applying well known theoretical
dynamic stress-strain equations (Rinehart, 1975; Timoshenko and
Goodier, 1970) and mixture theory (Richart, Hall, and Woods, 1970).
It is also assumed that the soil skeleton undergoes the same strains
as the mixture; however, the effective stress-strain behavior of the
skeleton is considered inelastic; i.e., hysteresis occurs. The radial

and tangential effective stresses are determined as functions of radial and tangential strains by applying the constrained moduli during loading and unloading. These stresses are combined with the total stresses to calculate the porewater pressure. Figure 3.1 is an example of calculations of strains, effective stress, total stress, and porewater pressure response occurring during exposure to the spherical stress wave. In this example, the detonation occurs at a time of zero, and the stress wave arrival is at about 2 milliseconds. It can be seen that the porewater pressure responds to spherical stress loading by first increasing to a value slightly less than the peak total stress and then decreases and stabilizes at a residual value greater than hydrostatic levels. The effective stress is seen to only slightly increase during loading and then decrease to a lower than initial value. The explosive mass for this example was 0.04 kg located in water 1.83 m above a saturated sand layer 1.83 m thick. The point in the sand where the calculations were made was 3.35 m below the explosive.

Once the stress wave has passed, the porewater pressure remains at an excess residual value until consolidation is complete. One-dimensional consolidation theory is applied during dissipation of this excess porewater pressure. The consolidation equation is solved using finite difference techniques. The boundary conditions are an impermeable layer at the bottom of the sand and a free draining surface at the top of the sand. The initial condition is the excess porewater pressure a function of depth in the sand. An example of calculations of porewater pressure dissipation as a function of time at a given depth and as a function of depth at different times is shown in Figure 3.2. The figure also illustrates the increase in
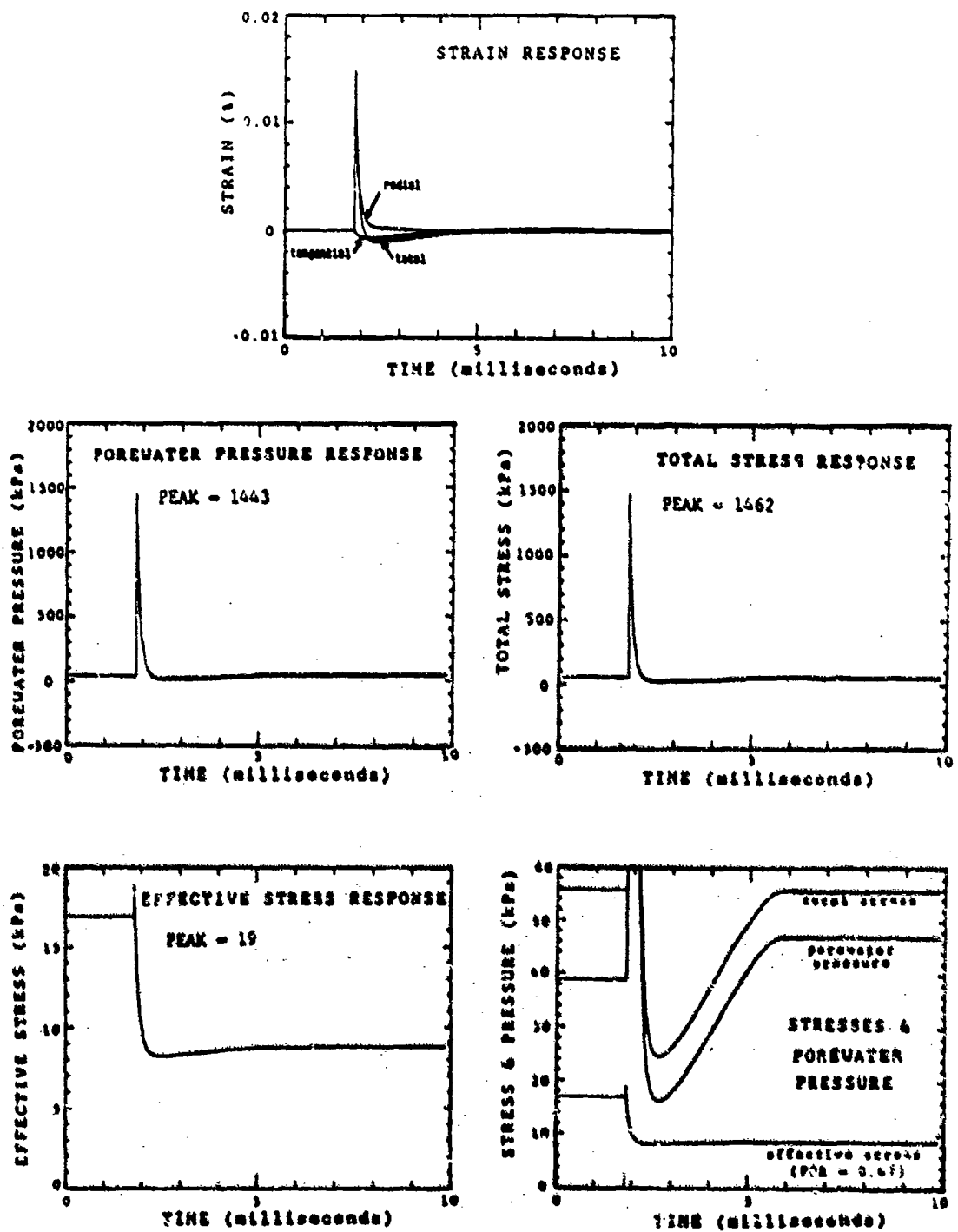
Figure 3.1 Model of dynamic response to detonation of a 0.04 kg
charge at 3.35 m.
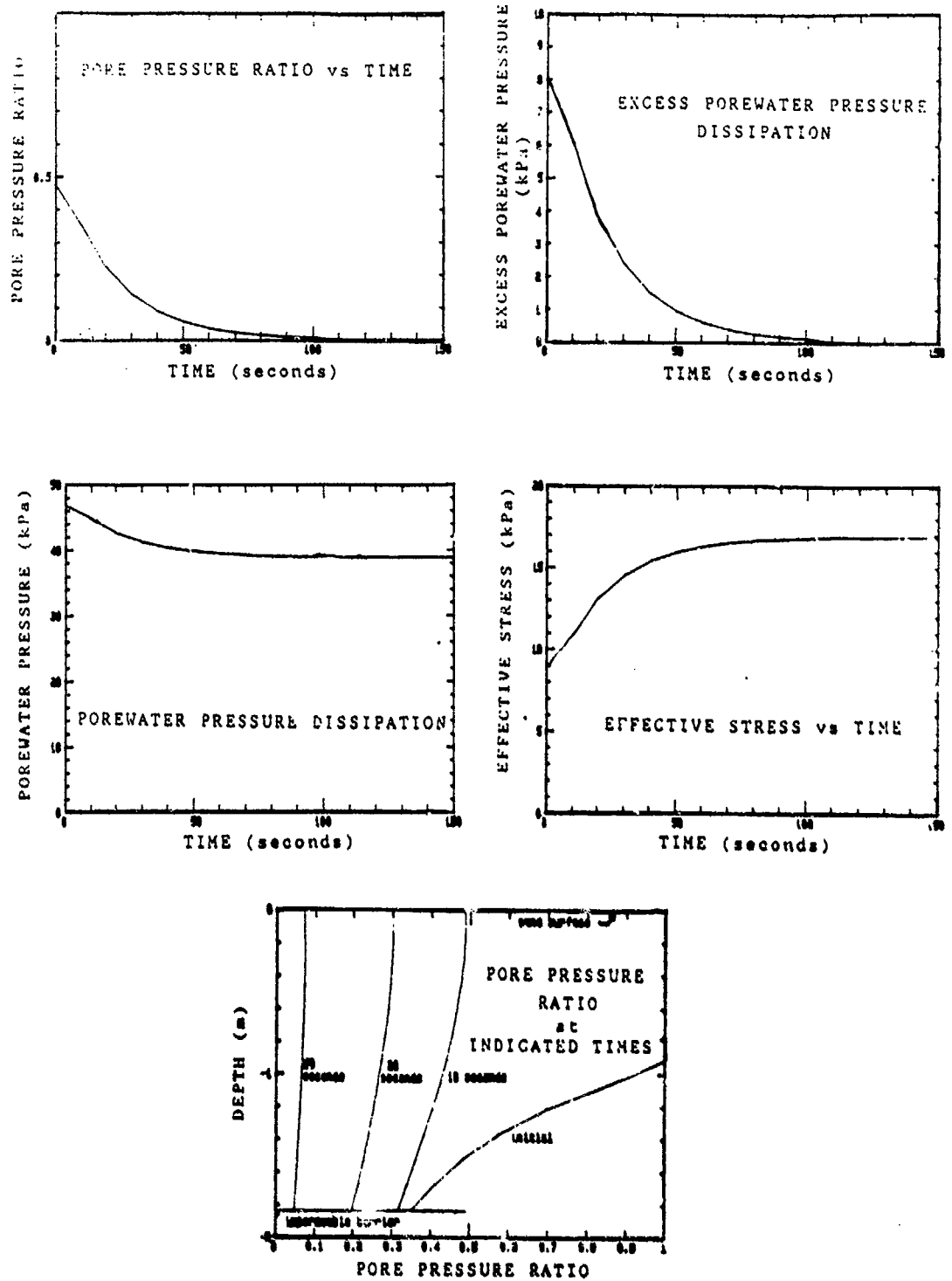
Figure 3.2 Model of porewater pressure after detonation of a
0.04 kg charge.

effective stress as the excess porewater pressure dissipates. The plots showing time as the abscissa represent a point 3.35 m from the charge. The plot with pore pressure ratio as the abscissa shows a cross section of the 1.83 m sand layer with pore pressure ratios at different times as functions of depth in the sand.

3.2   DEVELOPMENT OF MODEL

3.2.1   Peak Radial Stresses

Chapter 2 describes several scaled distance relationships for calculating peak stress from a detonation in saturated soil or water. Basically, all the equations are of the same form:

$$\sigma_0 = f \left(\frac{r}{w^{1/3}} \right)^{-\alpha} \tag{2.14}$$

where

σ_0 = peak stress (radial)

f = a site constant

w = charge mass

r = distance from charge

α = attenuation coefficient

The analytical model is formulated to calculate σ_0 with f and α values described in the literature or with user-developed values. By applying the f and α values, σ_0 is determined at radii, r, representing increments of distance from the charge. The result of the calculations is peak radial stress as a function of distance from the charge (the peak radial stress occurs as the stress wave arrives

at each point in space).   It is assumed that the stress wave is of the form

$$\sigma(\tau) = \sigma_o \, e^{-\alpha_d \tau} \tag{3.1}$$

where $\sigma(\tau)$ is the radial stress as a function of the peak radial stress at time τ which is time after arrival of the stress wave, and α_d is a time decay constant (units 1/msec).

It is assumed that the saturated sand and overlying water behave as a homogeneous system. The assumption may be reasonable. First, the reported scaled distance equations are based solely on test results and, at best, provide only rough estimates of peak stresses. Second, in comparing Cole's (1948) equation for stresses in water with equations for saturated sand (Table 2.4), the results are reasonably close. For example, at a radius of 1.8 m with a 0.08 kg charge, Cole's equation gives a peak stress of 10,400 kPa in water, and Lyakhov's (1961) equation yields 13,100 kPa in saturated sand. The equation used in POUDRE is based on actual results from testing described in later chapters.

3.2.2   Elastic Strains and Stresses

The procedure for calculating radial, tangential, and volumetric strains is based on the assumption that the sand-water mixture behaves elastically during exposure to the stress wave loading and unloading. It is also assumed that the solids are suspended in the water, and the resulting mixture is elastic (e.g., Richart, et

al., 1970). The bulk modulus of the mixture, B_m, can be determined as follows (Richart, et al., 1970):

$$B_m = \frac{(1 + e) \, B_s \, B_w}{B_s \, e + B_w} \qquad (3.2)$$

and the density, ρ, as

$$\rho = \rho_w \left\{ \frac{G_s + Se}{1 + e} \right\} \qquad (3.3)$$

where

> e = void ratio
>
> B_s = bulk modulus of solid particles
>
> B_w = bulk modulus of water
>
> ρ_w = density of water
>
> G_s = specific gravity of solids
>
> S = degree of saturation

The method for determining the radial, tangential, and volumetric strains is described in Rinehart (1975), Timoshenko and Goodier (1970), and Sharpe (1942). The method uses the solution to the wave equation where a stress wave is generated by the application of an instantaneous pressure (zero rise time) to the inner surface of a spherical cavity in an ideally elastic medium. The resulting spherical stress wave propagates outward from the cavity, producing radial and tangential stresses (σ_r and σ_t) in the surrounding medium. The equations for the stresses are:

$$\sigma_r = \frac{E}{(1 + \mu)(1 - 2\mu)} \left[(1 - \mu) \frac{\partial u^*}{\partial r} + 2\mu \frac{u^*}{r} \right] \qquad (2.6a)$$

$$\sigma_t = \frac{E}{(1 + \mu)(1 - 2\mu)} \; [\mu \; \frac{\partial u^*}{\partial r} + \frac{u^*}{r}] \tag{2.6b}$$

where

E = modulus of elasticity

μ = Poisson's ratio

u^* = displacement in radial direction

r = radius at which u^* occurs

The equations for the radial, tangential and volumetric strains (ϵ_r, ϵ_t and ϵ_v, respectively) are:

$$\epsilon_r = \frac{\partial u^*}{\partial r} \tag{2.5a}$$

$$\epsilon_t = \frac{u^*}{r} \tag{2.5b}$$

$$\epsilon_v = \epsilon_r + 2\epsilon_t \tag{2.5c}$$

and the equation for u^* is

$$u^* = \frac{\partial \phi}{\partial r} \tag{2.7}$$

where ϕ is a scalar displacement potential or a single stress function that satisfies the wave equation, which in spherical notation is

$$\frac{\partial^2 \phi}{\partial t^2} = \frac{1}{r} \; \frac{d^2 (r\phi)}{dr^2} \tag{3.4}$$

Rinehart (1975) provided an expression for ϕ as

$$\phi = \frac{\sigma_o a}{\beta^2 \rho r} \; [-e^{-\alpha_d t} + (\frac{\bar{\beta}}{\omega_o}) \; e^{-\alpha_o r} \; \cos(\omega_o r - \beta)] \tag{3.5}$$

where

σ_o = peak pressure at cavity surface from detonation

a = radius of cavity

ρ = density of the medium

α_d = time decay constant (from Equation 3.1)

τ = time after arrival of stress wave at r

$$\tau = t - (r - a)/v_c \tag{3.6}$$

t = time after after detonation)

v_c = compression wave velocity

$$\alpha_o = (v_c/a)(1 - 2\mu)/(1 - \mu) \tag{3.7}$$

$$\omega_o = (v_c/a)(1 - 2\mu)^{1/2}/(1 - \mu) \tag{3.8}$$

$$\bar{B}^2 = \omega_o^2 + (\alpha_o - \alpha_d)^2 \tag{3.9}$$

$$\beta = \tan^{-1}[(\alpha_o - \alpha_d)/\omega_o] \tag{3.10}$$

Rinehart (1975) and Sharpe (1942) also provided an expression for ϕ when Poisson's ratio equals 0.25. This expression is

$$\phi = (\frac{\sigma_o a}{\rho r}[(\frac{\omega}{\sqrt{2}} - \alpha_d)^2 + \omega^2])(-e^{-\alpha_d \tau} + e^{-\omega\tau/\sqrt{2}}[(\frac{1}{\sqrt{2}} - \frac{\alpha_d}{\omega})\sin\omega\tau + \cos\omega\tau]) \tag{3.11}$$

where $\omega = 2\sqrt{2}\, v_c/3a$. It is of interest that Equations 3.5 and 3.11 give similar values for ϕ if μ of 0.25 is used in Equation 3.5.

Equation 2.7 is solved to obtain an expression for u^* by differentiating Equation 3.5 with respect to r. This expression is

$$u^* = \frac{p'}{r} e^{-\alpha_d r} \left(\frac{1}{r} - \frac{\alpha_d}{v_c}\right) - \frac{B p'}{r} e^{-\alpha_o r} \left[\frac{1}{r} \cos(\omega_o r - \beta) - \right.$$

$$\left. \frac{\alpha_o}{v_c} \cos(\omega_o r - \beta) - \frac{\omega_o}{V_c} \sin(\omega_o r - \beta)\right] \tag{3.12}$$

where $p' = \dfrac{\alpha_o a}{B^2 \rho}$ and $B = \dfrac{\bar{B}}{\omega_o}$.

Expressions for ϵ_r and ϵ_t are obtained using Equations 2.5a and 2.5b with Equation 3.12. The resulting equations are:

$$\epsilon_r = \frac{2p'}{r^3} [-e^{-\alpha_d r} + B e^{-\alpha_o r} \cos(\omega_o r - \beta)] +$$

$$\frac{2p'}{v_c r^2} (\alpha_d e^{-\alpha_d r} - B e^{-\alpha_o r} [\alpha_o \cos(\omega_o r - \beta) + \omega_o \sin(\omega_o r - \beta)]) +$$

$$\frac{p'}{v_c^2 r} (-\alpha_d^2 e^{-\alpha_d r} + B e^{-\alpha_o r} [\alpha_o^2 \cos(\omega_o r - \beta) + 2\alpha_o \omega_o \sin(\omega_o r -$$

$$\beta)]) - \omega_o^2 \cos(\omega_o r - \beta)]) \tag{3.13}$$

and

$$\epsilon_t = -\frac{p'}{r^3} [-e^{-\alpha_d r} + B e^{-\alpha_o r} \cos(\omega_o r - \beta)] - \frac{p'}{v_c r^2} (\alpha_d e^{-\alpha_d r} +$$

$$B e^{-\alpha_o r} [\alpha_o \cos(\omega_o r - \beta) + \omega_o \sin(\omega_o r - \beta)]) \tag{3.14}$$

At this point, the one unknown value in Equations 3.13 and 3.14 is the cavity radius, a. To obtain this value, a method of equivalency is used in which it is assumed that when $r - 0$, i.e., the stress wave is arriving at a spatial point of radius r, the tangential strain is zero ($\epsilon_r - 0$). Thus, Equation 2.6a can be written at $r - 0$ as

$$\sigma_r = \frac{E}{(1 + \mu)(1 - 2\mu)} \left[(1 - \mu) \, \epsilon_r \right] \qquad (3.15)$$

or, rewritten,

$$\epsilon_r = \frac{\sigma_r \, (1 + \mu)(1 - 2\mu)}{(1 - \mu) \, E} \qquad (3.16)$$

It is convenient to use the bulk modulus, B_m, rather than modulus of elasticity, E, which from Lambe and Whitman (1969) is

$$B_m = \frac{E}{3(1 - 2\mu)} \qquad (3.17)$$

Thus, Equation 3.16 becomes

$$\epsilon_r = \frac{\sigma_r \, (1 + \mu)}{3 \, B_m \, (1 - \mu)} \qquad (3.18)$$

Since σ_r at $r = 0$ is known from Equation 2.14, B_m is known from Equation 3.2, and μ is estimated or assumed for the soil-water mixture, a value of ϵ_r can be obtained. Once ϵ_r is determined. Equation 3.13 is used (at $r = 0$) to calculate a value for equivalent cavity radius, a. This value is then used in Equations 3.13 and 3.14 to calculate ϵ_r and ϵ_t as functions of time, r, during passage of the stress wave through points at various radii, r. The only remaining unknown values are the tangential stresses and the radial stresses as functions of time, r. These stresses are determined with equations 2.6a and 2.6b, since all values on the right hand sides of the equations are known.

The technique described deviates from conventional methods described in the cited references for cavity explosion problems with respect to the cavity radius. The references described problems with materials of high moduli (e.g., metals), and cavities of known dimensions are provided in which an explosion takes place. In the case for saturated sand, the modulus is much lower and the stress waves travel significantly slower. The method here assumes that the cavity radius is an unknown value, but an equivalent (or artificial) radius can be determined. This equivalent radius is then used to calculate the strains and stresses as functions of time and distance from the center of the cavity.

3.2.3 Dynamic Effective Stresses and Porewater Pressures

By knowing the radial and tangential strains in the soil-water mixture during passage of the stress wave, it is possible to determine the radial and tangential effective stresses ($\bar{\sigma}_r$ and $\bar{\sigma}_t$) as functions of time, r. These calculations are performed by applying Equations 2.6a and 2.6b to the soil in terms of the skeleton constrained moduli. The constrained modulus, D, is used since it is a commonly determined value from laboratory oedometer tests. Equations 2.6a and 2.6b are rewritten as

$$\bar{\sigma}_r = \frac{D}{(1 - \mu_s)} \left[(1 - \mu_s)\, \epsilon_r + 2\mu_s\, \epsilon_t \right] \qquad (3.19)$$

$$\bar{\sigma}_t = \frac{D}{(1 - \mu_s)} \left[\mu_s\, \epsilon_r + \epsilon_t \right] \qquad (3.20)$$

where μ_s is the soil skeleton Poisson's ratio. The conversion from E to D given in Lambe and Whitman (1969) is

$$D = \frac{E\ (1 - \mu)}{(1 + \mu)(1 - 2\mu)} \qquad (3.21)$$

In the model, $\bar{\sigma}_r$ and $\bar{\sigma}_t$ are calculated based on the secant constrained moduli for loading and for unloading. Thus, hysteresis is accounted for, and, although the soil-water mixture behaves elastically, the effective stresses show an inelastic response as illustrated in Figure 3.1.

Once the effective stresses are obtained as a function of time, porewater pressure is determined as a function of time during passage of the stress wave by taking the difference between the total and effective stress.

3.2.4 Porewater Pressure Dissipation

The method of calculating porewater pressure dissipation is based on the one-dimensional consolidation equation (Lambe and Whitman, 1969):

$$C_v \frac{\partial^2 u_e}{\partial z^2} = \frac{\partial u_e}{\partial t} \qquad (2.26)$$

where

C_v = coefficient of consolidation

u_e = excess porewater pressure

z = coordinate in vertical direction

t = time

One-dimensional drainage is assumed to begin after the stress wave has fully attenuated throughout the entire sand layer, and time zero for

consolidation is after the stress wave has fully attenuated in the sand layer. This assumption is reasonable since dissipation is measured in seconds rather than milliseconds as in stress wave propagation. The next assumption is that the vertical total stress remains constant once dissipation begins.

The boundary conditions assumed are: (1) at the bottom of the sand, there is no drainage; i.e., an impermeable liner is present; and (2) the top of the sand layer is free flowing with zero excess porewater pressure at all times. The initial condition is the excess porewater pressure immediately after passage of the stress wave at each point on the vertical profile of the sand (as determined by methods described in section 3.2.3). The coefficient of consolidation, C_v, is estimated using a procedure described in Lambe and Whitman (1969) as

$$C_v = \frac{kD}{\rho_w} \qquad (3.22)$$

where k is permeability, D is the constrained modulus (loading is assumed), and ρ_w is the density of water. Both k and D can be readily determined in the laboratory, or reasonable assumed values are available in the literature.

Given the assumptions, the initial condition, and the boundary conditions, Equation 3.22 is solved using finite difference methodology. The Crank Nicolson technique and central difference formulation (Burden, et al., 1981) are used in the solution. The result of the calculations is excess porewater pressure as a function of depth and time in sand. Once the excess porewater pressure is

determined, and since the total stress is static, the effective stress is obtained as a function of depth and time by subtracting the porewater pressure (hydrostatic plus excess) from the total stress.

3.3 SENSITIVITY STUDIES

During development of the analytical model, sensitivity studies were performed to identify the input variables that significantly affected the calculations. The variables most affecting pore pressure ratio (PPR) are listed in Table 3.1. Also shown are standard values which were independently varied in the sensitivity study.

Table 3.1. Sensitivity Study Variables

Variable	Standard
Relative Density	90%
Soil skeleton Poisson's ratio	0.45
Soil-water mixture Poisson's ratio	0.45
Soil constrained modulus during loading	14,000 kPa
Soil constrained modulus during unloading	69,000 kPa

A test matrix was developed to examine the effects of these variables. A charge mass of 0.03 kg, a radius of 3.5 m, and a time decay constant of 10,000 (1/sec) were used for the studies (varying the time decay constant has no effect on PPR results). Figure 3.3 shows the relative impact of each variable. The least effect is the skeleton Poisson's ratio; the mixture Poisson's ratio has a slightly higher effect; relative density has a significant effect; and the greatest effect is the ratio of the loading to unloading constrained modulus.
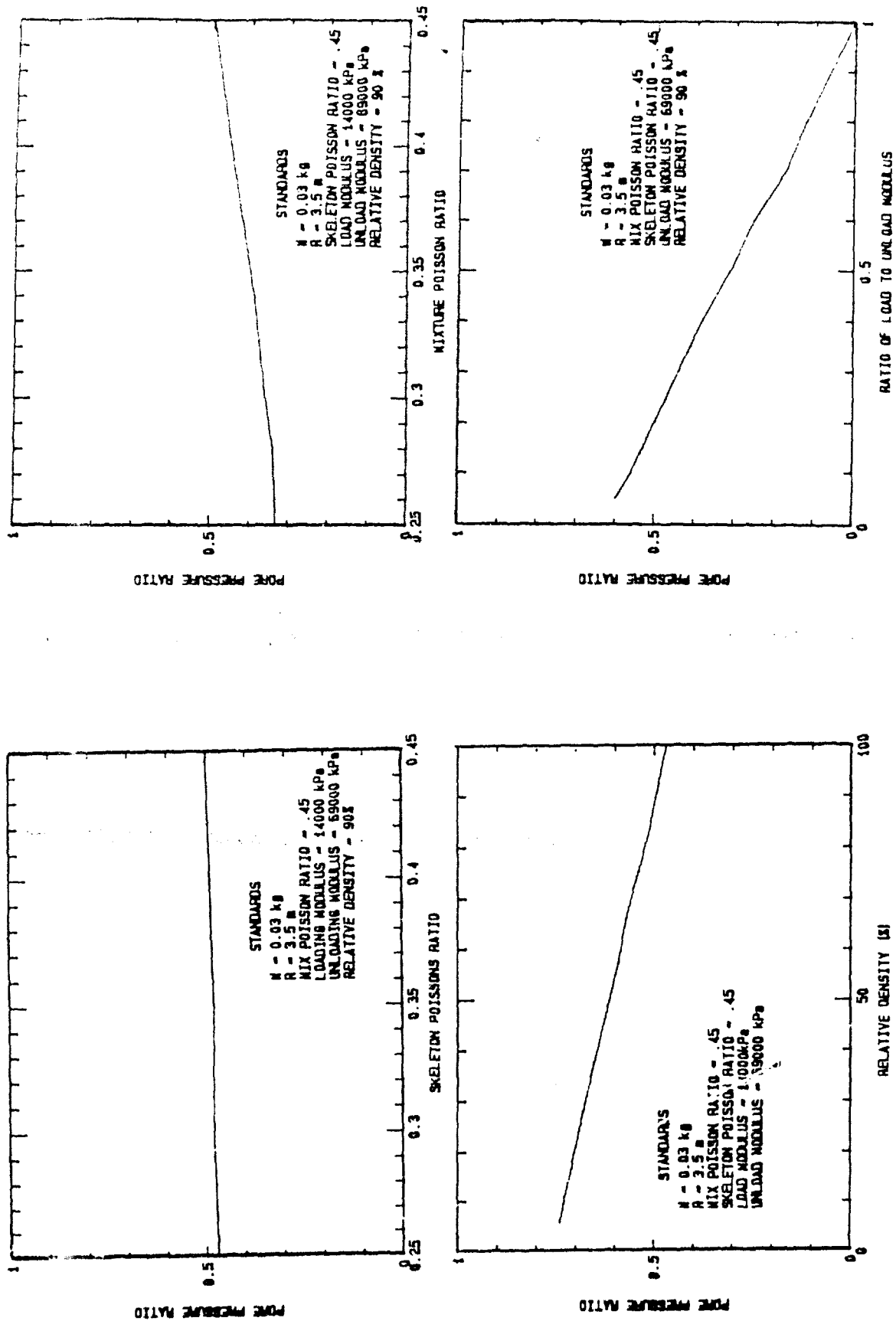
Figure 3.3 Model sensitivity study.

3.4   GENERAL COMMENTS ON MODEL

The methodology described in Sections 3.2 and 3.3 is the basis of the analytical model developed to predict porewater pressure resr se following the detonation of a point charge in saturated sand. It is recognized that a number of assumptions were made. and that some of the input data may be difficult to obtain. Nevertheless, the model does provide a mathematical explanation of phenomena associated with blast-induced porewater pressure increases and subsequent dissipation.

The only non-theoretical routine in the model is the initial calculation of peak stress as a function of distance from a charge of a given mass. It is assumed that during exposure to loading and unloading from the stress wave, the soil and water bet ve as an elastic mixture; thus, radial and tangential strains are determined elastically. Effective stress is calculated using these strains and skeleton constrained moduli for loading and unloading. Porewater pressure response is determined as the difference between the total stress and effective stress during wave passage. Consolidation theory is used to calculate dissipation of the porewater pressure after the stress wave has fully attenuated throughout the sand layer.

CHAPTER 4

TEST SITE

4.1   INTRODUCTION

One objective of this research was to develop a data base
by performing well controlled experimental explosives tests that
generate spherical stress waves in saturated sand. A test site was
developed at Colorado State University, Fort Collins, Colorado, to
accomplish this objective. Site development included excavation of a
pit for explosives testing below the surrounding ground surface,
construction of support facilities, placement of power and
communication lines, and construction of an access road and security
fence. This chapter provides a brief description of the test site.
Details of the site investigation and development are provided in
Appendices A and B.

4.2   SITE DESCRIPTION

4.2.1   Geology

The test site is in a relatively flat bottomed valley formed
by colluvial and alluvial activity (Figure 4.1). A sandstone bedrock
is estimated to lie between 8 and 9 m below the ground surface with a
series of folded shale layers over the sandstone. The top soil is a
5.5 m layer of bentonite clay, and the water table is at a depth of
approximately 3.7 m. Additional details are provided in Appendix A.

Figure 4.1 Blast-induced liquefaction test site.

4.2.2 Test Bed

To maximize safety, control, and repeatability of explosives tests and to minimize stress wave reflections, testing was performed in a pit excavated to approximately 4 m below the ground surface. A steel tank, 4.27 m in diameter and 1.83 m high, was placed in the bottom of this pit to contain sand and instrumentation (Figures 4.2 and 4.3). The top of this open ended tank was at the same level as the water table. The bottom of the tank was sealed with an impermeable pond liner. A network of pipes was placed inside the tank to permit full saturation of the sand prior to testing. A cross-sectional drawing of the test bed is shown in Figure 4.4, and Table 4.1 provides relative depths of features in the bed. Details of the test bed construction are provided in Appendix B.
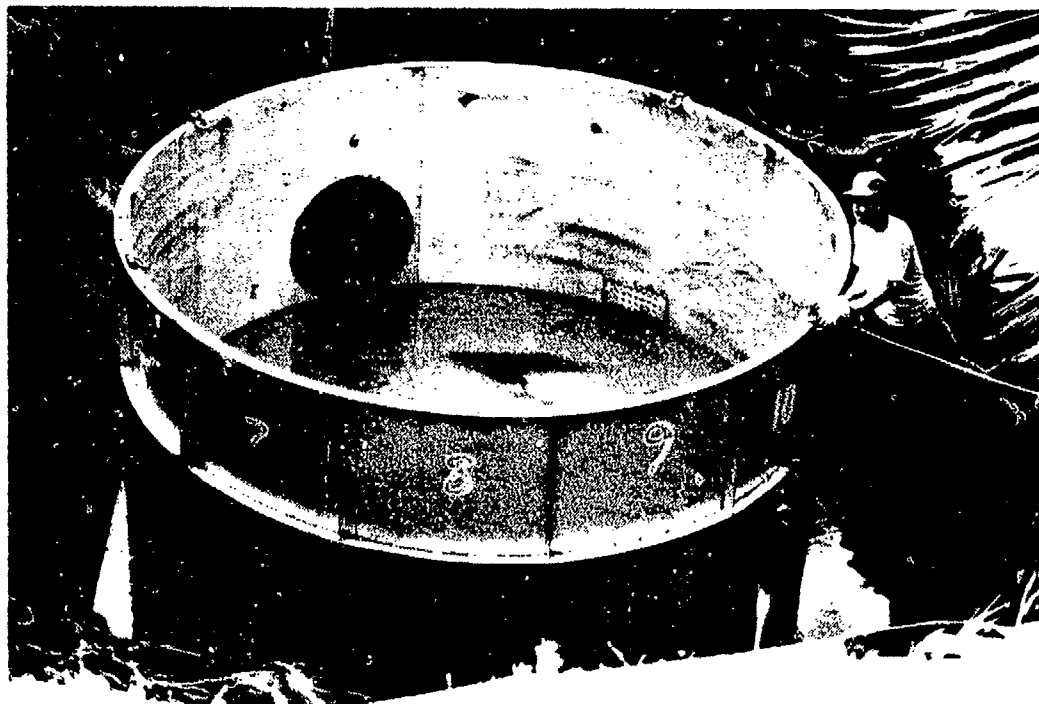
Figure 4.2   Test sand container below water table.
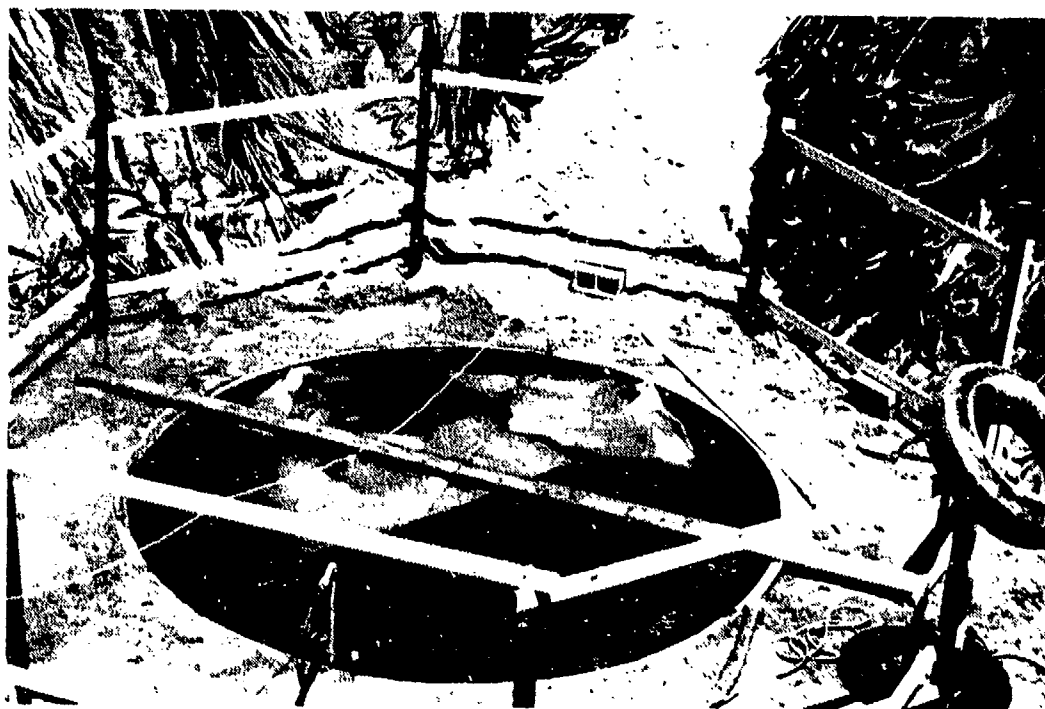
Figure 4.3   Completed test tank.

Table 4.1 Relative Depths in Test Pit

Description	Depth (m)
ground surface	0
water table	3.66
top of steel tank	3.66
gravel surface in tank	5.39
saturation pipe	5.44
bottom of steel tank	5.49
pond liner	5.49
masonry sand	5.49-5.60
gravel	5.60-5.90
bottom of pit	5.90
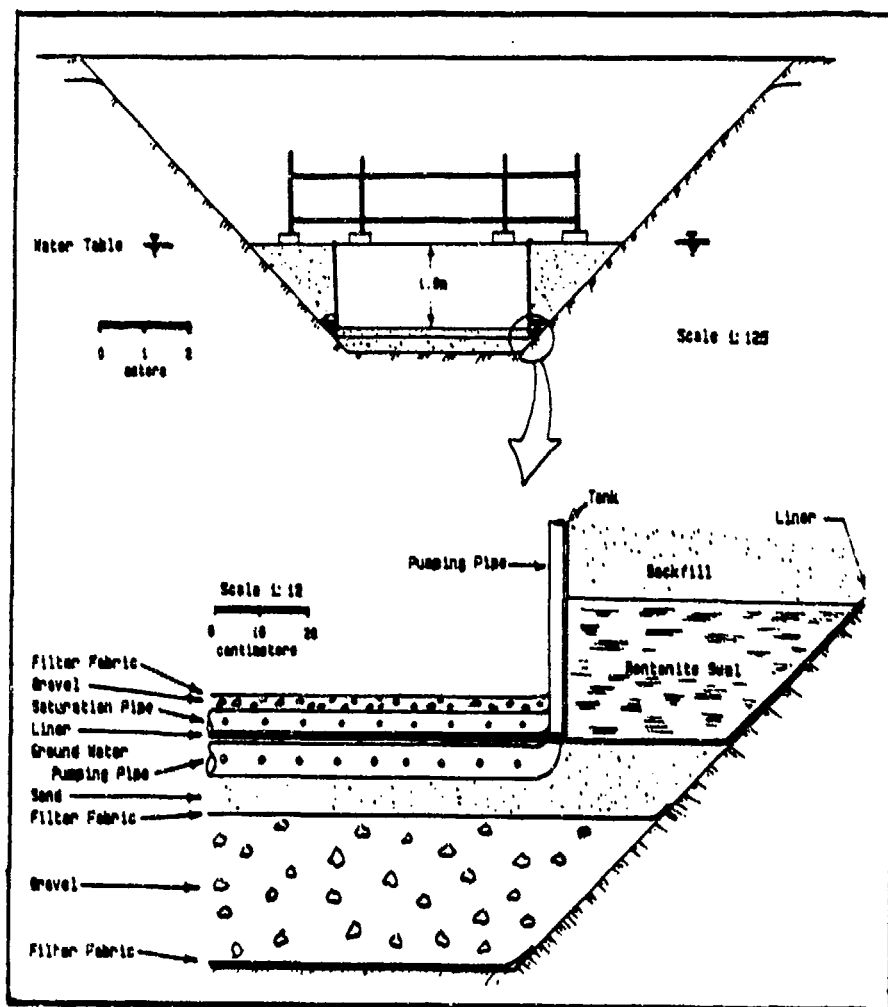
Figure 4.4 Cross-section of test tank and large pit.

The test bed was developed to permit detonation of explosives in water placed in the pit above the instrumented, saturated sand as shown in Figure 4.5. This procedure permitted safe detonation of explosives and propagation of spherical stress waves from the explosives, through the water, and into the sand. Reflected stress waves were minimized since the native clay around the sand was below the water table and had an acoustic impedance approximately the same as the saturated sand.

4.2.3 Support Facilities

Support facilities consisted of a water treatment system, an instrumentation relay building, a command post, and storage building.

CROSS SECTION OF TEST BED WITH EXPLOSIVES LAYOUT

wiring from cap to blaster   rope traversing pit   ground surface   post

blasting cap   rope   water surface

0.5m*   detonating cord   spherical explosive   pit

1.8m   water   water table

sand   instrumented sand   sand   test tank

1.8m

— 4.3m —

* = 0.9m for final detonation
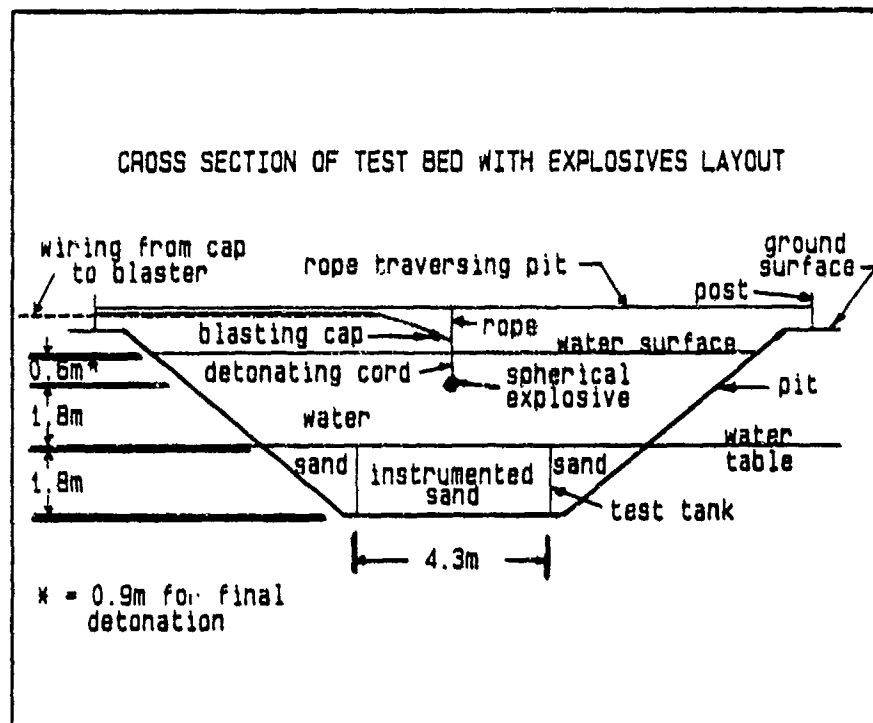
Figure 4.5 Cross-section of test bed.

The water treatment system was developed to deair and store water for saturating the test sand. It consisted of a commercial water heater, a vacuum tank, and a storage tank. The instrumentation relay building was built near the pit to house signal conditioners and power supplies. The command post was a salvaged U.S. Army mobile missile tracking station located over 100 m from the test pit. Testing was controlled from the command post in which a personal computer and transient data recorders were located. Figure 4.6, a plan view of the test site, illustrates the locations of the above features (the test pit is labeled as "large pit"). Additional details are provided in Appendix B.
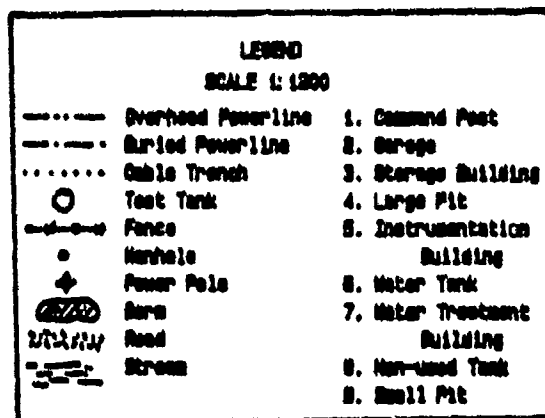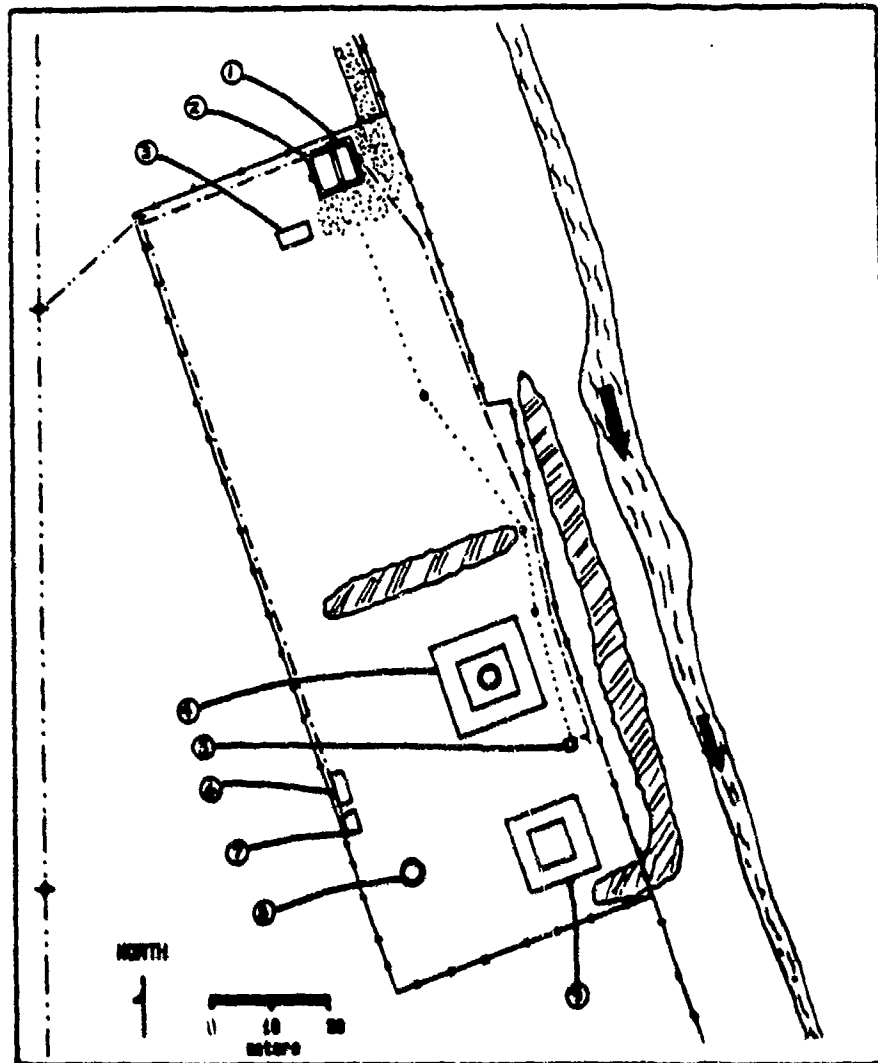
Figure 4.6 Plan view of test site.

CHAPTER 5

TEST MATERIAL, EQUIPMENT, AND EXPLOSIVES

5.1 INTRODUCTION

This chapter provides a description of the sand, instrumentation, and explosives used in the experimental phase of the research. Each of these items is discussed in the following sections.

5.2 TEST SAND

The sand used in this program was a crushed gravel obtained locally from the Poudre River near Fort Collins, Colorado, and, henceforth, will be referred to as Poudre Valley sand. The sand was supplied by Sterling Sand and Gravel of Fort Collins, Colorado. Grain size distribution analyses of random samples of the sand were performed according to ASTM D422. The results of three analyses are shown superimposed in Figure 5.1 and indicate that less than three percent of the material is finer than 0.075 mm. The D_{50} particle size for the sand is between 0.54 and 0.60 mm, and the coefficient of uniformity (C_u) is between 3.7 and 4.3. The sand is classified as poorly graded (SP) under the Unified Soil Classification System (ASTM D854). Stress-strain relationships for Poudre Valley sand at two densities were determined with static one-dimensional, confined compression tests. The results of these tests at two densities are shown in Figure 5.2.
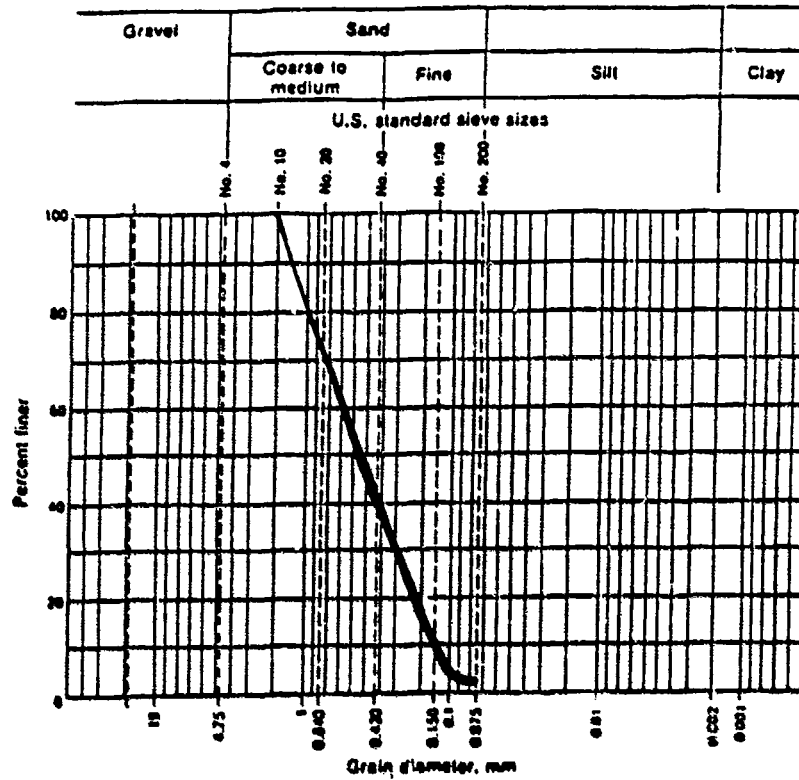
Figure 5.1 Pre-test gradation curves (superimposed) for Poudre Valley sand.
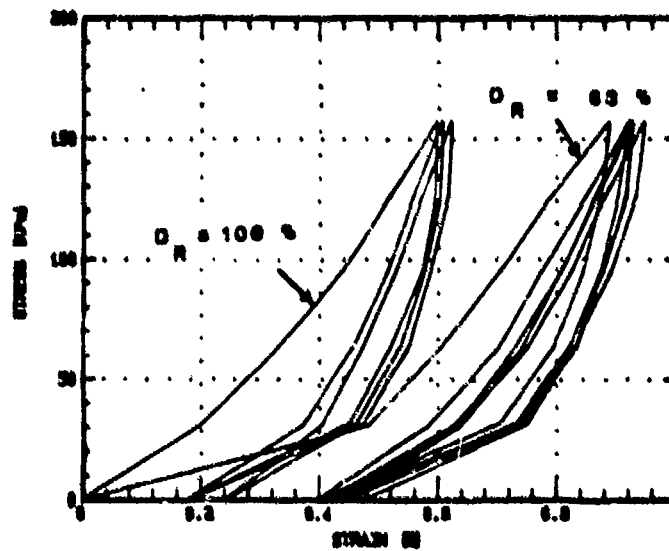
Figure 5.2 Confined stress-strain curves for Poudre Valley sand.

The specific gravity of the sand solids was determined to be 2.65 (ASTM D854). The minimum dry density is 1522 kilograms per cubic meter (kg/m^3) and the maximum is 1860 kg/m^3, as determined by the Bureau of Reclamation Soil Mechanics Laboratory in Denver, Colorado, using ASTM D2049 procedures with a calibrated shaker table. The permeability of the sand, determined using constant head tests (ASTM D2434), ranges from 0.005 centimeters per second (cm/sec) at 20 percent relative density (D_R) to 0.001 cm/sec at 80 percent D_R.

A spectographic analysis of the Poudre Valley sand was also performed by the Bureau of Reclamation in Denver, Colorado. The results showed that the predominate mineral component is silicon with a small presence of aluminum and iron and with traces of several other components. These results are given in Figure 5.3, and Figure 5.4 is a photomicrograph of the sand.

5.3 INSTRUMENTATION

The instrumentation was selected to measure transient and residual porewater pressure, soil acceleration, total stress, and soil strain in the soil during and after detonation of explosives. To record transient porewater pressure data, piezoresistive pore pressure transducers were used. These devices receive voltage from signal conditioners which also amplify the voltage output. The analog output is digitized in a transient data recorder (TDR). Piezoresistive accelerometers were selected to obtain soil accelerations. The accelerometers receive voltage from signal conditioners, which then amplify output voltage for the TDR's. Total stress gages were used to measure total stresses in the soil. These gages receive a constant

U.S.G.S. SEM LABORATORY   FRI 25-OCT-85 10:16
Cursor: 0.000keV = 0

0.000   VFS = 4096   10.240
30   POUDER RIVER SAND
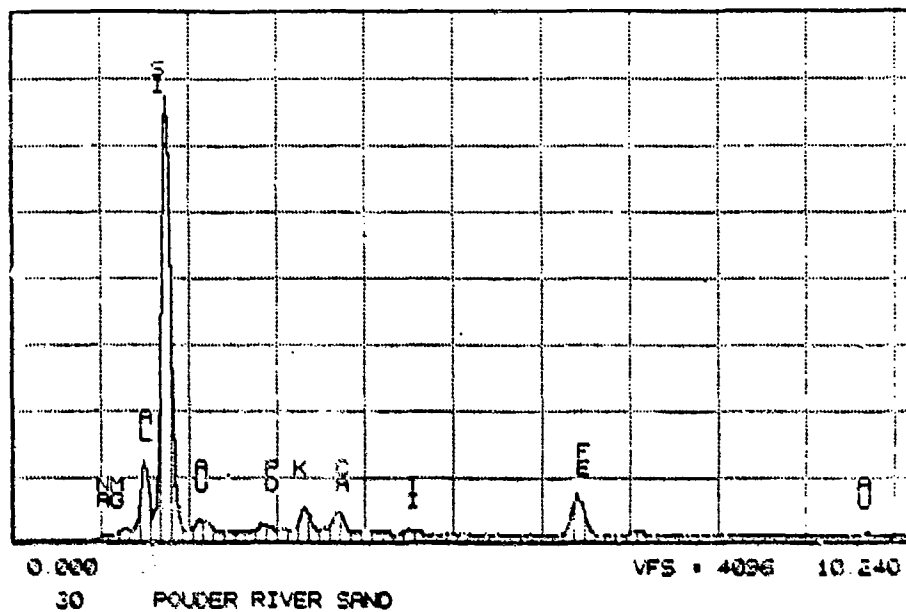
Figure 5.3   Spectrographic analysis of Poudre Valley sand.

Figure 5.4   Photomicrograph of Poudre Valley sand.

voltage input from a direct current (DC) power supply, and they send output voltage directly to the TDR's without amplification. To measure soil strains, inductive strain gages were used with a Bison Soil Strain Gage. Strains were determined before and after each detonation; i.e., transient strains were not measured. Residual porewater pressures were measured using a piezometer (Figure 5.5) with video cassette cameras recording water rise in the piezometer tubing. A personal computer was the core of the data system. It communicated directly with the TDR's and was used to analyze the data from the instrumentation gages and piezometer. Additional instrumentation details are provided in Appendices C and D.

5.4   EXPLOSIVES

The explosives selected for this test program were manufactured by the Ensign-Bickford and Dupont companies. Two types of explosives were used, Primacord[R] and Tovex[R], along with instantaneous electric blasting caps to initiate detonation.

Primacord[R], a detonating cord rated at 10.66 grams of explosive per meter, was used as the explosive for the smaller detonations and to detonate the Tovex[R] used in the larger detonations. It is relatively insensitive to premature or accidental initiation due to heat, impact, friction, static stray current, and lightning (Ensign-Bickford Company, 1984). There is a central core of explosive known as PETN (pentaerythritol tetranitrate) and a core encasement of polypropylene yarn, plastic tape, and textile yarn count-rings. The energy rating of PETN is approximately 1,500 calories per gram, which is about 50 percent greater than TNT. The outer diameter of

Figure 5.5 Piezometer board to measure residual porewater pressure.

Primacord[R] is 4.677 mm, and the detonation velocity is about 6700 m/sec (Dupont, 1980).

For the larger detonations in this test program, Tovex 800[R] was used. This explosive is a cap sensitive, high energy, medium density and medium velocity water gel relatively safe from impact tests, shock tests and burning tests (Dupont, 1980). Tovex[R] consists of oxidizing salts, fuels, and sensitizers dissolved or dispersed in a continuous liquid phase. The system is made water resistant by adding gellants and cross linking agents. The oxidizing salts consist of ammonium nitrate, sodium nitrate, or calcium nitrate; and the fuels frequently used are aluminum, gilsonite, or oil. This explosive is packaged in cartridges 40.6 cm long and 6.3 cm in diameter. The cartridge casing consists of a film that is easily cut for obtaining desired charge weights. The density is 1.20 grams per cubic centimeter; the detonation velocity is 4800 m/sec; and it has excellent water resistance (Dupont, 1980). The energy rating for Tovex 800[R] is 894 calories per gram, compared to TNT, which is approximately 1000 calories per gram (German, 1986).

To initiate the detonation of both Primacord[R] and Tovex[R], instantaneous electric blasting caps (Dupont CWAS) were used. These blasting caps have cylindrical aluminum shells containing powder charges. Electrical energy is input to the cap through two 3 m long plastic insulated, copper wires. The ends of the wires are joined inside the cap by a high-resistant bridge wire embedded in the cap ignition mixture. The ignition mixture causes the primer charge to

detonate which subsequently detonates a high-explosive base charge (Dupont, 1980).

To generate spherical stress waves, the explosives were shaped by coiling the detonating cord or by molding the Tovex^R into approximately spherical configurations. The desired explosive masses were obtained by varying the amount and type of explosive. Figures 5.6 and 5.7 are photographs of the explosives used in the testing.
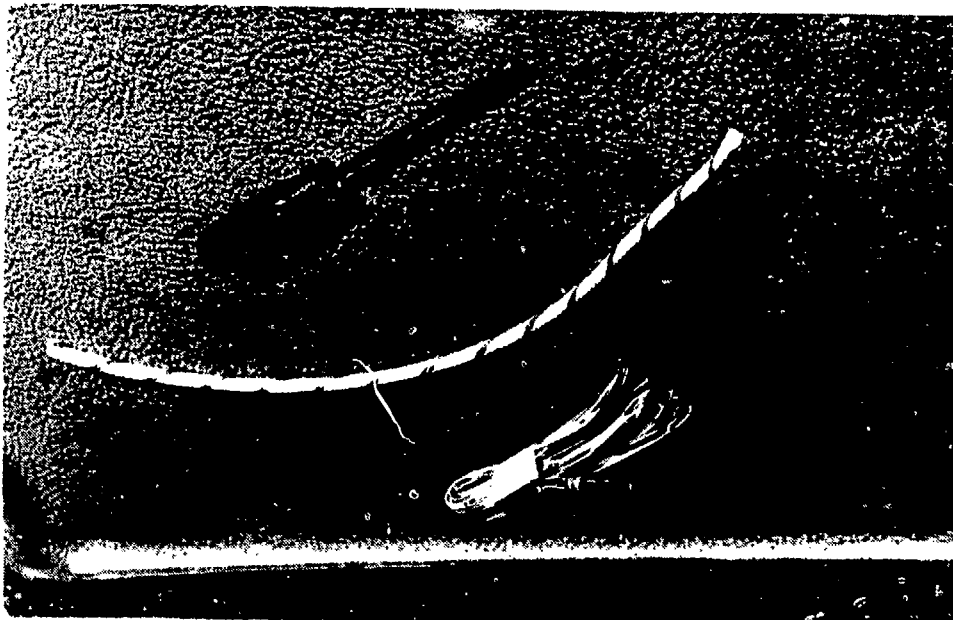
Figure 5.6   Detonating cord and blasting cap.
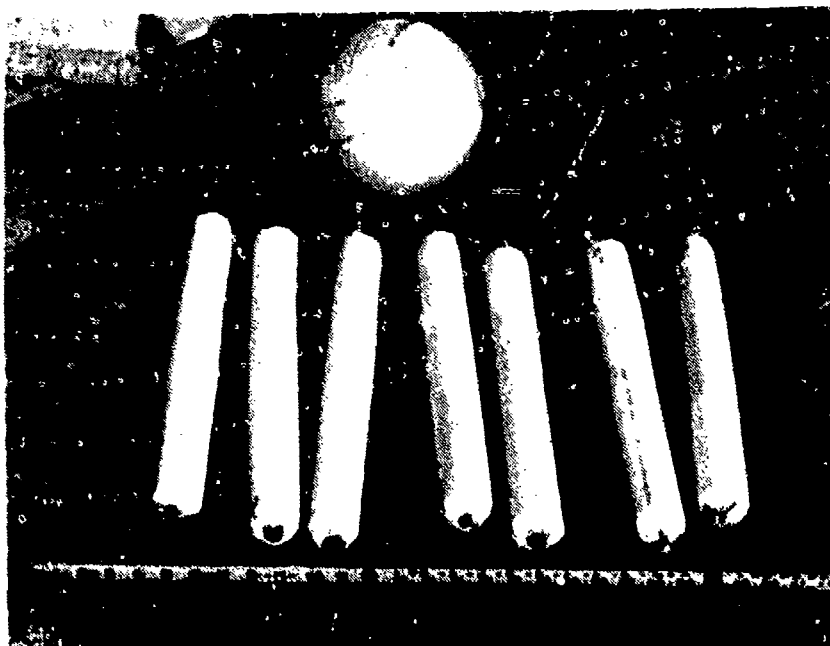
Figure 5.7   Tubes of Tovex 800^R

CHAPTER 6

TEST PROCEDURES

6.1   GENERAL OVERVIEW

The test program consisted of 13 detonations, seven of which were spherically shaped charges and six of which were planar arrays. The spherical charges consisted of either detonating cord (Primacord^R) bundled into a ball shape or Tovex^R tubes bundled together to create different charge masses. The spherical charges were all detonated 180 cm above the sand surface, and the first six had a 60 cm water overburden above the charges (Figure 4.5). The seventh detonation had a 90 cm water overburden. The planar arrays were formed by creating a horizontal checkerboard or grid of detonating cord, i.e., running the cords parallel and perpendicular to one another. The spacing and detonating cord type (explosive weight per length) were varied to obtain different charge-induced stresses. To obtain a planar stress wave traveling down through the water and sand, the detonating cord grid was suspended horizontally over the sand. The center of the grid in all cases was at a height of 180 cm above the rim of the tank. It is beyond the scope of this dissertation to present procedures and results from the planar charges, although referral to these tests is necessary for continuity. Details of the planar tests are given by Hassen (1989). Table 6.1 is a summary of all the detonations in this program. The remainder of this chapter is a detailed description of

Table 6.1 Test Sequence

Test	Description	Explosive Quantity	Explosive Type
I*	Coil	2.74 m (30 gm)	Primacord^R (50)
P1	Planar	61x61 cm grid	Primacord^R (18)
S1	Spherical	0.03 kg	Primacord^R (50)
S2	Spherical	0.08 kg	Primacord^R (50)
P2	Planar	61x61 cm grid	Primacord^R (25)
S3	Spherical	0.25 kg	Tovex 800^R
P3	Planar·	61x61 cm grid	Primacord^R (50)
S4	Spherical	0.76 kg	Tovex 800^R
P4	Planar	61x61 cm grid	Primacord^R (50)
S5	Spherical	2.25 kg	Tovex 800^R
P5	Planar	30x30 cm grid	Primacord^R (50)
S6	Spherical	0.76 kg	Tovex 800^R
P6	Planar	30x30 cm grid	Primacord^R (25)
S7	Spherical	7.02 kg	Tovex 800^R

Notes

*test to verify saturation

Primacord^R (50) = 10.66 grams of explosives per meter

Primacord^R (25) = 5.33 grams of explosives per meter

Primacord^R (18) = 3.84 grams of explosives per meter

the test procedures including sand placement and saturation, instrumentation operations, and explosive testing.

6.2   SAND PLACEMENT

To place the sand in the steel tank, the groundwater was first pumped out. Sand was then thrown into the tank with hand shovels from the working level and raked to a level 20 cm thick layer. The sand's water content at time of placement ranged from 2 to 8 percent with an average of 4.3 percent. A Wacker soil compactor (VPG 1450A) was lowered onto the sand, and four compaction coverages were made over the entire sand surface (Figure 6.1). The result was a compacted, 15 cm high lift with a relative density ranging from 84 to 91 percent which corresponds to dry density of about 1,800 kg/m^3. The tank was filled with twelve 15 cm lifts of sand for a total sand thickness of 1.8 m.

6.3   INSTRUMENTATION INSTALLATION

Instrumentation was placed in the sand at prescribed locations during the sand filling process described above. A template (Figure 6.2), precisely centered in the tank at predetermined depths, was used as a guide during instrumentation installation. Each device was accurately placed at horizontal locations identified by an X-Y coordinate system. The X,Y coordinate 0,0 was at the center of the tank. This placement accuracy was used because it was essential that strain gage pairs be parallel and at known initial separation distances; compression wave velocity calculations required known distances between devices; and scaled distance to each device was
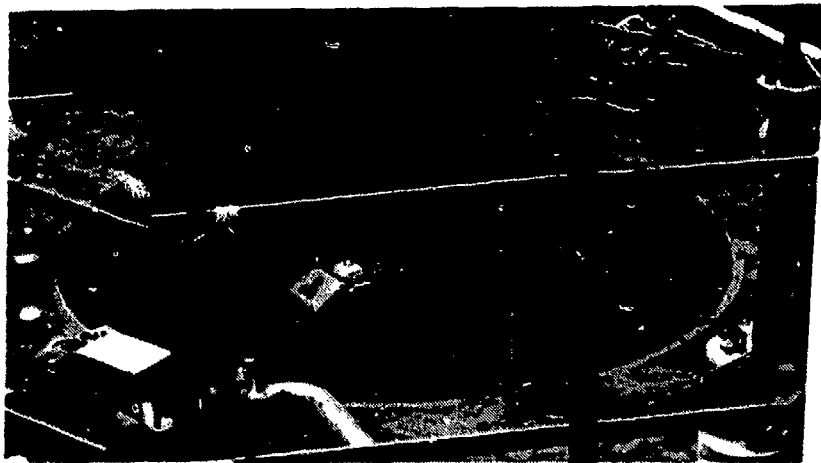
Figure 6.1 Compacting sand in test tank.

Figure 6.2 Template to position instrumentation in sand.

required for analysis purposes. Table 6.2 provides the location of each device placed in the sand.

The cabling for the instrumentation was routed horizontally over the sand to the side of the tank and then upwards. Effort was made to ensure that cabling was not taut; i.e., sufficient slack was allowed to permit movement during tests without excessive stretching (Figure 6.3). From the point where all cabling emerged from the top of the tank, it was bundled together and routed through a 23 cm aluminum pipe over the rim of the tank and to the edge of the pit. The aluminum pipe was angled slightly upwards from horizontal to permit escape of air while filling the pit with water. Upon exiting from the pipe, the cable bundle was routed out of the pit and into the instrumentation relay building.

6.4 VARIABLE DENSITY INCLUSIONS

Four items of different densities were placed in the sand at known locations (Figure 6.4). The items were: 1) bowling ball (1,330 kg/m^3), 2) soccer ball (≈ 0 kg/m^3), 3) steel cylinder (7,881 kg/m^3), and 4) can filled with foam (200 kg/m^3). The items were placed near the wall of the tank to insure they would not interfere with the instrumentation. The precise depth to the top of each item and horizontal location of the center of each item is given in Table 6.2.

6.5 SATURATION

Once the tank was filled with sand, it was necessary to obtain 100 percent saturation. To saturate the sand, the groundwater was continuously pumped from pipes beneath the impermeable liner at the bottom of the tank. Carbon dioxide was initially added to the sand

Table 6.2 Placement Location of Items in Sand

Device	Depth (cm)	X (cm) (E - W)	Y (cm) (N - S)
Strain Gage 1	152.4	0	20.3
Strain Gage 2	121.9	0	20.3
Strain Gage 3	91.4	0	20.3
Strain Gage 4	61.0	0	20.3
Strain Gage 5	30.5	0	20.3
Strain Gage 6	160.0	15.2	0
Strain Gage 7	160.0	-15.2	0
Strain Gage 8	99.1	15.2	0
Strain Gage 9	38.1	-15.2	0
Strain Gage 10	38.1	15.2	0
Strain Gage 11	38.1	-15.2	0
Accelerometer CN82A	152.4	0	-29.2
Accelerometer CR53A	91.4	0	-29.2
Accelerometer CR42A	30.5	0	-29.2
Pressure Transducer 65AJ	152.4	20.3	-24.1
Pressure Transducer 11AK	91.4	20.3	-24.1
Pressure Transducer 01AK	30.5	20.3	-24.1
Total Stress Gage 7422185	152.4	-16.5	-9.5
Total Stress Gage 8426885	91.4	-16.5	-9.5
Total Stress Gage 8426285	30.5	-16.5	-9.5
Bowling Ball	91.4	-121.9	0.0
Soccer Ball	91.4	-182.9	-61.0
Steel Cylinder	91.4	-121.9	-61.0
Foam Can	91.4	-91.4	-61.0

Note: X,Y coordinate system based on center of tank being 0,0; East is +X, North is +Y.
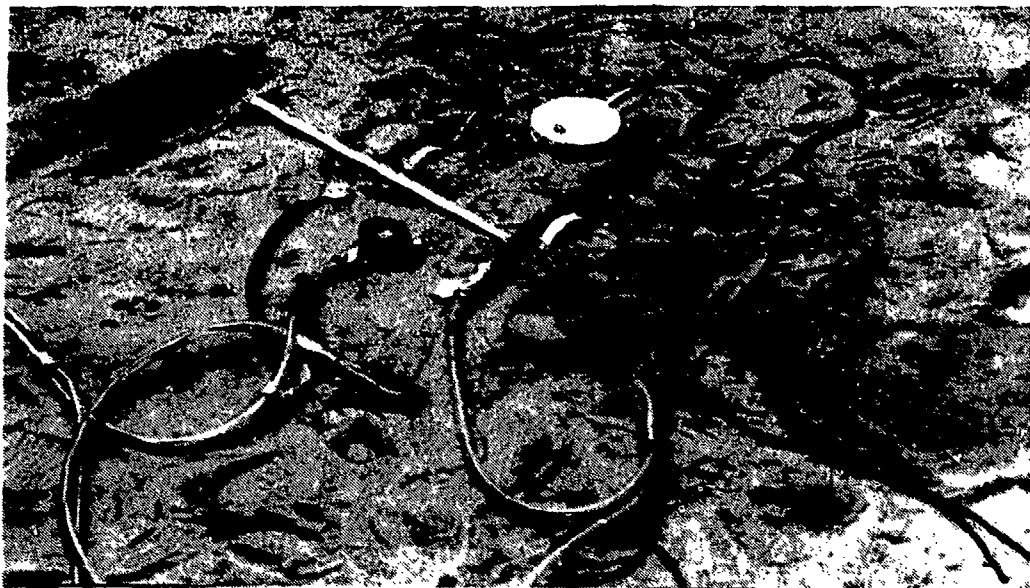
Figure 6.3   Instrumentation placed in sand.

Figure 6.4   Variable density inclusions.

through a saturation pipe network at the bottom of the tank above the impermeable liner. The carbon dioxide method has been shown to be simple, quick method for displacing air in sand voids (Butler, 1986). Carbon dioxide is denser than air and approximately 50 times more soluble. When deaired water is introduced into carbon dioxide-filled voids in the sand, it is much easier to displace the carbon dioxide with water than air. The carbon dioxide was flushed upward through the sand for approximately 4 1/2 hours until it reached the surface. This determination was made with an oxygen monitor (Hudson model 5550) which detected a decrease in oxygen at the surface of the sand as the oxygen was replaced with carbon dioxide. The total volume of carbon dioxide flushed through the sand was approximately 102 cubic meters or ten pore volumes. Deaired water was next introduced into the sand through the saturation pipe network that had been used for carbon dioxide. Water was added at approximately 0.005 cubic meters per hour which was well below the rate of capillary rise for the sand. The water reached the surface of the sand after about 15 hours.

At this point, it was assumed that the sand in the tank, although wet, was not fully saturated. A previous test on Poudre Valley sand, placed and saturated in a similar tank in the same manner, showed that three weeks were required for full saturation as indicated by a seismic velocities. Table 6.3 gives the compressional wave velocity versus time results for that previous test. Figure 2.1, a plot of velocity versus saturation for Ottawa sand (from Allen, et al., 1980), illustrates the effects of very small amounts of air on wave velocity.

Table 6.3 Compression Wave Velocities - Previous Test

Time (Days)	Velocity (m/sec)
0	167
1	305
2	201
8	1097
14	1448
20	1539

Note: Velocities calculated by comparing times of wave arrival at instrumentation at known depths. Time shown is after water was initially added to sand.

After twelve days of continued upward flushing with deaired water, a test was conducted to ensure that the compression wave velocity in the sand indicated full saturation. The test was performed by placing approximately 30 cm of water above the sand surface (Figure 6.5) and detonating a blasting cap attached to 2.74 m of detonating cord (50 grain) coiled into a 0.3 m diameter spiral in the water at the center of the tank. Compression wave velocities were calculated by dividing separation distances between transducers by the differences in wave arrival times at the transducers (Table 6.4). The test showed that mean compression wave velocity in the sand was 1854 m/sec (standard deviation of 43 m/sec), indicating full saturation.

Once the sand was saturated, the pit was filled with water to a level 2.4 m above the top of the sand surface. Figure 6.6 is a photograph of the pit filled with water.

Table 6.4 Saturation Test Results

Transducers	Separation Distance (cm)	Difference in Times of Arrival (msec)	Compression Wave Velocity m/sec
CN82A-CR53A	61.72	0.326	1893
CR53A-CR42A	56.90	0.309	1841
01AK-11AK	61.72	0.326	1893
11AK-65AJ	56.90	0.318	1789
			mean = 1854

6.6   EXPLOSIVES TESTING

6.6.1   Detonation Procedures

There were seven separate detonations of different masses of spherically shaped charges in this program. All charges were placed in water which was added on top of the test sand to maximize the explosive effect and minimize debris and noise (Figure 6.6). The explosive charges were suspended 1.8 m above the sand at the center of the tank from a rope transversing the pit. The first six charges had a 60 cm water overburden; the final had a 90 cm overburden (Figure 4.5).

A blaster certified by the state of Colorado performed all explosive tasks. Detonations were initiated with a blasting cap taped to detonating cord connected to the explosive to be used. After insuring with an amp meter that no stray current was present, the wires from the cap were attached with alligator clips to 20 gage wires running from the pit to the command post. After a warning and safety check of the area, ends of the 20 gage wires were attached to a Geometrics Nimbus Instruments High Voltage Blaster, Model HVB-1, which
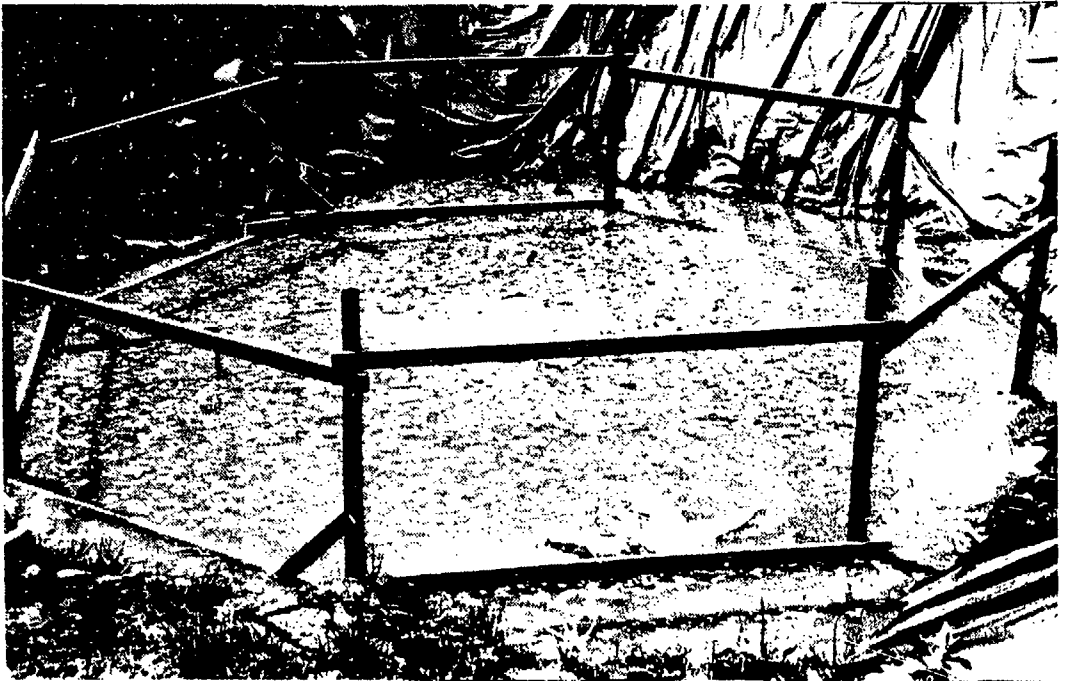
Figure 6.5   Completed test pit.

Figure 6.6   Test pit prepared for detonation.

uses a capacitor for discharge of 300 milliamps (mA). Also attached
to the Blaster was a set of wires to the TDR's; thus, when the fire
button on the Blaster was depressed, the capacitor discharged, sending
current to the blasting cap and an independent trigger signal to the
TDR's.

Safety practices outlined by the explosives manufacturer were
strictly followed at all times (Dupont, 1983 and Ensign-Bickford,
1984) along with local safety procedures. Explosives were always
stored in a designated bunker at Colorado State University.
Explosives were placed without electric caps or detonators. Five
minutes before the detonation, the electric caps were taped to the
detonating cord. During blast preparation, a series of siren warnings
was given, and safety spotters prevented non-authorized personnel and
animals from entering the blast area. After detonation, the licensed
blaster insured that the site was safe before allowing personnel to
approach. Ground shock and airblast safety was insured by monitoring
blast response as described in Allard and Norquist (1985). A blasting
permit was obtained for the test program and renewed as required.
Appendix E contains the local written directives governing blasting
operations at the test site.

6.6.2   Data Recording

Immediately prior to each detonation, the accelerometers and
pore pressure transducers were balanced, pre-detonation strain gage
readings were taken, and the total stress gage power supply was set to
the prescribed voltage. Red dye was placed in the piezometer tubes
for visibility, and two video cameras were aimed at the piezometer
with internal stop watches running.

The detonations were initiated from the command post with the High Voltage Blaster. The blaster also triggered the TDR's for recording data from accelerometers, pore pressure transducers and total stress gages. For the first six spherical detonations, the TDR's sampling rate was set at 156,000 samples per second (one sample every 0.064 msec). For the final detonation, three of the instruments were each connected to two different TDR's, and the data from each were collected at two different rates of 500,000 and 156,000 samples per second (one sample every 0.002 msec and 0.064 msec) to determine the significance of digitization rate on results. In addition to the data recorded with the TDR's, strain gage data were obtained before and after each detonation by reading the induced voltage output on the Bison Soil Strain Gage for each pair of strain gages.

After detonations, a scuba diver inspected the condition of the tank, sand, and accessible instrumentation/cables. While in the water, the diver measured the elevation of the sand surface in the tank at 30.5 cm increments across the tank. After the last detonation, the water was pumped from the pit and final sand elevations were obtained with a tape measure. The water was then pumped from the sand, and the sand was removed from the tank. The final locations of all instrumentation and varying density inclusions were recorded.

CHAPTER 7

TEST RESULTS

7.1 INTRODUCTION

This chapter presents the results of the experimental program to substantiate the analytical model described in Chapter 3 and to provide data for empirical relationships describing blast-induced liquefaction.

Seven spherically shaped charges detonated in this program are identified S1 through S7 as seen in Table 6.1. Also shown in this table are six planar tests that were performed in a separate experimental program (Hassen, 1989). The seven spherical tests consisted of charges detonated in water 1.8 m above the sand surface. A typical detonation is shown in Figure 7.1.

7.2 DYNAMIC MEASUREMENTS

The results of the efforts to measure dynamic total stress, porewater pressure, and acceleration are discussed in this section. Two problems were encountered with these measurements. First, none of the accelerometers yielded dynamic data that could be analyzed (Appendix F provides accelerometer records). Second, as testing progressed, several of the pressure transducers and total stress gages became inoperative. Table 7.1 lists the detonations and shows which devices were active (yielded usable data).
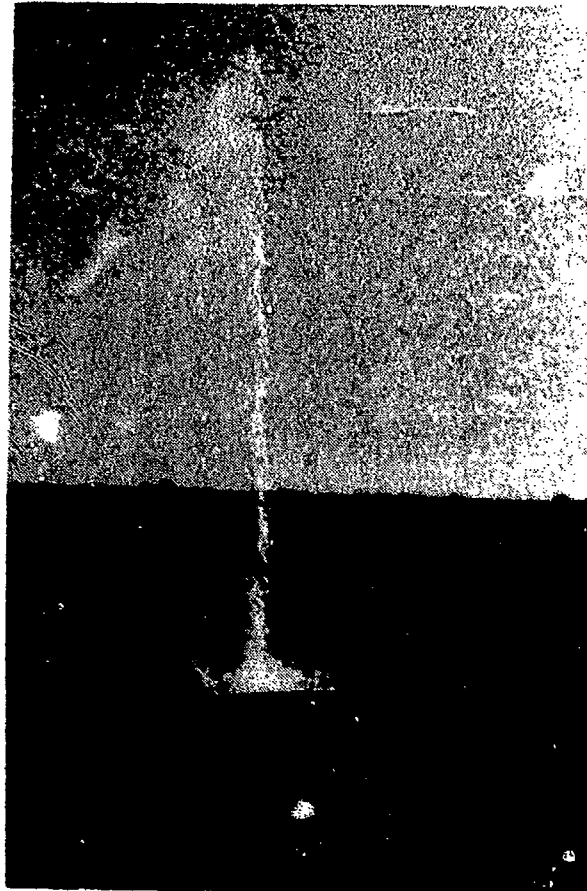
Figure 7.1 Spherical Detonation.

Table 7.1 Spherical Charge Detonation Sequence

Test	Charge Mass (kg)	Explosive Type	Active Instrumentation
S1	0.03	Primacord^R	SP, TP, MP, BP, ST, MT
S2	0.08	Primacord^R	SP, BP, ST, MT
S3	0.25	Tovex 800^R	SP
S4	0.76 (#1)	Tovex 800^R	SP, BP, ST, MT
S5	2.25	Tovex 800^R	SP, ST, MT
S6	0.76 (#2)	Tovex 800^R	SP, BP, ST, MT
S7	7.02	Tovex 800^R	SP

Notes:
  SP - pore pressure transducer on surface of sand
  TP - upper pore pressure transducer originally at 30.5 cm depth
  MP - middle pore pressure transducer originally at 91.4 cm depth
  BP - bottom pore pressure transducer originally at 152.4 cm depth
  ST - total stress gage on surface of sand
  MT - middle total stress gage originally at 91.4 cm depth
#1 and #2 - differentiates between first (#1) 0.76 kg detonation and
        second (#2) 0.76 kg detonation.

Figures 7.2 through 7.8 represent the time-history data from the instrumentation listed as active in Table 7.1. The figures are arranged in the sequence of detonations. The data points, i.e., the measured stresses or pressures, were obtained at intervals of 0.064 msec except in Test S7 where two sampling rates were used. In that test, one set of data was sampled at intervals of 0.064 msec (slow), and the other at intervals of 0.002 msec (fast). It is noteworthy that the slow rate caused significant difficulty in analyzing the data, because peak values were not recorded (Chapter 8).
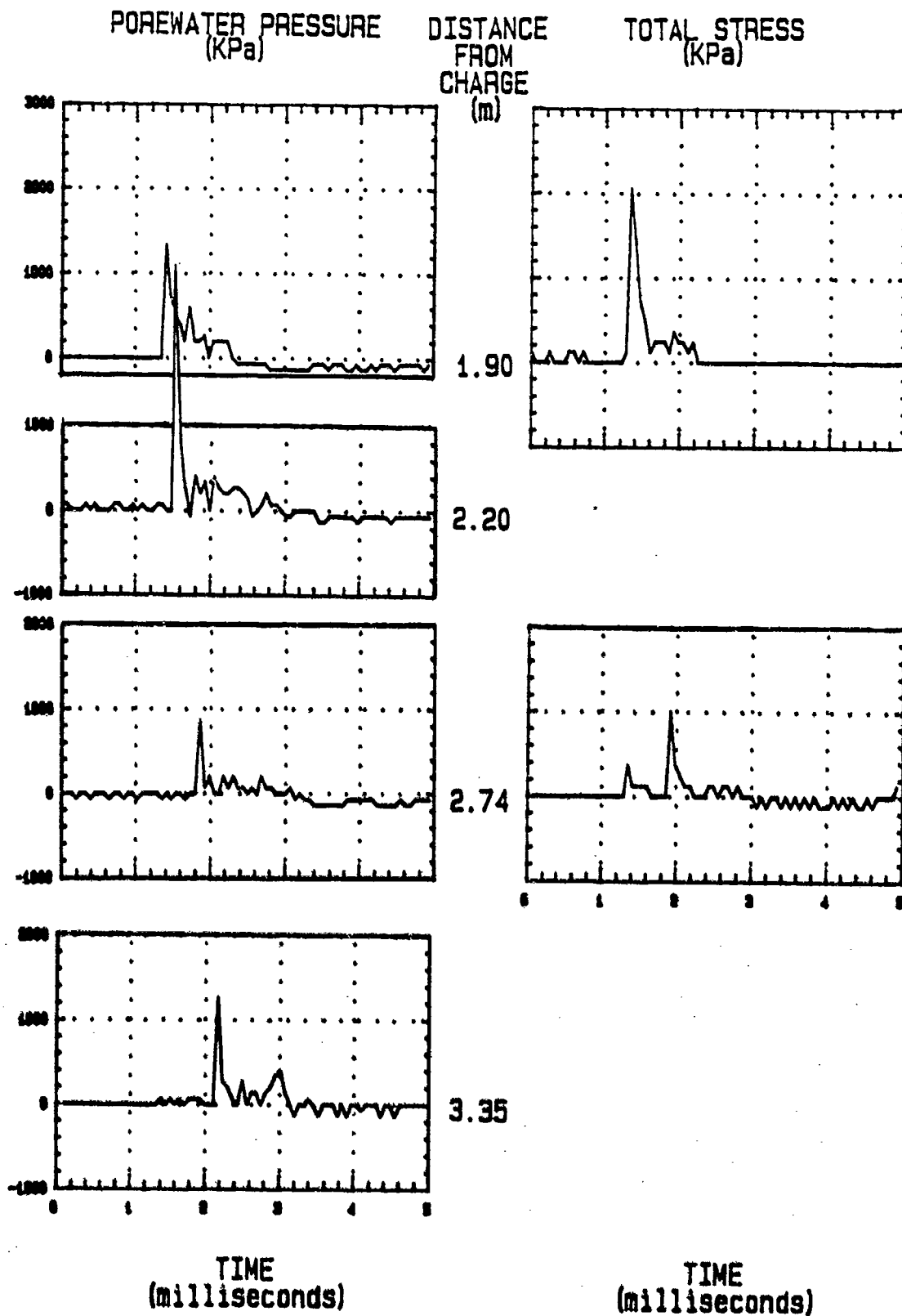
Figure 7.2 Dynamic response to 0.03 kg charge.
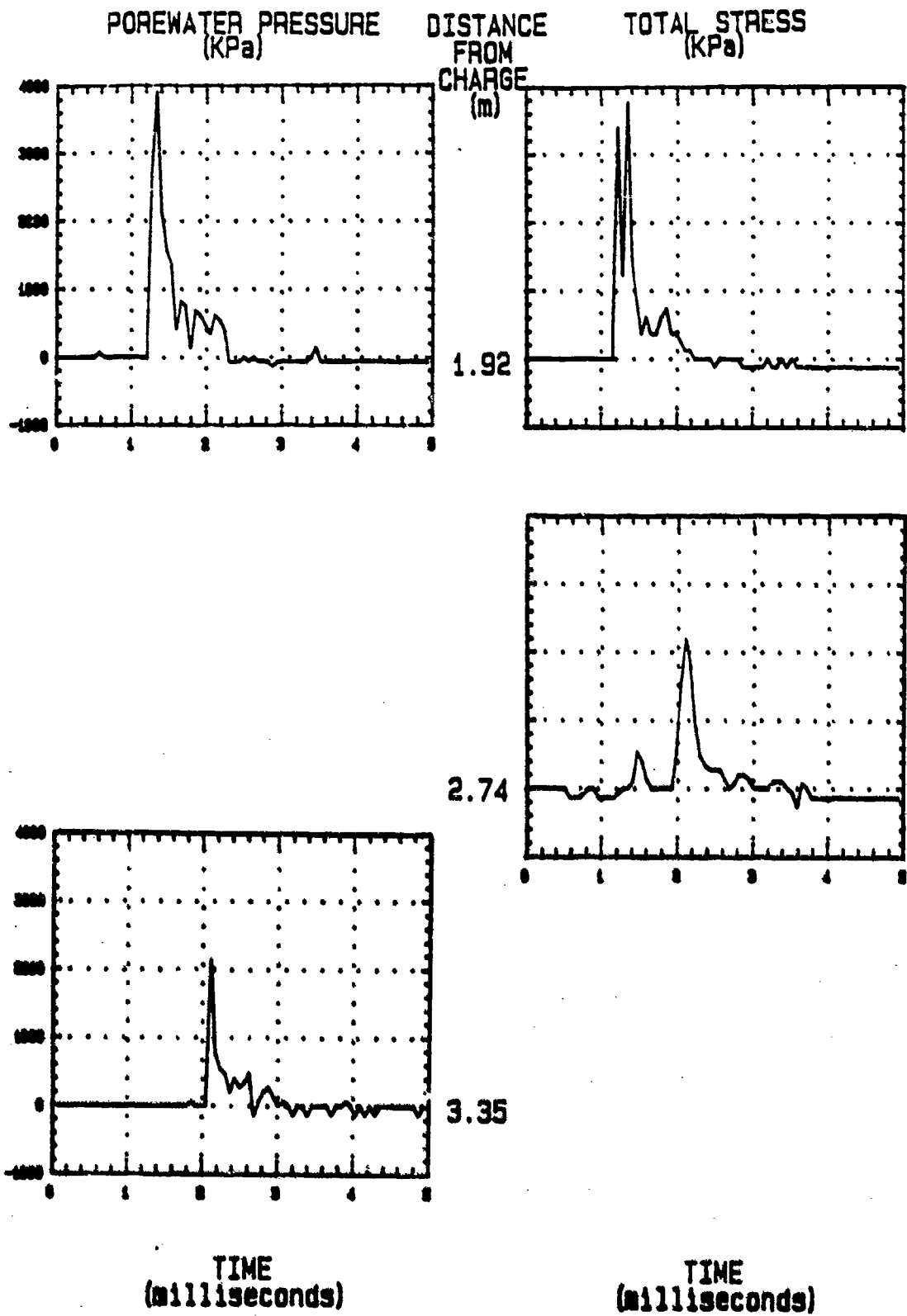
Figure 7.3 Dynamic response to 0.08 kg charge.

POREWATER PRESSURE
(KPa)

DISTANCE
FROM
CHARGE
(m)

TOTAL STRESS
(KPa)

1.98
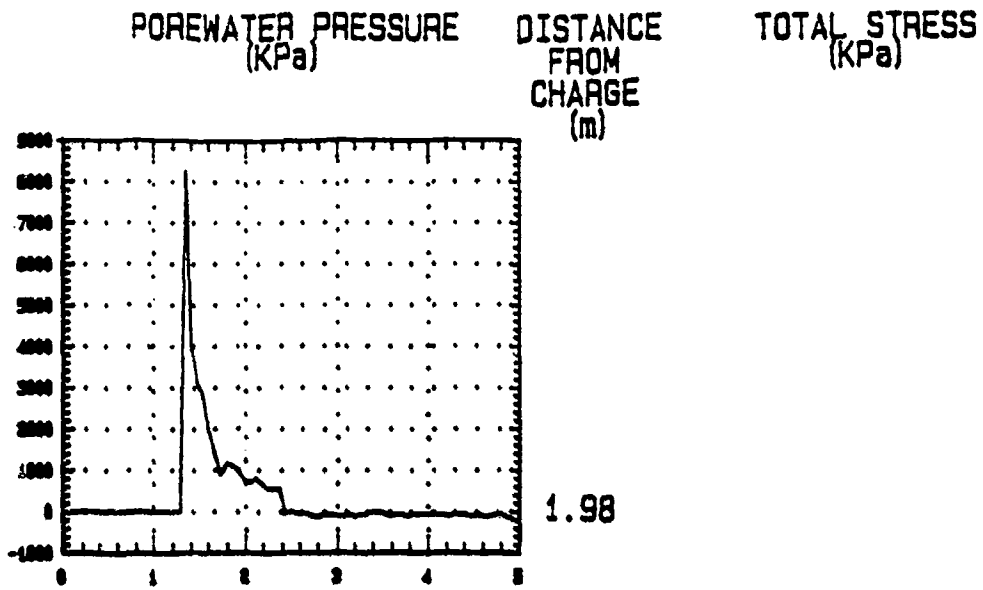
TIME
(milliseconds)

TIME
(milliseconds)

Figure 7.4   Dynamic response to 0.25 kg charge.
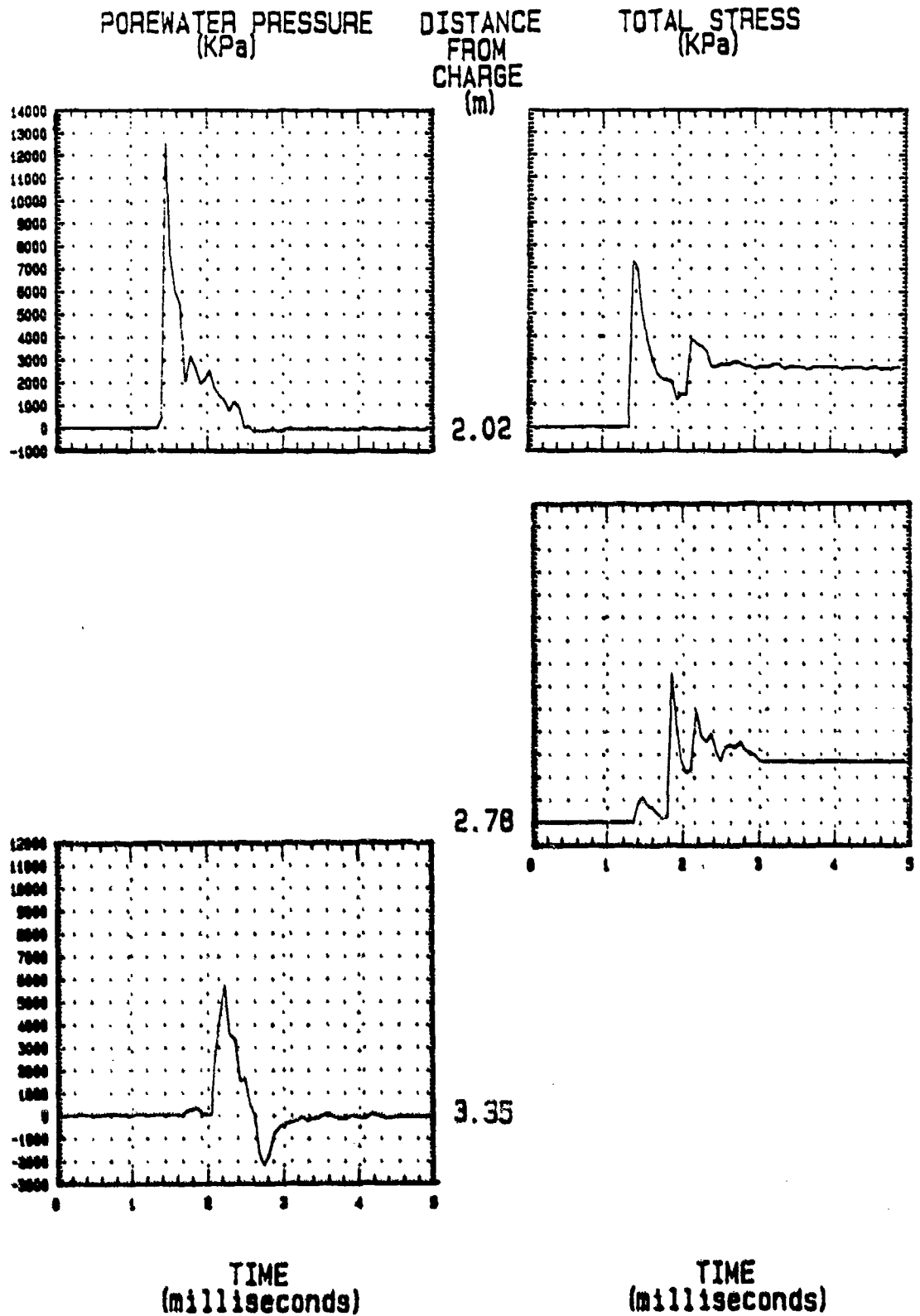
Figure 7.5 Dynamic response to 0.76 kg charge (#1).
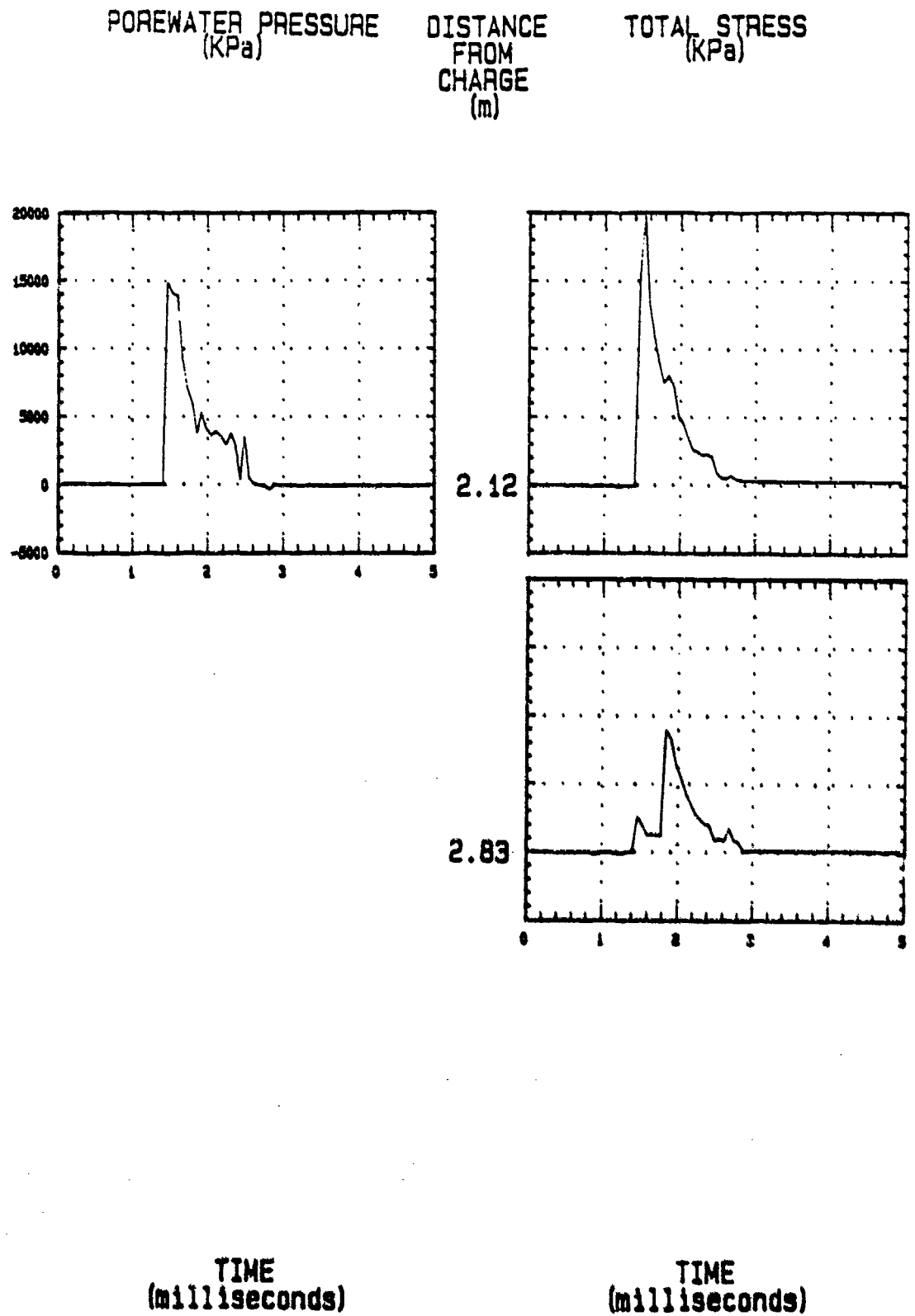
Figure 7.6   Dynamic response to 2.25 kg charge.
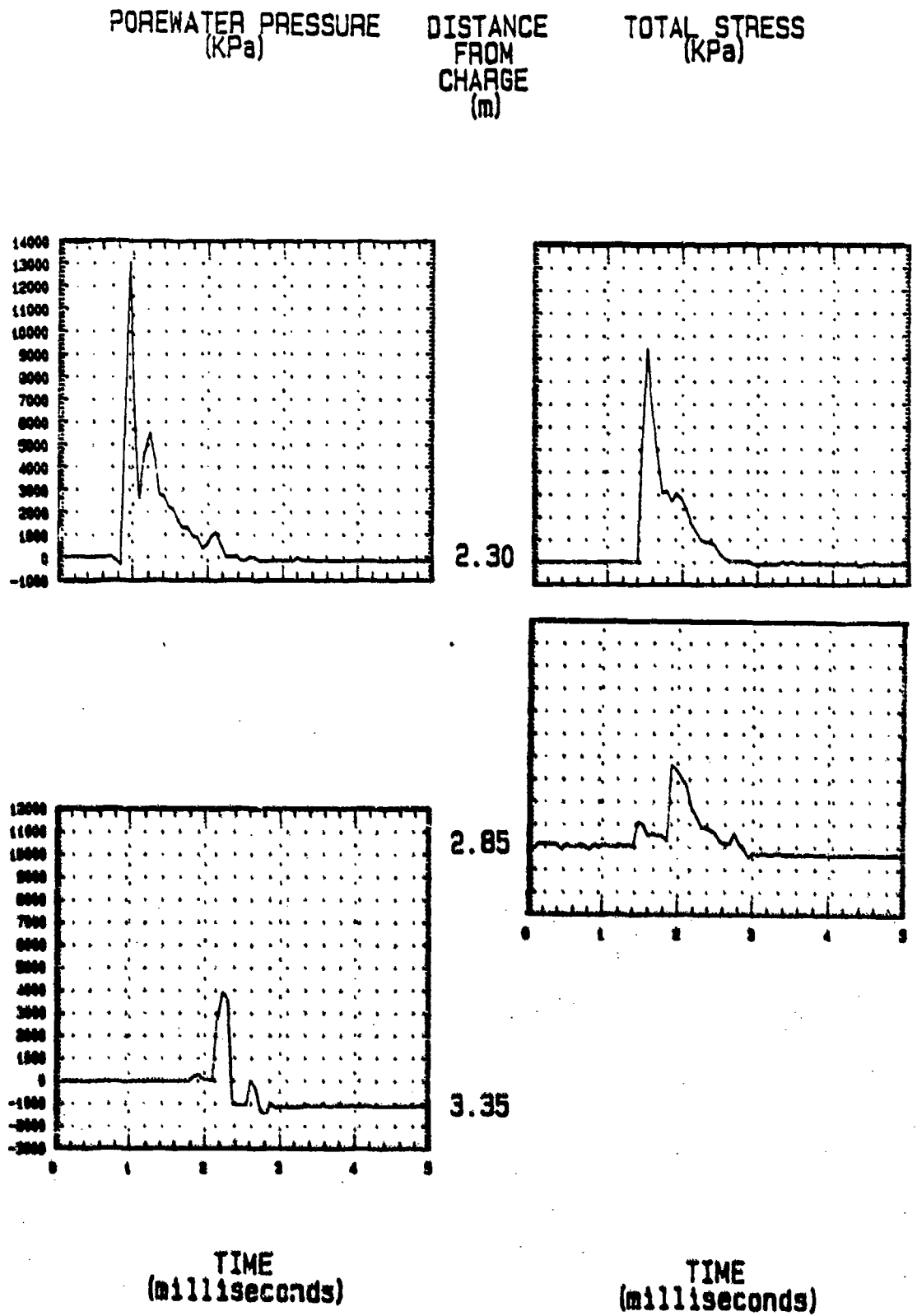
Figure 7.7 Dynamic response to 0.76 kg charge (#2).

POREWATER PRESSURE
(KPa)

DISTANCE
FROM
CHARGE
(m)

TOTAL STRESS
(KPa)

2.35

FAST RATE

2.35

SLOW RATE
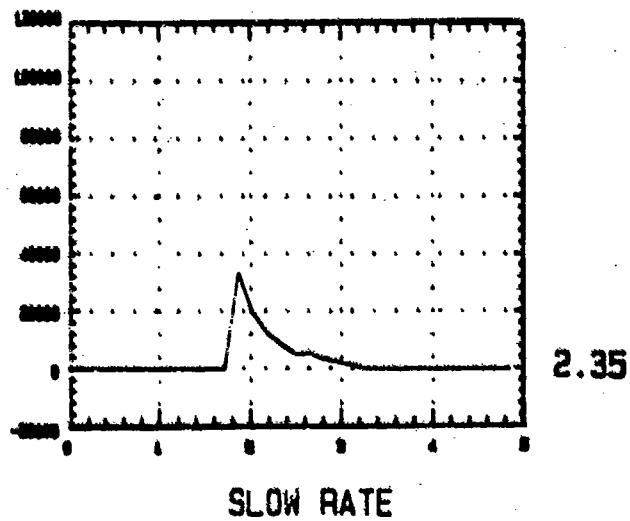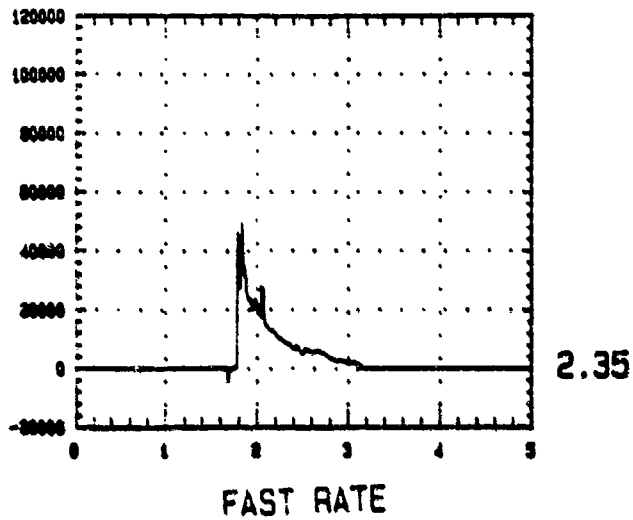
TIME
(milliseconds)

TIME
(milliseconds)

Figure 7.8 Dynamic response to 7.02 kg charge.

Based on the time-history results, compression wave velocities in the water and in the sand were determined. The water calculations were made by dividing the distance from the charge to devices in the water on the sand surface by the time of wave arrival at the device. For the sand velocities, the distances between buried devices were divided by the differences in the times of arrival at the devices. Tables 7.2 and 7.3 give the results of these calculations. The mean compression wave velocity in water was 1480 m/sec (standard deviation of 90 m/sec), and in sand, 1812 m/sec (standard deviation of 313 m/sec).

In addition to the time-history responses of the transducers, relations showing peak total stress and peak porewater pressure as functions of scaled-distance (distance from charge divided by cube root of charge mass) were obtained. The distance to each device was determined from the post-test strain gage readings (described later). The scaled distances are given in Table 7.4, and the peak total stress and porewater pressure for each scaled distance is shown in Table 7.5.

7.3 PIEZOMETER READINGS

During the detonations, two video cassette cameras were aimed at the piezometer standpipe to record water rise and time data from the bottom of the sand bed. Red dye was injected into the piezometer tubing to make the rising water more visible, and the video cameras' built-in stop watches were running during and after detonations. The piezometer results are shown in Figures 7.9 through 7.15 as water rise in meters versus time. The water rise represents the change in water pressure at the bottom of the sand due to passage of the stress wave. As seen in Figures 7.9 through 7.15, data sets for several of the

Table 7.2 Compression Wave Velocity in Water

Test	Device	Distance from Charge (m)	Compression Wave Time of Arrival (msec)	Compression Wave Velocity (m/sec)
S1	SP	1.905	1.344	1417
S1	ST	1.905	1.280	1488
S2	SP	1.920	1.280	1500
S2	S:	1.920	1.216	1579
S3	SP	1.984	1.280	1550
S4	SP	2.018	1.408	1433
S4	ST	2.018	1.344	1501
S5	SP	2.118	1.408	1504
S5	ST	2.118	1.472	1439
S6	SP	2.298	1.408	1632
S6	ST	2.298	1.472	1561
S7	SP	2.347	1.784	1316
S7	ST	2.347	1.782	<u>1317</u>
			mean:	1480

Table 7.3 Compression Wave Velocity in Sand

Test	Device	Distance from Sand Surface (m)	Compression Wave Time of Arrival (msec)	Time of Arrival at Sand Surface (msec)	Compression Wave Velocity (m/sec)
S1	TP	0.299	1.472	1.344	2333
S1	MT	0.838	1.856	1.344	1637
S1	MP	0.838	1.792	1.344	1871
S1	BP	1.448	2.112	1.344	1885
S2	MT	0.838	1.920	1.280	1310
S2	BP	1.433	2.112	1.280	1722
S4	MT	0.756	1.792	1.408	1968
S4	BP	1.335	2.048	1.408	2086
S5	MT	0.707	1.792	1.472	2210
S6	MT	0.546	1.856	1.472	1421
S6	BP	1.055	2.176	1.472	1498
				mean:	1812

Table 7.4 Distances and Scaled Distances from Charges to Devices

Test	Explosives Mass (kg)	SP	TP	MP	BP	ST	MT
S1	0.03	1.90/6.11	2.20/7.08	2.74/8.82	3.35/10.78	1.90/6.11	2.74/8.82
S2	0.08	1.92/4.70	—	—	3.35/8.21	1.92/4.70	2.74/6.72
S3	0.25	1.98/3.14	—	—	—	—	—
S4	0.76	2.02/2.21	—	—	3.36/3.68	2.02/2.21	2.78/3.05
S5	2.25	2.12/1.62	—	—	—	2.12/1.62	2.83/2.16
S6	0.76	2.30/2.52	—	—	3.35/3.67	2.30/2.52	2.85/3.12
S7	7.02	2.35/1.23	—	—	—	—	—

Notes:

1 - first number is distance in m, second number is scaled distance in $m/kg^{1/3}$

2 - see Table 7.1 for device identification

3 - dashes indicate inoperative instrumentation

Table 7.5 Scaled Distances and Peak Stress and
Porewater Pressure Readings

Test	Device	Scaled Distance $(m/kg^{1/3})$	Peak Recorded Porewater Pressure (kPa)	Peak Recorded Stress (kPa)
S1	SP	6.11	1350	--
	TP	7.08	3200	--
	MP	8.82	900	--
	BP	10.78	1250	--
	ST	6.11	--	2050
	MT	8.82	--	1000
S2	SP	4.70	3900	--
	BP	8.21	2150	--
	ST	4.70	--	3800
	MT	6.72	--	2200
S3	SP	3.14	8200	--
S4	SP	2.21	12500	--
	BP	3.68	5800	--
	ST	2.21	--	7300
	MT	3.05	--	6600
S5	SP	1.62	15000	--
	ST	1.62	19800	--
	MT	2.16	--	9000
S6	SP	2.52	13000	--
	BP	3.67	3900	--
	ST	2.52	--	9500
	MT	3.12	--	3700
S7	SP	1.23	4500	

Note: see Table 7.1 for device identification

Figure 7.9 Measured residual porewater pressure, 0.03 kg charge.

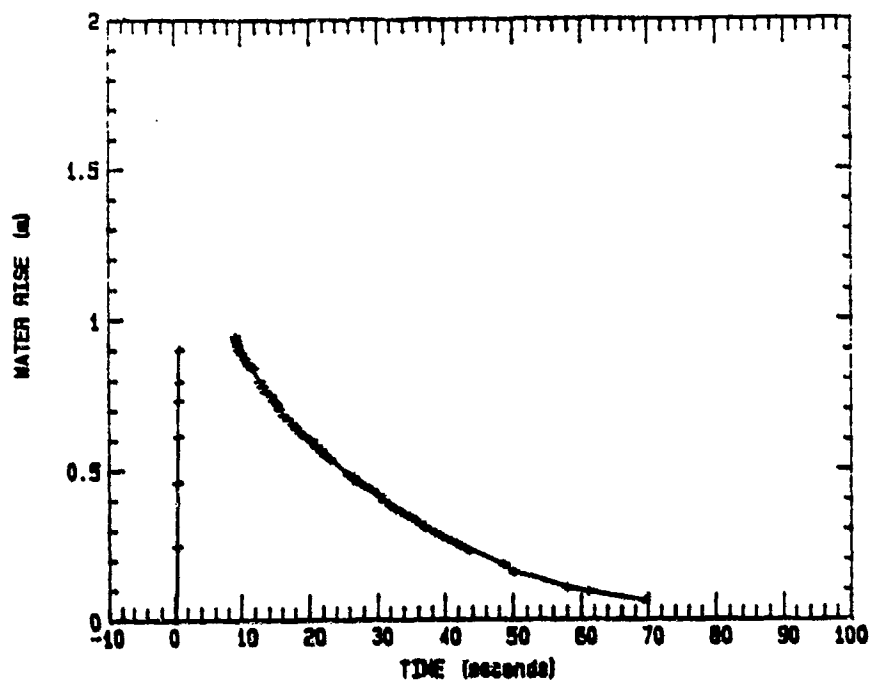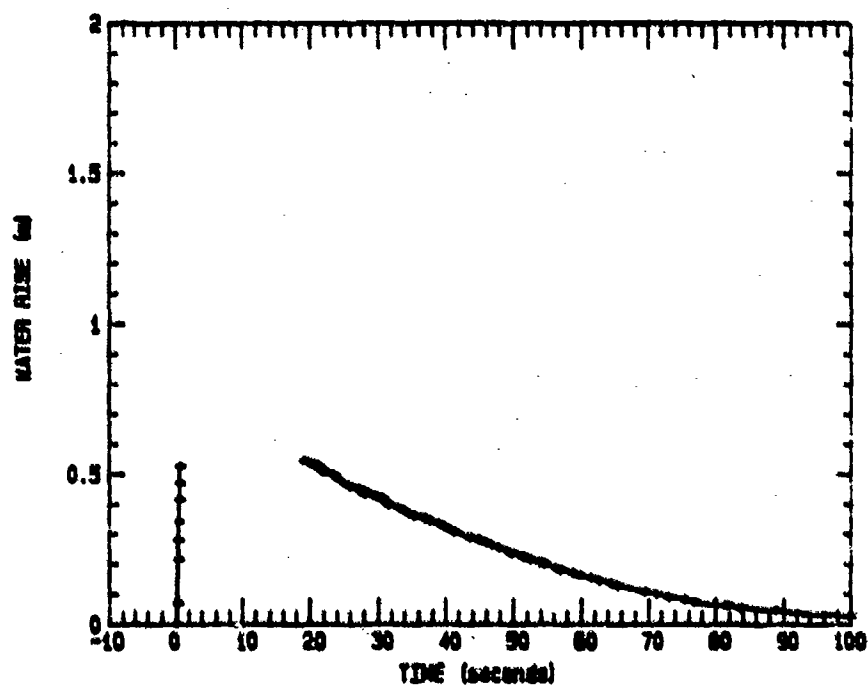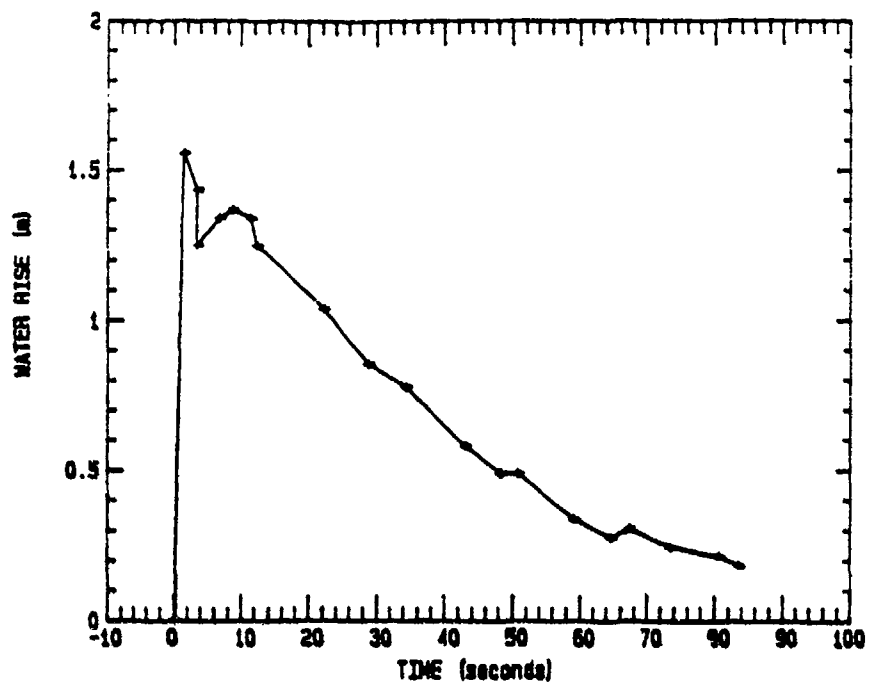Figure 7.10 Measured residual porewater pressure, 0.08 kg charge.

Figure 7.11 Measured residual porewater pressure, 0.25 kg charge.
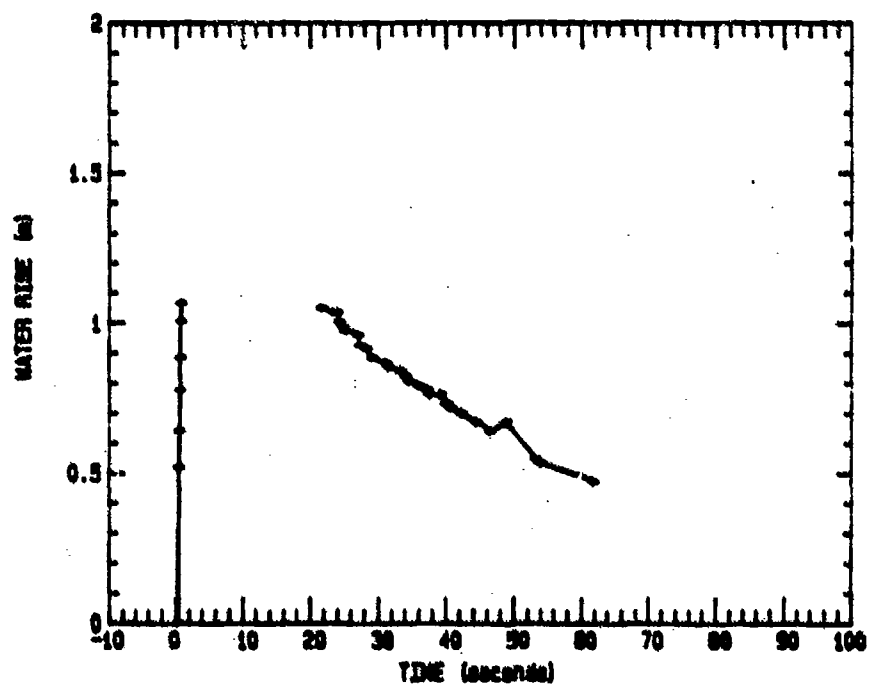

Figure 7.12 Measured residual porewater pressure, 0.76 kg charge (#1).
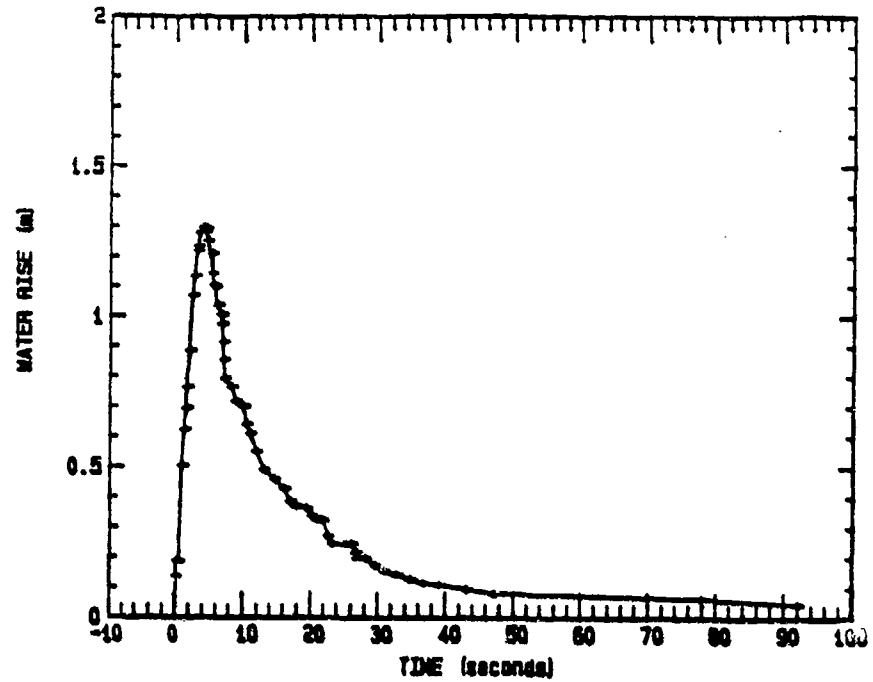
Figure 7.13 Measured residual porewater pressure, 2.25 kg charge.
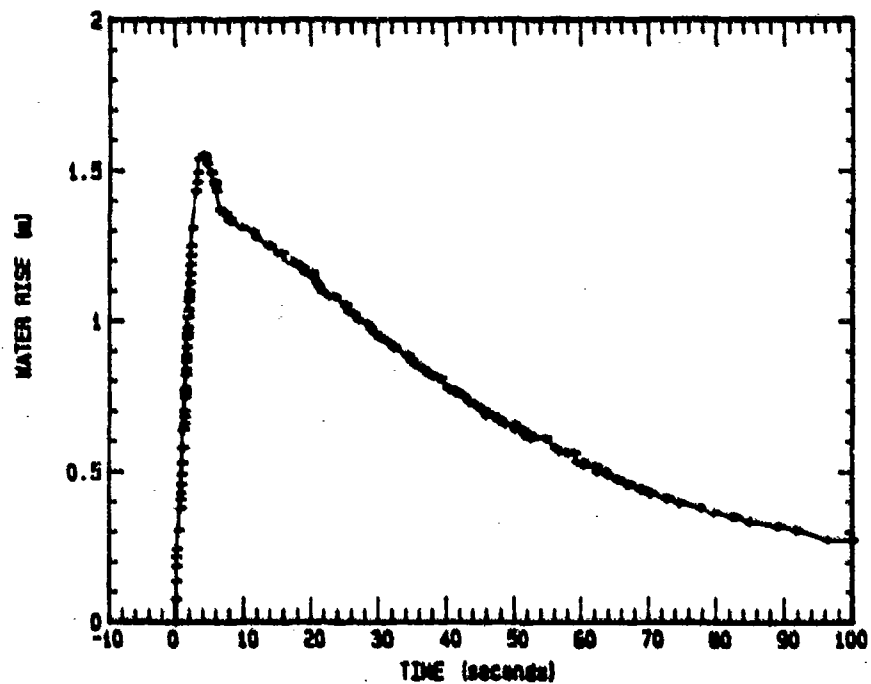
Figure 7.14 Measured residual porewater pressure, 0.76 kg charge (#2).
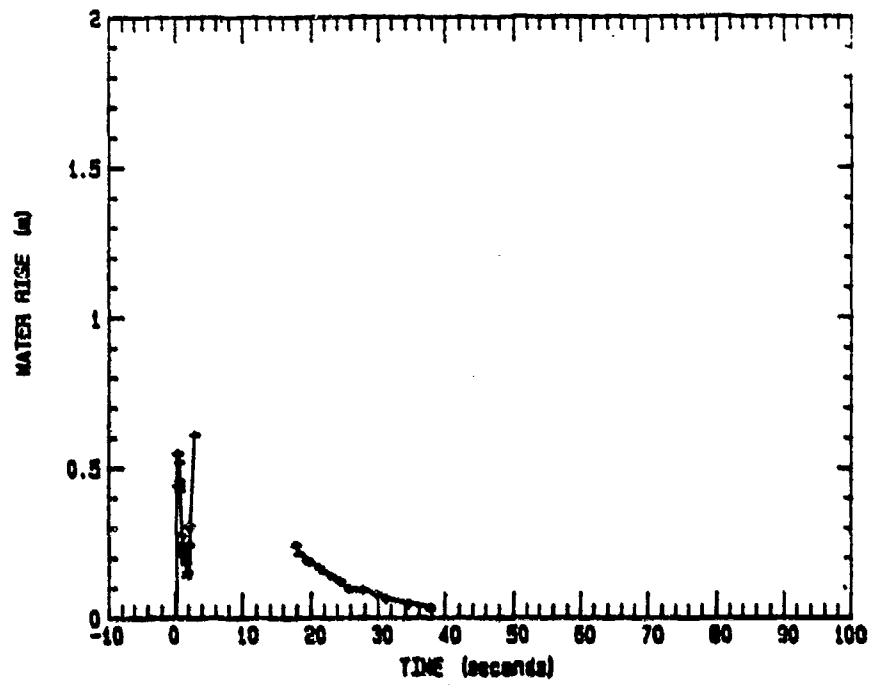
Figure 7.15   Measured residual porewater pressure, 7.02 kg charge.

detonations are incomplete. Data points on the plots are indicated by
"+" marks, and where data is continuous, a line is shown connecting
the data points. Incomplete data were due to video recording
malfunctions which included obstruction by water spray, smoke, focus
problems, and water damage to recording equipment.

7.4   POST-TEST MEASUREMENTS

7.4.1   Sand Surface Profiles

The elevation of the sand surface in the tank was initially
known and then measured by a scuba diver after each detonation. The
elevations for Tests S1 through S7 and P1 through P6 (planar tests)
are given in Table 7.6 and shown graphically in Figure 7.16. The
elevations were measured on an east-west line across the tank at 30.5
cm (1 foot) intervals, with station 0 at the west rim, station 14 at
the east rim, and station 7 at the tank center. The elevations after
the final detonation were also measured in perpendicular directions
after the water was pumped from the pit. During this pumping, there
was some disturbance of the sand surface by water, sand, and clay
flowing from around the tank to a depression in the sand in the center
of the tank (clay eroded into the water from above the pond liner).

It is of interest to note the formation of a "crater"
following the later spherical detonations. On the last two
detonations, a rim of sand was formed above and outside the edge of
the tank. After detonation S6, the scuba diver estimated this rim to
be about 20 cm high and 60 cm wide. After S7 the sand rim was
measured to be between 30 and 45 cm high and 75 to 90 cm wide.
Figures 7.17 and 7.18 are photographs of the pit showing the sand
surface after the water was pumped out.

Table 7.6 Sand Surface Elevations

Station	Initial	After Saturation	Sand Elevations (cm) Below Tank Rim Following Designated Detonation[1]											
			P1	S2	P2	S3	S4	P4	S5	P5	S6	P6	S7[4]	S7[4,5]
0	0	3.1[2]	3.1	8.5	9.1	6.1[2]	11.6	8.5	5.5[2]	11.6	+1.2[6]	4.0	0.0	7.6
1	0	5.2	3.7	9.1	9.1	7.6[2]	14.0	13.4	9.1	12.8	11.6	14.0	5.2	15.2
2	0	4.6	4.0	10.1	9.4	8.8[2]	14.0	17.4	11.6	14.3	12.2	16.5	7.6	17.7
3	0	5.2	4.9	10.4	11.6	11.0[2]	17.1	11.0	15.2	16.5	12.5	21.6	25.3	25.3
4	0	5.5	5.8	10.7	12.8	12.2[2]	18.2	19.2[2]	21.6	38.4	24.4	26.5	35.6	45.7
5	0	6.1	6.4	13.7	14.0	14.6	26.5	22.6	32.9	39.3	39.6	44.2	48.2[3]	51.8
6	0	6.4	7.0	16.8	15.2	17.7	36.6	29.0	43.0	46.9	46.9	51.8	64.9[3]	68.6
7	0	6.4	7.6	15.2	15.5	18.9	39.9	29.0	49.4	46.9	51.8	51.8	68.6[3]	68.6
8	0	5.8	7.9	13.7	15.2	17.7	39.9	31.7	45.7[2]	36.3	50.6	51.8	67.4	65.8
9	0	5.5	7.9	12.2	14.6	14.6	37.2	27.4[2]	30.5	32.9	46.9	49.4	53.3	50.9
10	0	5.2	7.9	11.0	13.4	14.0[2]	24.1	21.3[2]	22.9[2]	29.0	26.5	34.1	48.2	42.1
11	0	5.5	7.9	9.8	12.5	12.2[2]	18.0	11.6[2]	18.3[2]	19.8	13.7	23.8	32.9	26.8
12	0	5.8	8.2	8.8	12.2	11.9[2]	13.1	16.5[2]	16.2	16.8[2]	11.0	15.8	20.4	15.2
13	0	7.6	8.5	9.7	12.2	10.7[2]	11.6	12.8	9.1[2]	12.8[2]	8.2	11.0	12.8	12.8
14	0	8.5[2]	8.5	11.9	12.2	9.1[2]	9.1	8.8	5.8	11.9[2]	3.4	3.4	0.0	2.4

Notes:

1 - S1 and P3 elevations were not measured.
2 - Elevations interpolated (not measured).
3 - 10.1 cm of clay on top of sand.
4 - Elevations measured after water was pumped from pit and sand.
5 - Elevations measured in south to north direction.
6 - + sign indicates elevation above tank rim.

INITIAL

AFTER P4

AFTER SATURATION

AFTER S5

AFTER P1

AFTER P5

AFTER S2

AFTER S6

AFTER P2

AFTER P6

AFTER S3

AFTER S7

AFTER S4

AFTER S7

(PERPENDICULAR DIRECTION)
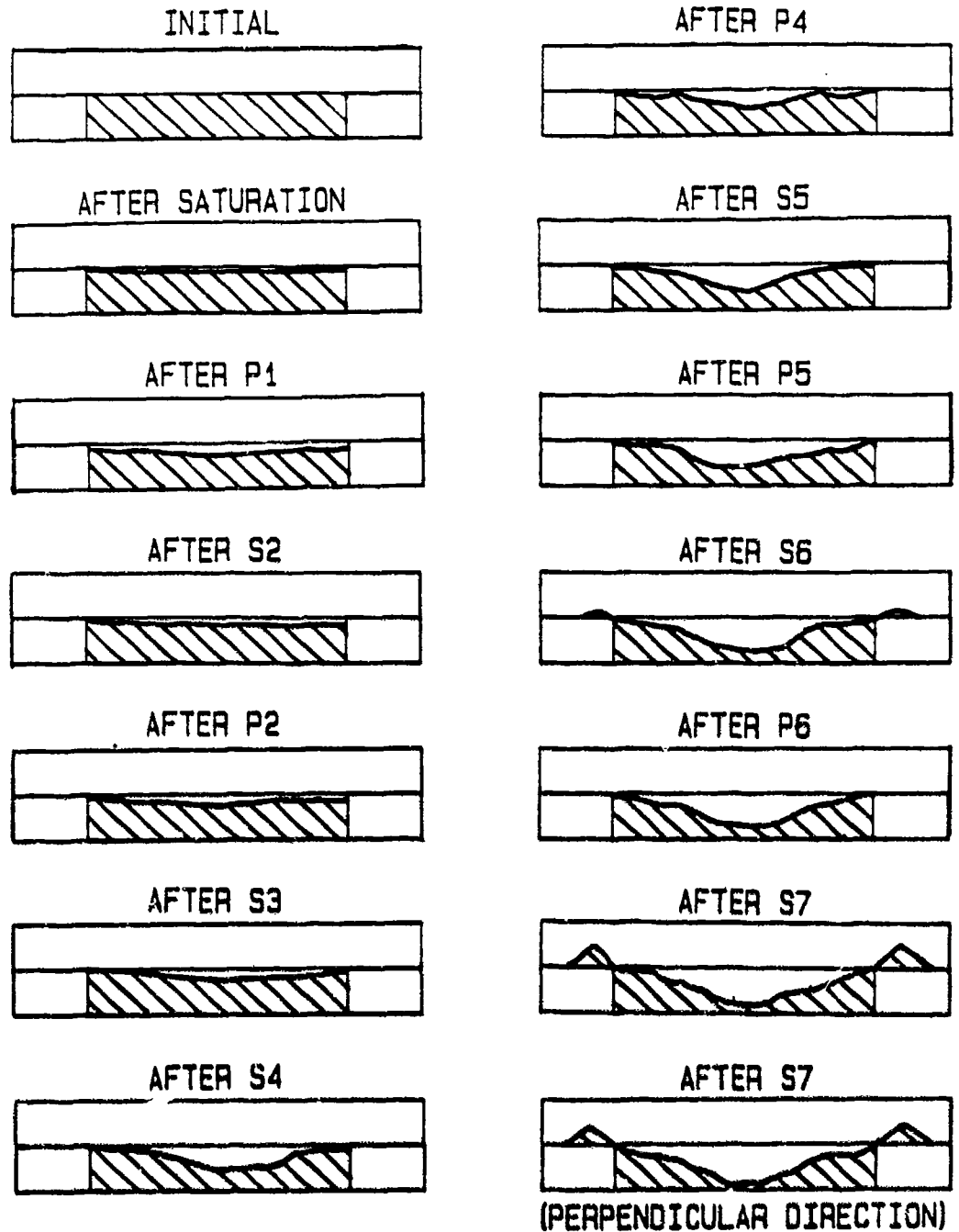
NOTES:

HORIZONTAL AND VERTICAL SCALE: [scale bar] meters
TANK IS AT RIGHT AND LEFT OF SAND
ORIGINAL SURFACE SHOWN
SHADED AREA IS SAND
ONLY TOP METER OF TANK IS SHOWN

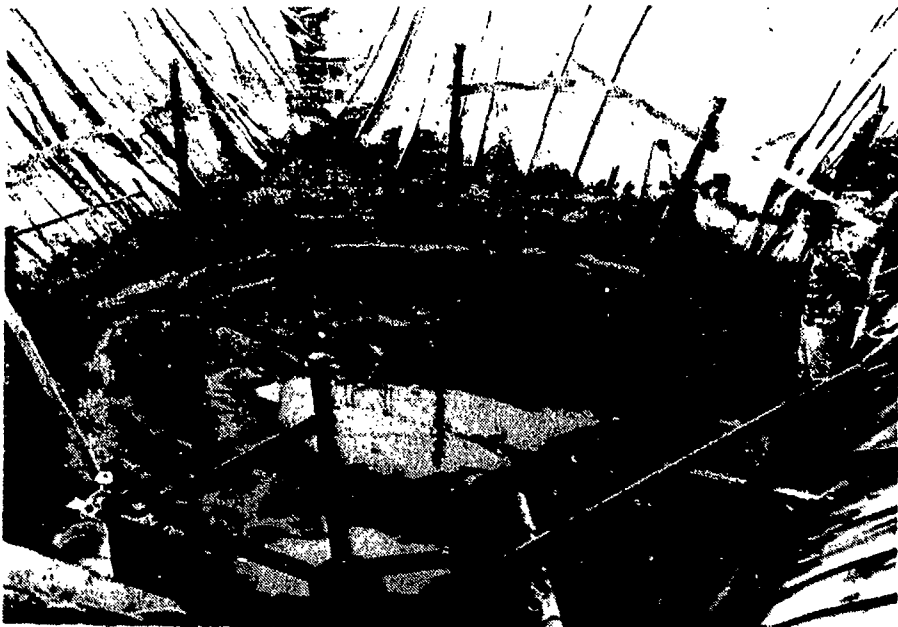Figure 7.16 Sand surface elevations.

Figure 7.17 View #1 of sand after final detonation (Test S7).

Figure 7.18 View #2 of sand after final detonation (Test S7).

A primary source of error in obtaining the sand elevations between detonations was zero visibility in the water. The scuba diver measured from a taut string (across the tank, rim-to-rim) to the sand surface at 30.5 cm stations with a straight edge. Since the straight edge could not be read, it was marked with a grease pencil where the string was felt. In this manner, the distance between the string and the sand surface was recorded at each station.

7.4.2 Soil Strains

Strain gage readings were obtained before and after each detonation during the testing. It was necessary to correct each set of strain gage readings because of inconsistencies in voltage output from one set to another (cause unknown). The correction, however, was relatively simple. Since gages 6 and 7 did not appear to have moved relative to one another during the testing (the post-test measured distance and pre-test measured distance between the two gages were the same), they were used as controls. The voltage output between these two gages was measured and then compared to the calibration voltage for their separation distance. The difference between calibration and measured voltage output for these two gages was then applied to the measured voltage output for the other pairs of gages. Once the voltages were corrected, corresponding separation distances were obtained using calibration curves of voltage versus distance for each pair of gages. The corrected strain gage readings are in Table 7.7.

One inherent source of error in the strain gage results was that the initial calibration was performed by placing gages parallel and directly above one another in air to obtain voltage output at different separation distances. If the gages were not parallel or

Table 7.7 Strain Gage Separation Distances

	Strain Gage Pairs						
Sequence	1-2[1]	2-3[1]	3-4[1]	4-5[1]	6-7[2]	8-9[2]	10-11[2]
Initial[3]	25.9	30.0	31.5	27.7	30.5	30.5	30.5
Before S1[4]	25.9	30.0	31.5	27.7	30.5	30.5	30.5
After S1	25.4	29.2	31.5	27.4	30.5	30.5	30.7
Before S2	25.4	29.2	31.5	27.4	30.5	30.5	30.7
After S2	24.6	29.0	31.5	26.9	30.5	30.5	31.0
Before S3	24.1	28.4	31.0	27.2	30.5	30.2	30.7
After S3	23.1	27.7	29.5	26.2	30.5	30.7	31.5
Before S4	25.4	30.0	34.8	29.2	30.5	30.5	31.2
After S4	27.4	28.7	32.5	26.7	30.5	31.0	31.8
Before S5	24.1	28.7	31.2	27.9	30.5	31.0	32.0
After S5	23.6	27.4	29.7	26.7	30.5	31.5	--[6]
Before S6[5]	--	--	--	--	--	--	--
After S6[5]	--	--	--	--	--	--	--
Before S7[5]	--	--	--	--	--	--	--
Final[3]	22.4	25.1	29.7	[6]	30.5	31.8	[6]

Notes:

1 - Vertical distances (cm)

2 - Horizontal distances (cm)

3 - Measured with tape during sand placement and excavation

4 - After saturation

5 - Voltage readings were highly erratic

6 - Strain gages 5, 10, and 11 were not in position

were slightly offset from one to another, the output voltage reading
was different even though the distance between gages was the same. A
second inherent source of error was due to the calibration having been
performed in air as opposed to saturated sand.

To convert the distances between strain gages to strains, the
difference between the initial and final distances was divided by the
initial distances for each pair of gages. These strains are given in
Table 7.8 along with vertical strains calculated from the elevation
changes (Table 7.6) to represent average vertical strain of the entire
mass of soil at the center of the tank.

7.4.3 Relative Densities

The relative density of the sand was determined in another
test in which the sand was placed and compacted under similar
conditions. The initial relative density was obtained using the sand
cone method (ASTM D1556). The equation used was

$$D_R = \frac{\rho_{max}(\rho_d - \rho_{min})}{\rho_d(\rho_{max} - \rho_{min})} \times 100\%$$ (7.1)

where D_R is relative density (%), ρ_{max}, ρ_{min}, and ρ_d are maximum dry
density, minimum dry density, and measured dry density, respectively.

The maximum and minimum densities for the test soil were 1860
kg/m^3 and 1522 kg/m^3, respectively (see Chapter 5). The initial
(before saturation) average relative density was 84 percent (standard
deviation of 9 percent) with an average dry density of 1797 kg/m^3
(standard deviation of 35 kg/m^3).

Table 7.8   Residual Soil Strains

Deton-	Vertical Strain At Vertical Gage Pair				Entire Mass	Horizontal Strain At Horizontal Gage Pair		
ation	1-2	2-3	3-4	4-5	Average	6-7	8-9	10-11
S1	0.020	0.025	0	0.009	--		0	0
S2	0.030	0.009	0	0.018	0.004	0	0	-0.008
S3	0.042	0.027	0.049	0.037	0.002	0	-.017	-0.008
S4	-0.08	0.042	0.066	0.087	0.128	0	-.017	-0.025
S5	0.021	0.044	0.049	0.045	0.132	0	-.016	--
S6	--	--	--	--	0.136	--	--	--
S7	--	--	--	--	0.147	--	--	--

Notes: Minus sign indicates expansion
         Entire mass average vertical strain from data in Table 7.6
         No entry (--) indicates lack of data to calculate strain

To estimate the relative densities for each of the detonations, calculations were made based on knowing the mass of sand and estimating for each detonation the volume of sand in the tank (using the procedures described in Figure 7.19). It was assumed that the total dry mass of sand in the tank was the same as the initial total dry mass except for Tests S6 and S7 where some sand was "blown" from the tank (the estimated mass of blown out sand ejecta was subtracted from the initial mass). This method gave a rough estimate of dry density and relative density of sand in the tank. The results of these estimates are shown in Table 7.9 along with estimates of crater and ejecta volumes.

7.4.4   Locations of Instrumentation and Inclusions in Sand

The locations of instrumentation and variable density inclusions were recorded during placement of sand in the tank and then again during excavation after Test S7. Table 7.10 gives these locations. For each device, a depth and X-Y coordinates are given.

STATION

0 1 2 3 4 5 6 7 8 9 10 11 12 13 14

TANK→

PROFILE
SAND SURFACE

PLAN VIEW
SAND SURFACE
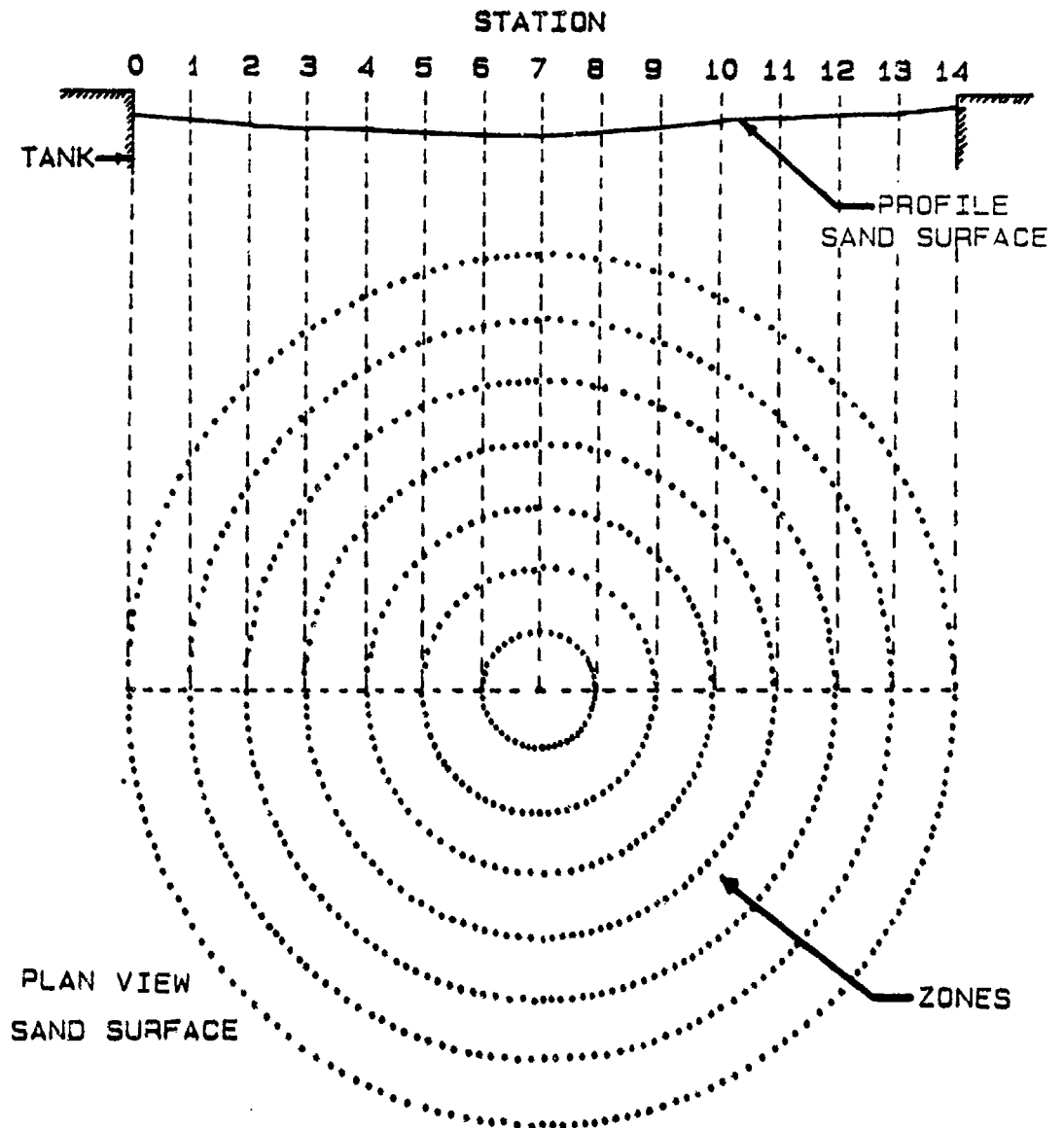
ZONES

SAND VOLUME CALCULATION PROCEDURES

AVERAGE VOLUME: SUM OF AVERAGE HEIGHT OF SAND
IN EACH ZONE TIMES AREA OF ZONE.

AVERAGE HEIGHT OF EACH ZONE: AVERAGE OF HEIGHTS
OF SAND AT ZONE STATIONS, EG.,
AVERAGE HEIGHT OF OUTER ZONE =
AVERAGE OF HEIGHTS AT STATIONS
0, 1, 13, 14.

ZONE AREA: PIx ((OUTER RADIUS)^2 - (INNER RADIUS)^2).

Figure 7.19 Sand volume calculation procedures.

Table 7.9 Estimated Average Sand Volumes and Densities

Sequence	Volume of Sand (m^3)	Apparent Volume of Crater (m^3)	Volume of Sand Ejected (m^3)	Dry Density (kg/m^3)	Relative Density (%)
Initial	26.14[1]	NA	NA	1798	84
After Saturation	25.32[1]	NA	NA	1856	99
After P1	25.23[1]	NA	NA	1862	100
After S1[4]	--	--	--	--	--
After S2	24.65[1]	0	0	1906	111
After P2	24.46[1]	NA	NA	1921	114
After S3	24.57[1]	0.7	0	1913	112
After P3[4]	--	--	--	--	--
After S4	23.67[1]	1.6	0	1986	129
After P4	23.89[1]	NA	NA	1967	125
After S5	23.83[1]	1.4	0	1972	126
After P5	23.27[1]	NA	NA	2020	136
After S6	23.82[2]	1.4	0.4	1830	93
After P6	23.18[2]	NA	NA	1998	131
After S7	22.76[3]	2.5	2.0	1871	103

Notes:
1 - mass of sand = 47,000 kg
2 - mass of sand = 42,400 kg
3 - mass of sand = 38,700 kg
4 - elevations not recorded
NA - not applicable

Table 7.10 Initial and Final Locations of Buried Devices

Device	Initial (cm)			Final (cm)		
	Depth	X	Y	Depth	X	Y
Strain Gage 1	152.4	0	20.3	160.0	0	20.3
Strain Gage 2	121.9	0	20.3	135.4	0	21.6
Strain Gage 3	91.4	0	20.3	110.2	0	20.3
Strain Gage 4	61.0	0	20.3	81.3	2.5	25.4
Strain Gage 5	30.5	0	20.3	7.6	154.9	109.2
Strain Gage 6	160.0	15.2	0	165.1	15.2	0
Strain Gage 7	160.0	-15.2	0	165.1	-15.2	0
Strain Gage 8	99.1	15.2	0	111.3	17.8	0
Strain Gage 9	38.1	-15.2	0	110.5	-15.2	0
Strain Gage 10	38.1	15.2	0	11.4	127.0	-114.
Strain Gage 11	38.1	-15.2	0	66.0	-5.1	-6.3
Accelerometer CN82A	152.4	0	-29.2	157.5	0	-29.2
Accelerometer CR53A	91.4	0	-29.2	110.5	0	-28.6
Accelerometer CR42A	30.5	0	-29.2	16.5	-11.4	-188.0
Transducer 65AJ	152.4	20.3	-24.1	157.5	20.3	-24.1
Transducer 11AK	91.4	20.3	-24.1	110.5	17.8	-20.3
Transducer 01AK	30.5	20.3	-24.1	20.3	6.4	-171.5
Stress Gage 7422185	152.4	-16.5	-9.5	157.5	-16.5	-24.1
Stress Gage 8426885	91.4	-16.5	-9.5	112.4	-16.5	-21.1
Stress Gage 8426285	30.5	-16.5	-24.1	22.9	-58.9	-119.9
Bowling Ball (1,330 kg/m^3)	91.4	-121.9	0	88.9	-162.6	15.2
Soccer Ball (0 kg/m^3)	91.4	-182.9	-61.0	78.7	-149.9	-88.9
Steel (7880 kg/m^3)	91.4	-121.9	-61.0	114.3	-152.4	-61.0
Foam Can (200 kg/m^3)	91.4	-91.4	-61.0	101.6	-127.0	-25.4
Concrete #1	**	**	**	76.2	12.7	-17.8
Concrete #2	**	**	**	81.3	15.2	-12.7
Sand Bag (on surface)	**	**	**	25.4	-152.4	-101.6

Notes:

North = +Y   East = +X
South = -Y   West = -X
** = not initially in sand

The depth is from the top of the tank to the top of each item; the X-Y coordinates are based on the center of the tank (in plan) being at 0,0. East is positive Y, and north is positive X. Figures 7.20 through 7.23 are photographs of gages and variable density items during excavation.

Several items of interest are evident in Figures 7.20 through 7.23. Except for the crushed foam can, the variable density inclusions having a density less than the saturated soil rose and those with a density greater sank. The foam can, which had an initial density of 200 kg/m^3, had an excavated density of 1,000 kg/m^3, was crushed (Figure 7.23), and was filled with water, so its density changed during testing. The top of the can was located 10 cm below its original position. Since the can's original height was 17.8 cm, and its final height was about 13 cm, it sank about 5 cm.

7.4.5 Gradations

The results of gradation tests performed on sand samples taken before and after the detonations are given in Table 7.11 along with the mean D_{50} for various combinations of depth and pre- or post-test results. Curves representing pre- and post-test gradations are shown in Figure 7.24, where it can be seen that the gradations, in general, did not change significantly during the tests. It did appear, however, that the samples near the surface had fewer fines than those at depth. The samples at 1 m appeared to have similar gradations as before the detonations. It also appeared that the finer particles of sand were "graded out" below the bowling ball, soccer ball, and foam can, and there appeared to be a 0.5 cm thick zone of sand with very few fines at a depth of between 15 and 30 cm below the sand surface.

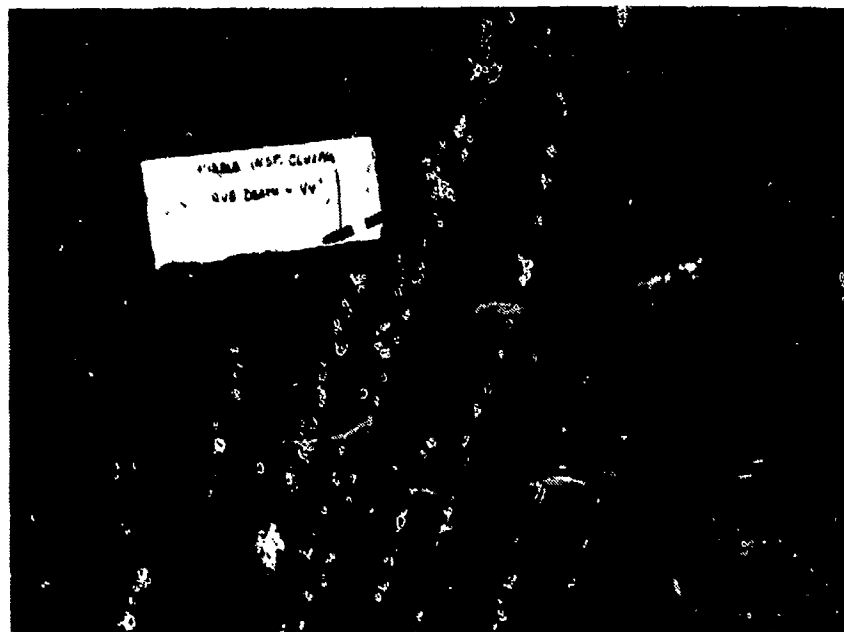Figure 7.20 Excavation of strain gage after Test S7.

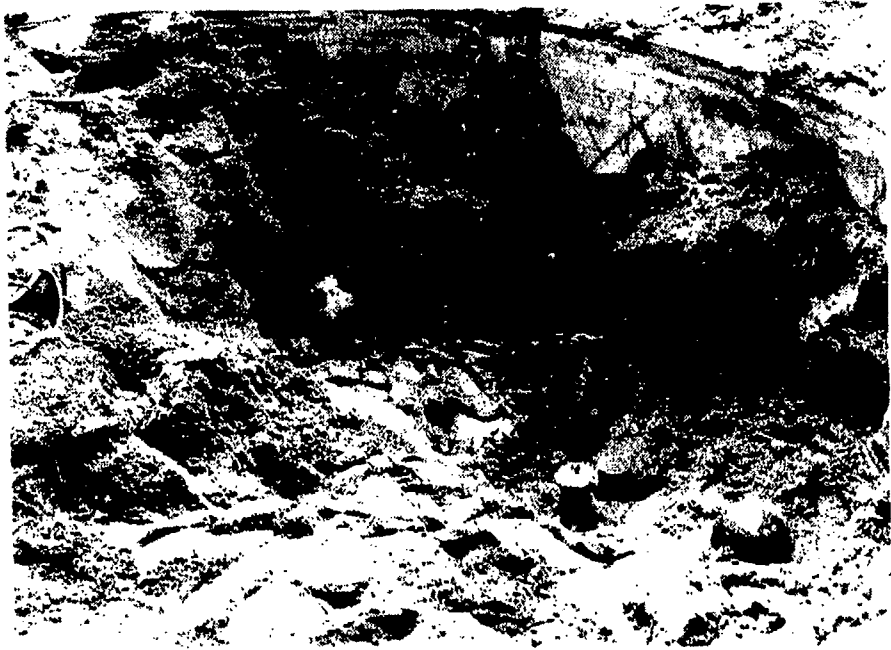Figure 7.21 Excavation of instrumentation cluster after Test S7.

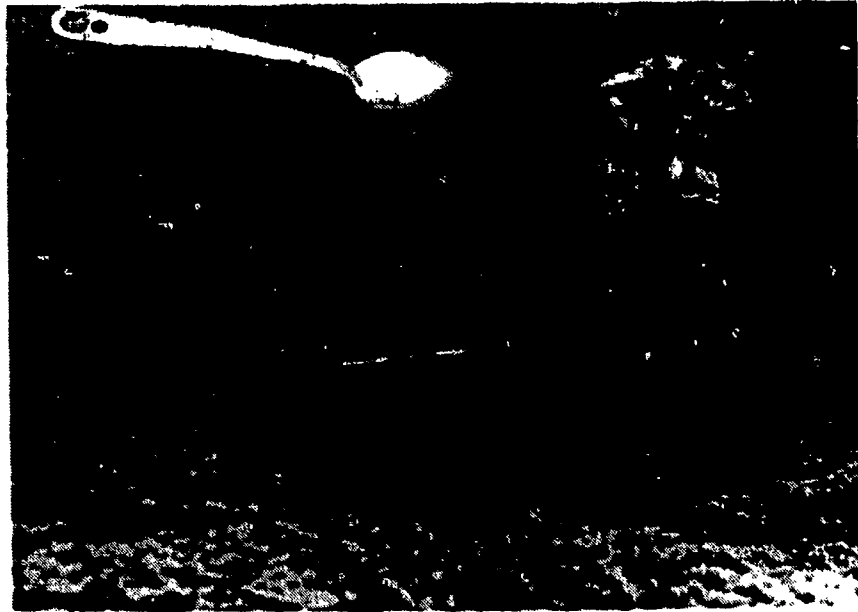Figure 7.22   Excavation of variable density inclusions after Test S7.

Figure 7.23   Recovery of foam can after Test S7.

Table 7.11 Gradation Results

	Depth from tank rim	D_{50}	C_u	Mean D_{50}	Standard Deviation
		(cm).	(mm)		
Pretest-A	152	.54	4.31		
Pretest-B	91	.60	3.89	0.567	0.025
Pretest-C	0	.56	3.68		
Post test-D	112	.60	3.65		
Post test-E	112	.56	4.31		
Post test-F	112	.55	4.31	0.577	0.023
Post test-G	104	.60	3.65		
Post test-H	30	.56	3.68	0.593	0.055
Post test-I	30	.72	3.60	0.685	0.140
Post test-J	30	.56	5.00		

Notes: Horizontal locations were all 1 m from center of tank.
Letters A through J refer to curves in Figure 7.24.
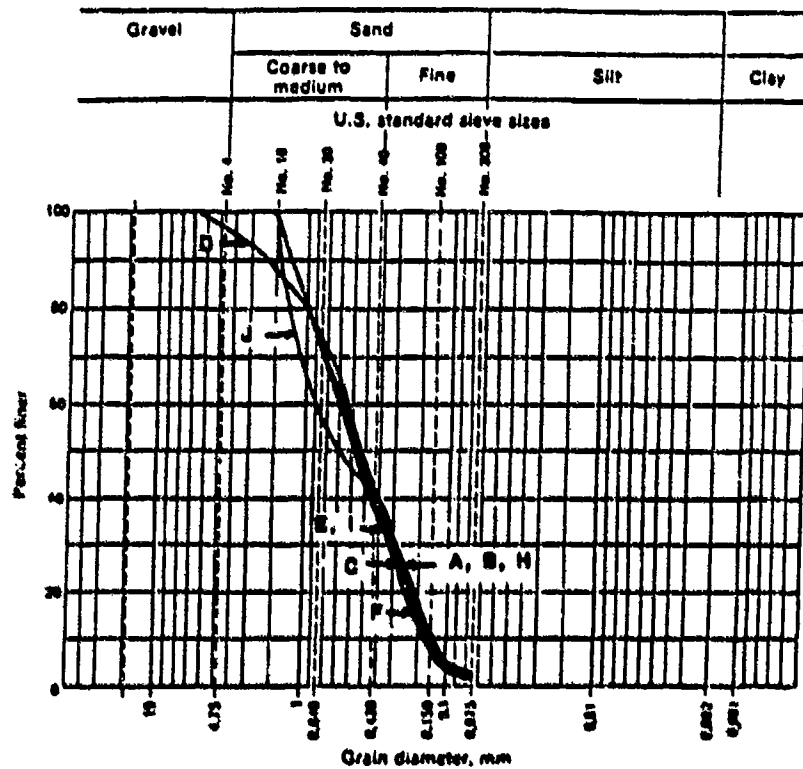

Figure 7.24 Pre- and post-test gradation curves
(curves defined in Table 7.11).

7.4.6 Observations

Several observations were made after the water was pumped from the pit and during excavation of the sand from the tank. These observations are as follows:

- Wood railings on the fence around the tank were nearly all broken at their centers.

- A sandbag full of sand ended up approximately 0.9 m in from the edge of the tank on the sand surface. This sandbag, prior to the last detonation, had been outside of the tank.

- Two small pieces of concrete were discovered buried near the center of the tank during excavation. These pieces were from one of the fence post footings. They were found at depths of 13 and 18 cm below the surface of the sand.

- Rigid plastic items and concrete footings were broken; e.g., a rigid polyvinylchloride (PVC) pipe cap was shattered, several resin transducer castings were cracked, and pieces of concrete footings had broken off.

CHAPTER 8

ANALYSIS

8.1   INTRODUCTION

This chapter is a summary of the analysis of the results presented in Chapter 7. The analysis also includes results from a series of similar tests conducted subsequent to the testing described herein. These subsequent tests were performed by Schure (1988) at the same site, with the same sand, following the same test procedures. The main differences between the two test series were that the subsequent series incorporated lower relative densities and smaller detonation charge sizes.

The analysis includes development of empirical relationships to describe peak stress, porewater pressure, strain, and particle velocity as functions of scaled distance from detonations. Also included is an empirical treatment of peak residual porewater pressure; i.e., the porewater pressure after passage of a stress wave, and dissipation of excess porewater pressure. The analytical model described in Chapter 3 is evaluated in this chapter, and the output of the model is compared to the test results.

8.2   DYNAMIC RESPONSE

8.2.1   Peak Total Stresses and Porewater Pressures

The peak dynamic porewater pressure and total stress results were analyzed to develop relationships between peak values and scaled

distance from charges. For this analysis, it was assumed that the peak values (σ_o) could be represented an equation of the form

$$\sigma_o = f \left(\frac{r}{w^{1/3}}\right)^{-\alpha} \tag{2.14}$$

which is a linear relationship between the logarithm of peak stress (or pressure) and logarithm of scaled distance ($r/w^{1/3}$), where f is the stress or pressure when $r/w^{1/3}$ equals 1 (i.e., intercept), and α is the slope of the line. Both f and α are constants dependent on site characteristics. Several references report this relationship between peak stress or pressure and scaled distance (Section 2.8.1).

A primary problem in determining the peak values of total stress and porewater pressure measured in Tests S1 through S7 was that the sampling rate of 0.064 msec per sample was too slow. This problem is explained by referring to Figure 7.8, which is dynamic response to the 7.02 kg detonation (Test S7). The figure labelled "fast rate" was based on data sampled every 0.002 msec. This record can be compared to that labelled "slow rate" which was recorded at 0.064 msec per sample. The transducer was the same in both cases, but the data were recorded at the two rates with different TDR's. There is a significant difference in the records. Since the 7.02 kg detonation (Test S7) was the only detonation in which a faster sampling rate was used, significant errors probably exist in the records of all the other detonations. Due to this problem, a procedure was developed for estimating peak values of total stress and porewater pressure.

To estimate peak values for each record during each detonation, it was assumed that a stress or pressure-time plot for unloading was of the form

$$\sigma(\tau) = \sigma_o e^{-\alpha_d \tau} \qquad (3.1)$$

which is a line on a semi-log plot of stress or pressure versus time, where $\sigma(\tau)$ is the stress or pressure as a function of time, τ is time after arrival of the stress wave, σ_o is the peak value occurring at stress wave arrival, and α_d is the slope of the line. To obtain α_d, each of the records was plotted as log of stress or pressure versus time, as shown in Figure 8.1. A straight line was fit through the
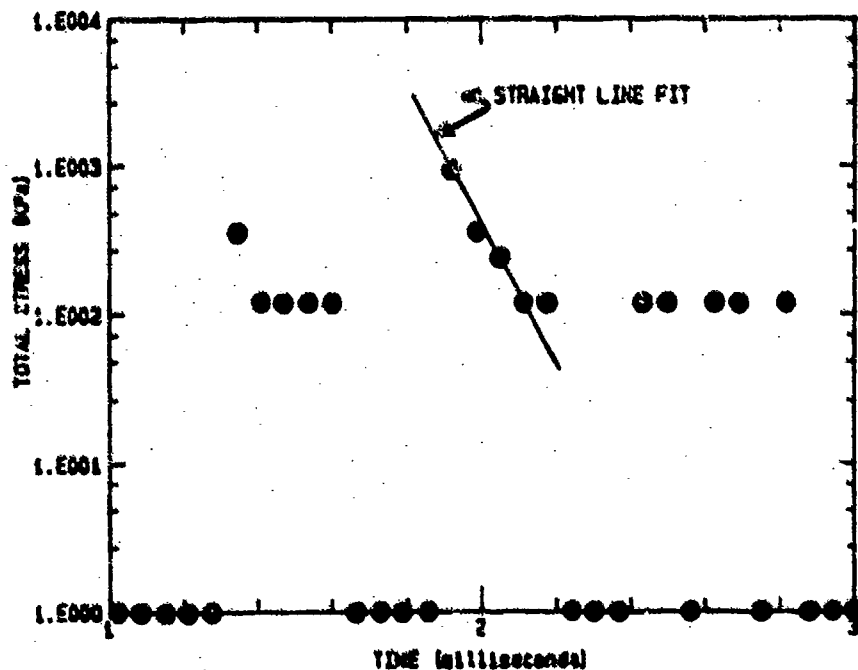

Figure 8.1 Log plot of total stress versus time, 0.03 kg charge at 2.74 m.

unloading data points to determine values for the slope. These values for each record were correlated, which resulted in a mean slope of 10.7 msec^{-1} with a standard deviation of 1.8 msec^{-1}. The large standard deviation is probably due to the slope of the unloading curves being represented by only two, three, or four data points and the use of judgement to obtain a line through these points from which individual α_d values could be obtained.

Given a value for α_d, equation 3.1 was rewritten to solve for σ_o. The equation, rewritten, becomes

$$\sigma_o = \sigma(r) \, e^{(10.7 \, r \, msec^{-1})} \qquad (8.1)$$

The next problem in solving for σ_o was that the time at which σ_o occurred was not known. It was assumed, however, that σ_o was probably within a range of 0.064 msec. To determine an upper limit for σ_o, it was assumed that the peak recorded value occurred at r of 0.064 msec. The upper limit peak, therefore, could have occurred 0.064 msec earlier. Equation 8.1 was, thus, used to calculate the upper limit for σ_o by setting r at 0.064 msec and by using the recorded peak value for $\sigma(r)$. The lower limit was assumed to be the recorded peak value.

The above procedure was used to calculate an upper and a lower value for peak stress and porewater pressure for each data record. These values are shown in Table 8.1 along with scaled distances for each record. In addition to the data shown in Table 8.1, the results from tests performed by Schure (1988) are provided in Table 8.2. The values in this table were recorded at 0.002 msec per sample; therefore, these values are more representative of the actual peaks.

Table 8.1 Recorded and Calculated Peak Pressures and Stresses

Test	Device[1]	Charge Mass (kg)	Distance (m)	Scaled Distance (m/kg$^{1/3}$)	Recorded Peak (kPa)	Calculated Peak (kPa)
S1	P-SS	0.03	1.90	6.11	1350	2700
S1	T-SS	0.03	1.90	6.11	2050	4100
S1	P-BS	0.03	2.20	7.08	3200	6300
S1	P-BS	0.03	2.74	8.82	900	1800
S1	T-BS	0.03	2.74	8.82	1000	2000
S1	P-BS	0.03	3.35	10.78	1250	2500
S2	P-SS	0.08	1.92	4.70	3900	7800
S2	T-SS	0.08	1.92	4.70	3800	7500
S2	T-BS	0.08	2.74	6.72	2200	4300
S2	P-BS	0.08	3.35	8.21	2150	4200
S3	P-SS	0.25	1.98	3.14	8200	16300
S4	P-SS	0.76	2.02	2.21	12500	24800
S4	T-SS	0.76	2.02	2.21	7300	14500
S4	T-BS	0.76	2.78	3.05	6600	13100
S4	P-BS	0.76	3.35	3.68	5800	11500
S5	P-SS	2.25	2.12	1.62	15000	30000
S5	T-SS	2.25	2.12	1.62	19800	39300
S5	T-BS	2.25	2.83	2.16	9000	18000
S6	P-SS	0.76	2.30	2.52	13000	27000
S6	T-SS	0.76	2.30	2.52	9500	19000
S6	T-BS	0.76	2.85	3.12	3700	7400
S6	P-BS	0.76	3.35	3.67	3900	7700
S7	P-SS	7.02	2.35	1.23	45000	--[2]

Notes: 1-P = pore pressure transducer, T = total stress gage, SS = on sand surface, BS = buried in sand
2-not calculated, peak is from faster sample rate

Table 8.2 Recorded Peak Dynamic Porewater Pressures
(from Schure, 1988)

Test	Charge mass (kg)	Distance (m)	Scaled Distance (m/kg$^{1/3}$)	Peak Porewater Pressure (kPa)
SF1	0.00044	3.51	46.1	92
SF1	0.00044	3.51	46.1	180
SF1	0.00044	2.59	34.1	453
SF2	0.00044	1.98	26.0	339
SF2	0.00044	1.98	26.0	581
SF3	0.00176	3.51	29.1	156
SF3	0.00176	2.59	21.5	717
SF3	0.00176	1.98	16.4	989
SF4	0.01410	3.51	14.5	284
SF4	0.01410	2.59	10.7	1936
SF4	0.01410	1.98	8.20	2859
SF5	0.0588	3.51	9.03	1199
SF5	0.0588	2.59	6.66	3906

Note: relative density 50% for SF series

The data shown in Tables 8.1 and 8.2 were analyzed to correlate peaks and scaled distances. The data were categorized into sets that are shown in Table 8.3. Each set was analyzed to determine values for f and α in Equation 2.14, which is

$$\sigma_o = f \left(\frac{r}{w^{1/3}}\right)^{-\alpha} \tag{2.14}$$

where σ_o is the peak total stress or porewater pressure in kPa, f is a constant representing σ_o when scaled distance $(r/w^{1/3})$ equals 1, r is distance from the charge in m, w is charge mass in kg, and α is a site constant. The statistical analysis was performed on each data set by applying power regression techniques. The results of the analysis gave values for f and α plus coefficients of determination and standard deviations for each set. The coefficient is a proportionate reduction of total variation associated with the independent variable, scaled distance. A value of 1.0 means all the data are explained precisely by the dependent variable. A value of 0.0 means there is no association between the variables. The standard deviation is an estimator of the variance of data. Low values indicate that the data variation from the regression relationship is small (Neter and Wasserman, 1974).

Values of f and α for each data set and for equations presented in the literature (Section 2.8.1) are provided in Table 8.3 along with statistical information for the test data. Each of the equations represented in Table 8.3 and the data in Tables 8.1 and 8.2 are shown in Figures 8.2 through 8.10. For the "slow rate" tests, two

Table 8.3 Empirical Equation Constants for Peak Stresses and
Porewater Pressures

Data Set	Tests	f (kPa)	α	Determin- ation Coefficient	Standard Devia- tion (kPa)	Equation Number
P-SS	S1-S7	69900	1.77	0.81	7100	2.14a
T-SS	S1-S7	49100	1.53	0.78	7000	2.14b
P,T-SS	S1-S7	60600	1.67	0.79	6400	2.14c
P-BS	S1-S7	39700	1.32	0.59	2000	2.14d
T-BS	S1-S7	36600	1.42	0.78	3400	2.14e
P,T-BS	S1-S7	33400	1.28	0.69	2600	2.14f
P,T-SS,BS	S1-S7	49000	1.50	0.79	5000	2.14g
P-BS	SF1-SF5 ?1-S7	59200	1.56	0.79	500	2.14h
P,T-SS, BS	all tests	50000	1.50	0.89	4400	2.14i
Lyakhov (1961)		59000	1.05	--	--	2.14j
Crawford, et al. (1971)		10000	3.90	--	--	2.14k
Drake and Little (1983)		47000	1.50	--	--	2.14l
Jacobs (1988)		50100	2.38	--	--	2.14m
Cole (1948) for water		52000	1.13	--	--	2.14n

Note: Data set key: P is porewater pressure, T is total stress, SS is
measurement in water at sand surface, BS is measurement in
sand; tests are identified in Tables 8.1 and 8.2, -- indicates
that values were not reported.
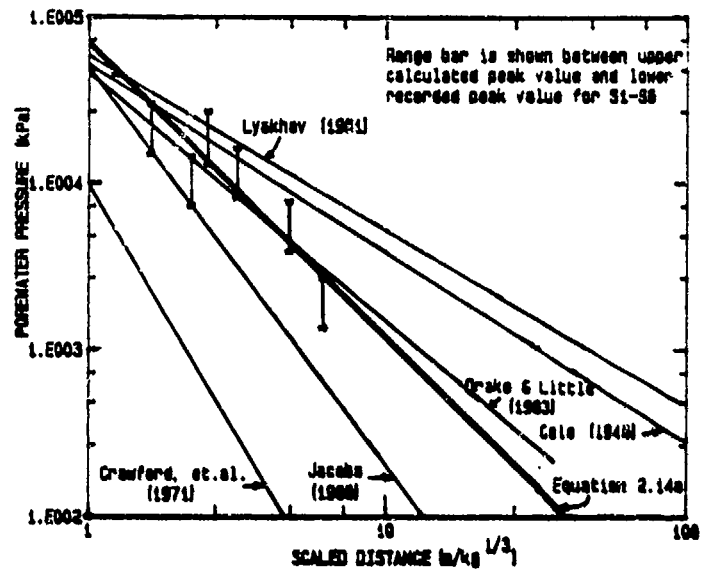
Figure 8.2   Peak porewater pressure at sand surface.
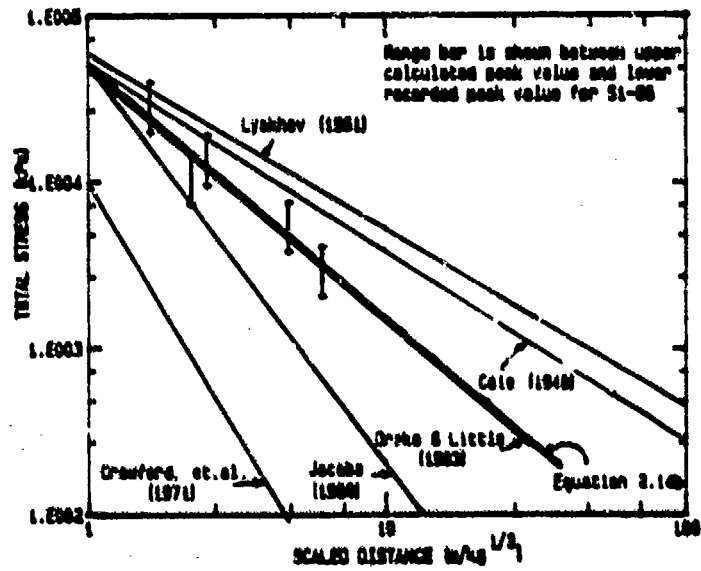
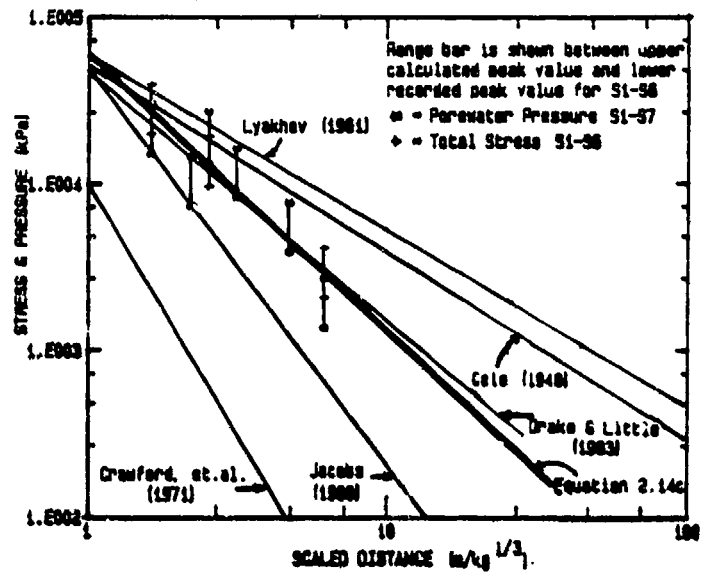Figure 8.3   Peak total stress at sand surface.

Figure 8.4 Peak total stress and porewater pressure at sand surface.
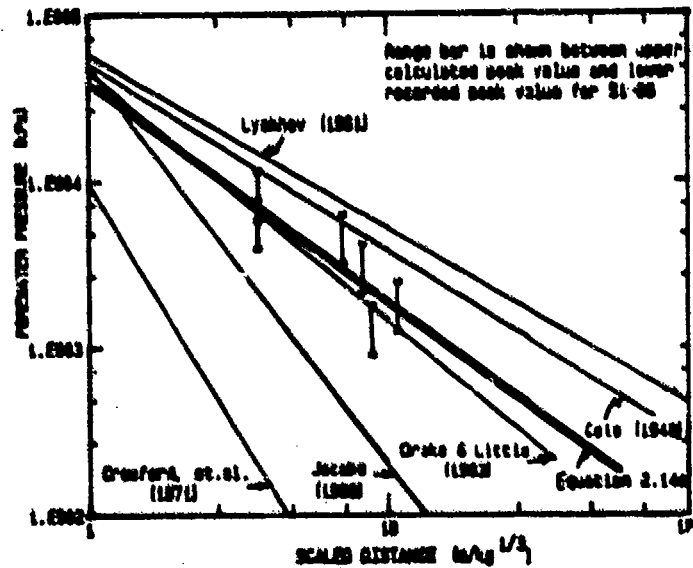

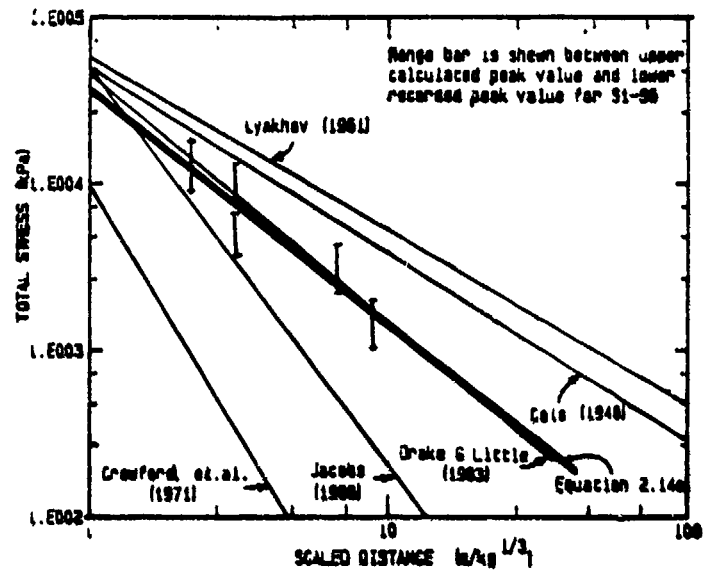Figure 8.5 Peak porewater pressure in sand.

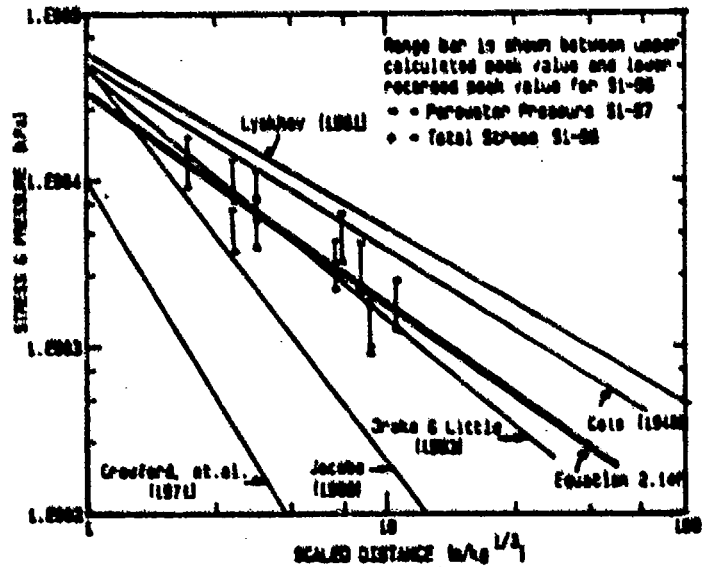Figure 8.6   Peak total stress in sand.

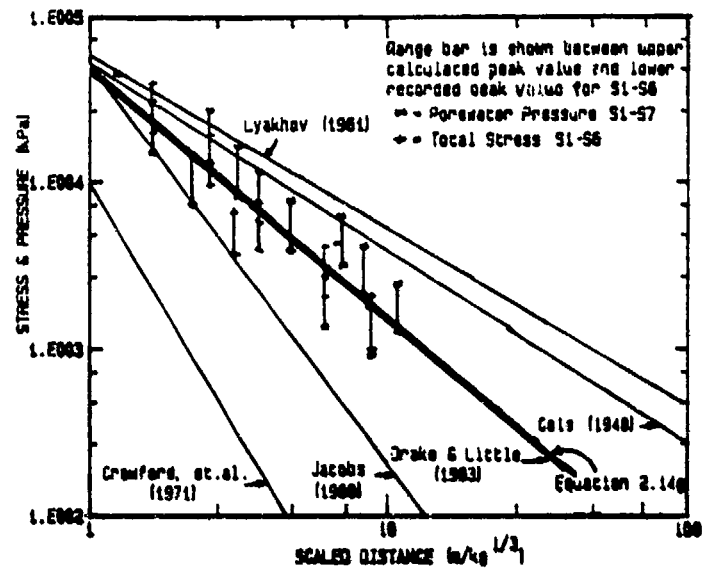Figure 8.7   Peak total stress and porewater pressure in sand.

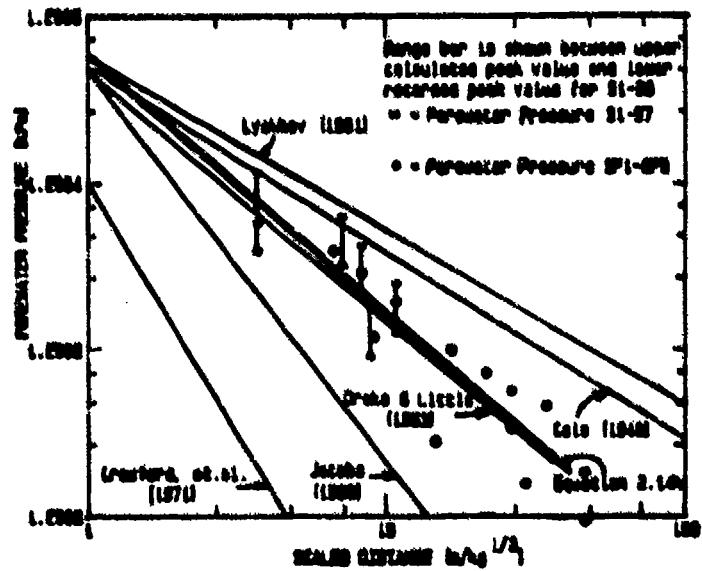Figure 8.8   Peak total stress and porewater pressure in sand and on sand surface.

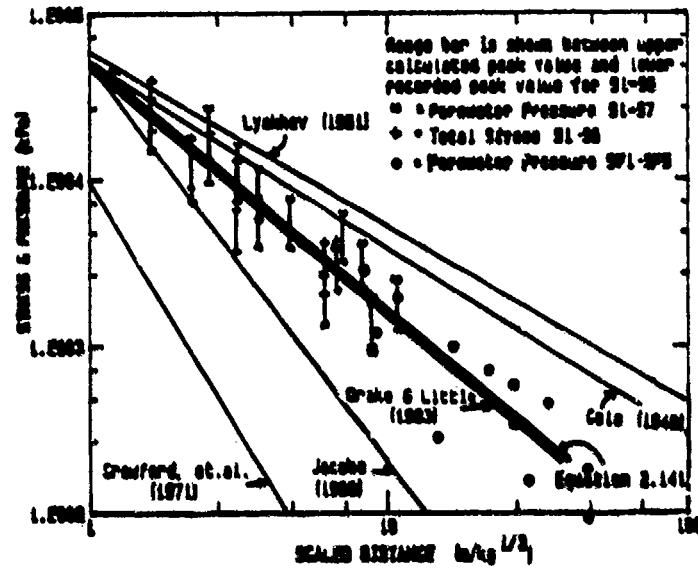Figure 8.9   Peak porewater pressure in sand - all tests.

Figure 8.10   Peak total stress and porewater pressure - all tests.

data points representing the recorded peak and the calculated peak (Table 8.1) are joined with a range bar.

The equation selected as most representative of the results was from the combined data (Equation 2.141 in Table 8.3 and Figure 8.10). This equation with a standard deviation of 4,400 kPa and a correlation coefficient of 0.89 is rewritten as

$$\sigma_o \text{ or } u_{pk} = 50,000 \left(\frac{r}{w^{1/3}}\right)^{-1.5} \text{ (kPa)} \qquad (8.2)$$

where σ_o is the peak total stress and u_{pk} is the peak porewater pressure (both in kPa) resulting from a detonation of a charge with mass w (kg) at a distance r (m).

There are several sources of error in the above analysis. The first was the slow sampling rate and the statistical approach used to analyze the data from Tests S1 through S7. It is strongly suspected that the minimum recorded peak values were lower than the actual peak values (as described in Section 8.2.1); thus, there is a tendency to force a lower than actual attenuation. A second factor is that all the results are for a non-homogeneous medium. The test data are from detonations in water causing stresses and pressures in a sand bed nearly 2 meters lower. A third factor in comparisons with the reference equations is that those equations are primarily based on tests in which the detonations were confined; i.e., there was no outbreak of explosive gases at the surface. In the tests described here, this was not the case since there was only a 0.6 m water cover

over the charge. Thus, some energy was lost to the atmosphere during
this testing.

8.2.2 Peak Strains and Peak Particle Velocities

Dynamic particle velocities and peak strains were calculated
from the following equations presented in Chapter 2:

$$v_{pk} = \frac{\sigma_r}{\rho v_c} \tag{2.2}$$

$$\epsilon_{pk} = \frac{v_{pk}}{v_c} \tag{2.3}$$

where:

ϵ_{pk} = peak radial strain (assumed to equal peak strain)

v_{pk} = peak particle velocity

v_c = compression wave velocity (1840 m/sec)

σ_r = peak radial stress (Equation 8.2)

The density of the soil-water mixture was calculated with the
equation:

$$\rho = \rho_w \left(\frac{G_s + Se}{1 + e} \right) \tag{3.3}$$

where ρ_w is the density of water, G_s is the specific gravity of the
sand, S is the degree of saturation (assumed to be 1.0), and e is the
void ratio of the sand. A void ratio of 0.47 was determined to be the
initial (pre-test) value from the data shown in Table 7.9. This value
was assumed for the calculation of density. The specific gravity was
2.65 as shown in Chapter 5. Using the above equations with Equation

8.2. relationships between peak particle velocity, peak strain and scaled distance were obtained as follows:

$$v_{pk} = 12.8 \; (\frac{r}{w^{1/3}})^{-1.5} \; (m/sec) \qquad (8.3)$$

$$\epsilon_{pk} = 0.7 \; (\frac{r}{w^{1/3}})^{-1.5} \; (\%) \qquad (8.4)$$

where r is in meters and w is in kilograms. Drake and Little (1983) presented an equation for peak particle velocity as

$$v_{pk} = 12.2 \; (\frac{r}{w^{1/3}})^{-1.5} \; (m/sec) \qquad (2.29)$$

for a confined point charge in saturated clay. Equation 8.3 is very close to Drake and Little's equation.

8.3   RESIDUAL POREWATER PRESSURES

This section presents the analysis to determine relationships for the residual peak porewater pressure after passage of the dynamic stress wave. The data used for the analysis are from Figures 7.9 through 7.15 and the Schure (1988) test series. The data represent the porewater pressure response at the piezometer levels during the tests. Since not all the plots in Figure 7.9 through 7.15 were continuous, it was necessary to estimate missing data points. Figures 8.11 through 8.17 are plots that include these estimates, which were made by comparing curve shapes in different tests and by applying judgement.

In Figures 3.11 through 8.17, one plot shows the data displayed as water rise in meters and porewater pressure versus time.
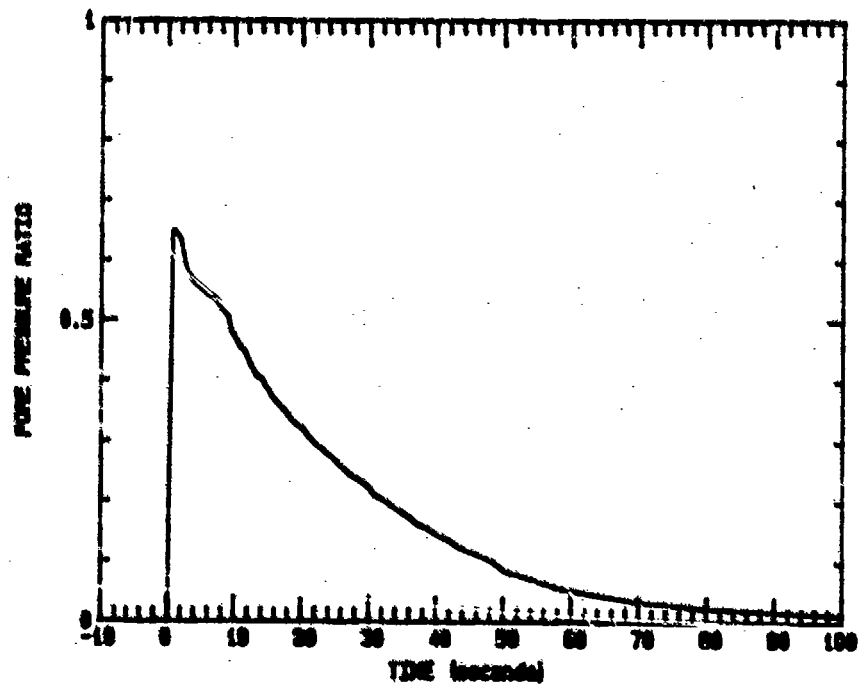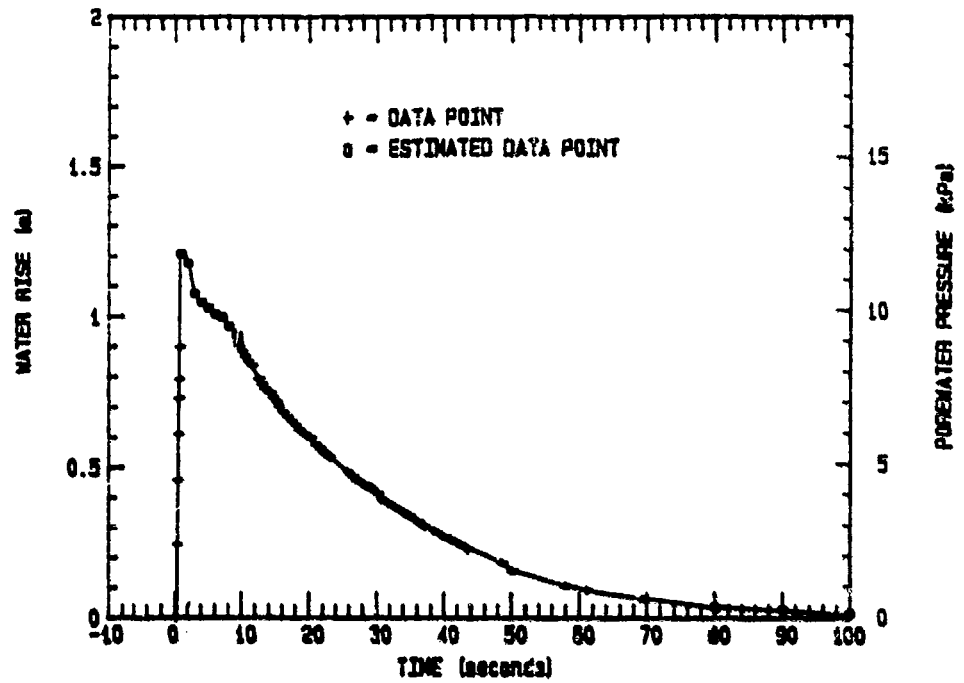
Figure 8.11 Porewater pressure dissipation - 0.03 kg charge.
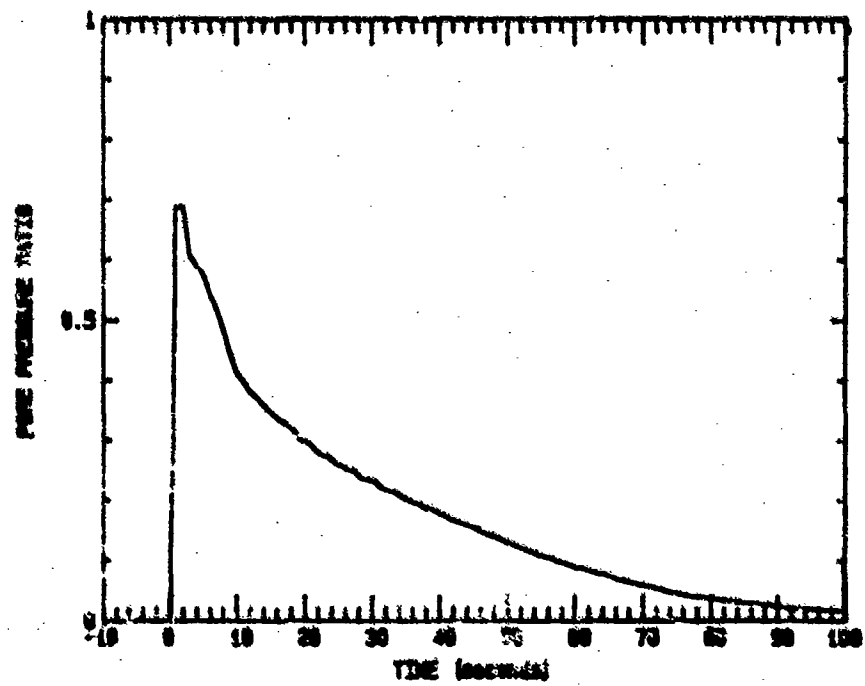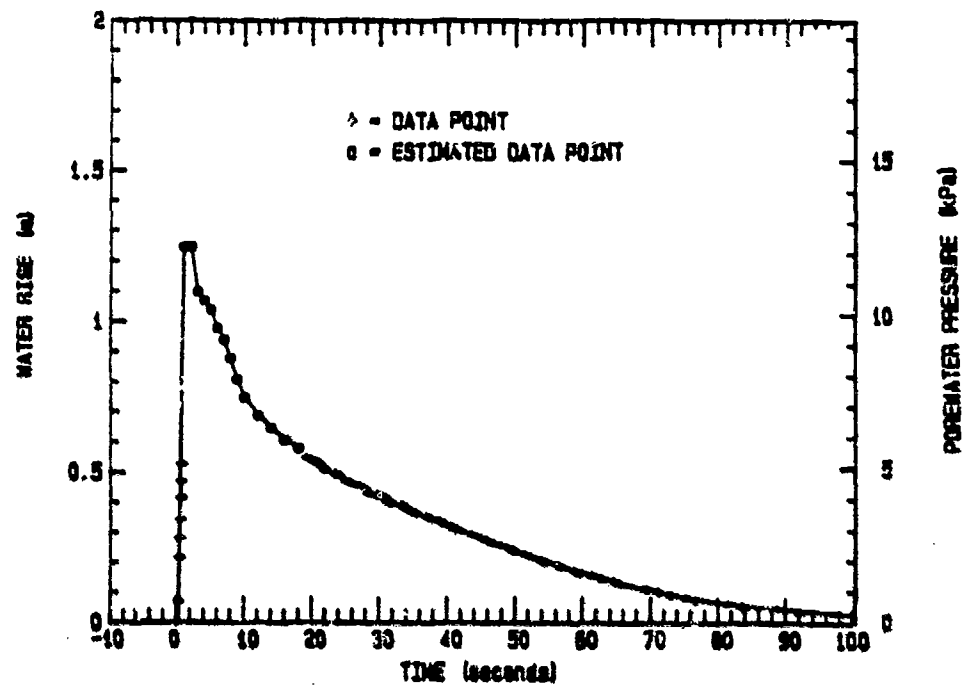
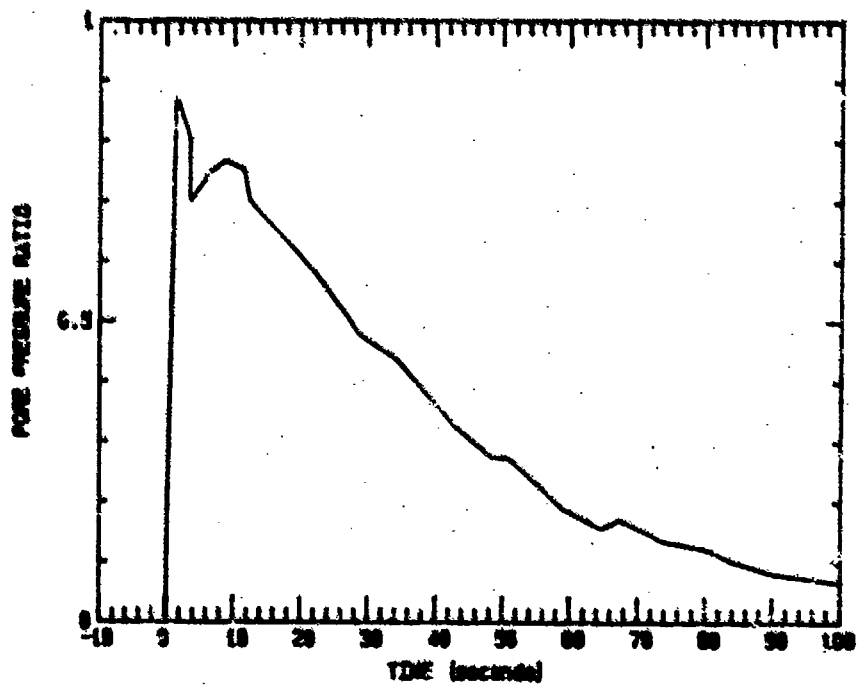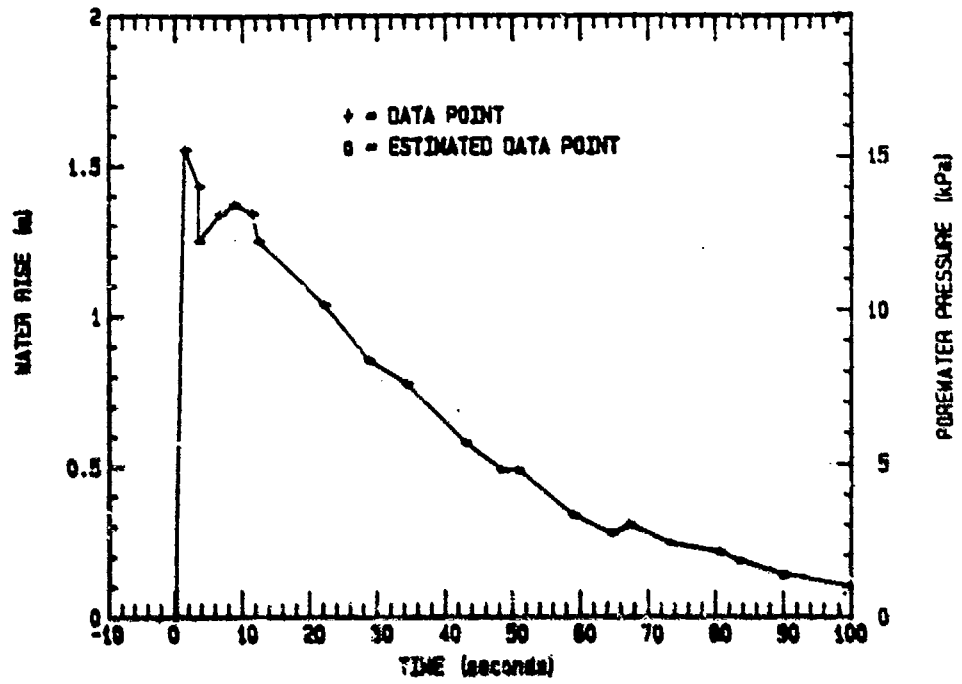Figure 6.12   Porewater pressure dissipation - 0.08 kg charge.

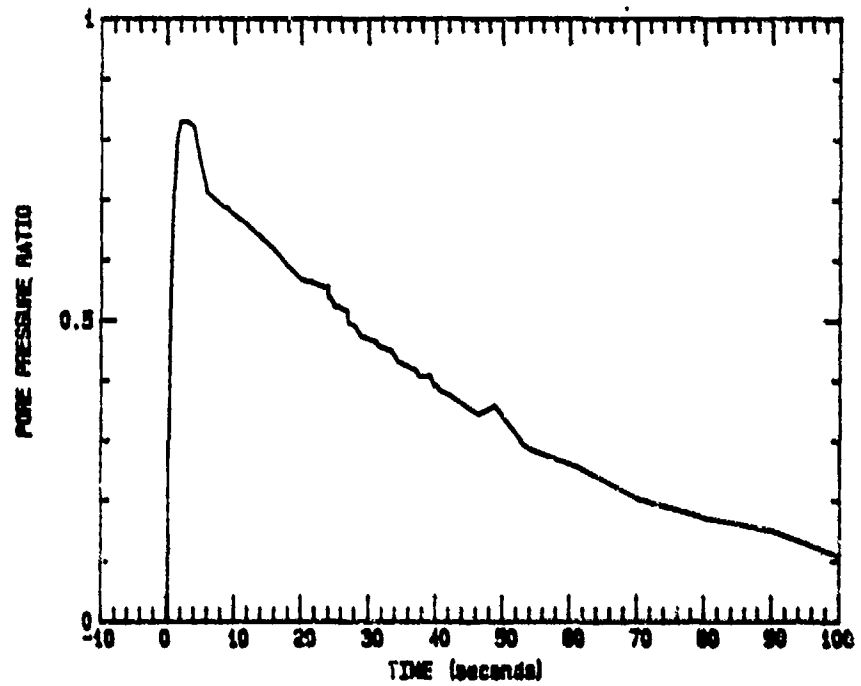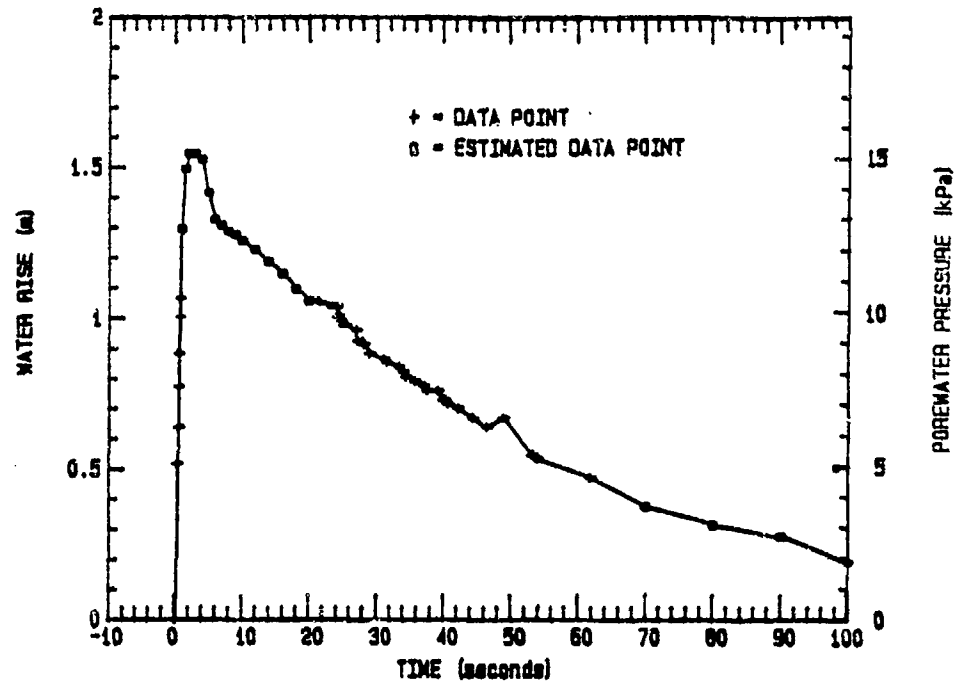Figure 8.13 Porewater pressure dissipation - 0.25 kg charge.

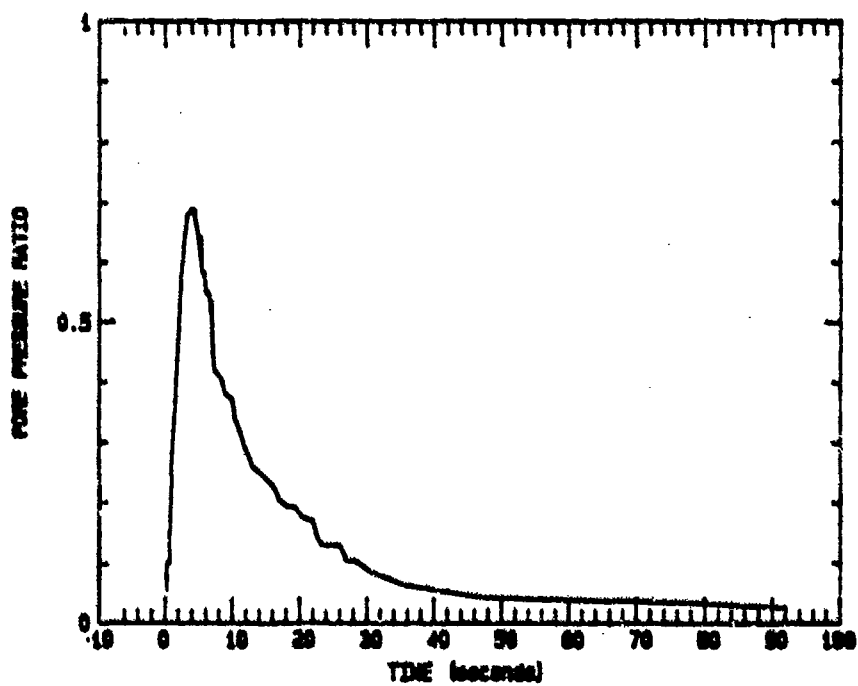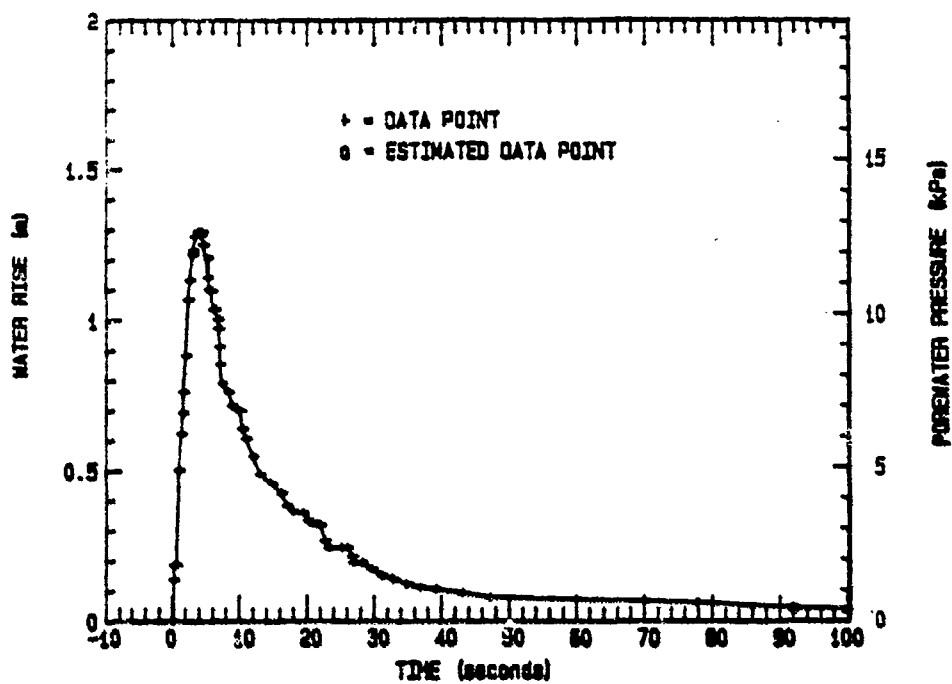Figure 8.14   Porewater pressure dissipation - 0.76 kg charge (#1).

Figure 8.15 Porewater pressure dissipation - 2.25 kg charge.
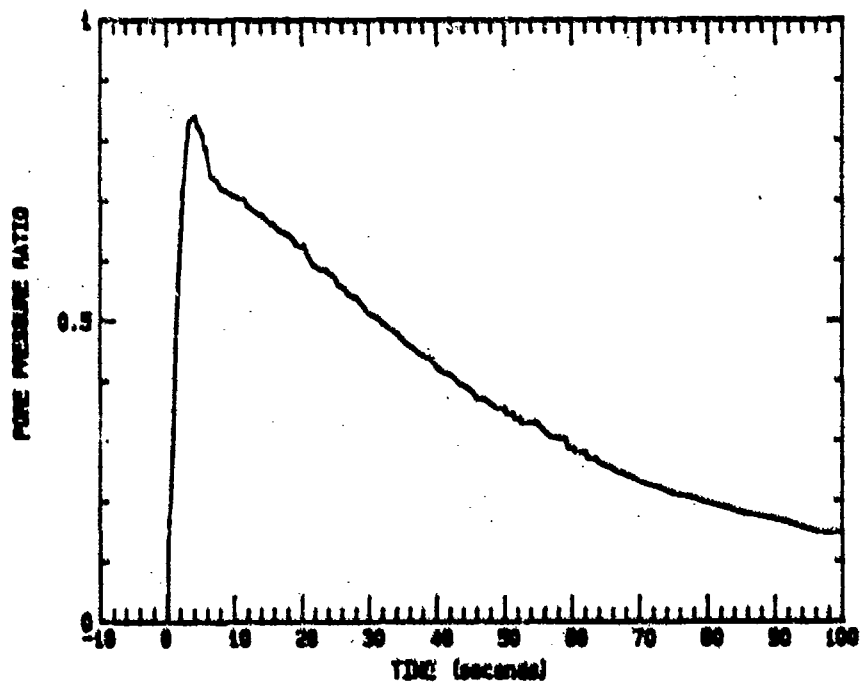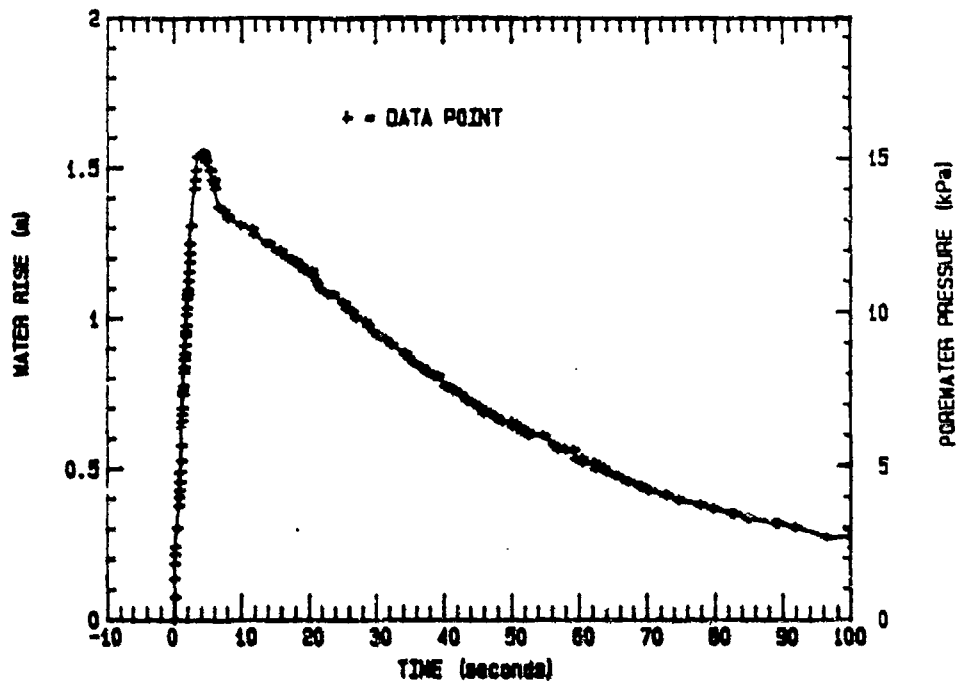
Figure 8.16   Porewater pressure dissipation - 0.76 kg charge (#2).
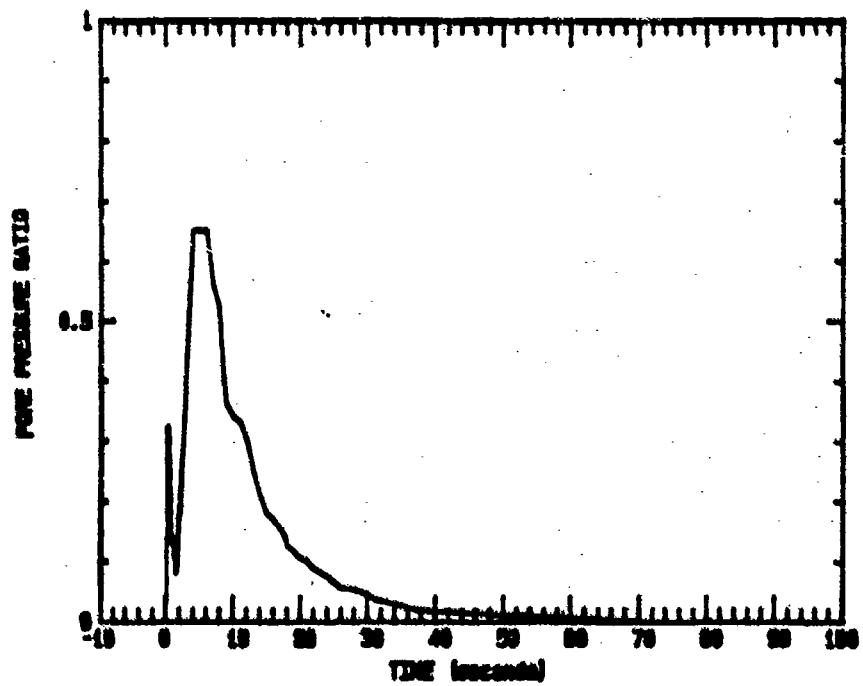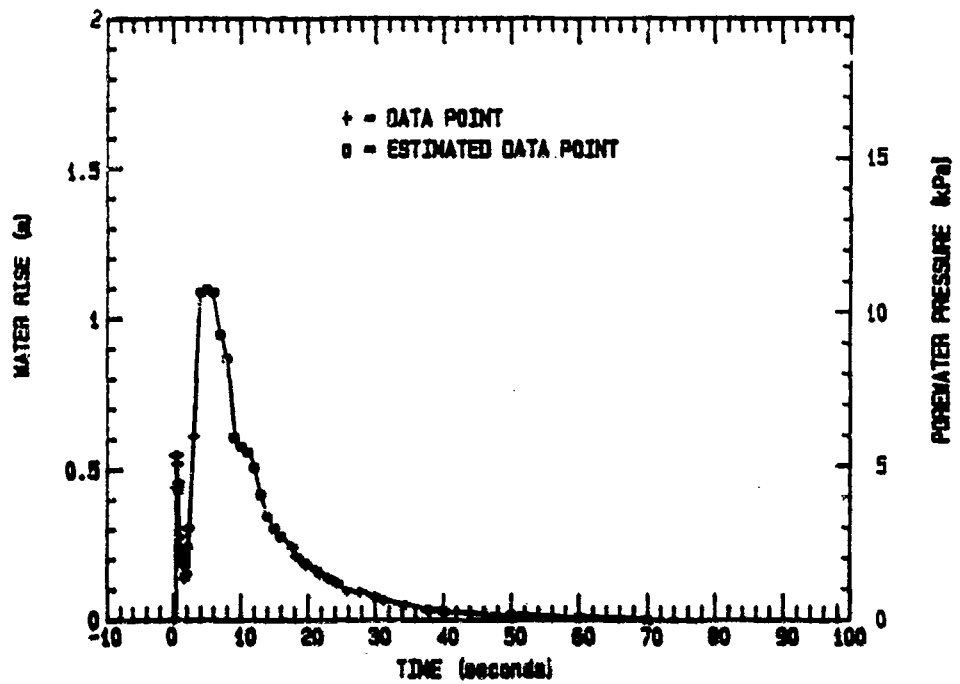
Figure 8.17   Porewater pressure dissipation - 7.02 kg charge.

The second plot in each figure represents the data as a curve to show the pore pressure ratio, PPR, versus time, where PPR is defined as:

$$PPR = \frac{\Delta u}{\bar{\sigma}_i} \qquad (8.5)$$

with Δu the difference between the residual and the hydrostatic porewater pressure, and $\bar{\sigma}_i$ the initial effective stress. When the PPR equals 1, liquefaction has occurred, while PPR values between 0 and 1 indicate that the soil is only partially liquefied.

There was some uncertainty in determining the PPR in Tests S1 through S7. The uncertainty was in part due to difficulty in establishing an accurate value for the initial effective stresses since the sand surface elevation became less defined as testing progressed (Figure 7.16). Also, the piezometer consisted of a horizontal perforated pipe spanning the bottom of the sand. The procedure selected for calculating the initial effective stress was to use an average sand elevation. This procedure gave a constant initial effective stress in each test although the actual value varied across the span of the sand.

In observing the plots in Figures 8.11 through 8.17, some anomalous behavior is evident. Figures 8.13 and 8.16 show initial data points representing peak pressures, and it appears that there is a sudden post-peak decrease in pressure before stabilized dissipation begins. A second anomalous condition is seen in Figure 8.17, which was the largest detonation. There is an initial peak pressure followed by a sudden decrease in pressure, but then the pressure again increases sharply to greater than the initial peak value. Data could

not be obtained after this second peak until well into the dissipation phase. Also, in Test S7 the dissipation time was markedly less than in the other tests. No explanation is evident for this behaviour.

Once the residual porewater pressure data were assimilated, relationships were sought for PPR as a function of scaled distance, peak stress, peak particle velocity, and peak strain. Table 8.4 provides the results of the data assimilation. In this table, data from Tests S1 through S7 and Tests SF1 through SF7 from Schure (1988) are shown. The results of peak stress, particle velocity, and strain calculations are also provided in the table. These peak values were calculated using Equations 8.2, 8.3 and 8.4. PPR values were obtained from Figures 8.11 through 8.17 and from the results of the Schure (1988) test series. To calculate the PPR for Tests S1 through S7, the results in Table 7.9 were used to obtain initial effective stresses which are also provided in Table 8.4.

The data were analyzed by performing power regressions (as described in section 8.2.1) which yielded the following relationship:

$$PPR = 43 \left(\frac{r}{w^{1/3}} \right)^{-1.8} \tag{8.6}$$

where the coefficient of determination is 0.99 and the standard deviation is 0.041 (Table 8.4). Equation 8.6 is compared to the following equations from similar testing (see Chapter 2):

Studer and Kok (1980) $PPR = 1.65 + 0.64 \ln \left(\frac{w^{1/3}}{r} \right)$ (from 2.24)

Jacobs (1988) $PPR = 4.82 \left(\frac{r}{w^{1/3}} \right)^{-1.478}$ (from 2.25)

Ivanov (1967) $PPR = 6 \left(\frac{r}{w^{1/3}} \right)^{-1}$ (from 2.30)

Table 8.4 Data for PPR Analysis

Scaled Distance to Piezometer (m/kg^1/3)	Test[1]	Pretest Soil Relative Density (%)	Charge Weight (kg)	Distance to Piezometer (m)	Average Sand Height above Piezometer (m)	Initial Effective Stress at Piezometer (kPa)	Peak Excess Residual Parameter Pressure (kPa)	Peak PPR	Peak Stress[2] (kPa)	Peak[3] Particle Velocity (m/sec)	Peak[4] Strain (%)	Coefficient[5] of Determination between PPR and Scaled Distance	Standard[5] Deviation of PPR to Scaled Distance
38.8	DJ1	38	0.00044	2.89	1.47	15.3	0.0	0.06	213	0.055	0.0030	.	.
37.1	DJ1	38	0.00044	2.82	1.52	14.0	1.2	0.07	221	0.057	0.0031	.	.
30.8	DJ1	38	0.00044	2.13	0.76	7.1	0.9	0.13	337	0.086	0.0047	0.785	0.020
29.9	DJ2	38	0.00176	2.89	1.47	15.3	2.3	0.15	428	0.110	0.0060	0.852	0.016
29.4	DJ2	38	0.00176	2.82	1.52	14.0	2.3	0.16	442	0.113	0.0061	0.869	0.014
17.4	DJ2	38	0.00176	2.89	0.76	7.1	1.8	0.26	477	0.173	0.0094	0.941	0.011
15.1	DJ3	38	0.00705	2.89	1.47	15.3	6.1	0.40	852	0.218	0.0118	0.962	0.021
14.7	DJ3	38	0.00705	2.82	1.52	14.0	5.2	0.38	887	0.227	0.0123	0.970	0.019
12.8	DJ6	38	0.041	2.89	1.67	15.3	8.6	0.56	1200	0.308	0.0167	0.980	0.017
11.7	DJ6	38	0.041	2.82	1.52	13.7	7.4	0.54	1250	0.320	0.0176	0.982	0.021
11.3	DJ3	64	0.05	3.51	1.46	18.3	11.9	0.65	1320	0.337	0.0183	0.984	0.023
11.1	DJ5	38	0.02705	2.13	0.76	7.1	4.9	0.71	1350	0.346	0.0188	0.986	0.031
9.40	DJ5	38	0.02682	2.89	1.67	15.3	12.0	0.78	1710	0.438	0.0238	0.986	0.036
9.26	DJ5	38	0.02682	2.82	1.52	14.0	12.0	0.86	1770	0.454	0.0247	0.988	0.035
8.82	DJ4	38	0.041	2.13	0.76	7.1	6.0	0.85	1910	0.489	0.0266	0.988	0.041
8.15	DJ2	64	0.05	3.51	1.57	17.8	12.3	0.69	1990	0.550	0.0299	0.976	0.093
7.43	DJ6	38	0.059	2.89	1.67	15.3	12.2	0.80	2670	0.632	0.0343	0.966	0.115
7.25	DJ6	38	0.059	2.82	1.52	14.0	12.0	0.86	2560	0.656	0.0356	0.960	0.121
7.00	DJ5	64	0.028	2.13	0.76	7.1	6.3	0.89	2700	0.691	0.0376	0.960	0.122
5.91	DJ7	38	0.117	2.89	1.67	15.3	12.5	0.81	3480	0.891	0.0484	0.941	0.166
5.79	DJ7	38	0.117	2.82	1.52	14.0	13.6	0.81	3620	0.926	0.0503	0.925	0.203
5.16	E5	64	0.25	3.51	1.55	17.4	15.2	0.86	3810	0.976	0.0530	0.916	0.186
5.10	DJ6	38	0.059	2.13	0.76	7.1	5.7	0.81	3900	0.998	0.0542	0.904	0.189
4.35	DJ7	38	0.117	2.13	0.76	7.1	5.4	0.76	5510	1.41	0.0766	0.872	0.224
3.84	E4	64	0.26	3.51	1.55	18.2	15.3	0.84	6650	1.70	0.0924	0.846	0.246
3.86	E6	64	0.78	3.51	1.56	18.1	15.3	0.83	6650	1.70	0.0926	0.828	0.269
2.47	E5	64	2.25	3.51	1.57	18.4	12.8	0.70	11500	2.93	0.159	0.766	0.296
1.83	E7	64	7.65	3.51	1.49	18.5	18.8	0.65	20200	5.17	0.281	0.676	0.343

Notes:

1 - DJ series are Schure (TNO) tests
   E series are tests described herein
2 - Equation 8.2
3 - Equation 8.3
4 - Equation 8.4
5 - Coefficient of determination and standard deviation are cumulatively calculated beginning with the higher scaled distances

Equation 8.6 is combined with Equation 8.2 to arrive at a relationship for PPR as a function of peak stress, σ_o (kPa); with Equation 8.3 for peak particle velocity, v_{pk} (m/sec); and with Equation 8.4 for peak strain, ϵ_{pk} (%). The resulting equations are:

$$PPR = 0.0001 \ (\sigma_o)^{1.2} \tag{8.7}$$

$$PPR = 2.0 \ (v_{pk})^{1.2} \tag{8.8}$$

$$PPR = 66 \ (\epsilon_{pk})^{1.2} \tag{8.9}$$

Equations 2.24, 2.25, 2.30 and 8.6 through 8.9 are shown in Figure 8.18 along with data points from Table 8.4. The relationships are fairly linear below a PPR of about 0.85 or 0.90. As the abscissa values decrease, the PPR appears to stabilize at a constant or slightly decreasing value. It is suspected that the recorded PPR's are somewhat less than the actual values, and the point where the curves level off are representative of an actual PPR of 1.0 (liquefaction). An explanation for the lower than actual readings could be a time lag in the piezometer system. Jacobs (1988) estimated that there was a time lag on the order of several seconds for a similar piezometer system. Therefore, the porewater pressure in the sand could be higher than in the piezometer for the first few seconds; i.e. the peak occurred before the piezometer reacted. Another observation from Figure 8.18 is that below scaled distances of about 5 $m/kg^{1/3}$, there is a decrease in PPR. A possible explanation is that this close-in range has considerable shearing activity with significant tangential dilative strain; thus, the volumetric compressive strain is less, and porewater pressure does not increase as much as at greater scaled distances. Additionally,
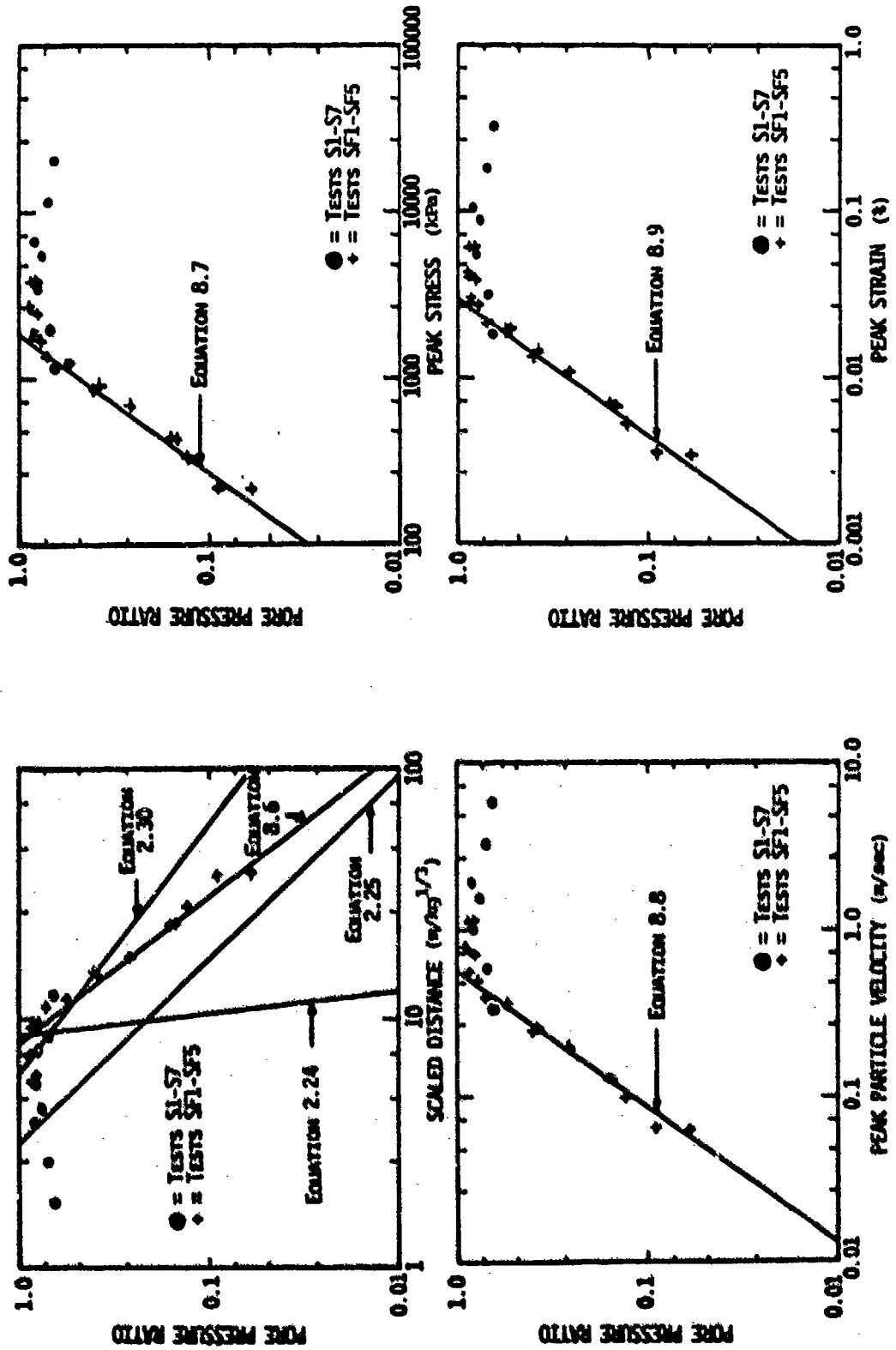
Figure 8.18 Pore pressure ratio relationships.

there could be errors in the piezometer results due to previously discussed difficulties in obtaining accurate readings.

Equation 8.9 is compared to laboratory shock tube tests by Veyera (1985), Hubert (1986) and Bolton (1989) and field tests by Jacobs (1988) in which it was shown that:

Veyera (1985)	$PPR = 3.1 \, \epsilon_{pk}^{(0.331)}$	(from 2.21)
Hubert (1986)	$PPR = 3.2 \, \epsilon_{pk}^{(0.429)}$	(from 2.22)
Bolton (1989)	$PPR = 2.9 \, \epsilon_{pk}^{(0.429)}$	(from 2.23)
Jacobs (1988)	$PPR = 11.2 \, \epsilon_{pk}^{(0.84)}$	(from 2.25b)

Equations 2.21, 2.22, 2.23, and 2.25b which represent laboratory and field liquefaction tests (see Chapter 2) are compared to Equation 8.9 in Figure 8.19. The initial effective stress and relative density representing the pre-test values in this test series were used in Equations 2.21, 2.22, 2.23 and 2.25b. For this comparison, it is significant that Equations 2.21, 2.22 and 2.23 were from laboratory tests with planar stress waves. Equation 2.25b was from tests where point charges were detonated at distances over twice as far as in the tests reported herein; thus, the curvature of the spherical stress wave is less than that represented by Equation 8.9. It, therefore, appears that the differences between the curves in Figure 8.19 are due to the geometry of the stress wave. As the wave becomes more spherical, the curves show steeper slopes and lower peak strains at which liquefaction occurs as indicated by a PPR of 1.0.

Threshold values of scaled distance, peak stress, peak particle velocity, and peak strain at which liquefaction is expected (PPR = 1) were calculated using Equations 8.6 through 8.9. Table 8.5 provides these values.
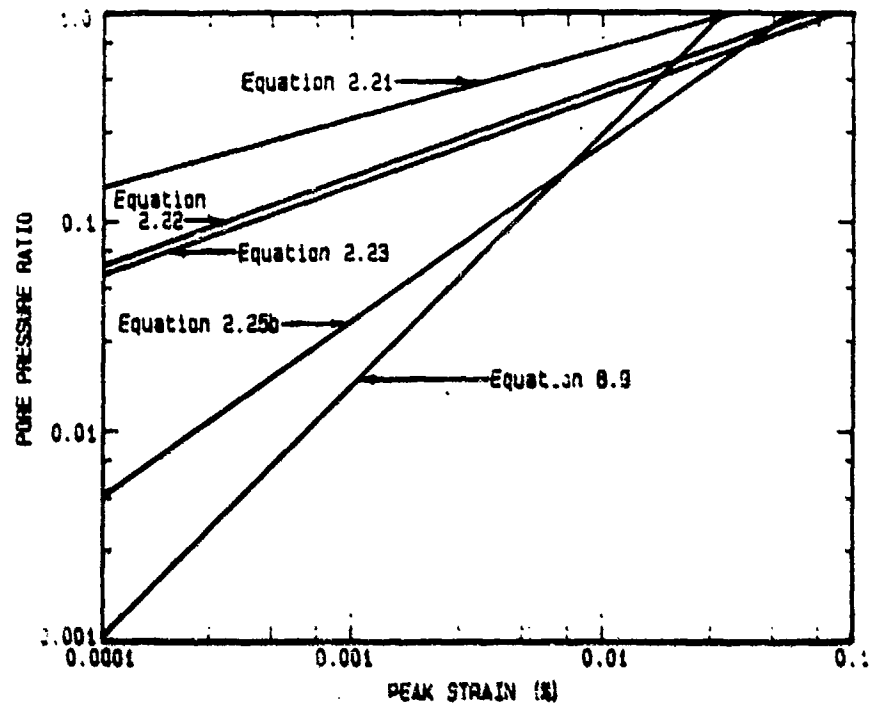
Figure 8.19 Comparison of empirical equations for PPR
versus peak strain.

Table 8.5 Liquefaction Thresholds

Equation	Variable	Value for Liquefaction
8.6	scaled distance	$8.0 \text{ m/kg}^{1/3}$
8.7	peak compressive stress	2,200 kPa
8.8	peak particle velocity	0.6 m/s
8.9	peak strain	0.03%

8.4 VARIABLE DENSITY INCLUSIONS

The vertical movement of the variable density inclusions as
shown in Table 7.10 was analyzed to determine a correlation between

each objects' density and the changes in elevation relative to the
steel tank's rim as determined post-test. The results of this
analysis are provided in Figure 8.20. In addition to the four data
points (one for each inclusion), a fifth theoretical data point was
included to represent zero vertical motion for an item with a density
equal to that of the sand-water mixture. A linear regression was
performed with the five data points, and the equation obtained was:

$$\Delta z = 7.1 - 0.004 \, \rho \qquad (8.10)$$

where Δz is the change in elevation in m, and ρ is the density of the
inclusion in kg/m^3. The coefficient of determination was 0.85 with a
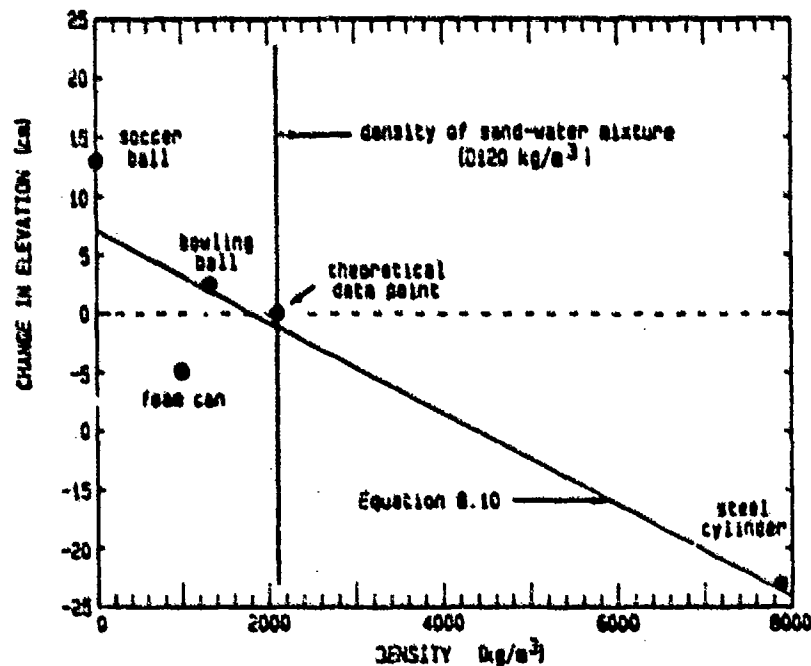

Figure 8.20 Variable density inclusion displacements.

standard deviation of 5.9 cm. The above equation is shown superimposed in Figure 8.20.

8.5   ANALYTICAL MODEL

The analytical model described in Chapter 3 was used to simulate the testing described in this dissertation. It was shown in Chapter 3 that the model is sensitive to certain variables including a time decay constant, Poisson's ratio, and soil skeleton constrained moduli for loading and unloading. For this analysis, the values shown in Table 8.6 were selected based on the best similarity to actual results.

Table 8.6   Analytical Model Variable Values

Variable	Value
time decay constant	$10,000 \text{ sec}^{-1}$
skeleton Poisson's ratio	0.45
mixture Poisson's ratio	0.45
loading bulk modulus	14,000 kPa
unloading bulk modulus	69,000 kPa

The analytical model was applied to the tests performed during this program as well as to the Schure (1988) test series. The model output consisting of strains, porewater pressures, and stresses is discussed in the following paragraphs.

8.5.1   Peak Stress

The model calculates peak radial stress with an empirical equation based on charge size and cube root of distance from the charge. Equation 8.2 was used in the model and was based on actual test results. Since the peak radial stress is calculated with the

same equation (8.2) as obtained from test data, the calculated stress
is the same for the model as for the test results. The model,
however, could be used with other empirical peak stress equations,
such as that in Drake and Little (1983).

8.5.2   Dynamic Strains

Given the peak radial stress described above, the analytical
model was used to calculate radial, tangential, and total strain as a
function of time. Figure 8.21 shows a plot of these strains for Test
S1 at a scaled distance of 11.3 $m/kg^{1/3}$. From this figure it is
apparent that the peak radial strain occurs before the tangential
strain begins. Thus, the peak volumetric strain equals the peak
radial strain which occurs as the stress wave arrives. It should be
noted in Figure 8.21 that the calculations for strains are based on
elastic theory. The shapes of the curves are very dependent on
Poisson's ratio for the soil-water mixture, which is assumed to be
elastic when the stress wave arrives. By changing Poisson's ratio,
the frequency of strain oscillations changes, but the strains at
"infinity" always return to zero.

With the assumption of an elastic mix, the peak radial (total)
strain from the model was determined for each test shown in Table 8.7,
and these strains were compared with those peaks calculated using
Equation 8.4. As shown in Figure 8.22, the peak model strains and the
peak empirically calculated strains compare very closely. In both
cases, there are similar cube root scaling relationships, with the
model resulting in the equation below:

$$\epsilon_{pk} = 0.72 \left(\frac{r}{w^{1/3}}\right)^{-1.46} \tag{8.11}$$

This equation is very similar to the empirically derived Equation 8.4.
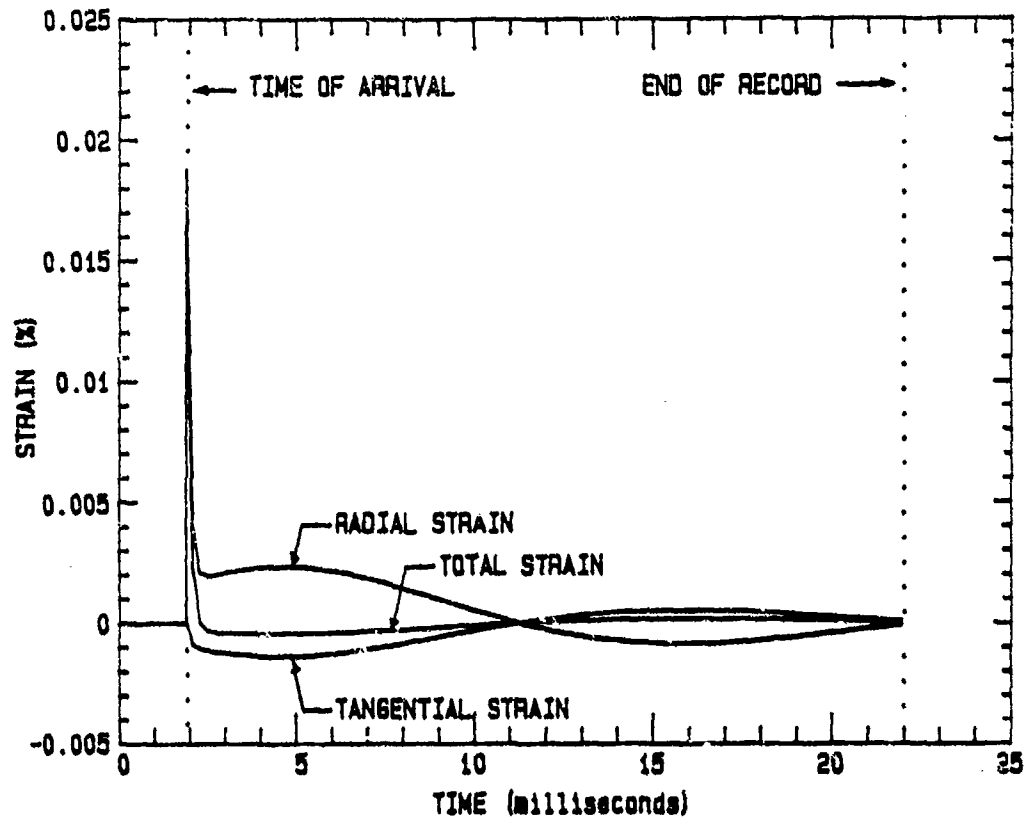
Figure 8.21 Model strain time history - 0.03 kg charge at 3.5 m.

Table 8.7 Analytical Model Versus Test Results

Test[1]	Scaled Distance to Piezometer (m/kg$^{1/3}$)	Charge (kg)	Sand Height above Piezometer (m)	Peak Radial Strain (%) Empirical[2]	Model	Peak PPR Measured	Empirical[3]	Model
SF1	38.0	0.00044	1.67	0.0030	0.0035	0.06	0.07	0.11
SF1	37.1	0.00044	1.52	0.0031	0.0037	0.09	0.06	0.13
SF1	28.0	0.00044	0.76	0.0047	0.0055	0.13	0.11	0.33
SF2	23.9	0.00176	1.67	0.0060	0.0070	0.15	0.14	0.22
SF2	23.4	0.00176	1.52	0.0061	0.0073	0.16	0.15	0.25
SF2	17.6	0.00176	0.76	0.0094	0.0110	0.26	0.25	0.76
SF3	15.1	0.00705	1.67	0.0118	0.0140	0.40	0.32	0.44
SF3	14.7	0.00705	1.52	0.0123	0.0147	0.38	0.34	0.51
SF4	12.0	0.0141	1.67	0.0167	0.0198	0.56	0.49	0.62
SF4	11.7	0.0141	1.52	0.0174	0.0212	0.54	0.51	0.74
S1	11.3	0.03	1.66	0.0183	0.0197	0.65	0.55	0.53
SF3	11.1	0.00705	0.76	0.0188	0.0226	0.71	0.56	1.0
SF5	9.49	0.0282	1.67	0.0238	0.0254	0.78	0.75	0.75
SF5	9.26	0.0282	1.52	0.0247	0.0299	0.86	0.78	1.0
SF4	8.82	0.0141	0.76	0.0266	0.0319	0.35	0.85	1.0
S2	8.15	0.08	1.57	0.0299	0.0325	0.69	0.98	1.0
SF6	7.43	0.059	1.67	0.0343	0.0414	0.80	1.0	1.0
SF6	7.25	0.059	1.52	0.0356	0.0434	0.86	1.0	1.0
SF5	7.00	0.282	0.76	0.0376	0.0451	0.89	1.0	1.0
SF7	5.91	0.117	1.67	0.0484	0.0582	0.81	1.0	1.0
SF7	5.76	0.117	1.52	0.0503	0.0610	0.81	1.0	1.0
S3	5.56	0.25	1.55	0.0530	0.0563	0.86	1.0	1.0
SF6	5.48	0.059	0.76	0.0542	0.0654	0.81	1.0	1.0
SF7	4.35	0.117	0.76	0.0766	0.0919	0.76	1.0	1.0
S4	3.84	0.76	1.55	0.0924	0.1003	0.84	1.0	1.0
S6	3.84	0.76	1.56	0.0924	0.1003	0.83	1.0	1.0
S5	2.67	2.25	1.57	0.159	0.1703	0.70	1.0	1.0
S7	1.83	7.02	1.49	0.281	0.3009	0.65	1.0	1.0

Notes:
1 - relative density 50% for SF series, 90% for S series
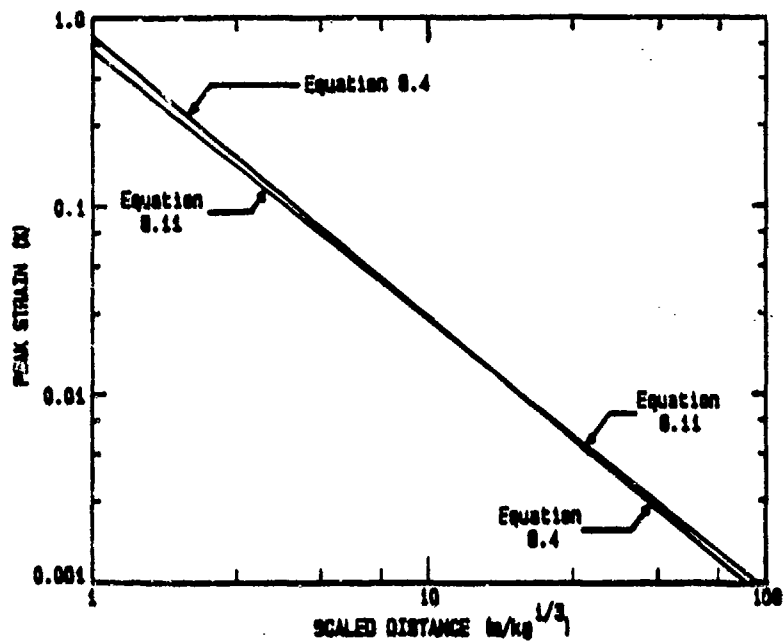2 - Equation 8.4
3 - Equation 8.6

Figure 8.22 Peak strain - analytical model versus empirical.

8.5.3   Dynamic Total Stress, Effective Stress, Porewater Pressures

The dynamic total stresses, effective stresses, and porewater pressures are calculated as functions of the dynamic strains occurring during passage of the stress wave. Figure 8.23 shows a model simulation of Test S1. In these figures, a time of zero is charge detonation.

The total stresses shown in Figure 8.23 are in the radial direction. These values are determined elastically as a function of the radial strain as described in Chapter 3.

The dynamic effective stresses shown in Figure 8.23 are calculated from the elastic dynamic strains. It is assumed that, although the mixture itself behaves elastically during passage of the stress wave, the soil skeleton undergoes hysteresis and the soil is in undrained conditions. As the mixture is compressed, the effective stress increases as a function of the loading constrained modulus, the skeleton Poisson's ratio, and time. As the stress wave passes, the mixture dilates, and the effective stress decreases as a function of the unloading modulus, Poisson's ratio and time. This behavior is inelastic with the final effective stress stabilizing at less than initial static levels as shown in Figure 8.24. In comparing the graphs in Figure 8.24, a peak total stress of 1,373 kPa and a peak porewater pressure of 1,352 kPa resulted in a peak effective stress increase of about 3 kPa and a final effective stress decrease of about 11 kPa below initial static levels. Liquefaction did not occur at this depth since the decrease in effective stress was less than the initial effective stress of 18.5 kPa. The dynamic porewater pressure response is shown in Figure 8.24 as the difference between the total stress and the effective stress.
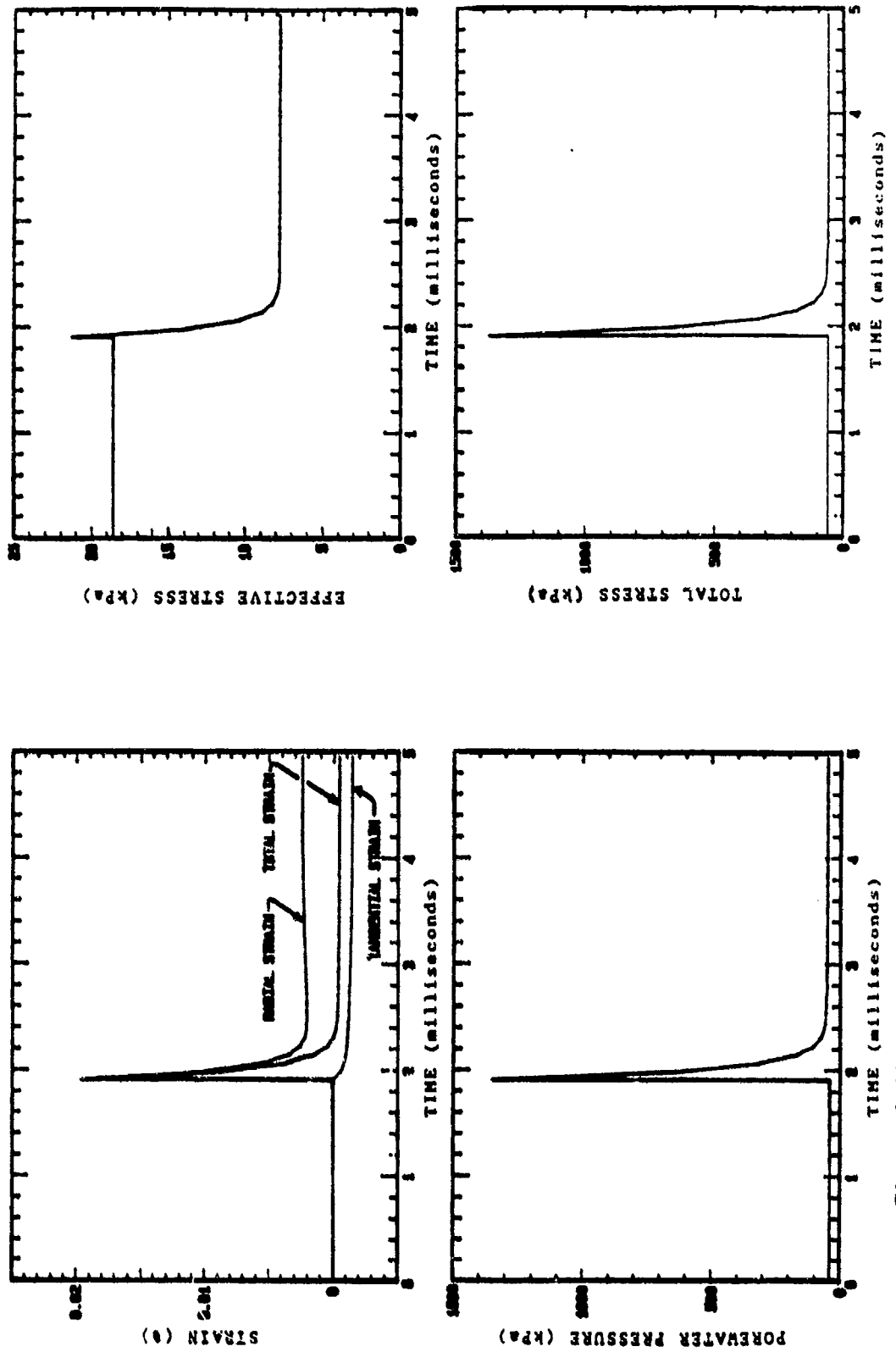
Figure 8.23   Analytical model showing dynamic activity during wave passage, Test S1.
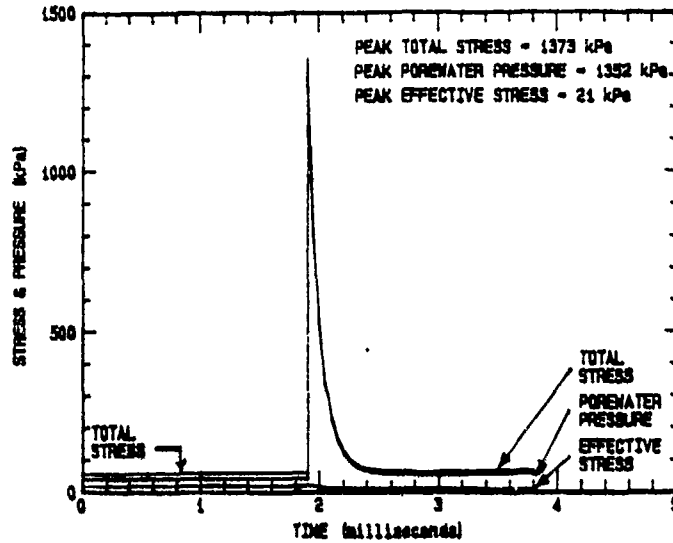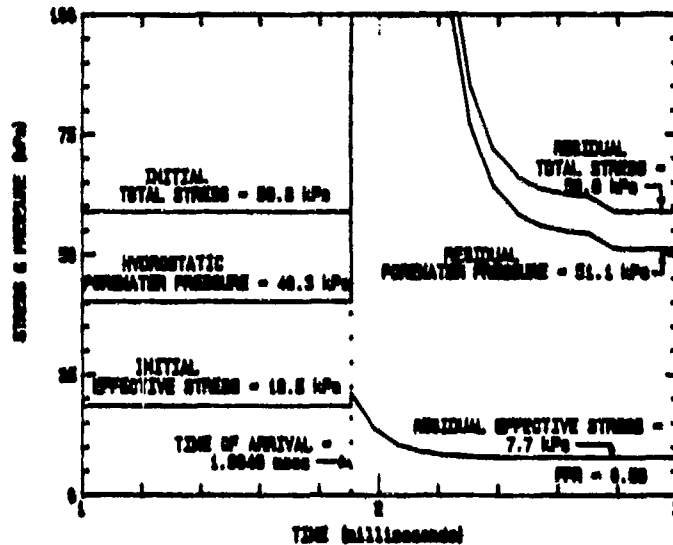
Figure 8.24a Total record.

Figure 8.24b Magnified record.

Figure 8.24 Superimposed analytical model simulation of
dynamic stresses and pressures, Test S1.

To better observe the behavior of the dynamic total stress, effective stress, and porewater pressure, Figure 8.24a is reproduced in Figure 8.24b with a shorter time duration and magnified vertical scale. In comparing the three curves, it is evident that an initial increase in effective stress occurs during the load phase of the stress wave. During the unloading phase, the effective stress decreases to below initial values. In this example, the resulting PPR is 0.58.

8.5.4 Peak Pore Pressure Ratios

Earlier in this chapter, Equations 8.6, 8.7, and 8.9 were shown to empirically represent peak pore pressure ratio as functions of scaled distance, peak stress, and peak strain. To compare the model output to these empirical equations, the model was used to simulate the tests from which the empirical equations were derived. The results of the model calculations for the depths shown in Table 8.7 are given in Figure 8.25a. The three plots represent the output for shallow, middle, and deep depths at which piezometers were located.

In observing the model plots in Figure 8.25a, there is an apparent anomalous condition in the curve labeled "deep" at a PPR of about 0.60. This condition may be due to the relative density of the soil being significantly different for the two tests simulated by the model (Tests SF4 and S1), but the scaled distance was nearly the same. The PPR was higher for Test SF1 because the relative density was lower. This condition does not show up at other points because the tests with higher relative densities (S-series) all showed a PPR of 1.0 (liquefaction) at scaled distances less than about 10 $kg/m^{1/3}$.
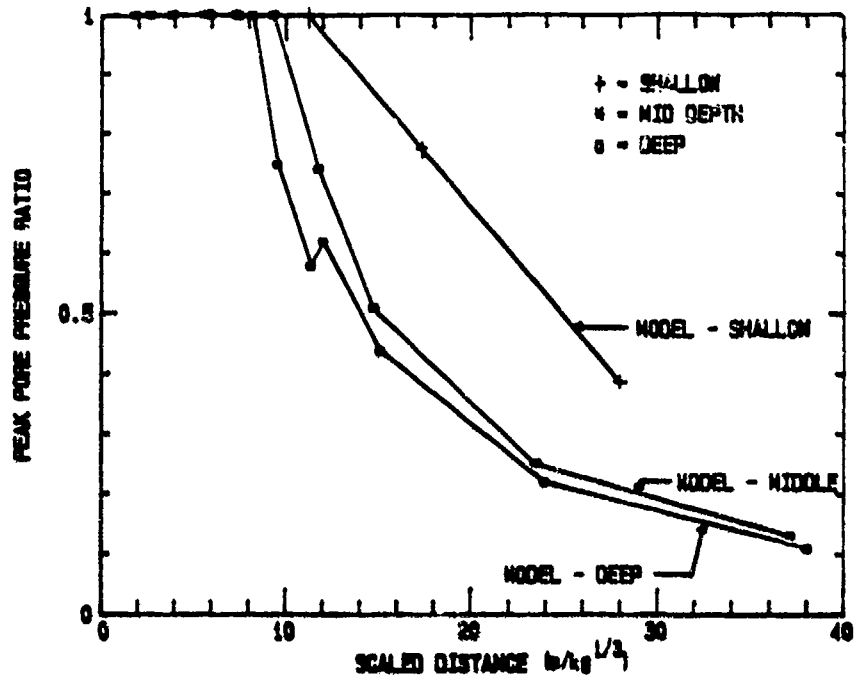
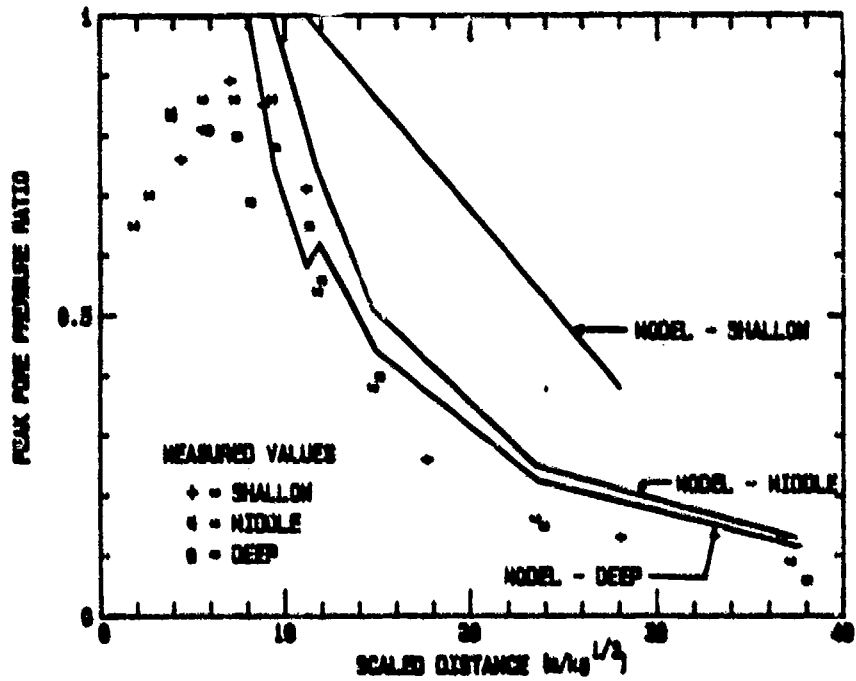Figure 8.25a Analytical model - peak pore pressure ratio.

Figure 8.25b Analytical model with test data.

Figure 8.25 Peak pore pressure ratios - analytical model
versus test results.

To compare the model with measured results, three plots in Figure 8.25a are shown superimposed with measured data points in Figure 8.25b. It initially appears that the data points and the model do not agree. The discrepancy can be attributed to the fact that there were no cases where measured porewater pressure response resulted in a PPR of 1.0; however, at a PPR between 0.8 to 0.9, there is a marked change in the slope of the PPR curve as seen in Figure 8.18. It is suspected that there is a time lag in the piezometer response, and the actual values were higher than shown. If this is the case, the data points in Figure 8.25b would be closer to the theoretical curves calculated by the model.

One final observation from Figure 8.25 is that the model indicates a PPR of 1.0 at a scaled distance of about 8 $kg/m^{1/3}$. This scaled distance is also the approximate point where the measured data show an abrupt change in slope.

As a comparison to the empirical Equations 8.6, 8.7, and 8.9, the output from the model at the middle and deep depths was analyzed using power regression techniques. The equations that resulted were:

$$PPR = 20 \left(\frac{r}{w^{1/3}}\right)^{-1.4} \tag{8.12}$$

$$PPR = 0.0008 \left(\sigma_o\right)^{0.935} \tag{8.13}$$

$$PPR = 28 \, \epsilon_{pk}^{1.0} \tag{8.14}$$

where r is in meters, w is kilograms, σ_o is kPa and ϵ_{pk} is percent. These equations are compared to Equations 8.6, 8.7 and 8.9 in Figure 8.26. The difference between the model equations and the empirical equations is possibly attributed to time lag in piezometer readings.
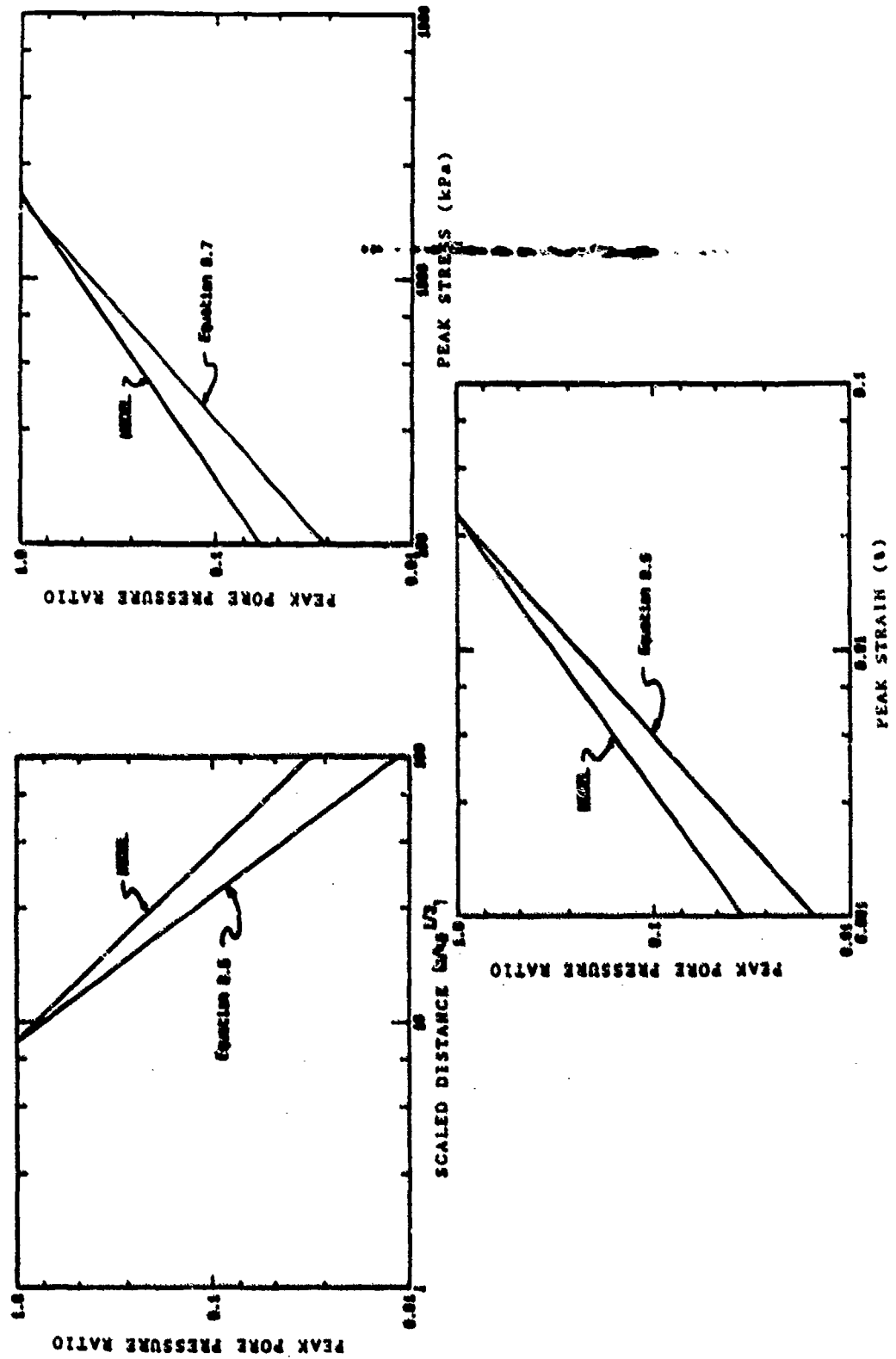
Figure 8.26 Pore pressure ratio relationship - analytical model versus empirical.

which has been previously discussed. With this explanation, the empirical curves would all be shifted upward towards the model curves since the PPR values would actually be greater than measured. A second possible explanation is that there were probable errors in calculating the initial effective stress for each test. These errors are mostly due to unknown and non-constant sand depths above the piezometer tip (see Figure 7.16). To calculate the PPR, an average depth was determined from the information in Figure 7.16. This average depth was used as the basis for determining the initial effective stress in each test.

8.5.5   Dissipation of Excess Porewater Pressures

Residual values of porewater pressure immediately after passage of the stress wave are used as the initial conditions for determining porewater pressure dissipation. It is assumed that consolidation theory describes the dissipation of the excess porewater pressure and the corresponding increase in effective stress. It is also assumed that the total stress remains at static levels during dissipation.

In order to calculate the porewater pressure dissipation at any depth, it is necessary to know the initial and boundary conditions. For the tests performed in this program, the lower boundary was assumed to be an impermeable barrier and the upper boundary was the free draining sand surface. The initial conditions are the porewater pressures at depth increments immediately after the stress wave has passed; i.e., the initial residual porewater pressures.

To calculate dissipation, a finite difference routine is used in the model to solve the consolidation equation. The excess porewater pressure is determined as a function of depth in sand and time. Figure 8.27 illustrates the results of the calculations for Test S1. In this figure, the PPR is shown as a function of depth at different times. The initial PPR shown in the figure is that immediately following passage of the stress wave. It should be noted that the initial distribution of porewater pressure is nearly linear from the impermeable liner (barrier) to where there is a pore pressure ratio of 1.0 at a depth of 1.2 meters. Above that depth, the PPR remains at 1.0, indicating full liquefaction. The PPR gradually decreases with time at all depths, as shown by the plots at 10+ seconds.

Figure 8.28 illustrates the dissipation process at the piezometer depth of Test S1. The test results from Figure 8.11 for Test S1 are superimposed for comparison purposes. The two curves show very similar trends; however, there are some differences. The first is during the initial porewater pressure rise. The curve labeled "model" has an instantaneous rise at $t = 0$ time; whereas, the "measured" curve shows a slight (but definite) time lag during rise. The actual initial peak residual porewater pressure probably occurs within milliseconds after the stress wave passage. Thus, on a plot of porewater pressure versus time in seconds, the initial peak porewater pressure should show up as an instantaneous rise at time zero which supports the explanation of time lag discussed earlier. A second difference in the curves is that the peak in the model is somewhat less than the measured peak. It should be recalled that the curve labeled "measured" was partly estimated because of incomplete early
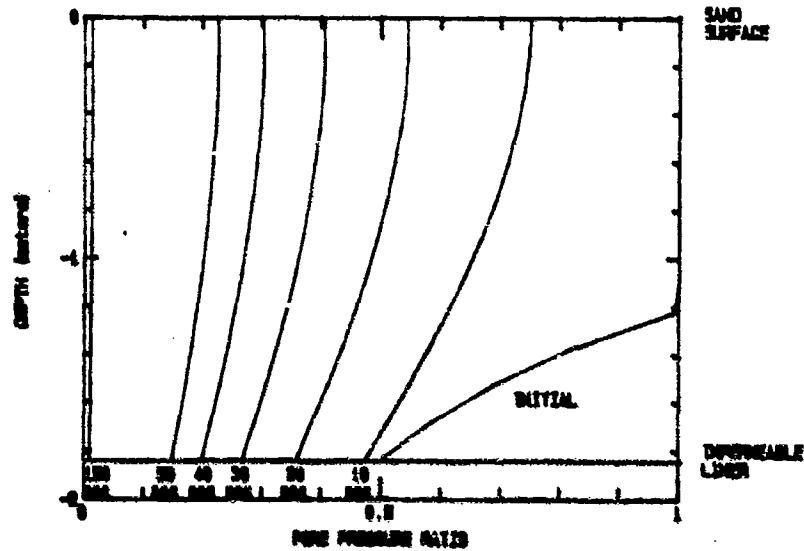
Figure 8.27   Dissipation of excess porewater pressure versus depth - analytical model simulation, Test S1.
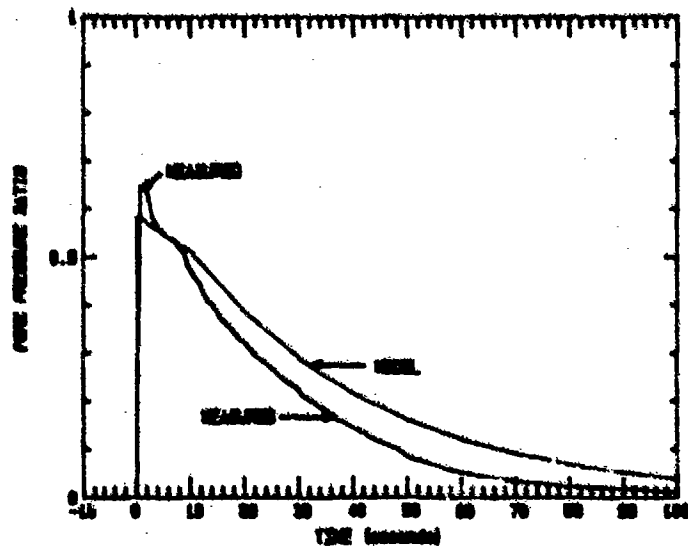

Figure 8.28   Dissipation of excess porewater pressure versus time - analytical model simulation, Test S1.

time data (see Section 8.3). Thus, the early part of the measured curve may be inaccurate. There is also a difference between the measured and model curve during dissipation. The difference is probably due to inaccuracies in selection of permeability for use in the model.

An additional observation from Figure 8.28 is that there is a marked change in slopes of both curves at early times. This change occurs between zero and 10 seconds, and in Tests S1 through S6, this behavior was observed (Figures 8.11 through 8.16). A explanation of this anomaly is not provided; however, it is represented in both the empirical and the theoretical modelling of the tests.

A final point in this section involves the effect of porewater pressure dissipation on soil strength. Since strength is directly related to effective stress, it is important to understand the interaction of porewater pressure and effective stress during dissipation. Figure 8.29 (from the model treatment of Test S1) illustrates this interaction. As the excess porewater pressure dissipates, the effective stress increases. Full recovery occurs if and when the porewater pressure becomes hydrostatic.

8.5.6   Summary of Analytical Model

The analytical model discussed in this section appears to reasonably simulate the response of a saturated sand to a detonation. The model is based on a theoretical treatment of radial stress waves and porewater pressure dissipation. The model has a number of assumptions which are discussed in detail in Chapter 3 and in this section. The results from the model include dynamic time histories of radial and tangential strains, effective stress, total stress, and
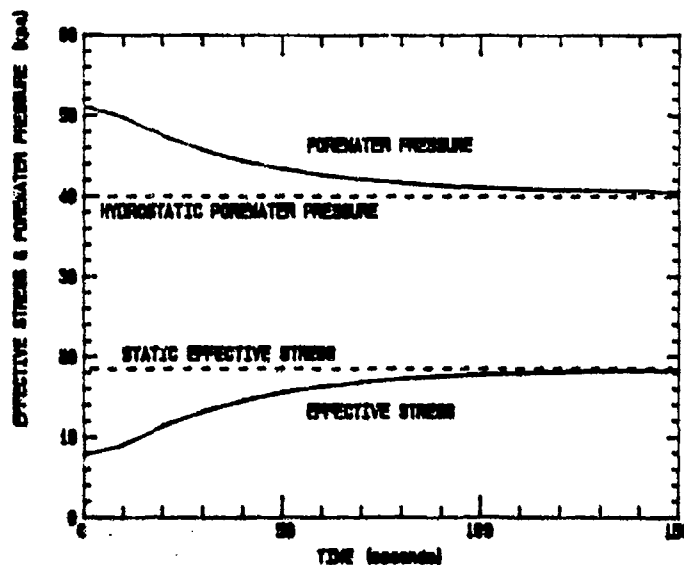
Figure 8.29 Effective stress and porewater pressure change during dissipation - analytical model simulation, Test S1.

porewater pressure Also included is the dissipation of residual excess porewater pressure.

The analytical model behaviour supports empirical results. For example, empirical treatments of peak strain versus scaled distance show very close agreement to the theoretical peak radial strain. Further, the model shows that tangential strain occurs after the peak radial strain, thus, the peak radial and peak total strains are the same (Figure 8.21)

The model indicates similar trends when comparing measured peak residual porewater pressures and calculated pressures as shown in Figure 8.25b; however, there are some differences. It may be that the measured values are in error due to time lag, and the model is perhaps in closer agreement with actual values than shown in the figure.

The treatment of porewater pressure dissipation in the model seems to reasonably simulate measured results (Figure 8.28). The model also illustrates the relationship between effective stress and excess porewater pressure dissipation. This relationship, shown in Figure 8.29, is perhaps the most important aspect of blast-induced soil liquefaction. Since the strength of cohesionless soil is directly related to effective stress, the duration that a soil is at less than static strength is known at any depth of interest. With this information, the effects on structures in the soil can be determined.

8.6 DISCUSSION

8.6.1 Analytical Model

The analytical model theoretically supports observed behavior in blast-induced liquefaction. Peak total strain equals peak radial strain, both of which occur as the spherical stress wave arrives, and both of which are compressive. Tangential strain begins after peak radial strain has reached a maximum value and is primarily tensile. Elastic theory and mixture theory are applicable to the soil-water mixture during passage of a blast-induced spherical stress wave. The soil skeleton behaves inelastically while responding to the elastic soil-water mixture behavior, and, as a result, residual excess porewater pressure is developed. Relative density and skeleton bulk moduli for loading and unloading are the most influential variables affecting porewater response in a saturated, cohesionless sand exposed to blast-induced stress waves.

The analytical model was used to simulate each test in the experimental program, and the model calculations were statistically analyzed to obtain Equation 8.11 for peak strain as a function of scaled distance. Equation 8.11 compares closely with Equation 8.4 which was derived from the test results.

In observing the dynamic porewater pressure, total stress, and effective stress output from the analytical model (Figure 8.24), there is an increase in effective stress during the loading of the soil. During unloading, after passage of the peak stress, the effective stress decreases to less than initial levels.

The analytical model was also used to evaluate initial residual porewater pressures. The model produced very similar trends to test data. The model calculations resulted in Equations 8.12, 8.13, and 8.14 for pore pressure ratio (PPR) as a function of scaled distance, peak stress, and peak strain, respectively. These equations compare fairly well to empirical Equations 8.6, 8.7, and 8.9. The difference in the model equations and the empirical equations is possibly due to time lag in the piezometers. If piezometer readings are increased 10 to 20 percent, the equations would show closer agreement (Figure 8.25). Thus, Equations 8.12, 8.13 and 8.14 may be more representative than Equations 8.6, 8.7, and 8.9.

Dissipation of excess porewater pressure is modeled by Terzaghi's consolidation theory. The initial conditions of excess porewater pressure at each depth in a soil layer are dependent on scaled distance. The upper portion of a layer may show an initial PPR of 1.0 while the lower layers may be less than 1.0. Thus, the initial excess porewater pressure conditions may have a non-linear distribution with depth.

The analytical model was fairly accurate in simulating dissipation of excess porewater pressure (Figure 8.28). The differences in model versus measured response are probably due to erroneous permeability and compressibility inputs in the model and piezometer inaccuracies in the testing. In summary, the analytical model was reasonable in predicting and explaining mathematically blast-induced liquefaction.

8.6.2   Experimental Test Results and Analysis

During the tests, the sand became denser with each detonation as shown by surface elevation measurements during larger detonations. Porewater pressure and total stress increased as scaled distance decreased. Piezometer results showed a definite residual porewater pressure in excess of initial, hydrostatic conditions. The increase in porewater pressure, however, never exceeded about 85 percent of the initial effective stress (PPR = 0.85). It is strongly suspected that these values were actually 1.0, but due to time lag effects in the piezometer the true peaks were not seen. After the peak values, the excess porewater pressure dissipated with times of over 100 seconds. Variable density inclusions later excavated from the sand had undergone significant movements from their pre-test position. The subsequent series of tests performed by Schure (1988), with smaller charge masses, showed similar porewater pressure and total stress trends as in the test series described herein.

The dynamic and dissipation data from all tests on Poudre Valley sand where the initial relative density was about 84% and the initial effective stress was 16 kPa were statistically analyzed to obtain the following relationships:

$$u_{pk} \text{ or } \sigma_o = 50,000 \left(\frac{r}{w^{1/3}}\right)^{-1.5} \text{ (kPa)} \tag{8.2}$$

$$v_p = 12.8 \left(\frac{r}{w^{1/3}}\right)^{-1.5} \text{ (m/sec)} \tag{8.3}$$

$$\epsilon_{pk} = 0.7 \left(\frac{r}{w^{1/3}}\right)^{-1.5} \text{ (\%)} \tag{8.4}$$

$$PPR = 43 \left(\frac{r}{w^{1/3}}\right)^{-1.8} \tag{8.6}$$

$$PPR = 0.0001 \left(\sigma_o\right)^{1.2} \tag{8.7}$$

$$PPR = 2.0 \left(v_{pk}\right)^{1.2} \tag{8.8}$$

$$PPR = 66 \left(\epsilon_{pk}\right)^{1.2} \tag{8.9}$$

In the above equations, σ_o is peak radial compressive stress (kPa), u_{pk} is peak porewater pressure (kPa), v_{pk} is peak particle velocity (m/sec), PPR is the residual pore pressure ratio, r is distance from charge (m), ϵ_{pk} is the peak strain (%), and w is charge mass (kg). Equations 8.6 through 8.9 were used to calculate liquefaction thresholds (PPR = 1.0) which are given in Table 8.5.

8.6.3   Correlation of Test Results with Previous Research

Equations 8.2 through 8.9 were compared to relationships reported by other researchers. Equation 8.2 is shown graphically in Figures 8.2 through 8.10 and is compared to the following equations:

$$\sigma_o = 59,000 \left(\frac{r}{w^{1/3}}\right)^{-1.05} \quad \text{Lyakhov (1961)} \tag{2.14j}$$

$$\sigma_o = 10,000 \left(\frac{r}{w^{1/3}}\right)^{-3} \quad \text{Crawford, et al. (1971)} \tag{2.14k}$$

$$\sigma_o = 47,000 \left(\frac{r}{w^{1/3}}\right)^{-1.5} \quad \text{Drake and Little (1983)} \tag{2.14l}$$

$$\sigma_o = 50,100 \left(\frac{r}{w^{1/3}}\right)^{-2.38} \quad \text{Jacobs (1988)} \tag{2.14m}$$

$$u_{pk} = 52,100 \left(\frac{r}{w^{1/3}}\right)^{-1.13} \quad \text{Cole (1948)} \tag{2.14n}$$

Equation 8.2 most closely agrees to that from Drake and Little (1983).
Equation 8.3 also compares closely with the Drake and Little (1983)
equation which is

$$v_p = 12.2 \ (\frac{r}{w^{1/3}})^{-1.5} \qquad (2.29)$$

Equation 8.9 is compared to shock tube tests by Veyera (1985), Hubert
(1986), and Bolton (1989) in which planar stress waves were generated
in different saturated sands and to field tests by Jacobs (1988) in
which spherical stress waves were generated in soil on the bank of a
river. The equations that resulted from the shock tube and field
tests are:

$$PPR = 3.1 \ \epsilon_{pk}^{(0.331)} \qquad \text{Veyera (1985)} \qquad \text{(from 2.21)}$$

$$PPR = 3.2 \ \epsilon_{pk}^{(0.429)} \qquad \text{Hubert (1986)} \qquad \text{(from 2.22)}$$

$$PPR = 2.9 \ \epsilon_{pk}^{(0.429)} \qquad \text{Bolton (1989)} \qquad \text{(from 2.23)}$$

$$PPR = 11.2 \ \epsilon_{pk}^{(0.84)} \qquad \text{Jacobs (1988)} \qquad \text{(from 2.25b)}$$

A graphic comparison of Equation 8.9 to Equations 2.21, 2.22, 2.23 and
2.25b is made in Figure 8.19, and certain trends are apparent despite
the differences in the equations. The trends seem to be based on the
geometry of the stress waves, with the planar waves (Equations 2.21,
2.22, and 2.23) showing a distinctively different behaviour than the
spherical waves (Equations 2.25b and 8.9).

CHAPTER 9

SUMMARY, CONCLUSIONS, AND RECOMMENDATIONS

9.1   SUMMARY

This dissertation documents a research program to investigate soil liquefaction induced by explosively generated, spherical stress waves. An analytical model was developed to simulate the response of a saturated soil to blast-induced spherical stress waves. The model which is based on mixture theory, spherical stress wave propagation in elastic media, soil skeleton inelasticity, and soil consolidation predicts and mathematically explains porewater pressure response in saturated sand. To establish a data base, experimental explosive testing in which spherical stress waves were generated in saturated sand was performed at a site developed at Colorado State University. Test preparation consisted of controlled placement and saturation of 26 cubic meters of sand. Tests were performed by detonating explosives with charge masses from 0.03 to 7.02 kg to induce the spherical stress waves in the sand which had an initial relative density of 84 percent. Data from the tests includes dynamic total stress and porewater pressure time histories from embedded instrumentation plus late-time piezometer readings. Empirical equations developed from the test data and data from a subsequent series of tests conducted by Schure (1988) relate scaled distance to peak dynamic strain, stress, and particle velocity and peak residual

pore pressure ratio to scaled distance, peak stress, peak particle velocity, and peak strain. From the relationships established, threshold limits of scaled distance, peak compressive stress, peak particle velocity, and peak strain at which liquefaction is expected to occur are established. The test results are compared to analytical model calculations of dynamic strain, total stress, and porewater pressure response during passage of the spherical stress wave as well as dissipation of excess residual porewater pressure following passage of the wave.

9.2   CONCLUSIONS

The analytical model demonstrates that elastic theory and mixture theory are applicable to soil-water mixture response during passage of a blast-induced spherical stress wave. The model predicts that peak total strain equals peak radial strain, both occurring as the spherical stress wave arrives and both being compressive, and tangential strain is initially tensile and begins after radial strain has reached a maximum value. The soil skeleton behaves inelastically while responding to the elastic soil-water mixture behavior, and, as a result, residual excess porewater pressure is developed. Relative density and skeleton bulk moduli for loading and unloading are the most influential variables affecting porewater response in a saturated, cohesionless sand exposed to blast-induced stress waves. The model also shows that dissipation of the excess porewater pressure is adequately described by consolidation theory. The overall conclusion is that the analytical model is reasonably accurate in predicting and mathematically explaining blast-induced liquefaction.

Experimental explosives testing was performed and established an adequate data base for evaluating blast-induced liquefaction. The site developed at Colorado State University is ideally suited for performing well-controlled tests with over 7 kilograms of explosives and 26 cubic meters of saturated sand. Included in the site development was a water deairing and sand saturation system. This system permitted full saturation of test sand, which most other researchers have not acccomplished, and which may have affected their results. Seven explosives tests with charge masses from 0.03 to 7.02 kilograms established an adequate data base for a preliminary validation of the analytical model and for development of empirical relationships. Additional explosives tests at the site by Schure (1988) added to the data base and were used to enhance the statistical validation of the analytical model and the empirical relationships.

Results of the seven tests and the Schure (1988) tests show close agreement to the analytical model predictions. The prediction of peak porewater pressure during passage of the spherical stress wave is close to the measured peak pressure. The prediction of the residual excess porewater pressure and its dissipation after the stress wave has passed is also similar to actual test results. Empirical Equations 8.2, 8.3, and 8.4 which relate scaled distance to peak porewater pressure, peak particle velocity, and peak strain are considered more accurate than equations reported in the literature for similar situations because of the fully saturated sand conditions and the controls on the testing. Empirical Equations 8.6, 8.7, 8.8, and 8.9 relating residual pore pressure ratio to scaled distance, peak stress, peak particle velocity, and peak strain are, likewise, considered more accurate than equations reported in the literature.

Empirical Equations 8.6, 8.7, 8.8, and 8.9 establish threshold values
of scaled distance, peak stress, peak particle velocity, and peak
strain at which blast-induced liquefaction is likely to occur.

9.3   RECOMMENDATIONS

The following recommendations are presented to further advance
the understanding of blast-induced liquefaction:

- Additional testing with a wider range of scaled distances,
  soil densities, and soil types should be performed at this
  site to raise confidence in empirical and analytical
  relationships and demonstrate repeatability of results.

- Measurements of dynamic radial and tangential stresses and
  displacements are needed for further validation of the
  models developed in this research.

- Instrumentation methodology needs improvement to permit
  measurement of accelerations which can be integrated for
  particle velocities and displacements.

- Electronic instrumentation should be used to obtain more
  accurate late time porewater pressure dissipation data.

- The analytical model should be modified to account for
  layered soil systems, such as dry soil over saturated sand,
  and horizontal separation between the explosives and sand.

- Testing should be performed at field locations with
  saturated cohesionless soil present to verify the
  applicability of the models developed in this research.

REFERENCES

Abt, S.R. and Patrone, H.D. (1983), "Standard Operation Procedures for Blasting to Enhance Scientific Research at the Colorado State University Engineering Research Center," Department of Civil Engineering, Fort Collins, Colorado, January, 17 p.

Allard, D. and Norquist, L. (1985), "Building Safety at Blast Site," Senior Project, CE-470, Colorado State University, Fort Collins, Colorado, 62 p.

Allen, N.F., Richard, F.E. and Woods, R.D. (1980), "Fluid Wave Propagation in Saturated and Nearly Saturated Sands," Journal of the Geotechnical Engineering Division, American Society of Civil Engineers, Vol. 106, No. GT 3, March, pp. 235-254.

Ambraseys, N. and Sarma, S. (1969), "Liquefaction of Soils Induced by Earthquakes," Bulletin, Seismological Society of America, Vol. 59, No. 2, April, pp. 651-664.

Arya, A.S., Nandakumaran, P., Puri, V.K. and Mukerjee, S. (1978), "Verification of Liquefaction Potential by Field Blast Tests," Proceedings, 2nd International Conference on Microzonation for Safer Construction, San Francisco, California, Vol. 1, November 26-December 1, pp. 865-869.

Baladi, G. and Rohani, B. (1979), "Elastic-Plastic Model for Saturated Sand," Journal of the Geotechnical Engineering Division, American Society of Civil Engineers, Vol. 105, No. GT4, April, pp. 465-480.

Begemann, H., Koning H., and Lindenberg, J. (1977), "Critical Density of Sand," Proceedings of the Ninth International Conference on Soil Mechanics and Foundation Engineering, Tokyo, Japan, Vol. 1, pp. 43-46.

Biot, M.A. (1956), "Theory of Propagation of Elastic Waves in a Fluid-Saturated Porous Solid, (Part I and Part II) (Low/High) Frequency Range," Journal of the Acoustical Society of America, Vol. 28, No. 2, pp. 158-178.

Bishop, A., and Hight, D. (1977), "The Value of Poisson's Ratio in Saturated Soils and Rocks Stressed Under Undrained Conditions," Geotechnique, 27, No. 3, pp. 369-384.

Blazquez, R., Krizek, R. and Bazant, Z. (1980), "Site Factors Controlling Liquefaction." Journal of the Geotechnical Engineering Division, American Society of Civil Engineers, Vol. 106, No. GT7, July, pp. 785-801.

Blouin, S.E. (1978), "Liquefaction Evidence Observed in Various Explosive Events," Transcripts of the International Workshop on Blast-Induced Liquefaction, Dames & Moore/U.S. Air Force, Maidenhead, United Kingdom, September 17-19, pp. 95-110.

Blouin, S. and Shinn, J. (1983), "Explosive Induced Liquefaction," Final Report to Air Force Office of Scientific Research, Bolling Air Force Base, Washington, D.C., September, 227 p.

Bolton, J. (1989), "Undrained Confined Compression Behavior of Saturated Sand and Silt," Master of Science Thesis, Colorado State University, Fort Collins, Colorado, 93 p.

Burden, R.L., Faires, J.D. and Reynolds, A.C. (1981), "Numerical Analysis," PWS Publishers, Boston, Massachusetts, 598 p.

Butler, W.L. (1986), Personal Communication, Department of Civil Engineering, Colorado State University, Fort Collins, Colorado.

Carnes, B.L. (1981), "The Influence of a Shallow Water Table on Cratering," Technical Report SL-81-6, Structures Laboratory, U.S. Army Corps of Engineers Waterways Experiment Station, Vicksburg, Mississippi, September, 122 p.

Castro, G. and Poulos, S. (1977), "Factors Affecting Liquefaction and Cyclic Mobility," Journal of the Geotechnical Engineering Division, Proceedings of the American Society of Civil Engineers. Vol. 103, No. GT6, June, pp. 501-516.

Charlie, W.A. (1978), "The Dial Pack Event," Transcripts of the International Workshop on Blast-Induced Liquefaction, Dames & Moore/U.S. Air Force, Maidenhead, United Kingdom, September 17-19, pp. 149-165.

Charlie, W.A., Hassen, H., Doehring, D. and Hubert, M. (1987), "Microcomputers in Shock Testing of Water Saturated Sands," The Shock and Vibration Bulletin, No. 57, The Shock and Vibration Information Center, Naval Research Laboratory, Washington, D.C., January, pp. 157-159.

Charlie, W.A., Hubert, M.E., Schure, L.A., Veyera, G.E, Bretz, T.E., and Hassen, H.A. (1988), "Blast-Induced Soil Liquefaction Summary of Literature," Report to Air Force Office of Scientific Research, Research Project AFOSR-85-0172, Bolling Air Force Base, Washington, D.C., 316 p.

Charlie, W.A., Mansouri, T. and Ries, E. (1981), "Predicting Liquefaction Induced by Buried Charges," Proceedings of the Tenth International Conference on Soil Mechanics and Foundation Engineering, Stockholm, Sweden, 15-19 June, pp. 77-80.

Charlie, W.A., Shinn, J., and Melzer, S. (1979), "Blast Induced Soil Liquefaction," Proceedings of the 2nd U.S. National Conference on Earthquake Engineering, Earthquake Engineering Research Institute, August 22-24, pp. 997-1005.

Charlie, W.A. and Veyera, G. (1985), "Explosive Induced Porewater Pressure Increases," Proceedings of the Eleventh International Conference on Soil Mechanics and Foundation Engineering, Vol. 2, pp. 997-1000.

Charlie, W.A., Veyera, G., and Abt, S. (1985b), "Predicting Blast Induced Porewater Pressure Increases in Soil," Civil Engineering for Practicing and Design Engineers, Vol. 4, Pergamon Press, New York, pp. 311-328.

Charlie, W.A., Veyera, G., Bretz, T. and Allard D. (1986), "Shock Induced Porewater Pressure Increases," The Shock and Vibration Bulletin, No. 57, The Shock and Vibration Information Center, Naval Research Center, Washington, D.C., January, pp. 161-166.

Charlie, W.A., Veyera, G., Doehring, D., and Abt, S. (1985a), "Blast Induced Liquefaction Potential and Transient Porewater Pressure Response of Saturated Sands," Final Report to Air Force Office of Scientific Research, Grant No. AFOSR-80-0260, Bolling Air Force Base, Washington, D.C., 198 p.

Cole, R.H. (1948), "Underwater Explosions," Princeton University Press, Princeton, New Jersey, 437 p.

Colton, R.B. (1978), Geologic Map of the Boulder-Fort Collins-Greeley Area, Colorado, U.S. Department of the Interior, U.S. Geologic Survey.

Committee on Earthquake Engineering (1985), "Liquefaction of Soils During Earthquakes," National Academy Press, Washington, D.C., 266 p.

Committee on Soil Dynamics of the Geotechnical Engineering Division, American Society of Civil Engineers (1978), "Definition of Terms Related to Liquefaction," Journal of the Geotechnical Engineering Division, American Society of Civil Engineers, Vol. 104, No. GT 9, September, pp. 1197-1200.

Crawford, R., et al. (1971), "Protection from Nonnuclear Weapons," Technical Report AFWL-TR-70-127, Air Force Weapons Laboratory, Kirtland Air Force Base, New Mexico, 507 p.

Crawford, R.E., Higgins, C.J. and Bultmann, E.A. (1974), "The Air Force Manual for Design and Analysis of Hardened Structures," AFWL-TR-74-102, Air Force Weapons Laboratory, Kirtland Air Force Base, New Mexico. 17th Printing, July, 1983, 1118 p.

Damitio, C. (1978a), "Empirical Predictions of Blast-Induced Liquefaction," Transcripts of the International Workshop on Blast-Induced Liquefaction, Dames & Moore/U.S. Air Force, Maidenhead, United Kingdom, September 17-19, pp. 390-400.

Damitio, C. (1978b), "Field Experience on Blast-Induced Liquefaction," Transcripts of the International Workshop on Blast-Induced Liquefaction, Dames & Moore/U.S. Air Force, Maidenhead, United Kingdom, September 17-29, pp. 137-148.

Dobry, R. and Swiger, W. (1979), "Threshold Strain and Cyclic Behavior of Cohesionless Soils," Proceedings Third Engineering Mechanics Division Specialty Conference, University of Texas at Austin, Austin, Texas, September 17-19, pp. 521-525.

Dobry, R., Ladd, R., Yokel, F., Chung, R., and Powell, D. (1982), "Prediction of Porewater Pressure Buildup and Liquefaction of Sands During Earthquakes by the Cyclic Strain Method," Report No. NBS BSS 138, National Bureau of Standards, Department of Commerce, Washington, D.C., July, 168 p.

Dowding, C.H. and Hryciw, R. (1986), "A Laboratory Study of Blast Densification of Saturated Sand," Journal of Geotechnical Engineering, Vol. 112, No. 2, February, pp. 187-199.

Drake, J. (1978), "Results of some Experiments Conducted Primarily for the Purpose of Understanding the Influence of Water Table Depth on the Size and Extent of Craters," Transcripts of the International Workshop on Blast-Induced Liquefaction, Dames & Moore/U.S. Air Force, Maidenhead, United Kingdom, September 17-19, pp. 250-266.

Drake, J. L. and Ingram, L. F. (1981), "Predictions of the Airblast and Ground Motions Resulting from Explosive Removal of the Birds Point-New Madrid Fuze Plug Levee," Miscellaneous Paper SL-81-30, U.S. Army Corps of Engineers, Waterways Experiment Station, Vicksburg, Mississippi, November, 23 p.

Drake, J.L. and Little, C.D. (1983), "Ground Shock from Penetrating Conventional Weapons," Symposium Proceedings, The Interaction of Non-Nuclear Munitions with Structures, U.S. Air Force Academy, Colorado Springs, Colorado, Part I, May 10-13, pp. 1-6.

DuPont Company (1980), "Blaster's Handbook," E.I. du Pont de Nemours & Co. (Inc.), Wilmington, Delaware, 494 p.

Ensign-Bickford Company (1984), "Primacord[R] Handbook," Simsburg, Connecticut, 500 p.

Finn W.D. (1978a), "A Model for Liquefaction Analysis Based on One-Dimensional Shear Propagation," Transcripts of the International Workshop on Blast-Induced Liquefaction, Dames & Moore/U.S. Air Force, Maidenhead, United Kingdom, September 17-19, pp. 331-336.

Finn, W.D. (1978b), "Mechanics of Liquefaction under Blast Loading," Transcripts of the International Workshop on Blast-Induced Liquefaction, Dames & Moore/U.S. Air Force, Maidenhead, United Kingdom, September 17-19, pp. 14-22.

Finn, W.D., Lee, K., and Martin, G. (1977), "An Effective Stress Model for Liquefact. u, " Journal of the Geotechnical Engineering Division, American Society of Civil Engineers, Vol. 103, No. GT6, June, pp. 517-52".

Florin, V.A. and Ivanov, P.L. (1961), "Liquefaction of Saturated Sandy Soils," Proceedings 5th International Conference on Soil Mechanics and Foundation Engineering, Paris, France, Vol. 1, July 17-22, pp. 107-111.

Forrest, J., Ferritto, J. and Wu, G. (1979), "Seismic Soil Liquefaction Studies, "TN NO. N-1566, Naval Civil Engineering Laboratory, Port Hueneme, California, 34 p.

Fragaszy, R.J., Voss, M.E., Schmidt, R.M. and Holsapple, K.A. (1983), "Laboratory and Centrifuge Modeling of Blast-Induced Liquefaction," Proceedings 8th International Symposium on Military Application of Blast Simulation, Gruppe fur Rustungsdienste, Spiez, Switzerland, pp. 1-20.

Fragaszy, R.J., and Voss, M.E. (1986), "Undrained Compression Behavior of Sand," Journal of Geotechnical Engineering, American Society of Civil Engineers, Vol. 112, No. 3, March, pp. 334-347.

German, (1986), Personal Communication, DuPont Company, Wilmington, Delaware.

Gilbert, P.A. (1976), "Case Histories of Liquefaction Failures," Miscellaneous Paper S-76-4, U.S. Army Engineer Waterways Experiment Station, Vicksburg, Mississippi, April, pp. 49-62.

Gill, J. (1989), "Interpretation of the Initial Results of the 500,000 LB (TNT Equivalent) Hayman Igloo Test," AFWL-NTE-TN-09-89, Civil Engineering Research Division, Air Force Weapons Laboratory, Kirtland Air Force Base, New Mexico, 27 February, 32 p.

Graftio, H. (1936), "Some Features in Connection with the Foundation of SVIR 3 Hydro-Electric Power Development," Proceedings of the International Conference on Soil Mechanics and Foundation Engineering, Graduate School of Engineering, Harvard University, Cambridge, Massachusetts, pp. 284-290.

Griffiths, D. and King, R. (1965), "Applied Geophysics," Pergamon Press, Elmsford, New York, 223 p.

Hardin, B.O. and Richart, F.E. (1963), "Elastic Wave Velocities in Granular Soils," Journal of the Soil Mechanics and Foundations Division, American Society of Civil Engineers, Vol. 89, No. SM1, February, pp. 33-65.

Harvey, M., (1986), Personal Communication, Department of Earth Resources, Colorado State University, Fort Collins, Colorado.

Hassen, H. (1989), Personal Communication, Department of Civil Engineering, Colorado State University, Fort Collins, Colorado.

Hazen, A. (1920), "Hydraulic-Fill Dams," American Society of Civil Engineers, Paper No. 1458, May, pp. 1719-1745.

Henrych, J. (1979), "The Dynamics of Explosion and Its Use," Elsevier Scientific, New York, pp. 81-341.

Hubert, M.E. (1986), "Shock Loading of Water Saturated Eniwetok Coral Sand," Master of Science Thesis, Colorado State University, Fort Collins, Colorado, pp. 145-154.

Ivanov, P.L. (1967), "Compaction of Noncohesive Soils by Explosions," Izdatel'stvor Literatury Po Stroitel'stvu, Leningrad, U.S.S.R., Translated by the Indian National Scientific Documentation Center, New Delhi, India; Published for the U.S. Department of the Interior, Bureau of Reclamation and National Science Foundation, Washington, D.C., 211 p.

Ivanov, P.L. and Sinitsyn, A.P. (1977), "Soil Liquefaction and Stability of Foundation," Proceedings of the Ninth International Conference on Soil Mechanics and Foundation Engineering, Vol. 2, Tokyo, Japan, pp. 265-268.

Jacobs, P. (1988), "Blast Induced Liquefaction of an Alluvial Sand Deposit," Master of Science Thesis, Colorado State University, Fort Collins, Colorado, 227 p.

Jones, G. (1976), "Complex Craters in Alluvium," Proceedings of the Symposium on Planetary Cratering Mechanics, U.S. Geologic Survey, Geologic Division Branch of Astrogeologic Studies, Flagstaff, Arizona, September, pp. 163-182.

Klonn, E.J., Garga, V.K. and Shukin, W. (1981), "Densification of Sand Tailings by Blasting," Proceedings of the Tenth International Conference on Soil Mechanics and Foundation Engineering, Stockholm, Sweden, Vol 3., Stockholm, Sweden, June 15-19, pp. 725-730.

Kok, L. (1977), "The Effect of Blasting in Water-Saturated Sands," Proceedings, 5th International Symposium on Military Applications of Blast Simulation, Stockholm, Sweden, May 23-26, pp. 7:6:1-7:6:10.

Kok, L. (1978), "Some Empirical Prediction on Blast-Induced Liquefaction," Transcripts of the International Workshop on Blast-Induced Liquefaction, Maidenhead, U.K., Dames & Moore/U.S. Air Force, September 17-19, pp. 408-444.

Kummeneje, O. and Eide, O. (1961), "Investigation of Loose Sand Deposits by Blasting," Proceedings 5th International Conference on Soil Mechanics and Foundation Engineering, Paris, France, Vol. 1, July, 17-22, pp. 491-497.

Lambe, W.T. and Whitman, R.V. (1969), "Soil Mechanics," John Wiley and Sons, New York, New York, 553 p.

Langley, N.P., Smith, C.R. and Pfefferle, W. (1972), "DIAL PACK Event Soil Pore Pressure and Shear Strength Test," Aerospace Report No. TOR-0172 (S2970-20)-1, The Aerospace Corporation, San Bernardino, California, Space and Missile Systems Organization, U.S. Air Force Systems Command, Los Angeles, California, February, 139 p.

Long, H., Ries, E.R., and Michalopoulos, A.P. (1981), "Potential for Liquefaction Due to Construction Blasting," Proceedings, International Conference on Recent Advances in Geotechnical Engineering and Soil Dynamics, University of Missouri-Rolla, St. Louis, Missouri, April 26 - May 3, pp. 191-194.

Lyakhov, G.M. (1961), "Shock Waves in the Ground and the Dilution of Water Saturated Sand," Zhurnal Prikladnoy Mekhanik i Tekhnicheskoy Fiziki, Moscow, U.S.S.R, No. 1, pp. 38-46.

Marcuson, W., Krinitzsky, E., and Kovanic, E. (1977), "Earthquake Analysis of Fort Peck Dam, Montana," Proceedings of the Ninth International Conference on Soil Mechanics and Foundation Engineering, Vol. 2, Tokyo, Japan, pp. 287-292.

Marti, J. and Cundall, P. (1978), "Discrete Particle Approach," Transcripts of the International Workshop on Blast-Induced Liquefaction, Dames and Moore/U.S. Air Force, Maidenhead, United Kingdom, September 17-19, pp. 308-330.

Maslov, N. and Ivanov, P.L. (1985), "Liquefaction Conditions for Saturated Cohesionless Soils," Proceedings of the Eleventh International Conference on Soil Mechanics and Foundation Engineering, Vol. 4, pp. 1905-1908.

McCracken, J. (1978), "Introduction," Transcripts of the International Workshop on Blast-Induced Liquefaction, Dames and Moore/U.S. Air Force, Maidenhead, United Kingdom, September 17-19, pp. 24-55.

Melzer, S. (1978), "Blast-Induced Liquefaction of Materials," Nuclear Technology Digest, AFWL-TR-78-110, Air Force Weapons Laboratory, Kirtland Air Force Base, New Mexico, August, pp. 21-38.

Miklowitz, J. (1978), "The Theory of Elastic Waves and Wave Guides," Series in Applied Mathematics and Mechanics, Vol. 22, North-Holland Publishing Company, Amsterdam, New York, Oxford, pp. 277-290.

Mulilis, J., Seed, H.B., Chan C., Mitchell, J , and Arulanandan, K. (1977), "Effects of Sample Preparation on Sand Liquefaction," Journal of the Geotechnical Engineering Division, American Society of Civil Engineers, Vol. 103, No. GT 2, February, pp. 91-108.

Neeter, J. and Wasserman, W. (1974), "Applied Linear Statistical Models," Richard D. Irwin, Inc., Homewood, Illinois, 842 p.

Nemat-Nasser, S. and Takahashi, K. (1984), "Liquefaction and Fabric of Sand," Journal of the Geotechnical Engineering Division, Vol. 110, No. 9, American Society of Civil Engineers, September, pp. 1291-1306.

Nishiyama, H., Yahagi, K., Nakagawa, S., and Wada, K. (1977), "Practical Method of Predicting Sand Liquefaction," Proceedings of the Ninth International Conference on Soil Mechanics and Foundation Engineering, Tokyo, Japan, Vol. 2, pp. 305-308.

Peck, R.B. (1979), "Liquefaction Potential: Science Versus Practice," Journal of the Geotechnical Engineering Division, American Society of Civil Engineers, Vol. 105, No. GT 3, March, pp. 393-398.

Perry, E.B. (1972), "Movement of Variable Density Inclusions in Wet Sand Under Blast Loading," Miscellaneous Paper S-72-37, U.S. Army Corps of Engineers, Waterways Experiment Station, Vicksburg, Miss., September, 59 p.

Prakash, S. (1981), "Soil Dynamics," McGraw Hill Book Co., New York, pp. 320-328.

Prakash, S. and Gupta, M.K. (1970), "Blast Tests at Tenughat Dam Site," Journal of the Southeast Asian Society of Soil Engineering, Southeast Asian Society of Soil Engineers, Bangkok, Thailand, Vol. 1, No. 1., June, pp. 41-85.

Prater, E.G. (1977), "Pressure Wave Propagation in a Saturated Soil Layer with Special Reference to Soil Liquefaction," Proceedings, 5th International Symposium on Military Application of Blast Simulation, Royal Swedish Fortifications Administration, Stockholm, Sweden, pp. 7:3:1-7:3:23.

Prugh, B.J. (1963), "Densification of Soils by Explosive Vibrations," Journal of the Construction Division, American Society of Civil Engineers, Vol. 89, No. CO 1, March, pp. 79-100.

Puchkov, S.V. (1962), "Correlation Between the Velocity of Seismic Oscillations of Particles and the Liquefaction Phenomenon of Saturated Sand," Problems of Engineering Seismology, Issue No. 6, Edited by Prof. S.V. Medvedev, Translated from Russian by Consultants Bureau, New York, pp. 92-94.

Quaak, M.P. (1978), "Shock Tube Test at TNO," Transcripts of the International Workshop on Blast-Induced Liquefaction, Dames & Moore/U.S. Air Force, Maidenhead, United Kingdom, September 17-19, pp. 231-238.

Queiroz, L., Oliveira, H., and Nazario, F. (1967), "Foundation Treatment of Rio Casca III Dam," Proceedings, Ninth International Congress on Large Dams, Istanbul, Turkey, Vol. 1, September 4-8, pp. 321-333.

Richart, F.E., Hall, J.R. and Woods, R.D. (1970), "Vibrations of Soils and Foundations," Prentice-Hall, Englewood Cliffs, New Jersey, 414 p.

Rinehart, J.S. (1975), "Stress Transients in Solids," Hyperdynamics, Inc., Santa Fe, New Mexico, 230 p.

Rischbieter, F. (1977), "Soil Liquefaction-A Survey of Research," Proceedings, 5th International Symposium on Military Application of Blast Simulation, Royal Swedish Fortifications Administration, Stockholm, Sweden, May 23-26, pp. 7:1:1-7:1:24.

Rischbieter, F., Corvin P., Metz, K. and Schaepermeier, E. (1977), "Studies of Soil Liquefaction by Shock Wave Loading," Proceedings, 5th International Symposium on Military Application of Blast Simulation, Royal Swedish Fortifications Administration, Stockholm, Sweden, May 23-26, pp. 7:4:1-7:4:12.

Robertson, P. and Campanella, R. (1985), "Liquefaction Potential of Sands Using the CPT," Journal of the Geotechnical Engineering Division, American Society of Civil Engineers, Vol. 111, No. 3, March, pp. 384-403.

Ruygrok, P.A. and Van der Kogel, H. (1980), "Some Results of Impact Experiments on Nearly Saturated and Dry Sand," Proceedings, International Symposium on Soil under Cyclic and Transient Loading, Swansea, U.K., January, pp. 211-224.

Sanders, S.G. (1982), "Assessment of the Liquefaction Hazards Resulting from Explosive Removal of the Bird's Point New-Madrid Fuze Plug Levee," Misc. Paper No. GL-82-5, U.S. Army Corps of Engineering Waterways Experiment Station, Vicksburg, Mississippi, April, 32 p.

Schaepermeier, M.E. (1978a), "Soil Liquefaction Field Test in Meppen Proving Ground, 1978, Synoptic Paper," Proceedings of the 6th International Symposium on Military Applications of Blast Simulation, Cahors, France, pp. 7.4.1-5.

Schaepermeier, M.E. (1978b), "Soil Liquefaction Field Test in Meppen Proving Ground, 1978, Structure Response," Proceedings of the 6th International Symposium on Military Applications of Blast Simulation, Cahors, France, pp. 7.5.1-27.

Schaepermeier, M.E. (1978c), "A Semi-Empirical Method for the Prediction of the Stability of Buried Shelters by Groundshock-Induced Liquefaction," Transcripts of the International Workshop on Blast-Induced Liquefaction, Dames & Moore/U.S. Air Force, Maidenhead, United Kingdom, September 17-19, pp. 401-407.

Schaepermeier, M.E. (1978d), "Liquefaction Induced by Compressional Waves," Transcripts of the International Workshop on Blast-Induced Liquefaction, Dames & Moore/U.S. Air Force, Maidenhead, United Kingdom, September 17-19, pp. 57-64.

Schure, L. (1988), Personal Communication, Department of Civil Engineering, Colorado State University, Fort Collins, Colorado.

Seed, H.B. (1979), "Soil Liquefaction and Cyclic Mobility Evaluation for Level Ground During Earthquakes," Journal of the Geotechnical Engineering Division, American Society of Civil Engineers, Vol. 105, No. GT 2, February, pp. 201-255.

Seed, H.B. and Idriss, I.M. (1967), "Analysis of Soil Liquefaction: Niigata Earthquake," Journal of the Soil Mechanics and Foundations Division, American Society of Civil Engineers, Vol. 93, No. SM3, Proc. Paper 5233, May, pp. 83-108.

Seed, H.B., Mori, K., and Chan, C. (1977), "Influence of Seismic History on Liquefaction of Sands," Journal of the Geotechnical Engineering Division, American Society of Civil Engineers, Vol. 103, No. GT 4, April, pp. 257-270.

Sharpe, J.H. (1942), "The Production of Elastic Waves by Explosion Pressures, I. Theory and Empirical Field Observations," Geophysics, Vol. VIII, No. 2, April, pp. 144-154.

Solymar, Z., Iloabachie, B., Gupta, R. and Williams, L. (1984), "Earth Foundation Treatment at Jebba Dam Site," Journal of Geotechnical Engineering Division, American Society of Civil Engineers, Vol. 110, No. 10, October, pp. 1415-1431.

Studer, J. (1978a), "Laboratory and Field Shock Tube Tests," Transcripts of the International Workshop on Blast-Induced Liquefaction, Dames & Moore/U.S. Air Force, Maidenhead, United Kingdom, September 17-19, pp. 67-187.

Studer, J., and Hunziker, E. (1977), "Experimental Investigation on Liquefaction of Saturated Sand Under Shock Loading," Proceedings, 5th International Symposium on Military Applications of Blast Simulation, Royal Swedish Fortifications Administration, Stockholm, Sweden, May 23-26, pp. 7:2:1-9.

Studer, J. and Kok, L. (1980), "Blast-Induced Excess Porewater Pressure and Liquefaction: Experience and Application," Proceedings, International Symposium on Soils under Cyclic and Transient Loading, Swansea, United Kingdom, January 7-11, pp. 581-593.

Studer, J., Kok, L. and Trense, R.W. (1978), "Soil Liquefaction Field Test - Meppen Proving Ground 1978 Free Field Response," Proceedings of the 6th International Symposium on Military Applications of Blast Simulation, Cahors, France, pp. 7.3.1-7.3.18.

Tanimoto, K. (1967), "Liquefaction of Sand Layer Subjected to Shock and Vibratory Loads," Proceedings, 3rd Asian Regional Conference on Soil Mechanics and Foundation Engineering, Haifa, Israel, Vol. 1, September 25-28, pp. 362-365.

Terzaghi, K. (1956), "Varieties of Submarine Slope Failures," Proceedings, 8th Texas Conference on Soil Mechanics and Foundation Engineering, Special Publication No. 29, Bureau of Engineering and Foundation Research, University of Texas, Austin, Texas, September 14-15, pp. 24 and 39.

Timoshenko, S.P. and Goodier, J.W. (1970), "Theory of Elasticity," McGraw-Hill, New York, New York, 546 p.

Trense, R.W. (1977), "Soil Liquefaction - New Results from Dutch Tests," Proceedings, 5th International Symposium on Military Application of Blast Simulation, Royal Swedish Fortifications Administration, Stockholm, Sweden, May 23-26, pp. 7:5:1-6.

True, D.G. (1967), "A Study of Pore Pressure Propagation in Sand," Proceedings, International Symposium on Wave Propagation and Dynamic Properties of Earth Materials, University of New Mexico, Albuquerque, New Mexico, August 23-25, pp. 541-544.

True, D.G. (1969), "Dynamic Pore Pressure Propagation in Sand," Technical Report R-610, Naval Civil Engineering Laboratory, Port Hueneme, California, 45 p.

Vesic, A., Boutwell, G., and Tai, T.L. (1967), "Theoretical Studies of Cratering Mechanisms Affecting the Stability of Cratered Slopes," Technical Report No. 3-699, Report No. 6, Phase III, Engineering Properties of Nuclear Craters, Final Report on Research by U.S. Army Nuclear Cratering Group and U.S. Army Corps of Engineers Waterways Experiment Station, Vicksburg, Mississippi, March, 140 p.

Veyera, G.E. (1985), "Transient Porewater Pressure Response and Liquefaction in a Saturated Sand," Ph.D. Dissertation, Colorado State University, Fort Collins, Colorado, Fall, 198 p.

Wu, S., Gray, D.H., and Richart, F.E. (1984), "Capillary Effects on Dynamic Modulus of Sands and Silts," Journal of Geotechnical Engineering, Vol. 110, No. 9, September, pp. 1188-1203.

Yamamura, K. and Koga, Y. (1974), "Estimation of Liquefaction Potential by Means of Explosion Test," Proceedings, 6th Joint Panel Conference of U.S. - Japan Cooperative Program in Natural Resources, National Bureau of Standards, Washington, D.C., Vol. 76, May, pp. III-38-51.

Youd, T. (1977), "Packing Changes and Liquefaction Susceptibility," Journal of the Geotechnical Engineering Division, American Society of Civil Engineers, Vol. 103, No. GT 8, August, pp. 918-922.

APPENDIX A

SITE INVESTIGATION RESULTS

A.1 DESCRIPTION

To accomplish the experimental work described in this dissertation, a test site was investigated and developed at Colorado State University. The site is located west of Fort Collins, Colorado, at the Engineering Research Center (Figure A.1). It consists of a 0.6-hector plot of grazing land in a valley about 0.8 kilometers (km) wide. The average elevation is 1,570 m above sea level. A small stream runs adjacent to the site and feeds College Lake, about 150 m to the south. Horsetooth Reservoir, elevation 1680 m, is about 0.8 km west of the site. A photograph of the site is shown in Figure A.2

Electric power is available from a transformer on a major North-South power line located to the west of the test site. Potable water is not available. The nearest structures are the Engineering Research Center hydromachinery laboratory about 120 m to the northeast; a hydraulic test flume building about 100 m to the southeast, and outdoor hydraulic test flumes about 60 m to the east.

A.2 GEOLOGY

The test site is in a relatively flat bottomed valley between the Niobrara Formation on the east and the South Platte Formation of the Dakota Group to the west. The Niobrara Formation is a Smokey Hill Shale, a chalky shale and limestone, and Fort Hays Limestone. The
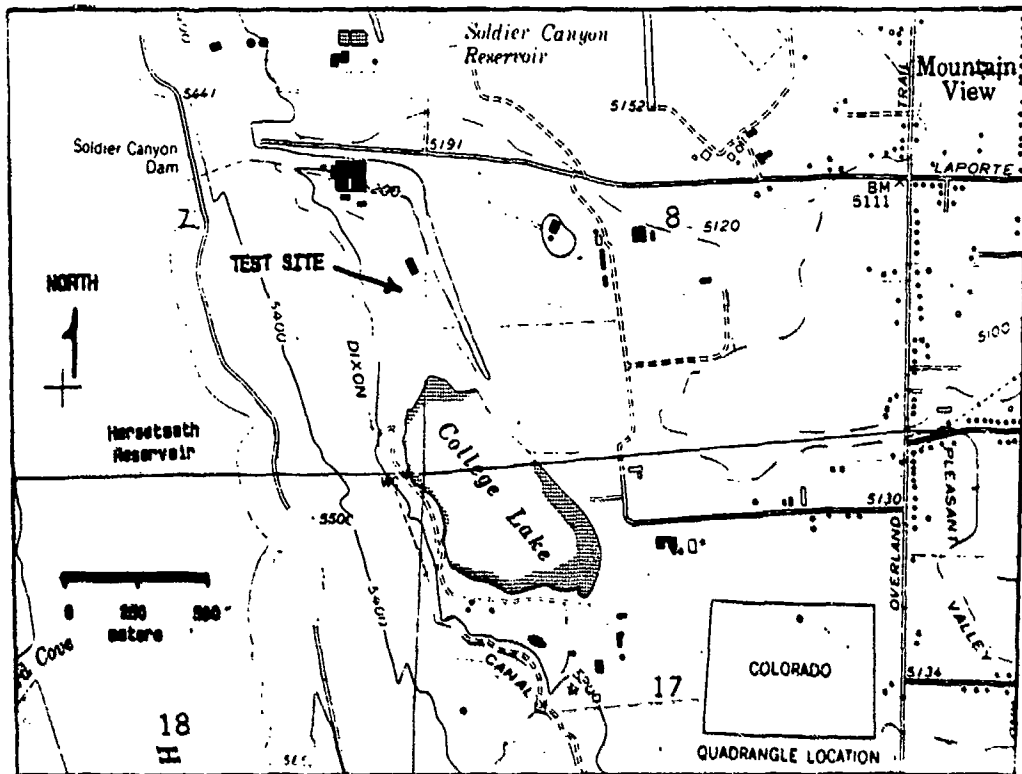
Figure A.1 U.S. Geological Survey map of site area (Horsetooth Reservoir, Colorado).

Figure A.2 Site seen from east before construction.

South Platte Formation consists of well-sorted, fine grained, cross-stratified ripple laminated sandstone, siltstone and shale (Colton, 1978 and Harvey, 1986). The valley appears to consist in part of alluvial deposits from the small stream as evidenced by the presence of bouldery to pebbly sandy silt and clay. There is also evidence of colluvial deposits from the formation to the west of the valley. Evidence is that the site is between what appears to be past debris flows that came from the South Platte Formation. In these debris flow areas, boulders of up to several meters in diameter are predominant on the surface and probably at depths of many meters. There is no evidence of boulders within the confines of the test site.

A.3   SEISMOGRAPH SURVEY

As part of the site investigation, a seismic refraction study was performed and bore holes were drilled to better understand the subsurface geologic features. The seismograph used was a Nimbaus ES-125, Single Channel Signal Enhancement Seismograph, by E.G.& G. Geometrics. To perform the refraction study, an elastic pulse was generated in the soil by applying a blow to the surface of the soil with a sledge hammer striking a steel plate on the ground surface. The blow triggered the seismograph, and geophores detected the resulting ground motion at known distances from where the pulse was input. With this method, the compression wave velocities of the soil layers were obtained. Interpretation of the data permitted estimates of the depths to the subsurface features. A description of the

methodology for data collection and analysis is given in the seismograph manual and in Griffiths and King (1976).

Six refraction lines were run during the seismograph study and three bore holes were drilled (Figure A.3). The lengths of the seismograph lines varied from 15 to 52 meters. The bore holes were drilled with a hand auger to depths of approximately 6 meters. The results, shown in Figure A.4 with an interpretation of these results in Figure A.5, indicated a ground water table at a depth of approximately 3.7 m. The soil appears to be predominantly bentonite clay to about 5.5 m under which there is a folded series of shale layers. The bedrock is estimated to be at a depth of 8 to 9 m, and is probably sandstone from the Dakota Group.
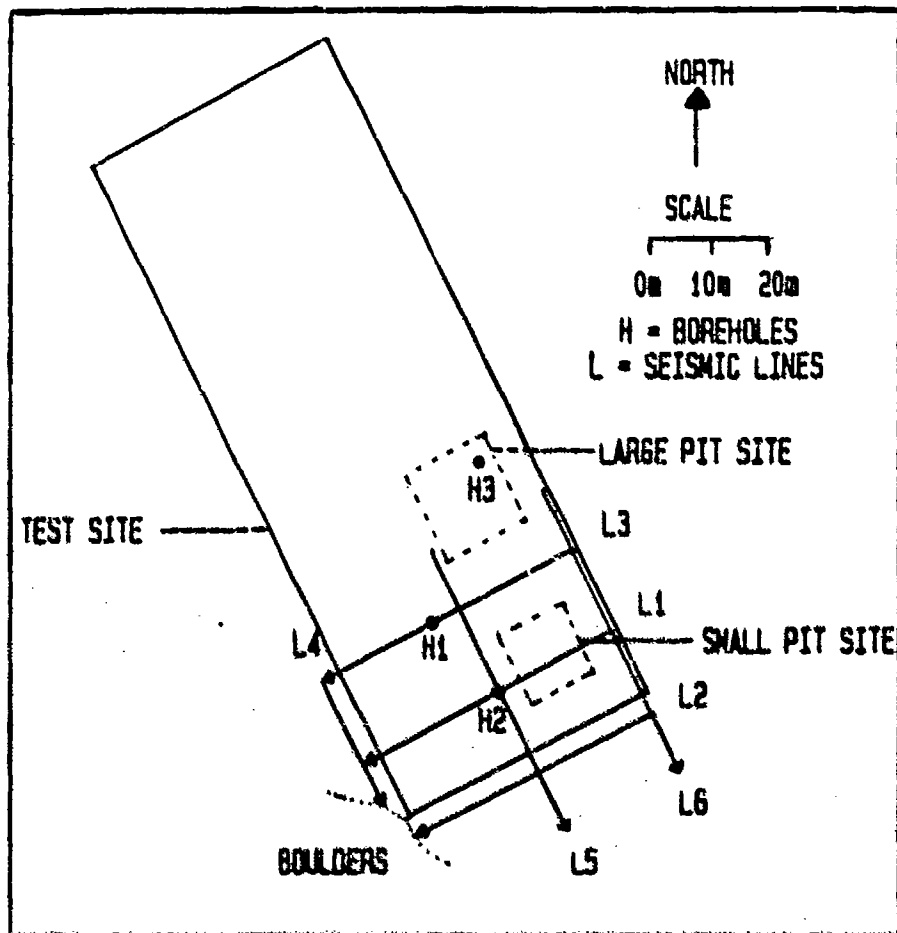
Figure A.3 Locations of seismic lines and boreholes.
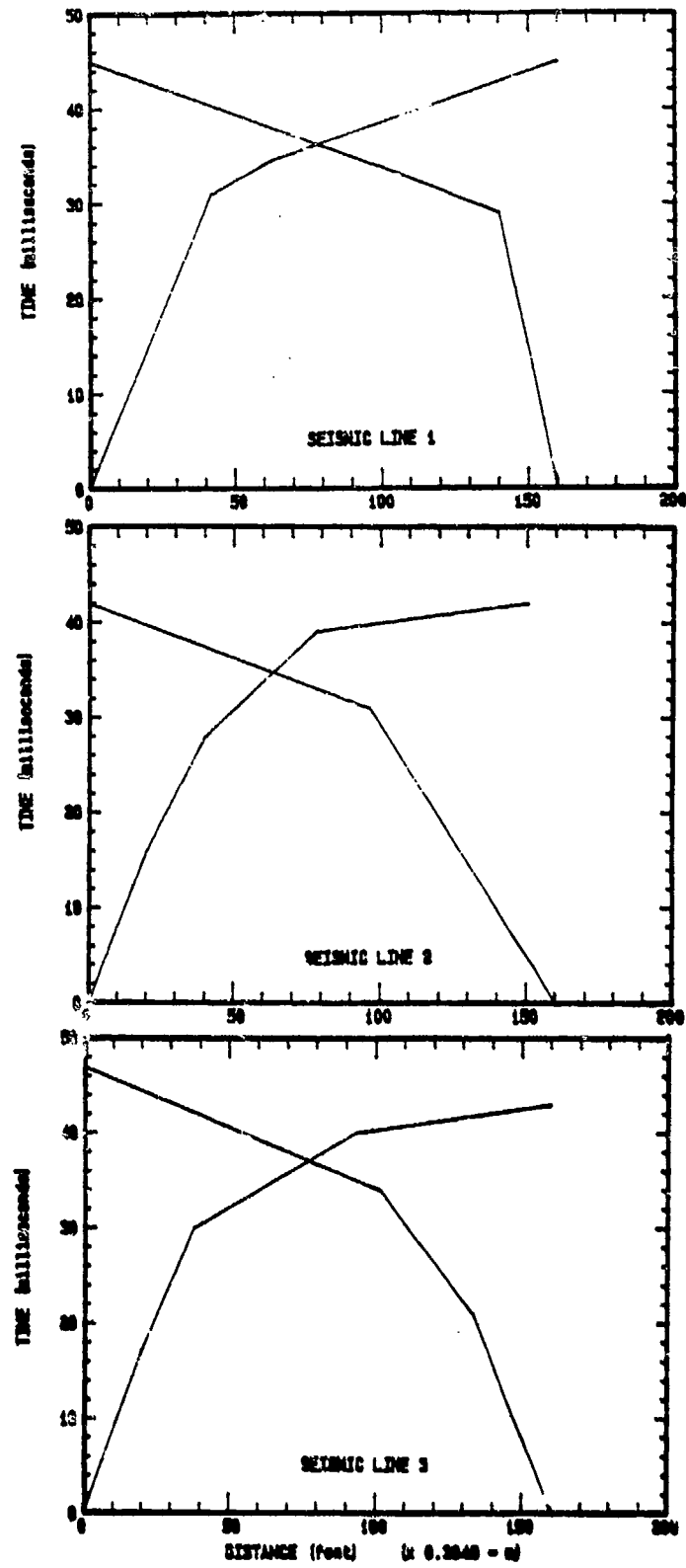
Figure A.4 Seismograph results.
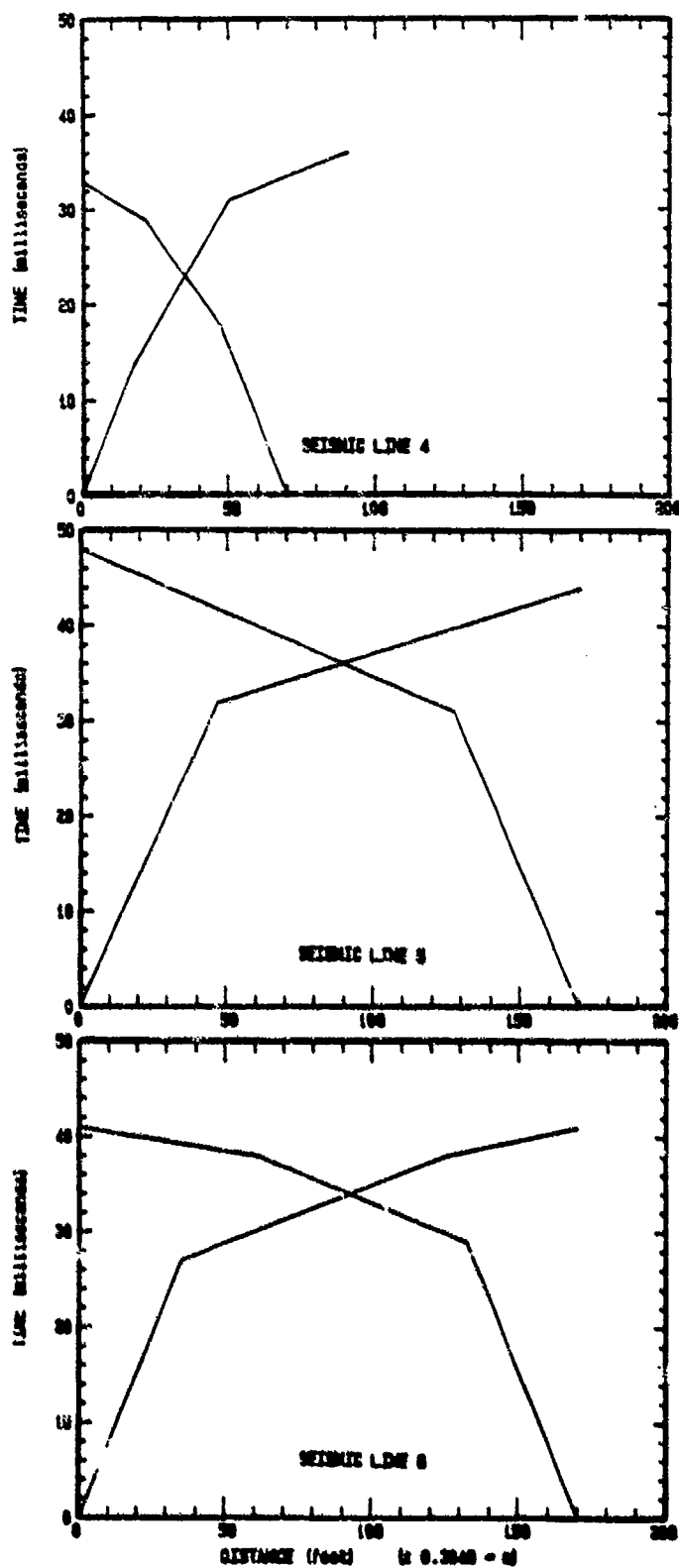
Figure A.4 (continued) Seismograph results.
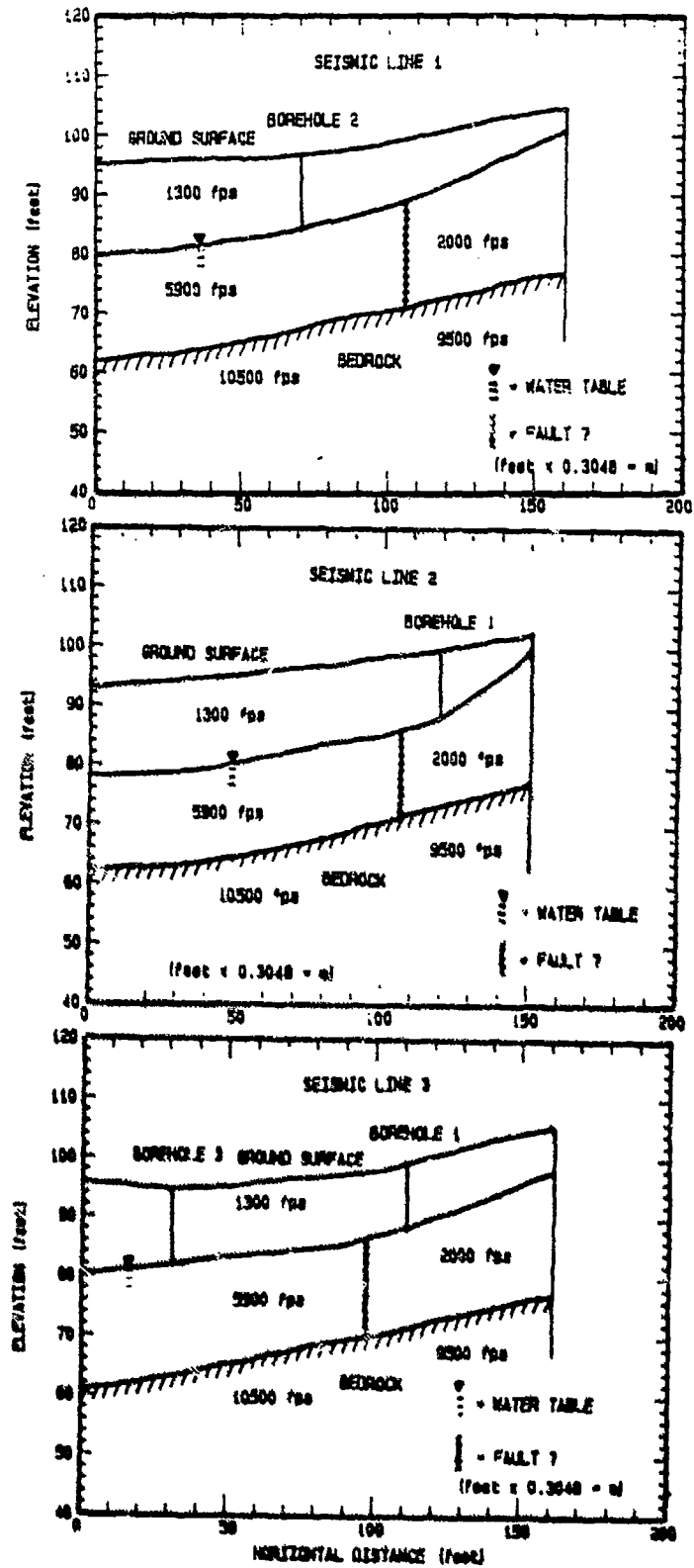
Figure A.5   Interpretation of seismograph and borehole results.
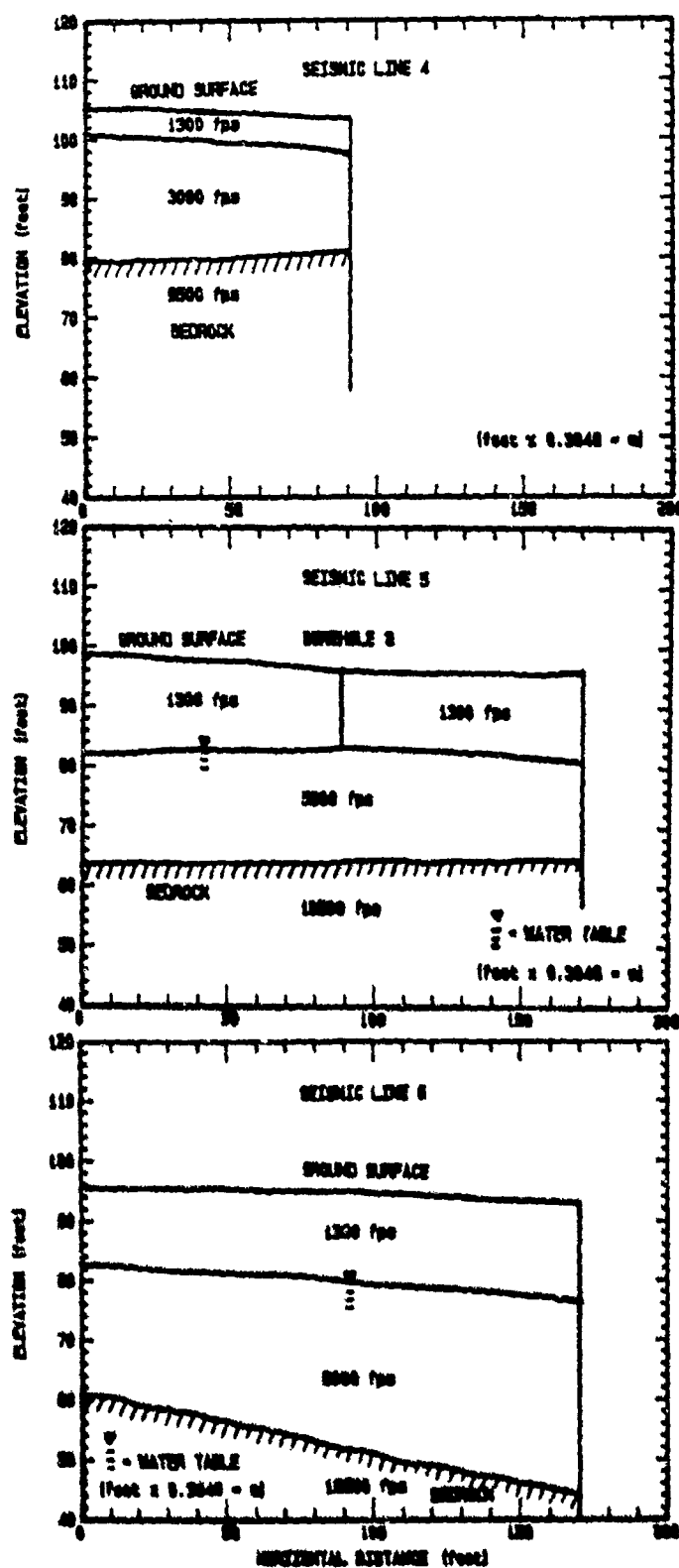
Figure A.5 (continued)   Interpretation of seismograph
and borehole results.

APPENDIX B

TEST SITE DEVELOPMENT

B.1   INTRODUCTION

Site development included excavation of test pits, construction of facilities, and placement of power and cable lines. Also included was construction of an access road and a security fence.

Three test pits were excavated at the test site for explosives testing below the ground level. The largest of these pits (Figure B.1) was 15.2 m square at the ground surface and 5.9 m deep. The four sides were sloped at a 1:1 angle from the surface to the bottom of the pit. The second pit was 12.8 m square at the ground surface, 7 m deep, and also sloped at 1:1. The third pit was 4.6 m square at the surface, 3 m deep and had nearly vertical sides. The first two pits extended through the water table which was at the 3.7 m level. The third pit was above the water table. The soil that was excavated from the pits was free of boulders and rocks and consisted of clay, with some shale evident at the 5.5 m level.

A water treatment facility (Figure B.2) was constructed to de-air and store water used for saturating the test sand. This facility included a 2.4 by 3.7 m wooden building on a 10 cm thick concrete slab and a 19,000 liter (1) stainless steel water storage tank. A 460 l commercial water heater (Figure B.3) and a water vacuum system were located in the building. Section B.3 provides a detailed
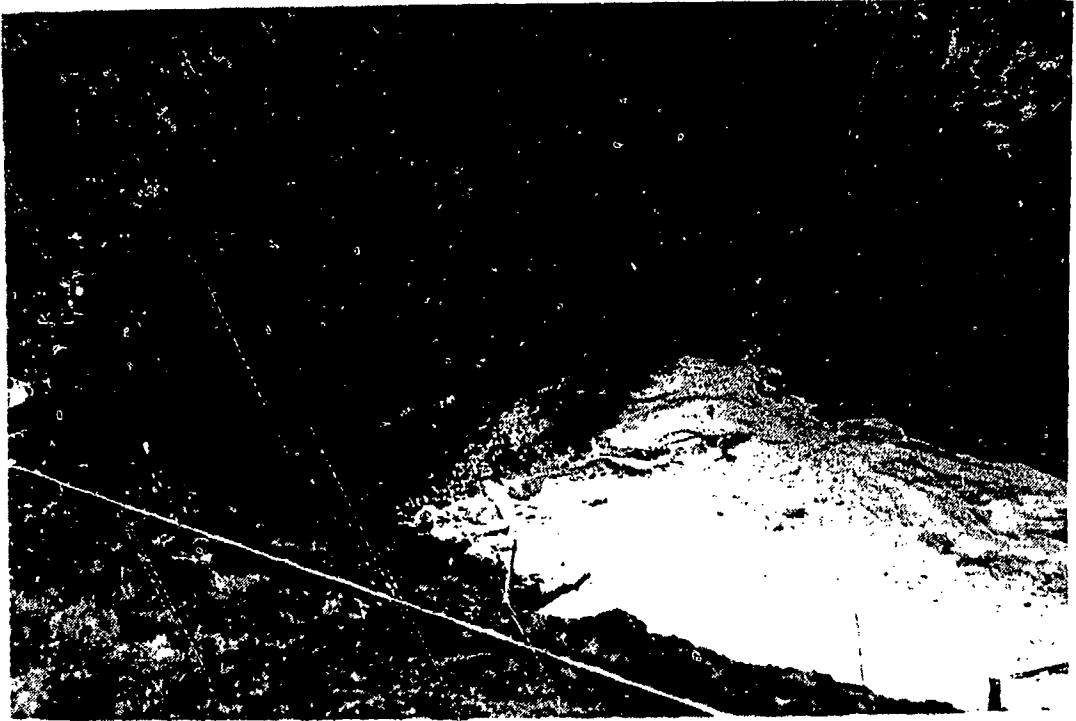
Figure B.1 Large pit.

Figure B.2 Water treatment facility.
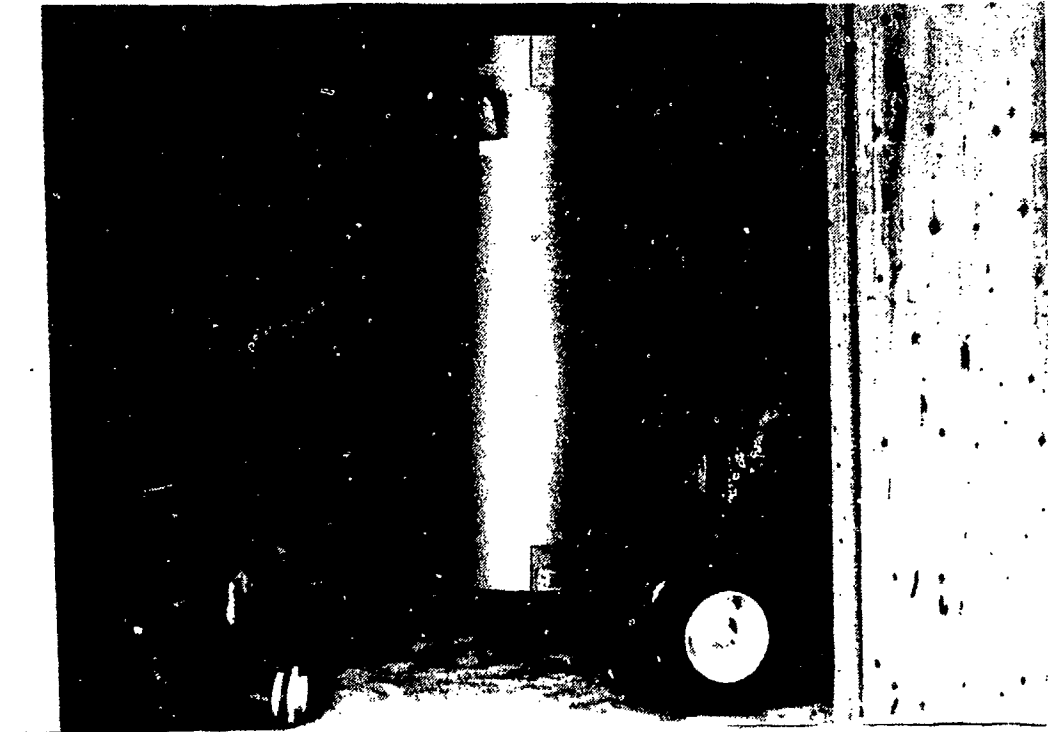
Figure B.3 Commercial water heater.

description of the water treatment system. Electric power was supplied to this structure via an underground line along the west edge of the site.

The instrumentation relay building (Figure B.4) was a 1.2 m square wooden structure on a 10 cm thick concrete slab. The building housed the instrumentation signal conditioners and power supplies. The cabling from the instrumentation in the test pit was routed to this building. Electric power from an uninterruptible power supply (UPS) was provided at this building through an underground line on the far eastern boundary of the site.

The command post (Figure B.5) was a 6.7 by 2.4 m salvaged U.S. Army mobile missile tracking station. It was a totally enclosed, magnesium structure placed on a 10 cm thick concrete slab. This
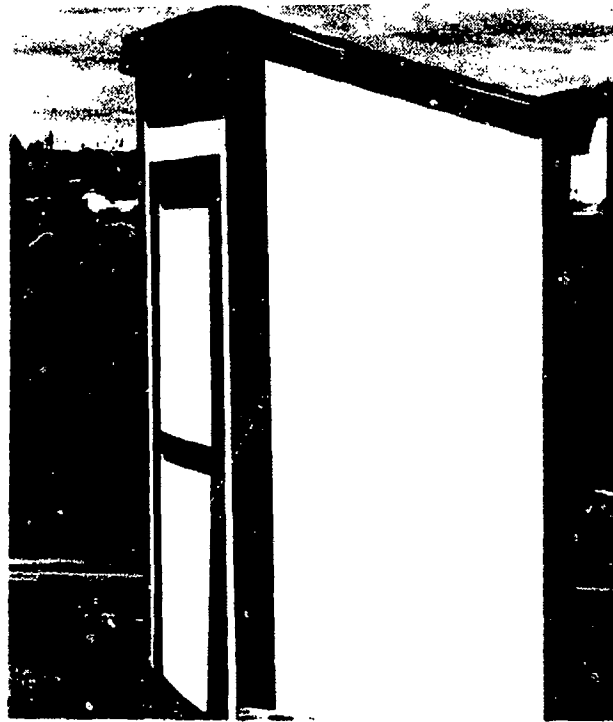
Figure B.4   Instrumentation relay building.

Figure B.5   Command post and garage.

structure was the nerve center of testing operations since it housed the transient data recorders and personal computer system. Power (110 VAC) was furnished to the command post underground from the main power pole at the northwest corner of the site. The electric power for the computer, data recording systems, and instrumentation relay building was through the UPS located in the structure.

Two storage facilities were erected at the site. One was a single-car garage located next to the command post. The other was a second salvaged missile tracking station.

In addition to the above facilities, a network of underground trenches was dug at a depth of 75-90 cm for placement of electric power lines. A separate trench from the instrumentation relay building to the command post contained an 8 cm polyvinyl chloride (PVC) conduit for instrumentation cabling. The cabling was accessible at three points between the relay building and the command post through manholes (Figure B.6).

B.2   TEST BED

The largest of the previously mentioned pits was selected for all testing in this program. The test scenario called for detonation of explosives in water above a saturated sand test bed in a steel tank at the bottom of the pit. This procedure maximized control over the test sand and minimized debris and noise hazards during blasting. The following paragraphs describe the large test pit and the installation of the steel tank.

The first step in preparing the pit was to construct a foundation for the steel tank. The groundwater was pumped out, and geotextile filter fabric was laid on the clay at the bottom of the

Figure B.6   Manhole and cabling conduit.

pit. A 30 cm layer of uniform gravel was placed on the filter fabric,
and then another piece of filter fabric was laid on this gravel.
Masonry sand was then placed on the second piece of filter fabric to a
thickness of 15 cm.

The next step was installation of a pond liner, Geogard^R,
furnished by Engineered Geotextile Products, Inc. The purpose of this
impermeable liner was to provide side slope stability in the pit and
to minimize groundwater movement. The liner, which was 22.9 m square,
was pulled across the pit with ropes. It was anchored by placing soil
over the four edges. A circular section was cut from the center of
the liner to prevent its floating due to groundwater.

Once the tank foundation and the liner were in place, the
steel tank was lowered into the pit. The tank was an open-ended

cylinder, 4.27 m in diameter by 1.83 m high (Figure B.7). The top of the tank was located at the water table level. This placement was selected to minimize reflections during testing since the native soil around the tank was saturated and had an acoustic impedance approximately the same as saturated sand.

A 30 cm thick layer of bentonite was placed around the bottom of the tank to minimize water movement. Water was added around the tank over the bentonite, and masonry sand was poured into the water to the level of the top of the tank. A concrete vibrator was used to densify the sand and force air out.

To provide control of groundwater movement through the sand and gravel into the steel tank, an 8 cm diameter PVC pipe was embedded in the sand on which the tank rested. This pipe was perforated every 15 cm with 9.5 mm holes. It was wrapped with filter fabric to prevent sand entry. At the inner edge of the tank, the PVC pipe was connected to a 2.5 cm vertical steel pipe. A check valve was installed at the lower end of the steel pipe, and the upper end above the tank was fitted with a pump connection. To further control ground movement, a round section of pond liner cut to the diameter of the tank was placed on the sand at the base of the tank.

A saturation pipe network (Figure B.8) was next placed at the bottom of the tank. The saturation pipes were 5.1 cm diameter PVC and were formed into a rectangular grid. These pipes were perforated at 15 cm intervals with 9.5 mm holes. Attached to this network were two vertical 1.9 cm steel pipes on opposite sides of the tank. These pipes were fitted with garden hose connections for later delivery of desired water from the water treatment facility.
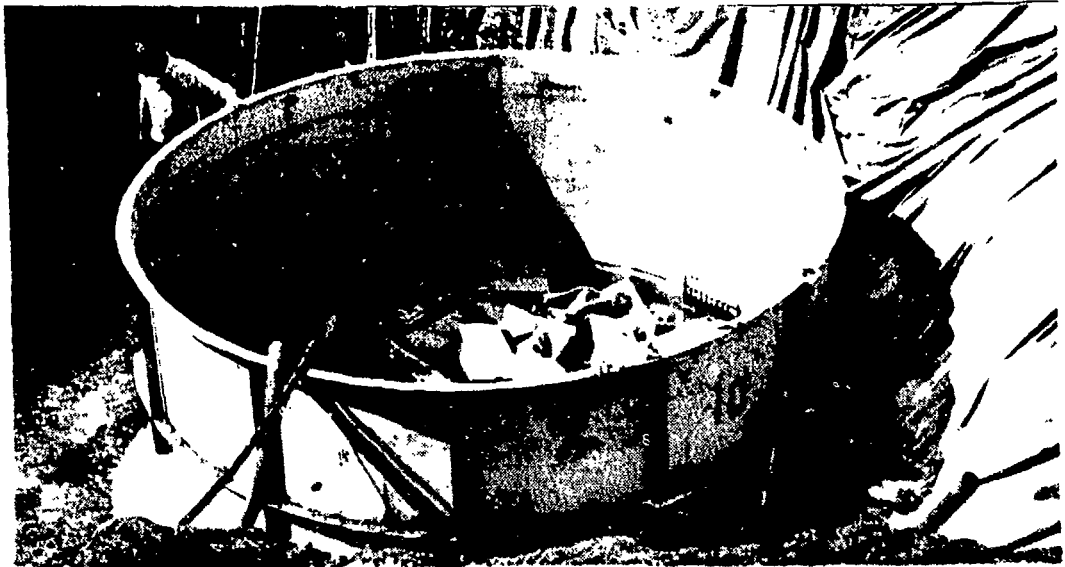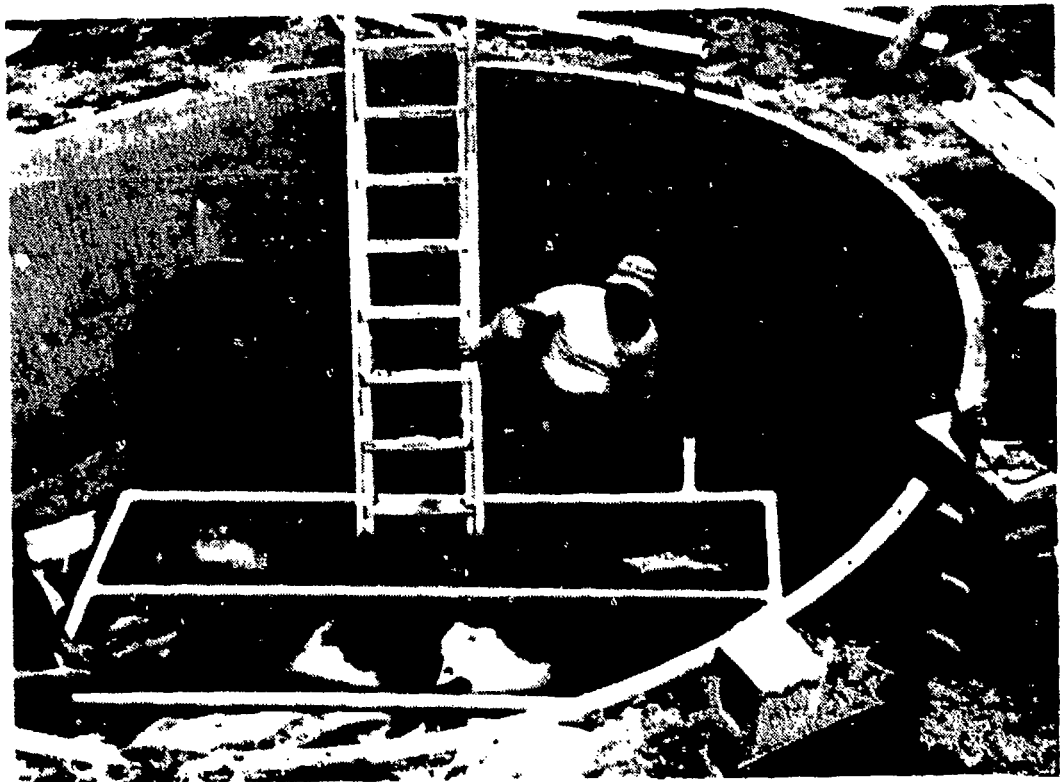
Figure B.7 Test tank in large pit.

Figure B.8 Saturation pipe network.

Uniform 1.9 cm gravel was placed around the saturation pipes to a thickness of 10 cm (Figure B.9). This gravel would permit an even flow of deaired water from the pipes into the test sand above the pipes. A layer of filter fabric was placed over the gravel to prevent sand migration into the gravel and pipes.

In addition to the above preparations, a wooden fence was built around the tank. This fence was used to suspend planar explosives above the sand in the tank (for another research project). The fence consisted of 10 cm wooden posts with concrete footings and 2x4 wooden railings.

B.3   WATER DEAIRING SYSTEM

To permit full saturation of the test sand, a water deairing system was constructed. The purpose of this system was to remove undissolved air from locally available water. Water and air are generally immiscible except for approximately two percent (by volume) of undissolved air which exists within the water (Butler, 1986). The deairing system consisted of a commercial water heater, a vacuum tank, a storage tank, and a series of pipelines. The heater was a Dayton commercial water heater with a capacity of 460 l and a recovery rate of 400 l to heat to 63 degrees Centigrade (^{o}C) per hour. The water was actually heated to about 65 ^{o}C. The vacuum system consisted of a steel vacuum tank, where hot water was subjected to approximately 38 cm of mercury vacuum. To store the deaired water, a 19,000 l stainless steel tank was used. Figures B.2 and B.3 are photographs of the water storage tank and the commercial hot water heater in the building next to the tank.
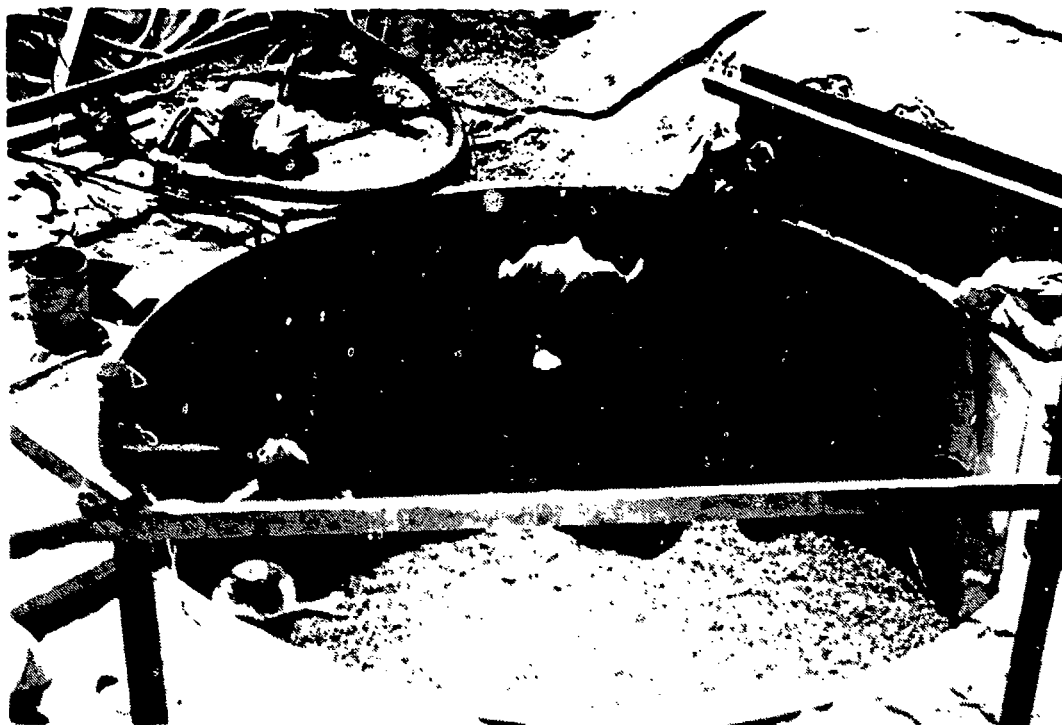
Figure 8.9   Placing gravel around saturation pipe.

The procedure for using the water deairing system is explained
by referring to the schematic in Figure 8.10. Locally available water
is pumped into the system through the inlet valve shown. The water is
routed through the heater and vacuum chamber for removal of air. Once
the air is removed, the water is transferred to the storage tank. A
number of by-pass lines, shown in the schematic, were installed to
permit movement of water through any combination of the heater, vacuum
chamber, or storage tank. This system permits supply of a continuous
flow of deaired water or storage of deaired water for later use.
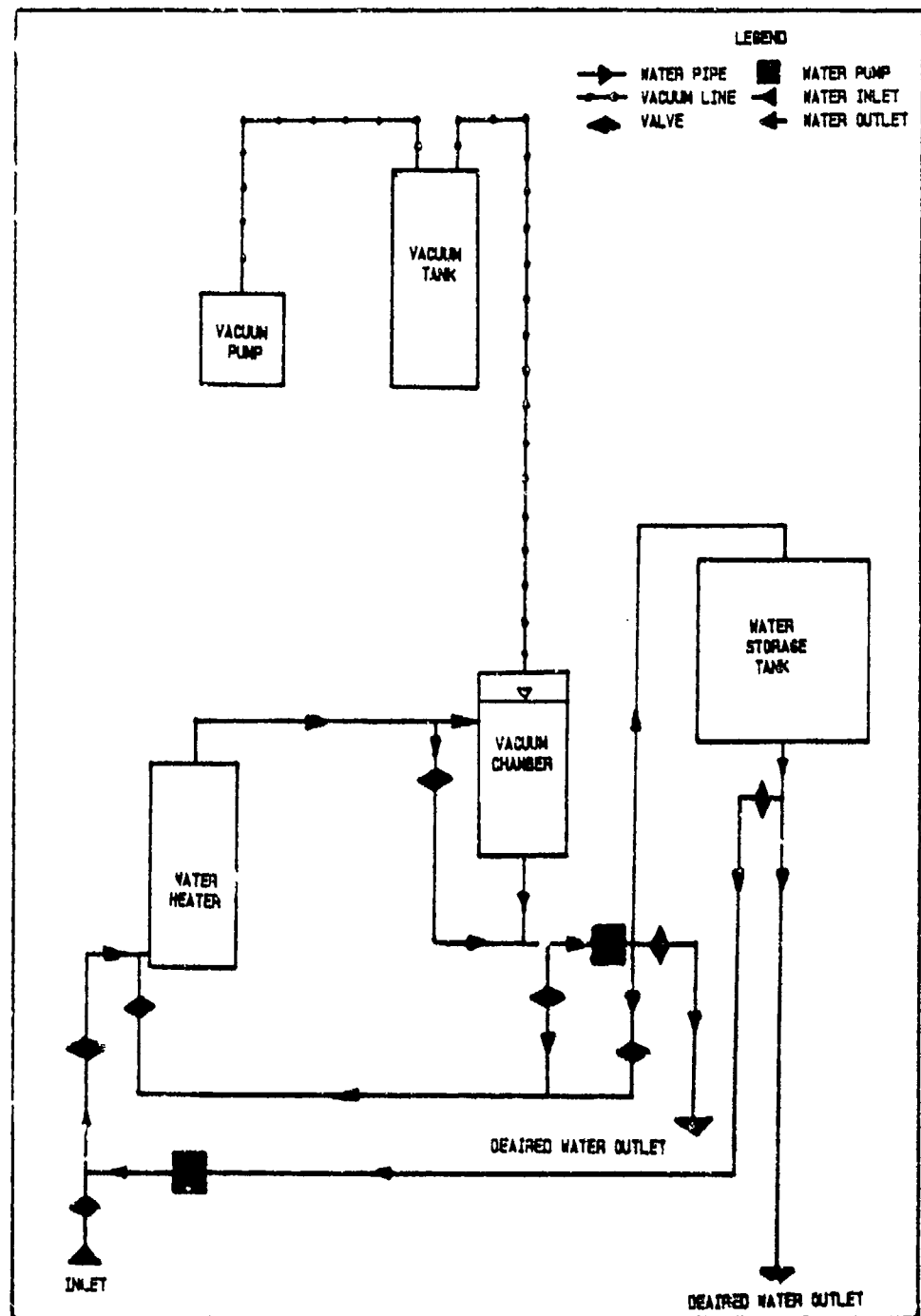
Figure B.10 Schematic of water deairing system.

APPENDIX C

TEST INSTRUMENTATION

C.1   INTRODUCTION

The instrumentation used in the experimental program is described in detail in this appendix. The instrumentation included accelerometers, pressure transducers, total stress gages, strain gages, and a vibration monitor. A piezometer system was also used in conjunction with a video cassette recorder. Figure C.1 is a schematic showing the relationships among the above devices, and each of the devices is discussed in detail below.

C.2   PORE PRESSURE TRANSDUCERS

Modified piezoresistive pressure transducers (ENDEVCO Model 8511a-5KM1) were used to measure transient porewater pressures. The specifications for these transducers are shown in Table C.1 and Figure C.2. Figure C.3 is a photograph of a transducer. Two modifications were necessary to permit use of these transducers. The first, performed by the manufacturer, was the mounting of a 1 mm thick, stainless steel circular plate over each transducer's diaphragm. This plate was perforated with small holes in a star shaped pattern to permit passage of water but to prevent soil grains from entering. The space between the plate and the diaphragm was filled with silicon oil. With this arrangement, the only transient stresses acting on the
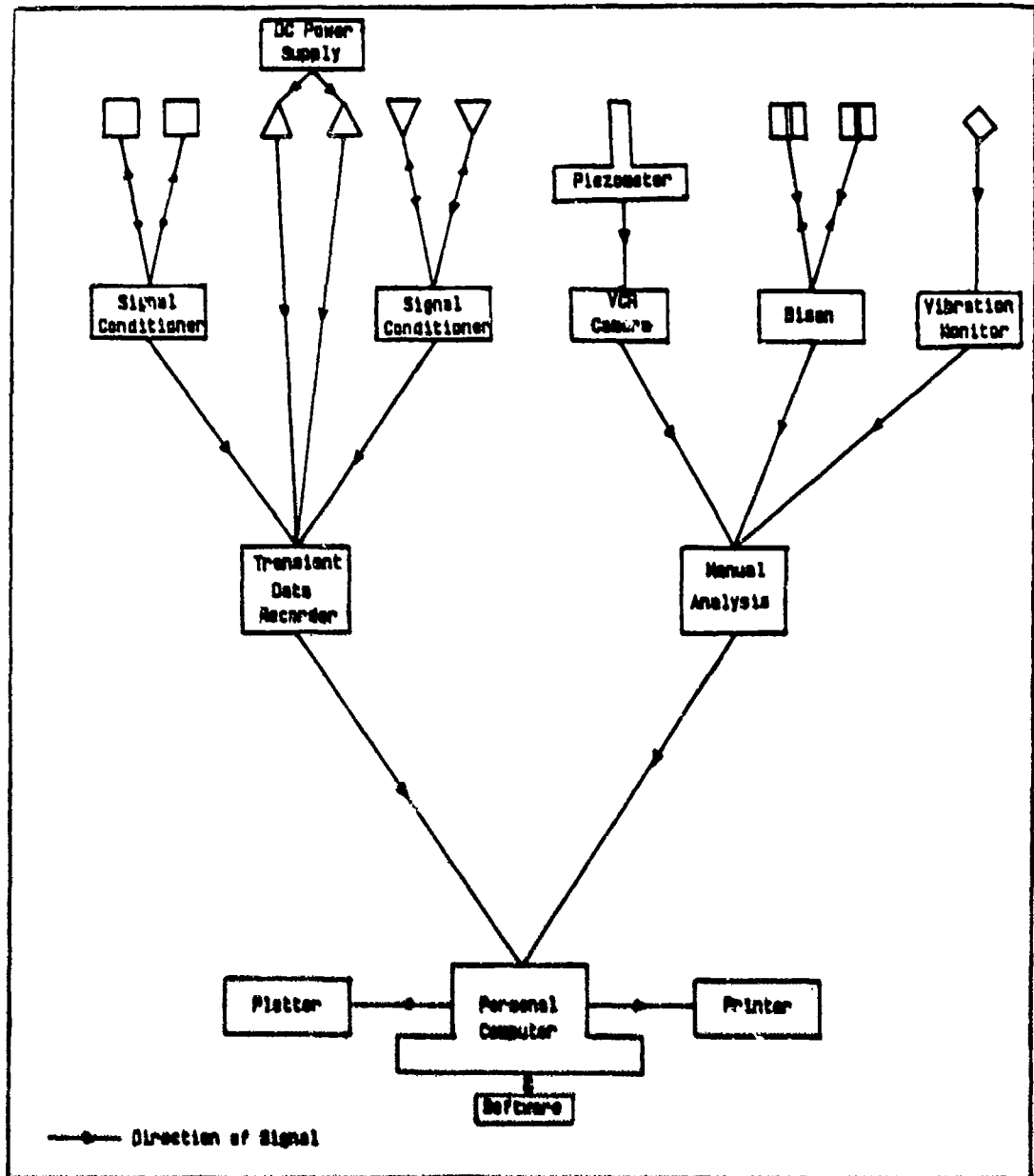
Figure C.1 Schematic of instrumentation system.
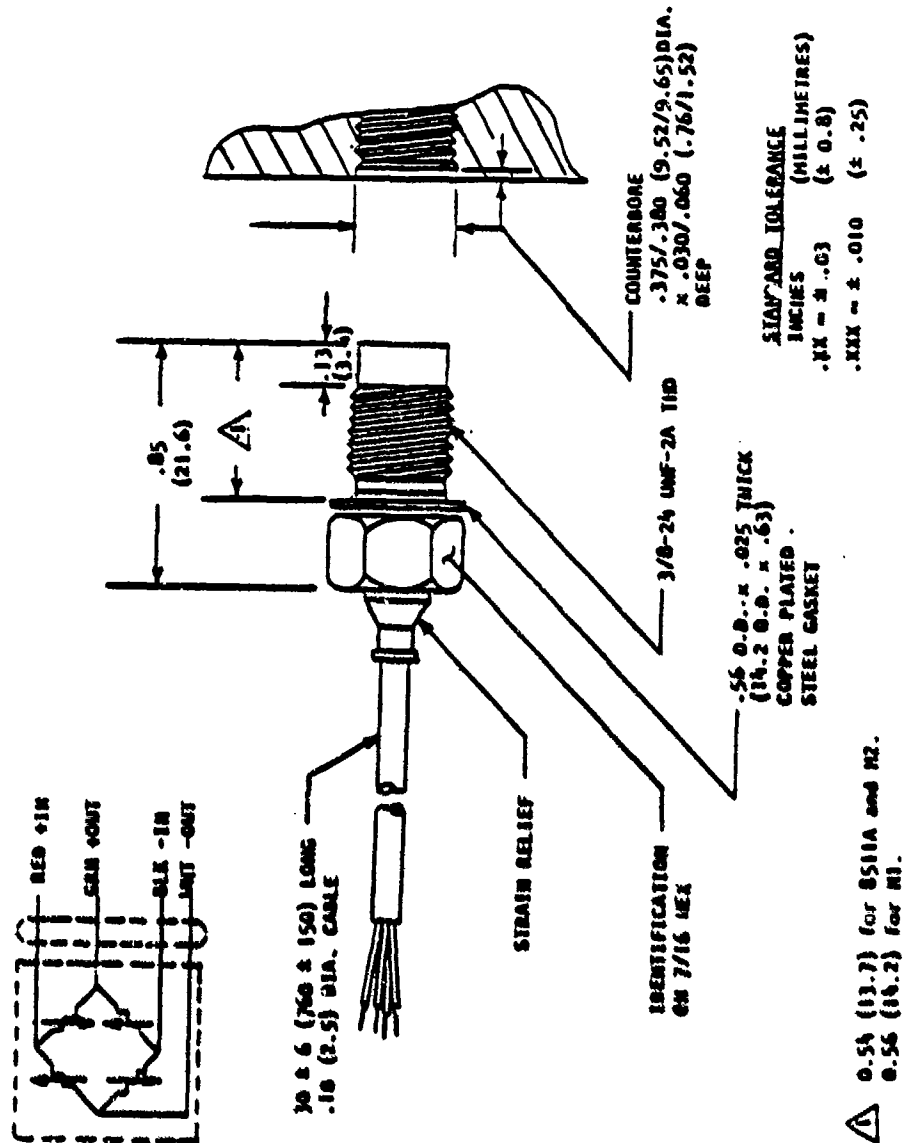
Table C.1. ENDEVCO Model 8511a-5KM1 Pressure Transducer

Specifications

Range	(0-34,450 kPa - gage)
Sensitivity @ 10VDC	(0.015 ± .004 mV/kPa)
Resonant Frequency	greater than 1 Megahertz
Linearity	± 0.3% Full Scale Output (FSO)
Hysteresis	0.3% FSO
Repeatability	0.3% FSO
Zero Measurand Output	± 10 mV @ 75°F and 10.00 VDC
Zero Shift @ 3X Range	± 0.1% of 3X FSO
Zero Shift with Temperature	± 3% FSO (maximum)
Sensitivity Shift with Temperature	± 4% FSO (maximum)
Warmup Time	15 seconds
Burst Pressure	(137,800 kPa) minimum
Temperature Range, Compensated	-18°C to 93°C
Vibration	1000g, sinusoidal
Shock	20000g, 100microsec pulse duration
Excitation Voltage	10.00 VDC, 18 VDC maximum
Polarity Output	Positive for increasing pressure
Input Resistance	1600 ohms
Output Resistance	1300 ohms
Insulation Resistance	100 megaohms
Cable	Integral, 4 conductor, shielded teflon insulated conductors
Weight	11 gm

Figure C.2   Porewater pressure transducer diagram (ENDEVCO specification sheet).
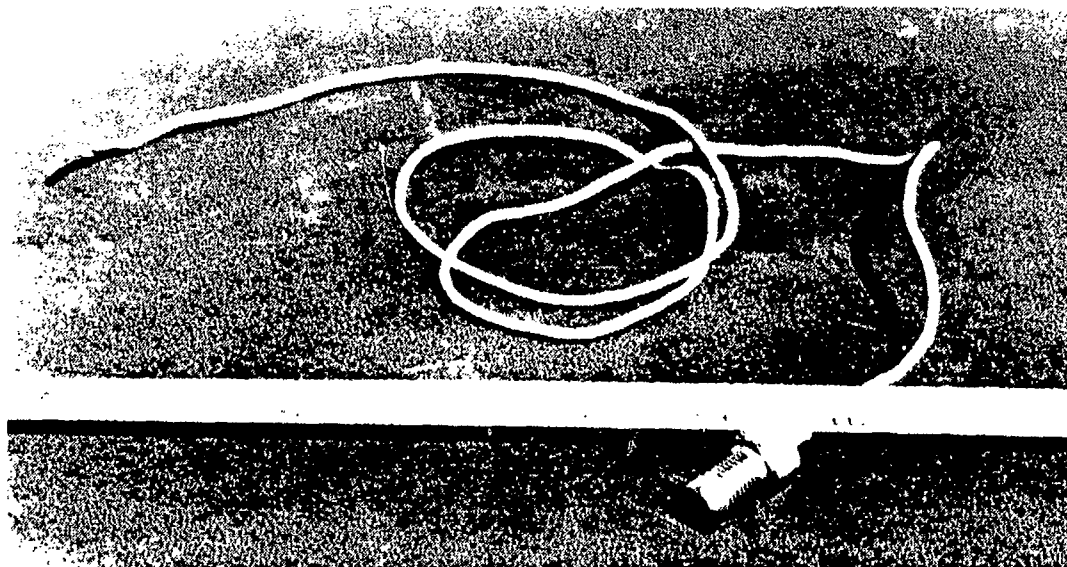
Figure C.3 Porewater pressure transducer.

diaphragm are from the water, and the voltage output represents only water pressure. This modification is described in Veyera (1985).

The second modification was performed locally to waterproof all but the perforated end plate of the transducers since the transducers were to be placed in saturated sand. Waterproofing was accomplished by embedding each transducer in casting resin. The mold was a 35 mm plastic film container, and the perforated end plate was protected by placing it through a hole in one end of the film container. The transducer cable was routed through a brass tube, one end of which was sealed to the body of the transducer with vacuum grease. This tube was placed through a hole in the film container lid, and the container was then filled with the casting resin. Once the resin hardened (about 24 hours), the mold was cut away, and a

coating of epoxy was placed around the protruding brass tube and perforated end plate for added waterproofing. The cable was next routed through a vinyl tube which was secured over the brass tube with a radiator hose clamp. Figures C.3 and C.4 are photographs of pressure transducers before and after waterproofing. A set of detailed procedures for waterproofing the transducers is provided in Appendix D.

C.3 ACCELEROMETERS

ENDEVCO Model 2264A-5K-R piezoresistive accelerometers were selected to measure acceleration in the soil during passage of the stress waves. The specifications for these accelerometers are given in Table C.2. As with the pore pressure transducers, it was necessary to waterproof the accelerometers. Casting resin was also used for this task. The mold was a 7.6 cm diameter by 2.54 cm high polyvinyl chloride disc. The disc was half filled with resin, and the accelerometer base plate was embedded in the resin as it began to set (approximately 45 minutes after mixing). A 0.3 cm thick piece of foam was placed on top of the accelerometer. The foam was coated with vacuum grease to prevent direct contact of the accelerometer and the resin. The accelerometer cable was routed through a brass tube which protruded through a hole in the side of the mold. To increase the average density of the casting resin to approximately that of the soil, 55 grams of lead beads were embedded in the resin around the accelerometer. A small section of aluminum screening was placed over the accelerometer for reinforcement and the mold was completely filled with resin. As with the pore pressure transducers, the accelerometer cable was routed through a vinyl tube secured to the brass tube with a
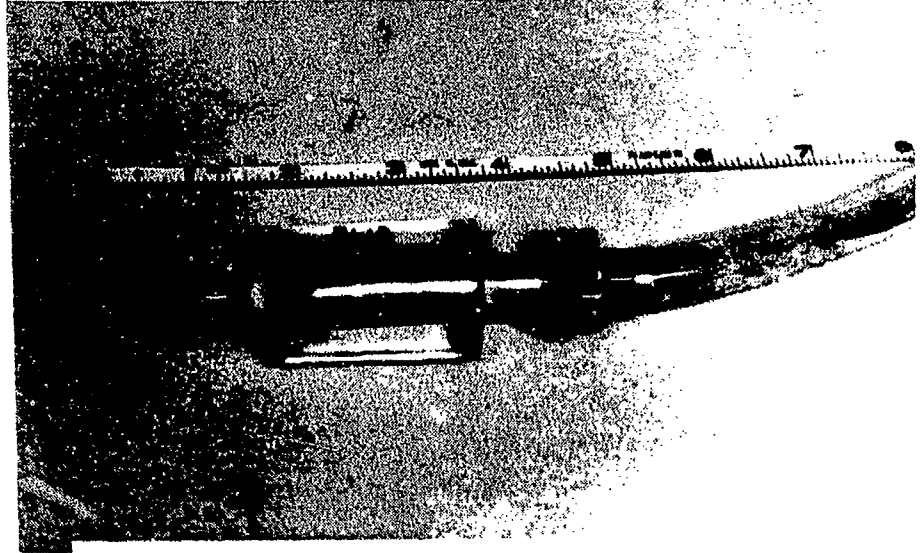
Figure C.4 Waterproofed porewater pressure transducer.

Table C.2.   ENDEVCO Model 2264A-2K-R Accelerometer

Specifications

Range	± 2000 g
Output, full scale	500 mV
Damping factor	0.002 typical
Excitation	10.00 VDC
Input resistance	500 ± 100 ohms
Output resistance	500 ± 100 ohms
Sensitivity at 10VDC	0.250 typical mV/g
Sensitivity at 10VDC	0.175 minimum *
Mounted resonance frequency	30,000 Hz
Acceleration limits	± 5000 g
Frequency Response	0 to 5000 Hz
Temperature	-18 to +66 °C
Size	13 mm x 5 mm x 12 mm
Weight	1.5 gm

radiator hose clamp. Figures C.5 and C.6 are photographs of accelerometers before and after waterproofing. A detailed procedure describing the waterproofing method is provided in Appendix D.

C.4   SIGNAL CONDITIONERS

An ENDEVCO Universal Signal Conditioning System, Series 4470, provided excitation voltage to the pore pressure transducers and accelerometers and amplified the output voltages. The master module of this system consists of a regulated power supply, calibration circuitry, and passive conditioning circuitry. All components are routed through mode cards, which are calibrated for specific transducers. The signal conditioners were mounted in ENDEVCO's Model 4942 Rack Adapter. Table C.3 provides specifications for the signal conditioners. Figure C.7 is a photograph showing conditioners mounted in the rack before being placed in the instrumentation relay building.

C.5   TOTAL STRESS GAGES

Kulite LQ-080U series soil stress gages were used to measure the total stress in the soil during the dynamic events. These stress gages have a pair of stiff diaphragms with a diameter to thickness ratio greater than 5 and a diameter to deflection ratio greater than 2000. The gage is energized by applying 10 volts DC. The sensing element is comprised of four active semiconductor strain gages bonded to the measuring diaphragm. The unit is waterproofed during manufacture. Specifications for this gage and a photograph are given in Figure C.8.
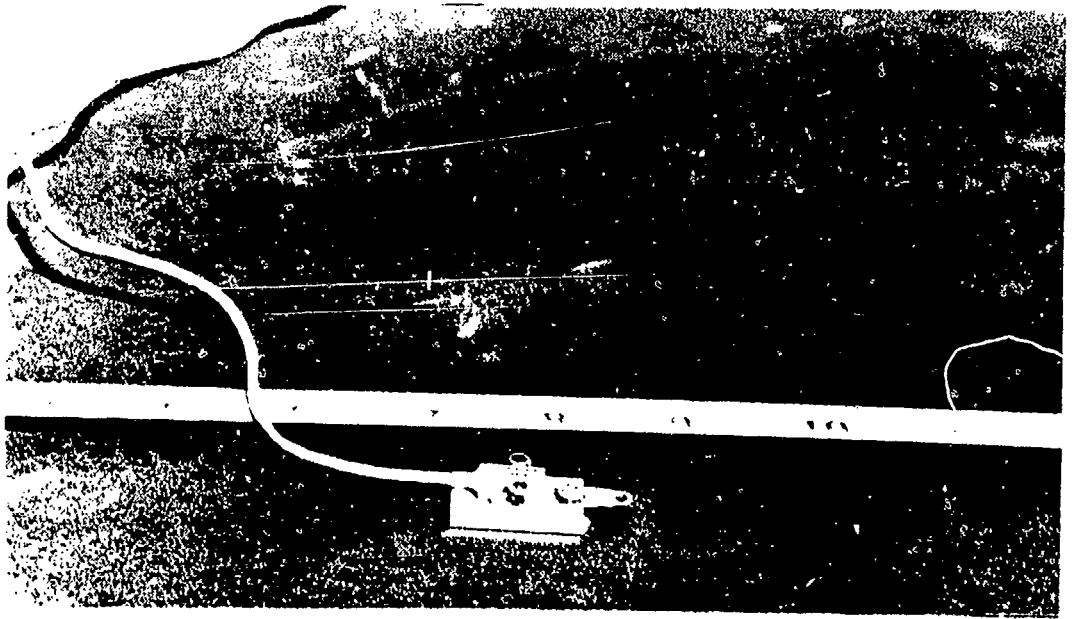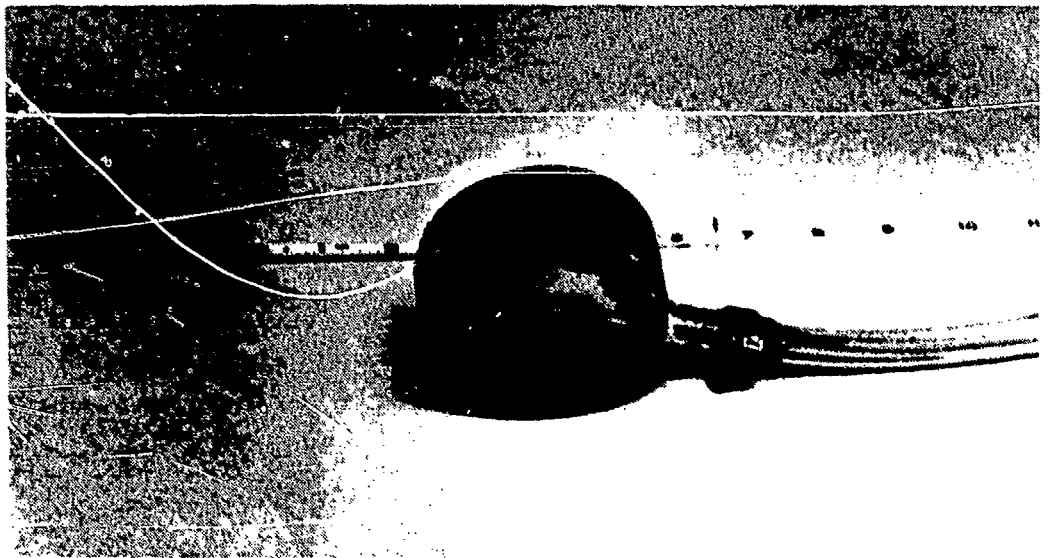
Figure C.5   Accelerometer.

Figure C.6   Waterproofed accelerometer.

Table C.3. ENDEVCO Universal Signal Conditioning System Series 4470
with 4476.1A Mode Card

Specifications

| Input Characteristics	
Transducers	2 or 4 arm resistive elements
Input Impedance	1 megaohm maximum
Source Resistance	2000 ohms maximum
Overload Recovery Time	50 microseconds
Common Mode Rejection	80 dB minimum at 60 Hz
	70 dB minimum at 1000 Hz
Common Mode Voltage	5 V peak, maximum
Output Characteristics	
Output Voltage	
Full Scale	± 2.5 V peak
Overvoltage	± 7.5 V peak maximum
Linear Output Current	± 10 mA peak maximum
Output Impedance	less than 20 ohms
Noise and Ripple	2 mV rms, maximum
Capacitive Load Effect	stable to 10 microfarads
Zero Stability and	
Temperature Coefficient	0.2% of FS for 24 hours plus
	0.02% per degree F
Transducer Excitation Regulator	
Output Voltage	Adjustable 9.5 to 10.5 VDC
Output Current	0 to 50 mA DC
Line and Load Regulation	Less than 0.2% change for line voltage change 95 to 135 VAC and load change 2000 to 300 ohms
Temperature Stability	Less than 0.005% per degree C over temperature range (-12° C to + 65° C)
Time Stability	Less than 0.03% for 48 hours
Transfer Characteristics	
Gain Ranges	Full Scale Output (FSO) for 20, 40, 60, 80, or 100% of full range acceleration
Accuracy	± 1.5% of full scale
Frequency Response	± 5% DC to 20,000 hz
Gain Stability	less than ± 0.1% for 24 hours plus ± 0.009% per degree C
DC Linearity	less than ± 2.5 mV
Balance Limiting	40.2 kilohm resistor

Figure C.7   Signal conditioners.

KULITE

LQ-080U

SOIL STRESS GAGE

Designed and developed in cooperation with the U.S. Army Corp of Engineer Waterways Experiment Station, Vicksburg, Mississippi.
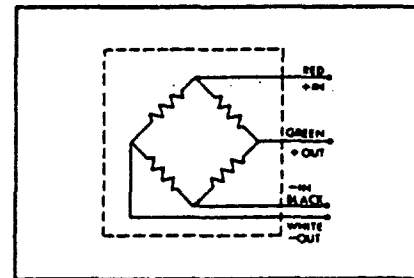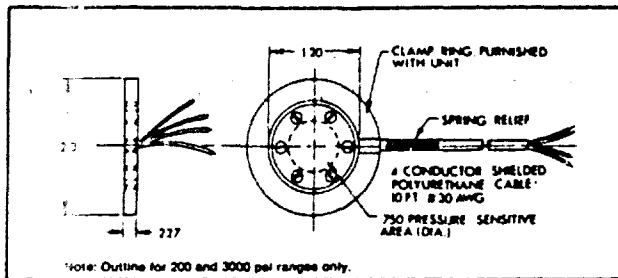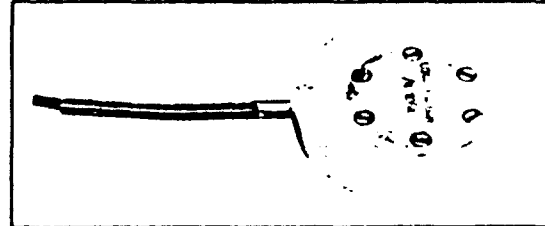
The LQ-080U series of soil stress gages are designed to meet the requirements of the civil engineering field to make accurate measurements of blast induced soil reactions.

Inclusion of a gage in soil disrupts the stress field and induces either stress concentrations or reliefs depending on gage thickness. This stress-transfer phenomenon can seriously affect gage accuracy. To overcome this problem, the LQ-080U employs a pair of extremely stiff diaphragms with a diameter-to-thickness ratio of greater than 5 and a diameter-to-deflection ratio of greater than 2000, this design together with good gage-medium matching ensures accuracy and repeatability of readings.

The DC energized sensing element of the LQ-080U comprises 4-active semiconductor strain gages directly bonded to the measuring diaphragms. The output may be conveniently monitored on most conventional instrument systems. During assembly, the entire unit is given a conformal coating to prevent any ingress of moisture after final on-site installation.

The LQ-080U Series is available calibrated or uncalibrated, with or without mounting ring.

SPECIFICATIONS

Pressure Range	200 psi	3000 psi	10,000 psi
Overpressure With No Change in Calibration	300%	200%	130%
Rated Electrical Excitation	10V (Nom), 12V (Max)		
Full Scale Output	900mV (Nom) for (H)	560mV (Nom) for (L)	
Input Impedance	350 Ohms (Nom)		
Output Impedance	350 Ohms (Nom)		
Operating Temperature	$-40°F$ to $+200°F$		
Combined Non-Linearity, Hysteresis and Repeatability	$\pm 0.5\%$ of F.S.		
Natural Frequency	50KHz (Nom) for (H)	17KHz (Nom) for (L)	
Acceleration Sensitivity Normal to Diaphragm	Less than 0.1 psi/G for (H) and .03 psi/G for (L)		
Response Time (To Step Input)	Less than 6×10^{-6} sec.		

Figure C.8 Total stress gage (Kulite specification sheet).

C.6   TRANSIENT DATA RECORDER

A Transient Data Recorder System (Pacific Instruments Model 9820) was used to record the dynamic test data from the pressure transducers, accelerometers, and total stress gages. The TDR digitizes the incoming analog signal at a programmable rate of up to 500,000 samples per second and stores the digitized data in memory. Triggering of the TDR can either result from exceeding a pre-programmed voltage signal level or from an external source such as the detonation circuitry. Data may be transferred for processing at rates up to 500 bytes per second. The TDR's are shown in Figure C.9. For additional information on this system refer to Charlie, et al. (1987).

C.7   STRAIN GAGES

In order to measure soil strain, inductive coil strain gages were locally manufactured (Figure C.10) and used with a Bison Soil Strain Gage, Model 4101A (Table C.4). These gages are used in pairs by applying a known voltage input to one and reading the change in induced voltage output in the other. The output voltage is a function of the distance between coils. The gages were manufactured by winding a 0.321 mm diameter (number 28) coated wire 80 times (Figure C.11) into an 8.9 cm nominal diameter, flat coil. The coil was then embedded in casting resin. The inner and outer ends of the coil wire were soldered to the inner core and outer shields of RGU-58 coaxial cable (through which voltage was sent). The result was a 15 cm diameter by 2 cm high resin disk with coaxial cable emerging from the side (Figures C.10 and C.12). The entry point of the cable was coated with adhesive, and the entire gage was covered with latex for waterproofing.
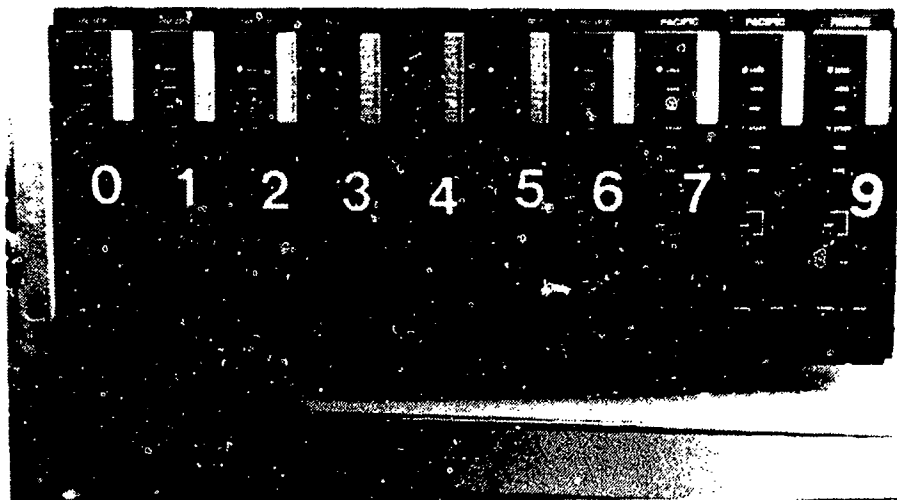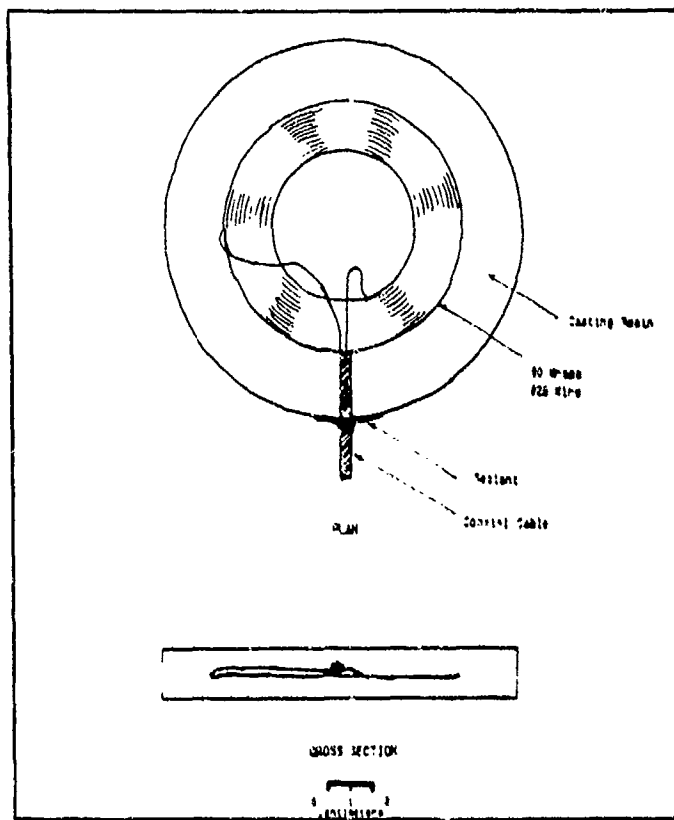
Figure C.9   Transient data recorder system.

Figure C.10   Views of strain gage.

Table C.4. Bison Soil Strain Gage Model 4101A

Specifications

Excitation Characteristics	
Frequency	20 kHz
Amplitude	15 volts peak to peak
Total Harmonic Distortion	0.3%
Short Term Frequency	
Stability	$\pm$ 0.1%
Response Time	0.25 msec
Output Voltage	$\pm$ 5 volts to full scale meter deflection
	$\pm$ 10 volts linear for recorders
Maximum Sensitivity	0.1% strain per volt
Resolution	infinite on recorder
	0.01% strain on meter
Temperature	operating range 0° to 70°C
	error 10 mV per 1°C at maximum sensitivity
Signal to Noise Ratio	50 to 1
Cable Length	0 to 305 m
Power Supply	+ 12 volt 1.2 ampere hour

Figure C.11   Wrapping strain gage coils.

Figure C.12   Strain gage.

Pairs of strain gages were calibrated in air with the Bison Soil Strain Gage (Figure C.13) by applying an input voltage to one and reading the output voltage induced from the other at various separation distances. Figure C.14 is a typical calibration curve for a pair of strain gages.

C.8   PIEZOMETER

A piezometer and video cassette recording system were used in the tests to provide information on late time porewater pressure responses. The piezometer was made using a vinyl tube, 10 mm outer diameter by 6 mm inner diameter by 2.44 m long. The vinyl tube was attached to a 0.6 m wide by 2.4 m high plywood board painted light blue and marked at 30.5 cm (1 foot) increments. The base of the plywood was 2.4 m above the rim of the tank. The lower end of the vinyl tube was secured to a 1.9 cm steel pipe at the top of the steel tank. The steel pipe was continuous down the side of the tank, where it was secured to a 7.6 cm diameter perforated PVC pipe spanning the bottom of the tank 1.68 m below the rim. Red dye was injected into the upper end of the piezometer tube prior to its use to permit better visibility of the water in the tube.

C.9   VIDEO CASSETTE RECORDING SYSTEM

The video cassette recording system consisted of two Panasonic Model WV3240/12X cameras, a Panasonic Model NV8420 portable recorder, and a Panasonic Model NV8950 video cassette recorder. The cameras were used to record piezometer response immediately following detonations. The cameras had built in timers which read to the
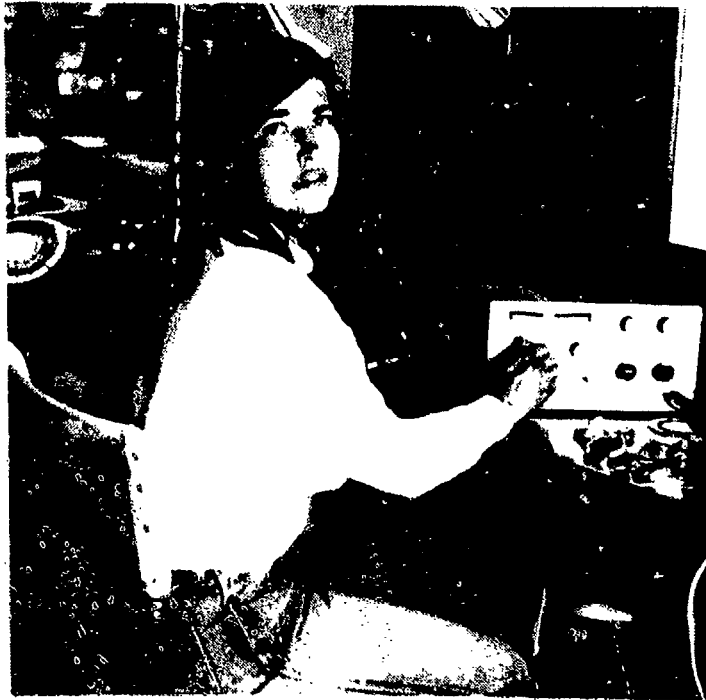
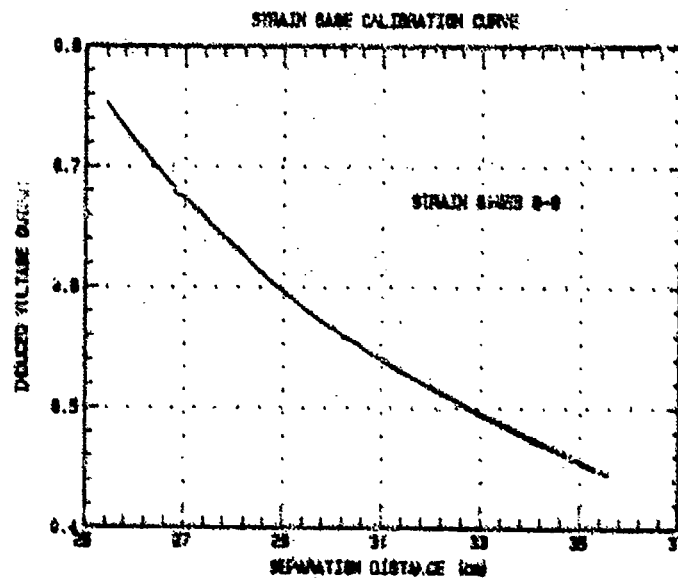Figure C.13   Bison Soil Strain Gage.

Figure C.14   Typical strain gage calibration curve.

nearest 0.01 second. Using this system, water level in the piezometer tube was recorded as a function of time.

C.10 PERSONAL COMPUTER SYSTEM

An IBM-XT personal computer was used to analyze all data. The computer was configured with 640 kilobytes of random access memory, a 360 kilobyte floppy disc drive, a high speed 10 megabyte hard disk, and an 8087 math coprocesser. Two serial and three parallel ports were used to drive an Epson dot matrix printer and a Hewlett-Packard 7475 plotter. An IEEE-488 connection interfaced with the TDR's.

The software included DEMOGPIB, a program to communicate with the TDR's, written by Pacific Instruments Incorporated; STATGRAPHICS by S.T.S.C., Incorporated, for data management, statistical and numerical functions, and plotting; and WORDMARC by MARC Software International, Incorporated for word processing. Additional information on this computer system is found in Charlie, et al. (1987).

APPENDIX D

WATERPROOFING INSTRUMENTATION

This appendix provides the detailed procedures for waterproofing the ENDEVCO pore pressure transducers and accelerometers. Procedures were locally developed with frequent consultation with ENDEVCO representatives.

Figure D.1 is a photograph showing the materials used and a waterproofed transducer and accelerometer. Figures D.2 and D.3 are drawings of the transducers.

D.1   ENDEVCO SERIES 8511 PIEZORESISTIVE PRESSURE TRANSDUCERS

The materials and procedures for waterproofing the pressure transducers are given in this section.

D.1.1   Materials

1. Acetone

2. Instrumentation cable extensions

3. 35 mm plastic film canisters

4. 3/8" diameter brass tubing, 3" long[*]

5. Poly-flo tube, 1/8" diameter, 0.040" wall thickness[*]

6. Vinyl tubing, 1/2" outer diameter, 1/16" wall thickness

7. Electric tape

8. Stainless steel pipe clamps (1/8-5/8" variable diameter)[*]

9. Emery cloth

Figure D.1 Materials for waterproofing transducers
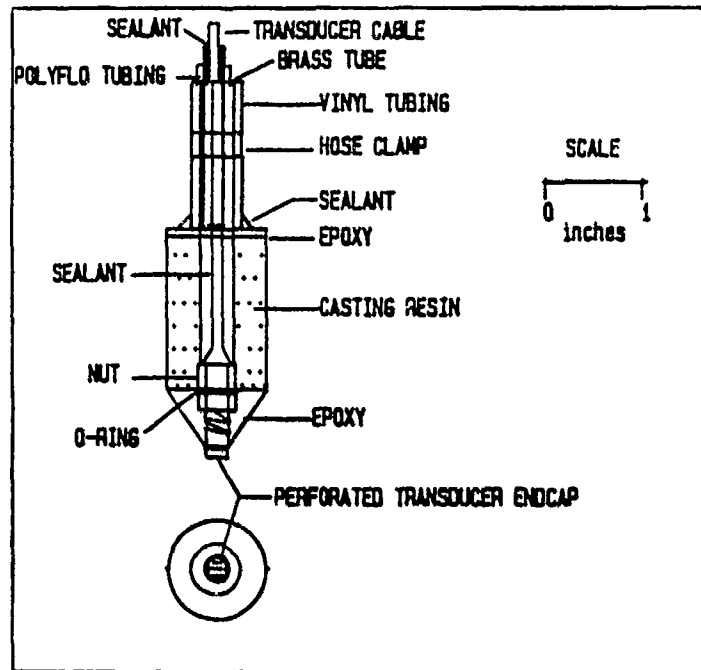
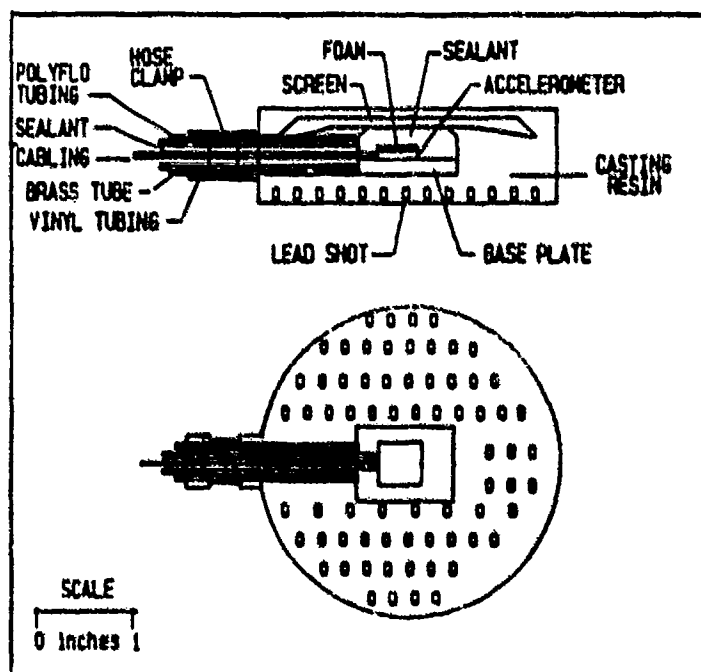Figure D.2 Porepressure transducers - waterproofing.

Figure D.3 Accelerometer - waterproofing.

10. Heat shrink tubing, 3/8" diameter*

11. Rosin core solder

12. Epoxy (Epoxy-patch[R], The Dexter Corporation, Hysol Division)

13. Casting resin (Chemco Clear Liquid Plastic Casting Resin[R])

14. Silicon vacuum grease (Dow Corning High Vacuum Grease[R])

15. Adhesive (Elmer's Stix-All High Technology Adhesive[R])

16. Vinyl cement (V.L.P. Clear Vinyl Liquid Repair[R], P.D.I., Inc.)

17. O-rings to fit over transducer end

18. Brass nuts to fit transducer threads

D.1.2   Procedure

1. Using a dull bladed pipe cutter, dimple around brass tubing every 1/2.*

2. Clean brass tubing with emery cloth/acetone.

3. Punch 3/8" hole in center of bottom of film canister.*

4. Punch 3/8" hole in center of film canister lid*.

5. Place silicon grease on base of transducer and around cable where cable enters transducer body. Do not cover holes in end of transducer.

6. Place brass washer and O-ring on threads of transducer and bring snug against groove.

7. Slide brass tube over transducer cable into contact with the silicon grease, making a seal between the transducer and the brass tube. Add additional grease as necessary.

8. Place transducer in canister (with threaded end through hole in bottom of canister).

9. Hand tighten nut on transducer threads to seal O-ring to bottom of canister.

10. Remove all grease and residue from brass tube and transducer except where cable emerges from transducer and enters tube.

11. Fill brass tube 1/3 full of grease using a syringe.

12. Mix sufficient casting resin to fill canister (use ratio of 4 drops catalyst per ounce of resin).

13. Place canister in upright position and fill with casting resin; insure that the silicon grease seal between brass tube and transducer is maintained.

14. Place lid on canister.

15. After 24 hour minimum cure (room temperature) remove nut and O-ring from transducer and remove casting from mold.

16. Replace O-ring and nut on transducer and tighten nut to form a seal between transducer threads and resin.

17. Mix epoxy and place 1/8" layer on resin around brass tube insuring that epoxy is in contact with entire circumference of brass tube and end of resin casting.*

18. Mix epoxy and apply 1/8" layer to other end of canister, covering the O-ring and nut entirely. Do not cover holes in end of transducer. Let epoxy harden (approximately one hour).*

19. Using a syringe, inject adhesive inside of brass tube around cable. Fill entire tube and avoid entrapping air.

20. Slide 4" piece of Poly-flo tubing over cable and embed in wet adhesive inside of the brass tube.

21. Add additional adhesive in and around Poly-flo tubing to form a thorough seal. Let adhesive cure.

22. If an extension cable is to be used, see steps 28-33.

23. Feed cable into vinyl tubing. Where cable emerges from tube, loop it (inside of vinyl tube) to provide slack.

24. Wrap several layers of electric tape around vinyl tube 1" from end nearest canister.*

25. Place silicon grease at base of brass tube and slide vinyl tube over brass tube making contact with grease.

26. Secure vinyl tube to brass tube by tightening pipe clamp over electric tape.

27. Use vinyl cement to repair vinyl tubing as necessary.

The following procedure is for adding extension cable.

28. Solder transducer cable wires to extension cable wires.

29. Place heat shrink tubing over each soldered joint and shrink to fit.

30. Coat joints with silicon grease.

31. Place heat shrink tubing over coated joints (extending 1/2" beyond silicon in both directions); shrink to fit.*

32. Place Poly-flo tubing over joint and seal with grease.

33. Return to step 23.

*Note: to convert from inches (") to centimeters, multiply by 2.54.

D.2.   ENDEVCO SERIES 2264A PIEZORESISTIVE SHOCK ACCELEROMETERS

This section provides a list of materials and detailed procedures for waterproofing the accelerometers.

D.2.1 Materials

1. Self sticking foam, approximately 1/8" thick[*]

2. Extension instrumentation cable

3. 3" diameter PVC sewer and pipe line, cut to 1" length[*]

4. 3/8" outer diameter brass tubing, 3" long[*]

5. Poly-flo tubing, 1/8" inner diameter, 0.040" wall thickness[*]

6. Vinyl tubing, 1/2" outer diameter, 1/16" wall thickness[*]

7. Aluminum window screen, cut into 2" diameter circle[*]

8. Stainless steel pipe clamp (1/4-5/8" variable diameter)[*]

9. Emery cloth

10. Heat shrink tubing, 3/8" diameter[*]

11. Rosin core solder

12. Epoxy (Epoxy-Patch[R], The Dexter Corporation Hysol Division)

13. Casting resin (Chemco Clear Liquid Plastic Casting Resin[R])

14. Silicon vacuum grease (Dow Corning High Vacuum Grease[R])

15. Adhesive (Elmer's Stix-All High Technology Adhesive[R])

16. Vinyl cement (V.L.P. Clear Vinyl Liquid Repair[R], P.D.I.. Inc.)

17. Electric tape

18. Lead shot (55 grams)

19. Silicon spray lubricant

20. Acetone

D.2.2 Procedure

1. Using a dull bladed pipe cutter, dimple around brass tube every 1/2".[*]

2. Clean brass tube with emery cloth/acetone.

3. Drill 3/8" hole through PVC mold, 1/2" from top.*

4. Place mold on flat, vinyl-like surface and seal around outside of bottom of mold.

5. Coat inside and bottom of mold with silicon lubricant.

6. Mix sufficient casting resin to fill half the mold. Use ratio of 4 drops catalyst to ounce of resin.

7. Pour liquid resin into mold to bottom of 3/8" hole.*

8. Let resin cure until it becomes gelled but not hard (approximately 45-60 minutes).

9. Clean bottom and sides of accelerometer base plate.

10. Place accelerometer cable through 3/8" hole (with accelerometer inside of mold).*

11. Place brass tube over cable and through 3/8" hole to within 1/4" of accelerometer-cable connection.*

12. Seal gaps between brass tube and 3/8" hole as necessary with silicon grease (on outside of mold).*

13. Embed accelerometer mounting plate horizontally in gelled resin. Depth of embedment should be approximately half the thickness of the plate.

14. Cut foam to dimension of top of accelerometer (0.48"x0.18") and stick on top of accelerometer.*

15. Carefully apply silicon grease to top of accelerometer, covering mounting plate, cable, and foam. Apply grease on cable and into end of brass tube. Form a continuous coating of silicon grease over accelerometer, around cable, and into brass tube.

16. Inject grease into brass tube, filling it about 1/3 full from end nearest accelerometer.

17. Mix sufficient casting resin to fill mold. Use ratio of 2 drops of catalyst to ounce of resin.

18. Bend screen into an arc and embed in resin over accelerometer.

19. Drop pre-weighed lead shot into liquid resin (spread evenly around accelerometer).

20. Allow resin to cure for at least 24 hours at room temperature.

21. Remove the PVC mold and clean brass tube with acetone.

22. Place 1/8" layer of epoxy on resin around brass tube insuring contact with entire circumference of tube.*

23. Using a syringe inject adhesive into brass tube around cable. Fill entire tube and avoid entrapping air.

24. Place 4" length of Poly-flo tubing over cable and slide tube into wet adhesive inside brass tube.*

25. Inject more adhesive into and around Poly-flo tubing from end furthest from accelerometer. Let adhesive cure.

26. If an extension cable is to be used, see steps 31-36.

27. Feed cable into vinyl tubing. Where cable emerges from tube, loop it (inside of vinyl tube) to provide slack.

28. Coat base of brass tube and resin with silicon grease. Slide vinyl tubing over brass tube insuring contact with grease.

29. Wrap several layers of electric tape around vinyl tube 1"
   from end nearest canister and secure vinyl tube to brass
   tube with pipe clamp (over electric tape).*

30. Use vinyl cement to repair vinyl tubing as necessary.

The following procedure is for adding extension cables.

31. Solder accelerometer cable wires to extension cable wires.

32. Place heat shrink tubing over each soldered joint and
   shrink to fit.

33. Coat joints with silicon grease.

34. Place heat shrink tubing over coated joints (and extending
   1/2" beyond silicon in both directions) and shrink to
   fit.*

35. Place Poly-flo tubing over joint and seal with grease.

36. Return to step 29.

* Note: To convert from inches (") to centimeters, multiply by 2.54

APPENDIX E

BLASTING PROCEDURES

Standard operating procedures for explosive testing at the Colorado State University Engineering Research Center (Abt and Patrone, 1983) were used for all explosive testing in this program. These procedures include county, state, and federal regulations. In addition, local procedures were developed for the testing described in this dissertation. A copy of these local procedures is included herein.

CIVIL ENGINEERING DEPARTMENT

303/491-5048

CSU
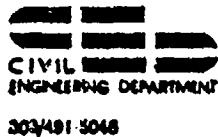
Colorado State University
Fort Collins, Colorado
80523

October 11, 1985

MEMORANDUM

TO: D. B. McWhorter - ERC
E. V. Richardson, ERC
F. W. Smith and F. A. Kulacki, Engineering College - Campus
C. N. Papadakis, Civil Engineering Dept. - Campus
J. H. Harper, Campus
W. Patzer - ERC
G. A. Greathouse, Animal Sciences Dept. - Campus
R. E. Taylor, Animal Sciences Dept. - Campus
W. I. Rahmeyer - ERC
Simons & Leu, Inc. - ERC, & Main Office   .
CSU Police Dept. - Campus (Tom Yates)
Larimer Sheriff's Dept. (Lt. Beam)
R. Conard - CSU
S. M. Waldrop, Environmental Health Services - Campus
S. A. Schumm, Earth Resources Dept. - ERC & Campus
Poudre Valley Fire Dept.

FROM: W. A. Charlie, Civil Engineering - CSU

SUBJECT: Use of small size buried explosives for Scientific Research
at CSU's Engineering Research Center

On or after October 15, 1985 we plan on conducting several tents
at the CSU Engineering Research Center (see attached location maps).
These tests will utilize small explosive charges which will be located
about 5 feet below the ground surface. As such, noise or ground
vibration will be minimal outside our research plot. Both noise and
ground vibration will be monitored at our site and along the site
boundaries. Noise control measures will be followed.

All blasting is being conducted under experienced and competent
supervision and will be done according to all applicable regulations
pertaining to explosives (University, County, State and Federal). Our
most important criteria is safety. Dr. Wayne Charlie and Dr. Steve Abt
are the P.I.'s and Tom Bretz is the site supervisor.

No explosives will be stored at our site. Warning signs will be
conspicuously posted around the site. When explosives are being
transported to the site and being placed a red flag will be up and only
authorized personnel will be admitted to the blasting site.

The following blasting signals will be sounded:

    WARNING SIGNAL   Series of long signals.
        (5 minutes prior to shot)

    BLAST SIGNAL   Series of Short signals
        (1 minute prior to shot)

    ALL CLEAR SIGNAL   One long signal

The following are EMERGENCY Phone Numbers:

        CSU Police 9-911
        Fire, Sheriff, Police, Ambulance 9-911

The research being conducted is a continuation of a three year laboratory study on the behavior of saturated soil under shock loads. These explosive field tests are needed to verify the experimental laboratory tests and theoretical models that were developed in the laboratory phase.

Two M.S. students and one Ph.D. student have received both funding and degrees from the laboratory phase. I expect three Ph.D. and three M.S. students will be able to receive degrees based on the field research. The research is being funded by the Air Force Office of Scientific Research.

Your cooperation is appreciated. If you have any questions, please feel free to contact me at 491-5354 or the following:

    OTHER PHONE NUMBERS

    Dr. Wayne Charlie   491-5354 (office)

                        491-8268 (site)
    Tom Bretz   482-8355 (home)
    Dr. Steve Abt   491-8203 (office)
    Dept. Civil Engineering   491-5048
    Environmental Health Services 491-6745
    CSU Police (Routine Calls) 491-6425
    CSU Emergency   9 - 911

WAC:taa

cc: Steve Abt   Mariann Kleinpeter
     Tom Bretz   Hassen Haasen
     Lynn Schure   Bill Bulter
     Dave Allard   Yu Pai Chen
     Lloyd Norquist   Field Site (to be posted)

N

COLORADO STATE UNIVERSITY MAP

APPENDIX F

ACCELEROMETER RECORDS

This appendix provides the available data records from accelerometers used in the testing described in this dissertation. The acceleration records were not used for the analysis because it was assumed the data were not representative of actual accelerations. The location of each accelerometer is described in Table 6.2 of Chapter 6. The records are shown in Figures F.1 through F.8 in which the vertical axis of each plot is in volts, where 1 volt equals 800 times the gravitational constant.
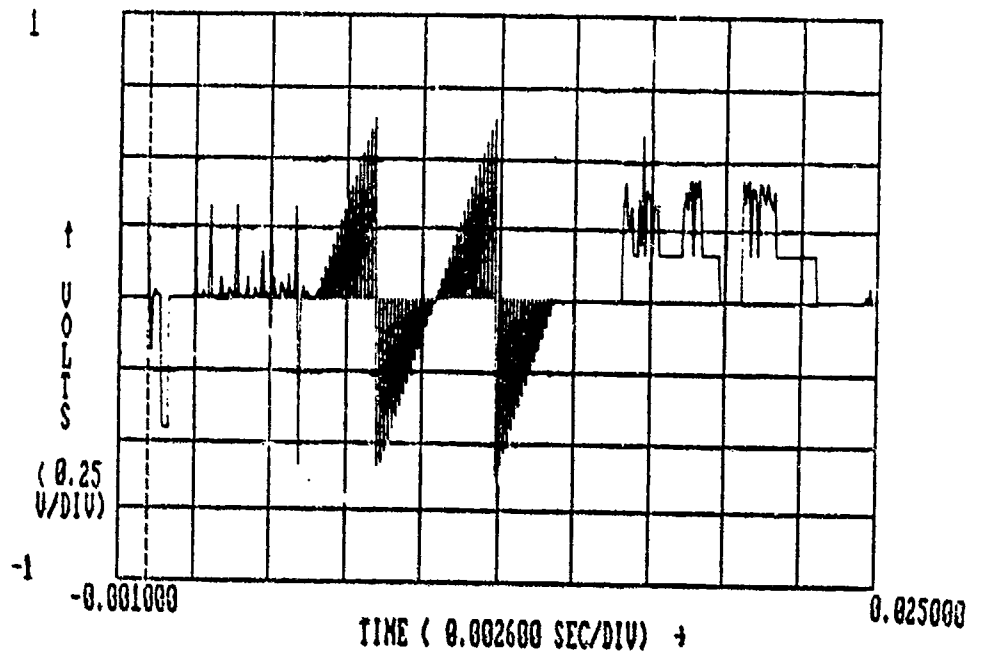
Figure F.1 Accelerometer CR53A, Test S2.
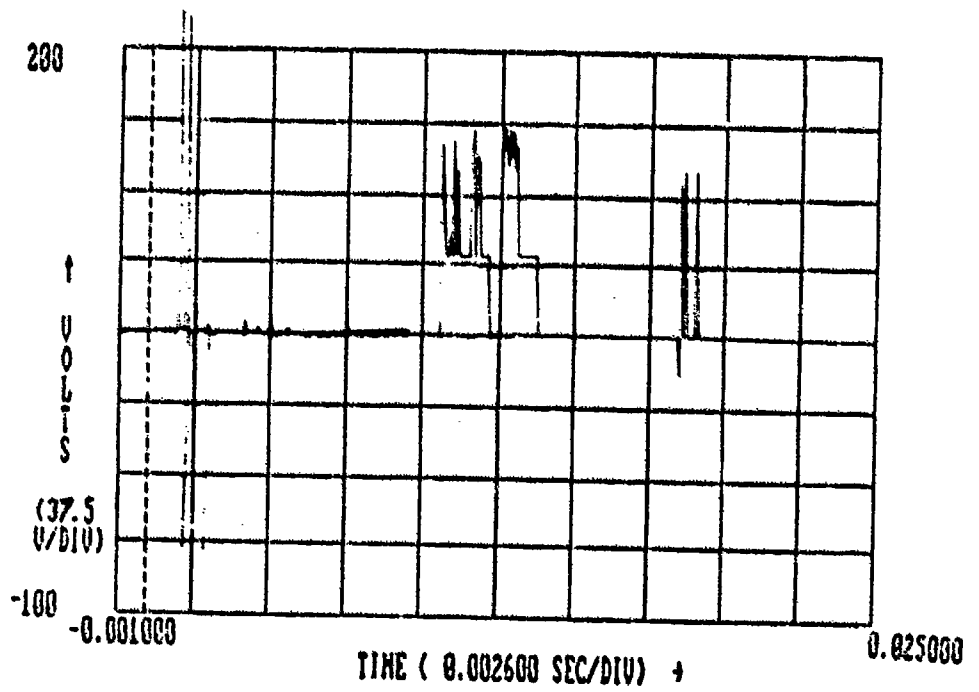
Figure F.2 Accelerometer CN82A, Test S2.
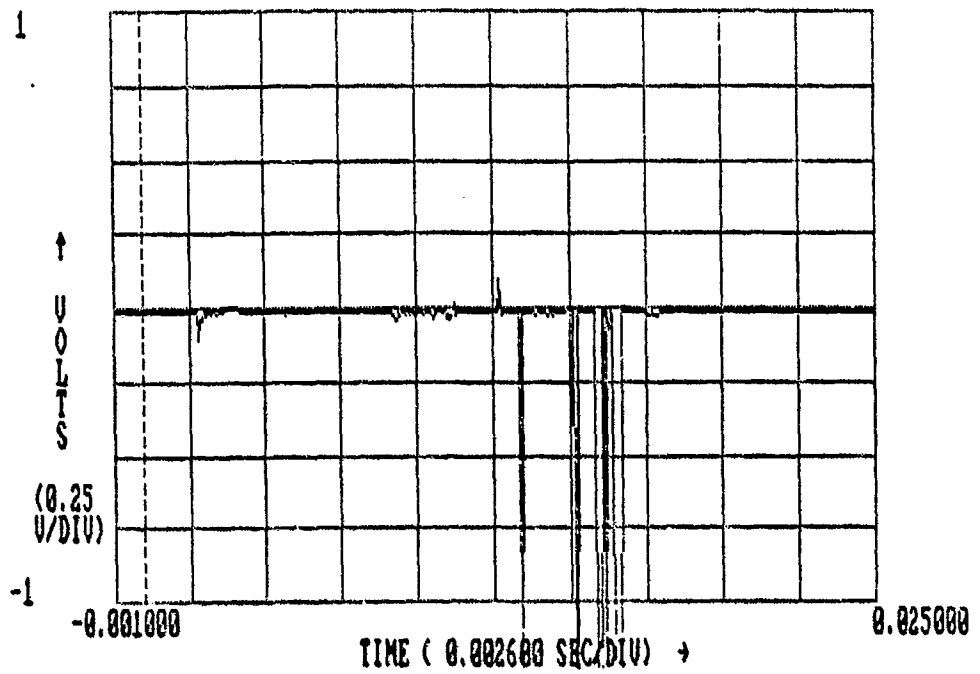
Figure F.3   Accelerometer CR53A, Test S3.
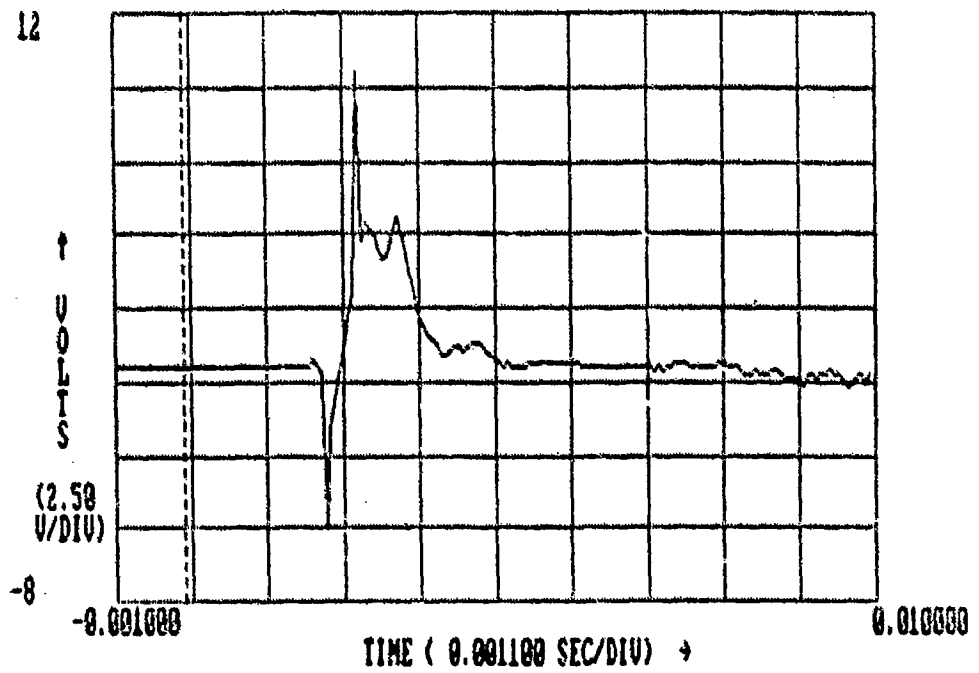
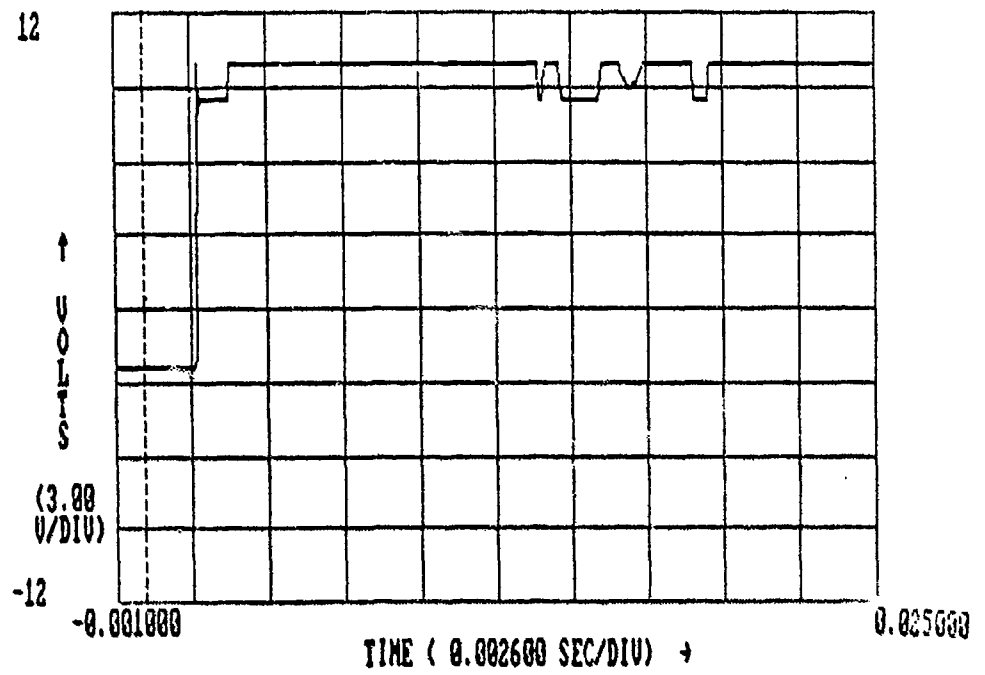Figure F.4   Accelerometer CR53A, Test S4.
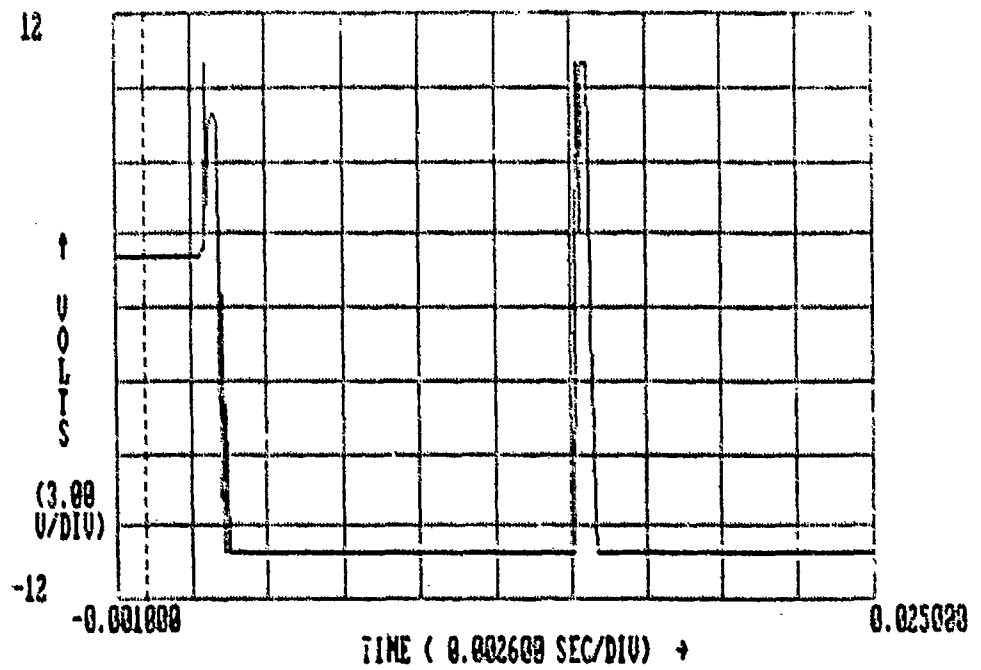
Figure F.5   Accelerometer CR53A, Test S5.

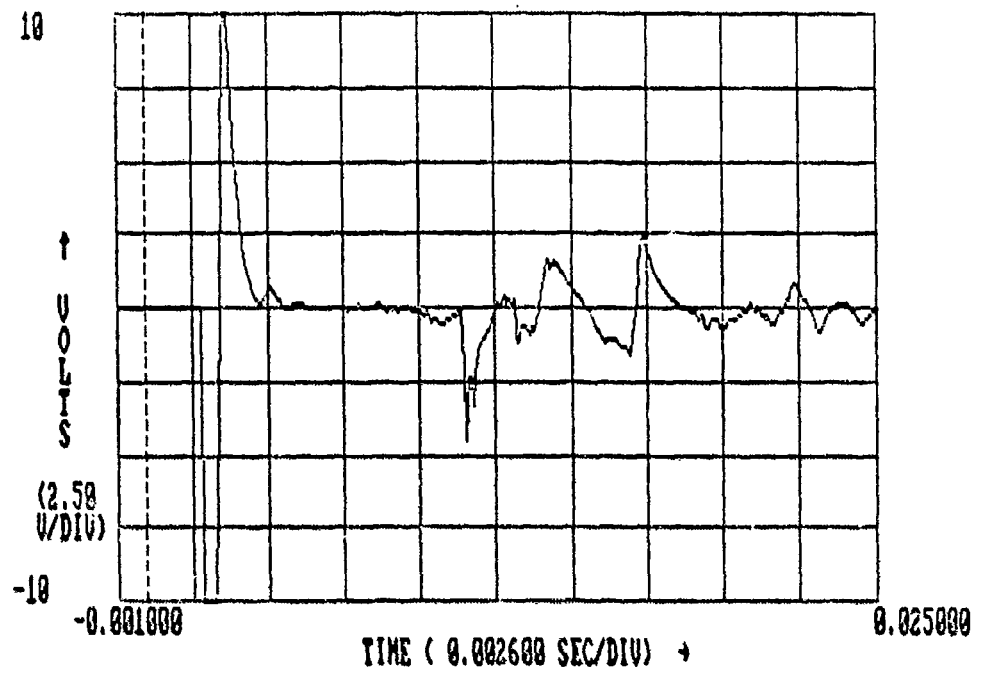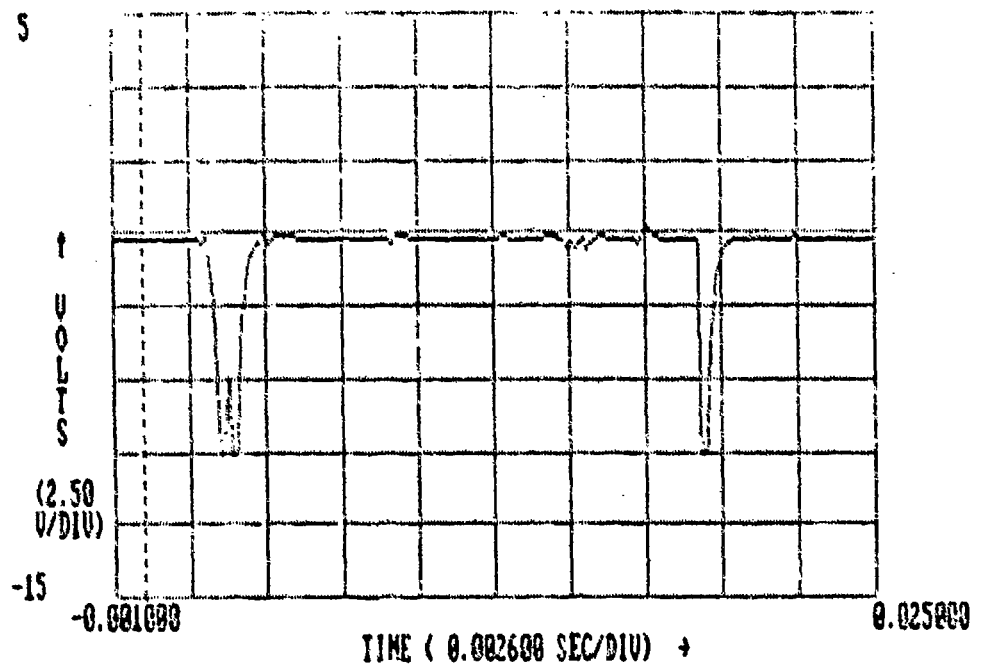Figure F.6   Accelerometer CN82A, Test S5.

Figure F.7 Accelerometer CR53A, Test S6.

Figure F.8   Accelerometer CN82A, Test S6.